

Structure near the  $K^- + p + p$  threshold in the in-flight  
 ${}^3\text{He}(K^-, \Lambda p)n$  reaction



Yuta Sada

佐田 優太

January, 2017



---

## Abstract

We have performed an experiment at J-PARC, E15, to search for an S=-1 dibaryonic state( $\bar{K}NN$ ) in the  ${}^3\text{He}(K^-, \Lambda p)n_{\text{missing}}$  reaction at 1.0 GeV/c. This is also a study of multi-nucleon absorption processes of  $K^-$  in in-flight reactions for the first time. The  $\Lambda$  and proton were detected with a cylindrical detector system which covered 49 to 131 degrees in the Lab., about 66% of  $4\pi$ , with the detection threshold of  $\sim 120$  MeV/c for low energy proton and  $\sim 30$  MeV/c for pions. The missing neutron was clearly identified in the missing-mass spectrum of X in the  ${}^3\text{He}(K^-, \Lambda p)X$  with a mass resolution of 45 MeV/c<sup>2</sup>. Thereby, a three-nucleon absorption mode of  $K^-ppn \rightarrow \Lambda + p + n$  were identified for the first time. From the Dalitz plot of these events, we can identify two components; one component widely distributed in the three-body phase space uniformly, and the other concentrates at a specific neutron energy in the forward direction in a low momentum transfer to the  $\Lambda p$  system. The former one is the first evidence of three-nucleon absorption following the three-body phase space. For the latter component, the  $\Lambda p$  invariant mass distribution showed a peak structure near the  $K^-pp$  threshold. From a fit with a Breit-Wigner type s-wave resonance introducing a gaussian form factor, a mass of  $2355^{+6}_{-8}$  (stat.)  $\pm 12$  (syst.) MeV/c<sup>2</sup> and a width of  $110^{+19}_{-17}$  (stat.)  $\pm 27$  (syst.) MeV/c<sup>2</sup> were obtained with a form factor parameter  $Q_x$  of 400 MeV/c.



# Contents

<b>1</b>	<b>Introduction</b>	<b>15</b>
1.1	Kaon nuclear bound state by strong interaction . . . . .	15
1.1.1	$\bar{K}N$ interaction . . . . .	15
1.2	Kaonic nuclear bound state . . . . .	22
1.2.1	$\Lambda(1405)$ . . . . .	22
1.2.2	kaonic nuclei . . . . .	22
1.3	Experiments to search for $\bar{K}NN$ bound state . . . . .	24
1.3.1	FINUDA experiment . . . . .	24
1.3.2	DISTO experiment . . . . .	25
1.3.3	OBELIX experiment . . . . .	26
1.3.4	HADES experiment . . . . .	26
1.3.5	LEPS experiment . . . . .	27
1.3.6	E27 experiment . . . . .	27
1.4	Theoretical situation of $\bar{K}NN$ bound state . . . . .	29
1.5	Summary of $\bar{K}NN$ situation . . . . .	30
1.6	J-PARC E15 experiment . . . . .	31
1.6.1	Semi-inclusive analysis of ${}^3\text{He}(K^-, n)$ reaction . . . . .	31
1.7	Exclusive analysis of ${}^3\text{He}(K^-, \Lambda p)n$ reaction . . . . .	33
1.8	Thesis overview . . . . .	35
<b>2</b>	<b>Experimental setup</b>	<b>37</b>
2.1	Overview of Apparatus . . . . .	37
2.2	Accelerator facility and primary beam line . . . . .	38
2.3	K1.8BR beam line . . . . .	40
2.4	Beam line detectors . . . . .	43
2.4.1	Beam hodoscope counter (BHD) . . . . .	43
2.4.2	Time zero counter (T0) . . . . .	43
2.4.3	Beam definition counter (DEF) . . . . .	43
2.4.4	Aerogel Cherenkov counter . . . . .	45
2.4.5	Beam momentum analyzer . . . . .	46
2.4.6	Vertex chamber (BPC) . . . . .	50
2.5	Target system . . . . .	51
2.5.1	Target cell . . . . .	51
2.5.2	The density of ${}^3\text{He}$ liquid target . . . . .	51
2.6	Cylindrical detector system . . . . .	53

2.6.1	Solenoid magnet . . . . .	53
2.6.2	Cylindrical drift chamber (CDC) . . . . .	56
2.6.3	Cylindrical detector hodoscope (CDH) . . . . .	58
2.6.4	Inner hodoscope counter (IH) . . . . .	58
2.6.5	Backward proton counter (BPD) . . . . .	59
2.7	Forward TOF detector system . . . . .	60
2.7.1	Beam sweeping magnet . . . . .	60
2.7.2	Neutron time-of-flight counter (NC) . . . . .	61
2.7.3	Charge veto counter (CVC) . . . . .	61
2.7.4	Proton time-of-flight counter (PC) . . . . .	62
2.7.5	Forward drift chamber (FDC) . . . . .	62
2.7.6	Beam veto counter (BVC) . . . . .	62
2.8	Trigger and Data Acquisition system (DAQ) . . . . .	64
2.8.1	Trigger scheme . . . . .	64
2.8.2	DAQ efficiency . . . . .	66
2.8.3	Trigger efficiency . . . . .	66
2.8.4	Data summary . . . . .	66
<b>3</b>	<b>Data Analysis</b>	<b>69</b>
3.1	Outline of the Data Analysis . . . . .	69
3.1.1	Definition of the axis coordinate . . . . .	69
3.2	Common procedure of all detectors . . . . .	70
3.2.1	Conversion to the time of TDC data . . . . .	70
3.2.2	Conversion to the gain of ADC data . . . . .	70
3.2.3	Time-walk correction for scintillation counters . . . . .	70
3.3	Beam analysis . . . . .	72
3.3.1	Single T0 hit event Selection . . . . .	72
3.3.2	TOF measurement between T0 and BHD for kaon identification . . . . .	72
3.3.3	Analysis for beam-line chambers . . . . .	74
3.3.4	Performance of the beam line chambers . . . . .	78
3.3.5	Distributions of the beam at final focus . . . . .	78
3.3.6	Beam momentum reconstruction . . . . .	80
3.3.7	Resolution of beam momentum . . . . .	80
3.3.8	Fine tuning of the absolute values of the beam momentum . . . . .	82
3.3.9	Event selection . . . . .	82
3.4	Effective luminosity . . . . .	84
3.4.1	Decay and reaction loss . . . . .	84
3.4.2	Summary of effective luminosity . . . . .	84
3.5	CDS analysis . . . . .	86
3.5.1	CDC hit calibration . . . . .	86
3.5.2	Track finding and reconstruction . . . . .	86
3.5.3	Associated CDH hits search and CDH calibration . . . . .	91
3.5.4	Vertex reconstruction . . . . .	91
3.5.5	Particle identification . . . . .	91
3.5.6	Fine correction of CDS track . . . . .	92

3.5.7	CDH calibration . . . . .	93
3.6	CDS performance . . . . .	94
3.6.1	CDC position resolution . . . . .	94
3.6.2	CDC momentum resolution . . . . .	95
3.6.3	Vertex resolution . . . . .	95
3.6.4	CDH performance . . . . .	95
3.6.5	Fiducial volume selection . . . . .	97
3.7	Adjustment of the CDS magnetic field strength . . . . .	97
3.8	CDC tracking efficiency . . . . .	101
3.8.1	tracking efficiency for a single track . . . . .	101
3.9	Event reconstruction for ${}^3\text{He}(K^-, \Lambda p)n$ reaction . . . . .	103
3.9.1	${}^3\text{He}(K^-, pp\pi^-)$ event selection . . . . .	103
3.9.2	Log-likelihood method for $\pi^-p$ pair selection . . . . .	103
3.9.3	Definition of the log likelihood function . . . . .	105
3.10	Detection efficiency . . . . .	107
3.11	Resolution of $\Lambda p$ invariant mass and missing mass of ${}^3\text{He}(K^-, \Lambda p)$ . . . . .	108
<b>4</b>	<b>Results and discussion</b>	<b>111</b>
4.1	${}^3\text{He}(K^-, \Lambda p)X$ events . . . . .	111
4.2	${}^3\text{He}(K^-, \Lambda p)n$ events . . . . .	111
4.3	Multi-nucleon absorption of $K^-$ . . . . .	112
4.3.1	Contamination of other processes in “ $\Lambda pn$ ” events . . . . .	114
4.3.2	Simulation study for expected processes in ${}^3\text{He}(K^-, \Lambda p)$ analysis . . . . .	114
4.3.3	Result of Multi-channel global fit . . . . .	116
4.3.4	Distribution of the $M_{\Lambda p}$ and $\cos\theta_n^{CM}$ . . . . .	117
4.4	Candidates for the peak structure . . . . .	120
4.4.1	Scattered $\bar{K}$ absorption ( $K^-N \rightarrow \bar{K}N$ following $\bar{K}NN \rightarrow \Lambda p$ ) . . . . .	120
4.4.2	$2NA + \Sigma\Lambda$ conversion ( $K^-NN \rightarrow \Sigma N$ following $\Sigma N \rightarrow \Lambda p$ ) . . . . .	120
4.4.3	$\Lambda(1405)\Lambda$ conversion ( $K^-NN \rightarrow Y^*N$ following $Y^*N_s \rightarrow \Lambda p$ ) . . . . .	121
4.4.4	Deeply bound $\bar{K}NN$ state . . . . .	121
4.5	S-wave single-pole structure . . . . .	123
4.5.1	Total cross section of each process . . . . .	124
<b>5</b>	<b>Conclusion</b>	<b>129</b>
<b>A</b>	<b>Target system</b>	<b>133</b>
A.1	Mechanism of cooling . . . . .	133
A.2	Performance of the operation . . . . .	133
<b>B</b>	<b>Forward Counter analysis</b>	<b>137</b>
B.1	NC hit selection . . . . .	137
B.1.1	Charged particles removal . . . . .	137
B.1.2	$\gamma$ - neutron separation with $1/\beta$ distribution . . . . .	137
B.2	Momentum resolution of the neutrons . . . . .	138
B.3	Precision of the Missing mass scale . . . . .	138
B.3.1	${}^3\text{He}(K^-, K^-pn)X$ reaction . . . . .	139

B.3.2	${}^3\text{He}(K^-, K_s^0 pn)X$ reaction . . . . .	140
B.3.3	${}^3\text{He}(K^-, K_s^0 n)X$ reaction . . . . .	140
<b>C</b>	<b>Simulation study for expected processes</b>	<b>143</b>
C.1	Spectra of $2\text{NA}(\Lambda pn_s)$ reaction . . . . .	143
C.2	Spectra of $2\text{NA}(\Lambda pn_s + \pi)$ reaction . . . . .	144
C.3	Spectra of $2\text{NA}(\Sigma^0 pn_s)$ reaction . . . . .	144
C.4	Spectra of $2\text{NA}(\Sigma^0 pn_s + \pi)$ reaction . . . . .	145
C.5	Spectra of $3\text{NA}(\Lambda pn)$ reaction . . . . .	145
C.6	Spectra of $3\text{NA}(\Lambda pn + \pi)$ reaction . . . . .	147
C.7	Spectra of $3\text{NA}(\Lambda pn + 2\pi)$ reaction . . . . .	147
C.8	Spectra of $3\text{NA}(\Lambda pn + 3\pi)$ reaction . . . . .	148
C.9	Spectra of $3\text{NA}(\Sigma^0 pn)$ reaction . . . . .	148
C.10	Spectra of $3\text{NA}(\Sigma^0 pn + \pi)$ reaction . . . . .	149
C.11	Spectra of $3\text{NA}(\Sigma^0 pn + 2\pi)$ reaction . . . . .	149
C.12	Spectra of $3\text{NA}(\Sigma^0 pn + 3\pi)$ reaction . . . . .	150
<b>D</b>	<b>Theoretical investigation of the data of <math>{}^3\text{He}(K^-, \Lambda p)n</math> events</b>	<b>151</b>
<b>E</b>	<b>Fermi momentum distribution of <math>{}^3\text{He}</math></b>	<b>155</b>

# List of Figures

1.1	The low energy $K^-p$ scattering data and the curves calculated from the M-matrix parameters [1]. . . . .	17
1.2	Comparison of the experimental results, KEK-PS E228, DEAR, and SHIDDHARTA. Taken from [14]. . . . .	19
1.3	Real part (left) and imaginary part (right) of the $K^-p \rightarrow K^-p$ forward scattering amplitude extrapolated to the subthreshold region. The SHIDDHARTA constraints are indicated by the dots including statistical and systematic errors. The shaded bands represent theoretical uncertainties. Taken from [21].	19
1.4	Missing mass spectra of $^{12}\text{C}(K^-, n)$ reaction (upper) and $^{12}\text{C}(K^-, p)$ reaction (lower) in the KEK 548 experiment. The solid curves represent the best fit spectra for potential with $\text{Re}(V) = -190$ MeV and $\text{Im}(V) = -40$ MeV (upper), and with $\text{Re}(V) = -160$ MeV and $\text{Im}(V) = -50$ MeV (lower), respectively. The dotted curves represent the calculated spectra for $\text{Re}(V) = -60$ MeV and $\text{Im}(V) = -60$ MeV in both figures. The do-dashed curves show a background process. Taken from [29]. . . . .	21
1.5	Calculated $\bar{K}N$ and $\bar{K}$ -nucleus potentials for light nuclei and their B.E.s and $\Gamma$ s. Taken from [39]. . . . .	23
1.6	The $\Lambda p$ invariant mass spectrum obtained in the FINUDA experiment. Taken from Ref. [44]. . . . .	24
1.7	The deviation spectrum of the missing-mass spectrum of $K^+$ in the DISTO experiment. Taken from Ref. [46]. . . . .	25
1.8	The obtained $\Lambda K^+$ , $pK^+$ , $p\Lambda$ invariant-mass spectra with the solutions of PWA evaluated in the HADES experiment. Taken from [52]. . . . .	26
1.9	The missing mass spectrum for $MM_d(K^+\pi^-)$ spectrum and fit result with the Monte Carlo generated processes(upper). The residue from the fitting function(lower). Taken from [53]. . . . .	27
1.10	Missing-mass spectrum of the $d(\pi^+, K^+)$ reaction for two-protons coincidence and the $\Sigma^0 p$ decay branch events. Taken from [54]. . . . .	28
1.11	2D plot of B.E.s and $\Gamma$ of $\bar{K}NN$ state calculated and observed in the past experiments. Theoretical calculations with the phenomenological potential are plotted by circle, and them with the chiral SU(3) potential are plotted by triangles. Variational model calculations are colored white and Faddeev model calculations are colored black. Red squares show experimental results. Error bars are sum of statistic and systematic ones. . . . .	30

LIST OF FIGURES

---

1.12	The total cross section of $K^-N$ reactions. The data was taken from Particle Data Group. . . . .	31
1.13	Comparison of the ${}^3\text{He}(K^-,n)X$ semi-inclusive missing-mass spectrum between experimental data (top) and the simulation (bottom). Taken from [64]. . . . .	32
1.14	Contour Dalitz plot of the reaction $\pi_{stopped}^- {}^3\text{He} \rightarrow pnn$ . Taken from [65] . .	33
1.15	Acceptance of $\cos\theta_n$ in $\Lambda pn$ events. $\theta = 0$ is the beam direction in the Lab. frame. . . . .	34
2.1	Picture of J-PARC K1.8BR experimental area . . . . .	38
2.2	Schematic view of J-PARC E15 spectrometers . . . . .	39
2.3	Layout of hadron experimental facility(the SY and the HD-hall ). [68] . . .	39
2.4	Schematic view of K1.8BR beamline. [70] . . . . .	40
2.5	First-order beam envelope of the K1.8BR. Taken from [69] . . . . .	41
2.6	Schematic view of spectrometer of K1.8BR beamline. Taken from [70]. . . .	44
2.7	Schematic view of beam definition counter (DEF). . . . .	45
2.8	Schematic view of aerogel Cherenkov counter (AC). . . . .	46
2.9	Cell and wire geometries of BLC1, BLC2(a) and BPC(b). . . . .	48
2.10	Schematic view of the BPC. . . . .	50
2.11	Schematic view of the target cell. . . . .	52
2.12	Schematic view of the CDS. . . . .	53
2.13	Design of the solenoid magnet for the CDS. All dimensions are in mm. . . .	54
2.14	Distribution of the strength of magnetic field calculated by TOSCA. Each value was scaled by the value at the center of the solenoid magnet. A red boxes, and black box show sensitive region of the drift chamber and target region, respectively. . . . .	55
2.15	Design of the CDC structure. All dimensions are in mm. . . . .	56
2.16	Cell geometry of the CDC. . . . .	57
2.17	Schematic view of Forward TOF walls . . . . .	61
2.18	Cell geometry of the FDC. . . . .	62
2.19	Trigger diagram. . . . .	68
3.1	Definition of the axis coordinate. . . . .	70
3.2	Distribution of multiplicity of the T0 hits. . . . .	73
3.3	A typical TOF distribution between the BHD and T0. A peak in the right is Kaons. Dotted lines indicate $\pm 3\sigma$ selection points for kaon identification. . . . .	73
3.4	(a) Typical distribution of the drift time of beam line chamber. (b) Typical beam-line chamber's correlation function of drift time and drift length. Both figures show those of the BLC1a. . . . .	75
3.5	$\chi^2/NDF$ distributions of beam line chambers . . . . .	76
3.6	Track times and multiplicity of each beam-line chambers. . . . .	77
3.7	Distributions (X, Y ,dX/dZ, and dY/dZ) of the beam at final focus. . . . .	79
3.8	$\chi^2/NDF$ Distribution of the connection fitting of the BLC1 and BLC2. Dotted line on $\chi^2/NDF = 20$ shows the threshold for event selection. . . . .	80

3.9	A distribution of the difference of the reconstructed beam momentum and the momentum calculated with TOF between the CVC and T0. It should be noted that absolute value of the momentum of TOF(CVC-T0) was not fixed due to energy loss correction in forward counters. . . . .	81
3.10	Mass deviations between the reconstructed values and the PDG ones for each particle. . . . .	82
3.11	Track matching between the BLC2 and BPC tracks at $z=-75$ cm where is the center of two chambers. The regions between dotted lines in each histogram show accepted regions as three $\sigma$ . . . . .	83
3.12	Kaon beam profile at the FF. The red colored circle shows the fiducial region at the FF. . . . .	84
3.13	Typical timing distribution of the CDC hit. . . . .	87
3.14	Typical correlation between the drift time and drift length (XT curve). Sign of drift length is plus (minus) when the center of the cell is left (right) side of the track from the view on the track direction. . . . .	87
3.15	Examples of hit clusters in the super layer of the CDC. . . . .	88
3.16	Parametrization of helix trajectory. Left is for negative track and right is for positive track. . . . .	90
3.17	$\chi^2/ndf$ distribution of the CDC tracks. . . . .	90
3.18	Definitions of the beam - CDC track vertex. . . . .	91
3.19	Correlation of Mass squared and squared of resolution of mass of each particle. Dotted lines show fitting result with PID function (Eq. 3.11). . . . .	92
3.20	Scatter plot between momentum and mass squared of the CDS. The cut region for each particle is indicated as black curves corresponding to $2.5 \sigma$ . Overlapped regions are excluded as shown gray colored regions. . . . .	93
3.21	Correlation of CDC timing residual and $1/\beta^2$ of particle. left figure is before the correction, right figure is after the correction. . . . .	94
3.22	CDC drift time and residual correlation and projected residual distribution in CDC layer 1. . . . .	94
3.23	CDC width distribution in each layer. . . . .	95
3.24	The simulated $p_t$ resolution $\delta p_t/p_t$ of the CDC for each particle as a function of $p_t$ . . . . .	96
3.25	(left) Reconstructed x position vertex distribution around $y=0$ and $z=0$ cm. The two peaks correspond to the target cell. (right) Reconstructed z position vertex distribution with $\sqrt{(x^2 + y^2)} < 2$ cm. The peak around $z = -16$ cm corresponds to the DEF. . . . .	96
3.26	Efficiencies for each segment of the CDH. . . . .	97
3.27	Typical distribution of difference of the TOF of T0-CDH. Time resolution of T0-CDH was estimated as $\sigma$ of Gaussian fitting. . . . .	98
3.28	Segments dependence of CDH-T0 TOF time resolution. . . . .	98
3.29	Reconstructed vertex distributions in zx (left) and zy (right) planes. The fiducial volume is defined as the black boxes. . . . .	99
3.30	The correlation between deviations of $K_s^0$ and $\Lambda$ mass from the PDG values and the CDS Magnetic field. . . . .	100

3.31	Invariant mass distribution of $p\pi^-$ pairs. Events were selected to DCA of $p\pi^- < 2$ cm. The reconstructed $\Lambda$ peak was fitted with Gaussian and third-order polynomial. A red curve shows the fitting result. . . . .	100
3.32	Invariant mass distribution . of $\pi^+$ and $\pi^-$ pairs. Events were selected to DCA of $\pi^+\pi^- < 2$ cm. The $K_s^0$ peak was fitted with Gaussian and third-order polynomial. The red curve shows the fitting result. . . . .	101
3.33	The $\phi$ angle dependence of the CDC tracking efficiency. . . . .	102
3.34	The $\theta$ angle dependence of the CDC tracking efficiency. . . . .	102
3.35	Definitions of the reaction vertex. . . . .	104
3.36	2D plot of $\pi^-p$ invariant mass distribution of each pair in $\pi^-pp$ events. . . . .	104
3.37	DCA distributions generated by Monte Colro simulation. . . . .	106
3.38	Likelihood function ( $\ln L$ ) distribution. Black crosses are $\ln L$ of data. Since there are two possible pairs, the pair having smaller $\ln L$ is plotted. The red histogram shows the simulated $\ln L$ of the correct $p\pi^-$ pair from $\Lambda$ decay in a $pp\pi^-$ event. The blue histogram is $\ln L$ of the incorrect pair of $p\pi^-$ in a $\Lambda$ decay. The blue histogram is vertically scaled 10 times. . . . .	106
3.39	Overall detection efficiency distributions as functions of $p_\Lambda^{lab}$ (a) , $p_p^{lab}$ (b), $p_n^{lab}$ (c), $\cos \theta_\Lambda^{lab}$ (d), $\cos \theta_p^{lab}$ (e), and $\cos \theta_n^{lab}$ (f). Red lines in (d) and (e) show the CDS geometry. . . . .	107
3.40	$\Lambda pn$ overall detection efficiency on the Dalitz plot. The 2NA process, $K^- + ^3\text{He} \rightarrow \Lambda pn_s$ events are expected in the region marked by the orange circle. . . . .	108
3.41	Relation of $\Lambda p$ invariant mass resolution and mass. This values were estimated by the Monte Colro simulation. Mass resolution in the region of interest, which is around $K^-pp$ mass threshold ( $2.37 \text{ MeV}/c^2$ ), is about $10 \text{ MeV}/c^2$ . . . . .	109
3.42	Relation of missing mass of $^3\text{He}(K^-, \Lambda p)$ . With a Gaussian fitting, we evaluated the missing mass resolution at neutron mass to be $45 \text{ MeV}/c^2$ . . . . .	109
4.1	(a) $\Lambda p$ invariant mass distribution and (b) missing mass $M_X$ spectrum of $^3\text{He}(K^-, \Lambda p)X_{miss}$ . . . . .	111
4.2	$\Lambda p$ invariant mass(a) distribution and Dalitz plot(b) of the selected $\Lambda pn$ events . . . . .	112
4.3	$\Lambda p$ invariant mass(a) distribution and Dalitz plot(b) of the simulated 2NA events ( $K^-pp \rightarrow \Lambda p$ ) . . . . .	113
4.4	$\Lambda p$ invariant mass(a) distribution and Dalitz plot(b) of the simulated 3NA events ( $K^-ppn \rightarrow \Lambda pn$ ) . . . . .	113
4.5	Inclusive spectra of the $^3\text{He}(K^-, \Lambda p)$ reaction and the global fit result of simulation with multi-nucleon absorption processes. (a) $\Lambda p$ invariant mass distribution. (b) missing mass $M(X_{miss})$ spectra of $^3\text{He}(K^-, \Lambda p)X_{miss}$ . and (c) the close up view of (b) around the missing neutron region. In Figure (c), 2NA( $\Lambda pn_s$ ) is vertically scaled 20 times. The dashed vertical lines in (c) shows the neutron selection gate. . . . .	116

4.6	(a) 2-D distribution of the $\Lambda p$ invariant-mass and the emission-angle of the missing neutron. The blue dashed lines shows crude CDS acceptance boundary for the $\Lambda pn$ events. (b) $\Lambda p$ invariant mass with simulated spectra obtained in the global fit in the neutron window. (c) Angular distribution of the missing neutron, kinematically reconstructed, as a function of $\cos\theta_n^{CM}$ . The histograms show the contributions of the three remaining channels in the $n$ -window, considered in the global fit. . . . .	118
4.7	(a) 2-D distribution of the $\Lambda p$ invariant mass and the momentum transfer to $\Lambda p$ . (b) the fit result of the $\Lambda p$ invariant mass spectrum. (c) distribution of the momentum transfer to $\Lambda p$ and the fit results of simulation. . . . .	119
4.8	$\Lambda p$ invariant mass(a) distribution and Dalitz plot(b) of the simulated scattered $\bar{K}$ absorption events . . . . .	120
4.9	$\Lambda p$ invariant mass(a) distribution and Dalitz plot(b) of the simulated $\Sigma\Lambda$ conversion events . . . . .	121
4.10	$\Lambda p$ invariant mass(a) distribution and Dalitz plot(b) of the simulated $\Lambda(1405)\Lambda$ conversion events . . . . .	122
4.11	$\Lambda p$ invariant mass(a) distribution and Dalitz plot(b) of the simulated deeply bound $\bar{K}NN$ state(B.E = 100, $\Gamma$ =100 MeV) events . . . . .	122
4.12	(a) two dimensional $\chi^2$ map of mass and width of pole structure. (b) $\chi^2$ change as a function of $Q_X$ . . . . .	124
4.13	(a) 2-D distribution of the $\Lambda p$ invariant mass and the momentum transfer to $\Lambda p$ . (b) the fit result of the $\Lambda p$ invariant mass spectrum. (c) distribution of the momentum transfer to $\Lambda p$ and the fit results of simulation. . . . .	126
4.14	2D plot of B.E.s and $\Gamma$ of $\bar{K}NN$ state calculated and observed in the past experiments and our result. Theoretical calculations with the phenomenological potential are plotted by circle, and them with the chiral SU(3) potential are plotted by triangles. Variational model calculations are colored white and Faddeev model calculations are colored black. Red squares show experimental results. Error bars are sum of statistic and systematic ones. . . . .	127
A.1	Schematic view of the target system. . . . .	134
A.2	Left : Stability of the temperature at the target cell during the production run. Right : Density equation of $^3\text{He}$ [74]. The hatched regions represent the uncertainty of the temperature measurement and the density of the liquid $^3\text{He}$ . The red dotted line represents the result of the test operation of the target system [73]. . . . .	135
B.1	$1/\beta$ distribution of the NC. . . . .	138
B.2	$1/\beta$ resolution distribution of the NC(left) and neutron momentum resolution (right). . . . .	139
B.3	Missing mass distribution of $^3\text{He}(K^-, K^-pn)X$ . . . . .	139
B.4	Missing mass distribution of $^3\text{He}(K^-, K_s^0pn)X$ . . . . .	140
B.5	Missing mass distribution of $^3\text{He}(K^-, K_s^0n)X$ . . . . .	141
C.1	Invariant mass (left) and missing mass spectra of simulated $2\text{NA}(\Lambda pn_s)$ reaction. . . . .	144

LIST OF FIGURES

---

C.2	Invariant mass (left) and missing mass spectra of simulated $2\text{NA}(\Lambda pn_s + \pi)$ reaction. . . . .	144
C.3	Invariant mass (left) and missing mass spectra of simulated $2\text{NA}(\Sigma^0 pn_s)$ reaction. . . . .	145
C.4	Invariant mass (left) and missing mass spectra of simulated $2\text{NA}(\Sigma^0 pn_s + \pi)$ reaction. . . . .	145
C.5	Invariant mass (left) and missing mass spectra of simulated $3\text{NA}(\Lambda pn)$ reaction. . . . .	146
C.6	Invariant mass (left) and missing mass spectra of simulated $3\text{NA}(\Lambda pn + \pi)$ reaction. . . . .	147
C.7	Invariant mass (left) and missing mass spectra of simulated $3\text{NA}(\Lambda pn + 2\pi)$ reaction. . . . .	147
C.8	Invariant mass (left) and missing mass spectra of simulated $3\text{NA}(\Lambda pn + 3\pi)$ reaction. . . . .	148
C.9	Invariant mass (left) and missing mass spectra of simulated $3\text{NA}(\Sigma^0 pn)$ reaction. . . . .	148
C.10	Invariant mass (left) and missing mass spectra of simulated $3\text{NA}(\Sigma^0 pn + \pi)$ reaction. . . . .	149
C.11	Invariant mass (left) and missing mass spectra of simulated $3\text{NA}(\Sigma^0 pn + 2\pi)$ reaction. . . . .	149
C.12	Invariant mass (left) and missing mass spectra of simulated $3\text{NA}(\Sigma^0 pn + 3\pi)$ reaction. . . . .	150
D.1	differential cross section of the in-flight ${}^3\text{He}(K^-, \Lambda p)n$ reaction for the $\Lambda(1405)$ p resonance. Taken from [87]. A blue colored line shows fitting result of Eq. 4.2. A plotted data points was scaled to fitting result of Eq. 4.2, and are shown in arbitrary units. . . . .	152
D.2	Differential cross section of the in-flight ${}^3\text{He}K^-, \Lambda p)n$ reaction for the $KNN$ bound state. Taken from [87]. A blue colored line shows fitting result of Eq. 4.2[87]. Fitting result was scaled to be total cross section becomes $7\mu\text{b}$ . A plotted data points was scaled to fitting result of Eq. 4.2, and are shown in arbitrary units. . . . .	153
E.1	Proton momentum distribution of ${}^3\text{He}$ and fitting result. The blue boxes show the data taken from [84]. . . . .	155

# Chapter 1

## Introduction

### 1.1 Kaon nuclear bound state by strong interaction

Exotic atoms such as  $\pi^-$  atoms and  $K^-$  atoms are meson-nucleus systems bound by Coulomb force. On the other hand, meson nuclear bound states such as kaonic nuclei are new form of hadron many-body systems including a meson bound by strong interaction. However, there has been no firm evidence of such bound states. About anti-kaon, there are many theoretical calculations predicting the existence of kaon nuclear bound states owing to the strongly attractive  $\bar{K}N$  interaction. Especially, the  $\bar{K}NN$  bound state draws strong attention of many theoretical studies because it is one of the simplest kaonic nuclear cluster. And various few-body techniques were applied for this system. All the calculations suggest existence of bound states, although the binding energy ranges from 20 to 80 MeV. There are large difference depending on the choice of energy dependence of the kaon-nucleon interaction. And various few-body techniques were applied for this system. There are several reports claiming the signal of the  $\bar{K}NN$  bound states. However, there is no solid experimental evidence to conclude the existence of the  $\bar{K}NN$  bound state without ambiguities.

We have used the  ${}^3\text{He}(K^-, \Lambda p)$  reaction at 1 GeV/ $c$  for the first time. The  $K^-$  kicks out a neutron from the  ${}^3\text{He}$  nucleus in the forward direction and  $K^-$  is left in the backward at low energy, which could be absorbed by two protons to form the  $\bar{K}NN$ . The major decay mode of the  $\bar{K}NN$  is expected to be  $\pi^-\Sigma N$  channel due to a strong coupling through  $\bar{K}N \rightarrow \pi^-\Sigma$ . However we used a non-mesonic mode of  $\Lambda p$  in which particles in the final state have rather high energy. By doing so, we can obtain kinematically complete information both on formation and decay stages of the  $\bar{K}NN$ .

#### 1.1.1 $\bar{K}N$ interaction

The  $\bar{K}N$  interaction has been investigated by  $\bar{K}N$  scattering experiments. Martin[1] estimated the scattering length by using self-consistent M-matrix description for the low energy  $\bar{K}N$  scattering data. The scattering data of  $K^-p \rightarrow K^-p$ (elastic),  $K^-p \rightarrow \bar{K}N$ (charge exchange),  $K^-p \rightarrow \Lambda\pi^0$ ,  $\Sigma^0\pi^0$ ,  $\Sigma^\pm\pi^\mp$ (inelastic)[2, 3, 4, 5, 6, 7, 8] were analyzed. The cross sections obtained for each reaction process though the analysis are shown in Fig. 1.1 together with the experimental data. The scattering length from those analysis at the  $\bar{K}p$

threshold are found to be

$$a^{I=0} = -1.70 + i0.65 \text{ fm}, \quad (1.1)$$

$$a^{I=1} = 0.37 + i0.60 \text{ fm}, \quad (1.2)$$

where  $a^{I=0}$  and  $a^{I=1}$  are the scattering lengths with isospin  $I = 0$  and  $I = 1$ , respectively. From this result,  $\bar{K}N$  interaction is strongly attractive at  $I = 0$ .

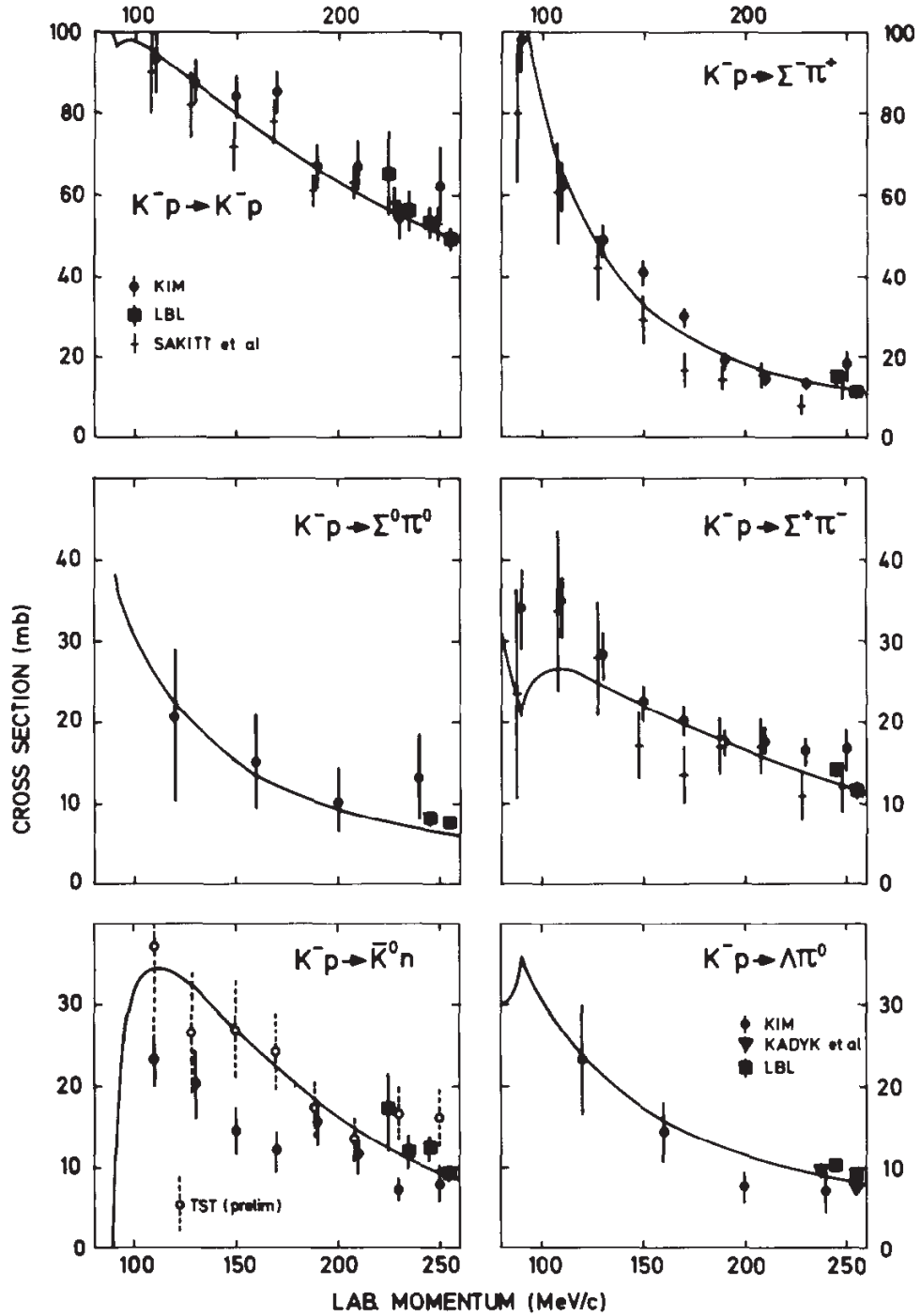


Figure 1.1: The low energy  $K^-p$  scattering data and the curves calculated from the M-matrix parameters [1].

On the other hand, measurements of the  $K_\alpha$  X-ray ( $2p \rightarrow 1s$  transition) of kaonic hydrogen, which is a bound state of  $K^-$  and proton with the Coulomb interaction also give us the information of  $\bar{K}N$  strong interaction. Because,  $K^-$  orbit of 1s state kaonic hydrogen is very close to the proton surface, the energy of orbit is influenced from strong interaction between kaon and core proton. The energy level shift from the electromagnetic calculation ( $\Delta E_{1s} = E_{1s}^{measured} - E_{1s}^{e.m.}$ ) and the finite width of ground state  $\Gamma_{1s}$ , are strongly dependent on the information of S-wave  $\bar{K}N$  interaction. These values are composed with the scattering length through Deser-Trueman formula [9, 10],

$$\Delta E_{1s} + \frac{i}{2}\Gamma_{1s} = 2\alpha^3\mu^2 a_{K-p}, \quad (1.3)$$

$$a_{K-p} = \frac{1}{2}(a^{I=0} + a^{I=1}), \quad (1.4)$$

where  $\alpha$  is the fine structure constant and  $\mu$  is the reduced mass of the  $K^-p$  system. However, the signs of the real part obtained with low-energy scattering data and  $K_\alpha$  X-ray data were in disagreement with each other. This large discrepancy between these two methods was called as “the kaonic hydrogen puzzle”.

This problem was solved by KEK-PS E228(KpX) experiment[11, 12]. They succeeded to reduce systematic error by using a gaseous hydrogen target and to improve the calibrations of detectors. They found the shift as  $\Delta E_{1s} = -323 \pm 63(\text{stat.}) \pm 11(\text{syst.})$  eV and width as  $\Gamma_{1s} = 407 \pm 208(\text{stat.}) \pm 100(\text{syst.})$  eV, which are in good agreement with the calculations based on the scattering data. The DEAR collaboration also published the kaonic hydrogen atom data in 2005[13], which were almost consistent with those of KEK-PS E228 but still had large systematic errors. In 2012, the SHIDDHARTA experiment was performed at DAΦNE [14, 15]. They measured shift and width very precisely by using silicon drift detectors (SDDs) which have both good energy resolution ( $\sim 150$ eV) and time resolution ( $\sim 1\mu\text{s}$ ). The obtained shift and width were  $\Delta E_{1s} = -283 \pm 36(\text{stat.}) \pm 6(\text{syst.})$  eV and  $\Gamma_{1s} = 541 \pm 89(\text{stat.}) \pm 22(\text{syst.})$  eV, respectively. Figure 1.2 shows a summary of the shifts and widths of 1s kaonic hydrogen atom from the three experiments. Then, “the kaonic hydrogen puzzle” was solved and it has confirmed that  $\bar{K}N$  interaction is strongly attractive at  $I = 0$ .

Based on the new kaonic hydrogen atom measurements, the  $\bar{K}N$  scattering amplitude in the NLO chiral SU(3) models was extracted. The SHIDDHARTA data provides strong constraint on the  $\bar{K}N$  scattering amplitude at  $\bar{K}N$  threshold[16, 17, 18, 19, 20, 21]. The scattering amplitudes were extrapolated in this theoretical framework to sub-threshold region. Figure 1.3 shows the examples of such scattering amplitudes[21]. One can see some uncertainty in the sub-threshold region in Fig. 1.3, which comes from the ambiguity in the model. The  $\bar{K}N$  interaction in the sub-threshold region still has large ambiguity.

### $\bar{K}$ -nucleus interaction

$\bar{K}$ -nucleus interaction, namely  $\bar{K}N$  interaction in nuclear medium has been studied by the systematic measurement of the heavier kaonic atom x-rays than hydrogen. A global fit of kaonic atom x-rays data was performed by Batty, Friedman and Gal[23, 24]. A simple  $t - \rho$  potential model are used for the evaluation of a  $\bar{K}$  potential in nuclei[23]. The value of the depth of the potential was found to be  $\sim -80$  MeV at Ni. The chiral SU(3) based model,

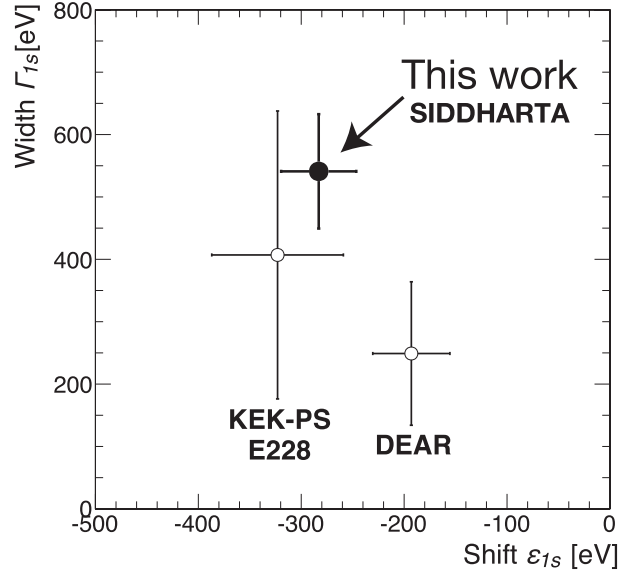


Figure 1.2: Comparison of the experimental results, KEK-PS E228, DEAR, and SHID-DHARTA. Taken from [14].

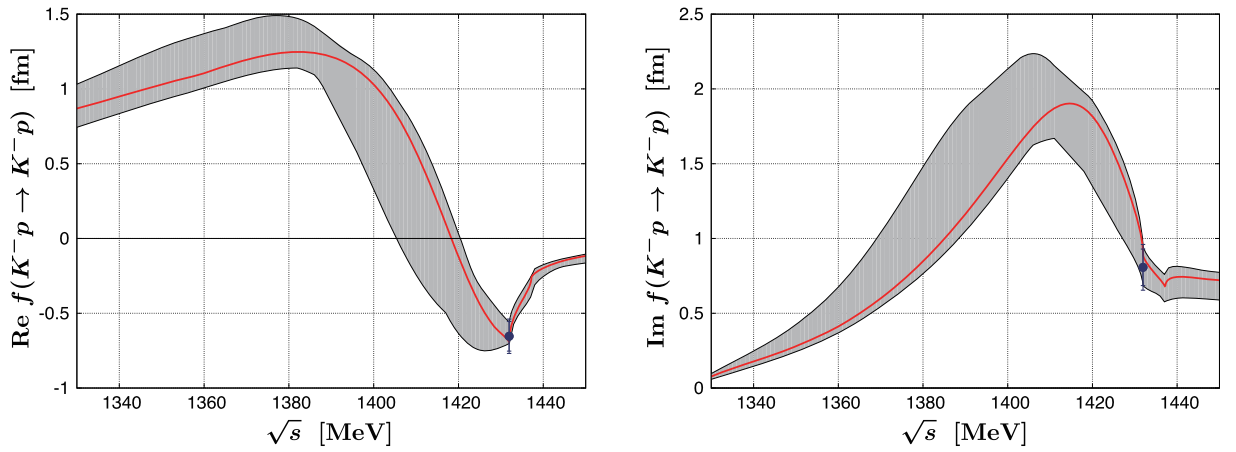


Figure 1.3: Real part (left) and imaginary part (right) of the  $K^-p \rightarrow K^-p$  forward scattering amplitude extrapolated to the subthreshold region. The SIDDHARTA constraints are indicated by the dots including statistical and systematic errors. The shaded bands represent theoretical uncertainties. Taken from [21].

which reasonably reproduced the low-energy  $K^-p$  scattering data[25, 26] also indicated the almost same potential as the result of the simple  $t - \rho$  potential model fitting. In addition, much shallower potential was derived by [27].

The fitting quality of the global fit of kaonic atom x-rays data was improved by using the density dependent optical potential. The result of the fitting with this potential showed rather deep potential,  $\sim -200$  MeV[24].

In addition, a microscopic study on the  $\bar{K}$  potential was performed[22] by using the  $\bar{K}N$  scattering amplitude extracted by Ikeda-Hyodo-Weise (IHW)[16, 17] as shown in Fig. 1.3. In their model, the potential was decomposed into two parts  $V_{K^-}^{(1)}$  and  $V_{K^-}^{(2)}$ .  $V_{K^-}^{(1)}$  is the self consistently constructed potential and  $V_{K^-}^{(2)}$  is an additional phenomenological potential to describe absorption effects. The resulted potential for the Ni target was  $-191-i79$  MeV. This value is consistent with the phenomenological potential obtained with the density dependent optical potential by Batty, Friedman and Gal[24].

Kishimoto[28, 29] tried to determine the  $\bar{K}$  potential depth from a measurement of  $(K^-, N)$  spectrum. The in-flight  $^{12}\text{C}(K^-, N)$  reaction was studied in KEK-PS E548. Figure 1.4 shows missing mass spectra of the  $^{12}\text{C}(K^-, p)$  and  $^{12}\text{C}(K^-, n)$  at 1 GeV/c. The potential depths were obtained to be -190 MeV for  $^{12}\text{C}(K^-, n)$  reaction and -160 MeV for  $^{12}\text{C}(K^-, p)$  reaction with the Green's function method. However, there is theoretical criticism[30] that fitting of these data with the Green's function method is too simple and there is a possibility to reproduce spectra with much shallower potential (-60 MeV).

In current situation, we found that the  $\bar{K}N$  interaction is strongly attractive in  $I=0$ , but the  $\bar{K}N$  interaction in the sub-threshold region is not well understood. About  $\bar{K}$ -nucleus potential, it is not concluded whether  $\bar{K}$ -nucleus potential is deep or shallow. The measurement of the kaonic bound state in nuclei will give us new information about  $\bar{K}$ -nucleus interaction.

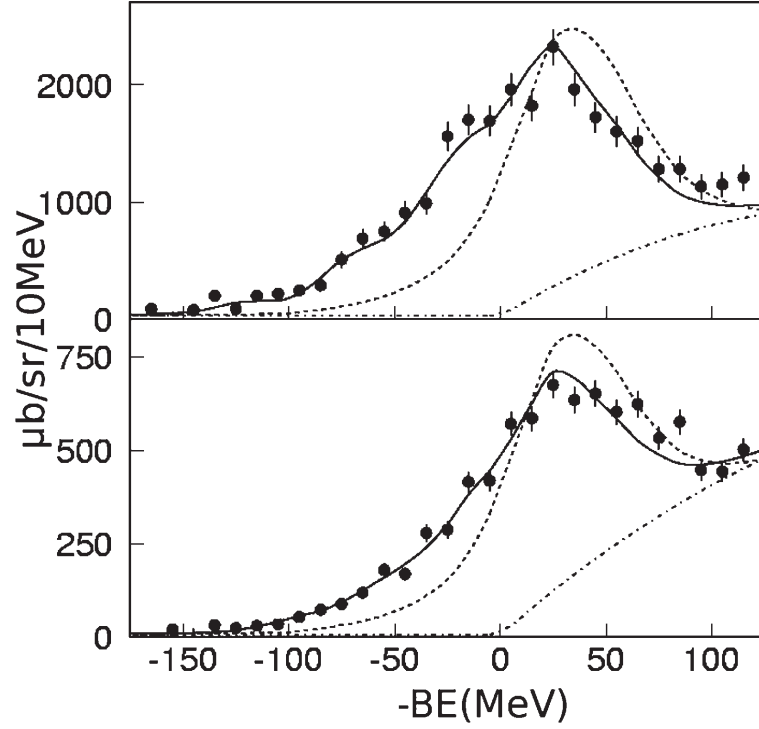


Figure 1.4: Missing mass spectra of  $^{12}\text{C}(K^-, n)$  reaction (upper) and  $^{12}\text{C}(K^-, p)$  reaction (lower) in the KEK 548 experiment. The solid curves represent the best fit spectra for potential with  $\text{Re}(V) = -190$  MeV and  $\text{Im}(V) = -40$  MeV (upper), and with  $\text{Re}(V) = -160$  MeV and  $\text{Im}(V) = -50$  MeV (lower), respectively. The dotted curves represent the calculated spectra for  $\text{Re}(V) = -60$  MeV and  $\text{Im}(V) = -60$  MeV in both figures. The do-dashed curves show a background process. Taken from [29].

## 1.2 Kaonic nuclear bound state

As described in the previous section,  $\bar{K}N$  interaction is strongly attractive in  $I = 0$  and we are able to consider attractive potential of  $\bar{K}$ -nuclei. These results suggest the existence of the bound state of  $\bar{K}$  and nuclei. The simplest bound state of  $\bar{K}$  and nuclei,  $\bar{K}N$  bound system is interpreted as the  $\Lambda(1405)$ . The existence of  $\Lambda(1405)$  about 20 MeV below the  $\bar{K}N$  threshold is considered to be a good reason to believe that it is a bound state of  $\bar{K}$  and  $N$ . If this is true, it can be the simplest Kaonic nuclei or five-quark molecular state.

### 1.2.1 $\Lambda(1405)$

The  $\Lambda(1405)$  is a baryon with strangeness  $S = -1$ , isospin  $I = 0$  and  $J^p = \frac{1}{2}^-$ . The existence of the  $\Lambda(1405)$  was confirmed by the Bubble-chamber experiments with  $\pi^-$  and  $K^-$  beam at Brookhaven[31] and CERN[32], respectively.  $J^p = \frac{1}{2}^-$  of  $\Lambda(1405)$  was determined by CLAS experiment[33]. The constituent quark model predicted that a mass of  $\Lambda^* \frac{1}{2}^-$  is about 1490 MeV/ $c^2$ [34]. However, observed mass of the  $\Lambda(1405)$  is not consistent to predicted one and is lighter than  $N(1535)$ , which is a nucleon excited state with  $\frac{1}{2}^-$ . Moreover, the constituent quark model can not explain the large mass difference between  $\Lambda(1405)$  and  $\Lambda(1520)(J^p = \frac{3}{2}^-)$ , which is considered as the spin-multiplet partner of the  $\Lambda(1405)$ .

Thus,  $\Lambda(1405)$  is interpreted as the  $\bar{K}N$  bound system not three-quark state[35]. In this assumption, the binding energy of  $\bar{K}N$  is about 27 MeV. Recently, a lattice QCD simulation also strongly suggested that the structure of  $\Lambda(1405)$  is dominated by a bound  $\bar{K} - N$  component[36].

On the other hand, the  $\Lambda(1405)$  can be interpreted as a composition of two poles located between  $\bar{K}N$  and  $\pi\Sigma$  thresholds in the chiral unitary model[37]. These two-pole locations were calculated by the NLO chiral SU(3) models with kaonic hydrogen data and found to be 1424+i26 MeV(a pole with a dominant coupling to  $\bar{K}N$ ) and 1381 +i81 MeV(a pole with a dominant coupling to  $\pi\Sigma$ )[16].

### 1.2.2 kaonic nuclei

The idea of kaon nuclear bound state( $A \geq 2$ ) with strong interaction was proposed by Nogami for the first time in 1963[38]. Akaishi and Yamazaki performed a quantitative calculation for kaonic nuclei in finite systems in 2002[39]. They constructed a phenomenological  $\bar{K}N$  potential using the  $\bar{K}N$  scattering data, kaonic hydrogen atom data and the mass and width of  $\Lambda(1405)$  by assuming that  $\Lambda(1405)$  is a bound state of  $\bar{K}N$  in  $I = 0$ . Binding energies and its width were predicted for light kaonic nuclear systems, ( $K^-p$ ,  $K^-pp$ ,  $K^-ppn$ ). Figure 1.5 shows results of the calculation. The result suggested that kaonic nuclei have a large B.E and narrow  $\Gamma$  to be observed as a peak structure in experimental spectrum. This prediction inspired current kaonic nuclei studies.

After this prediction, the KEK-PS E471 experiment was performed to search for the  $K^-ppn$  bound state via the  ${}^4\text{He}(K^-_{stopped}, p)$  reaction[40, 41]. They claimed a peak structures in both proton and neutron missing mass spectra. However, they did not confirmed the peak structures in KEK-PS E549 experiment, which was carried out with upgraded setup

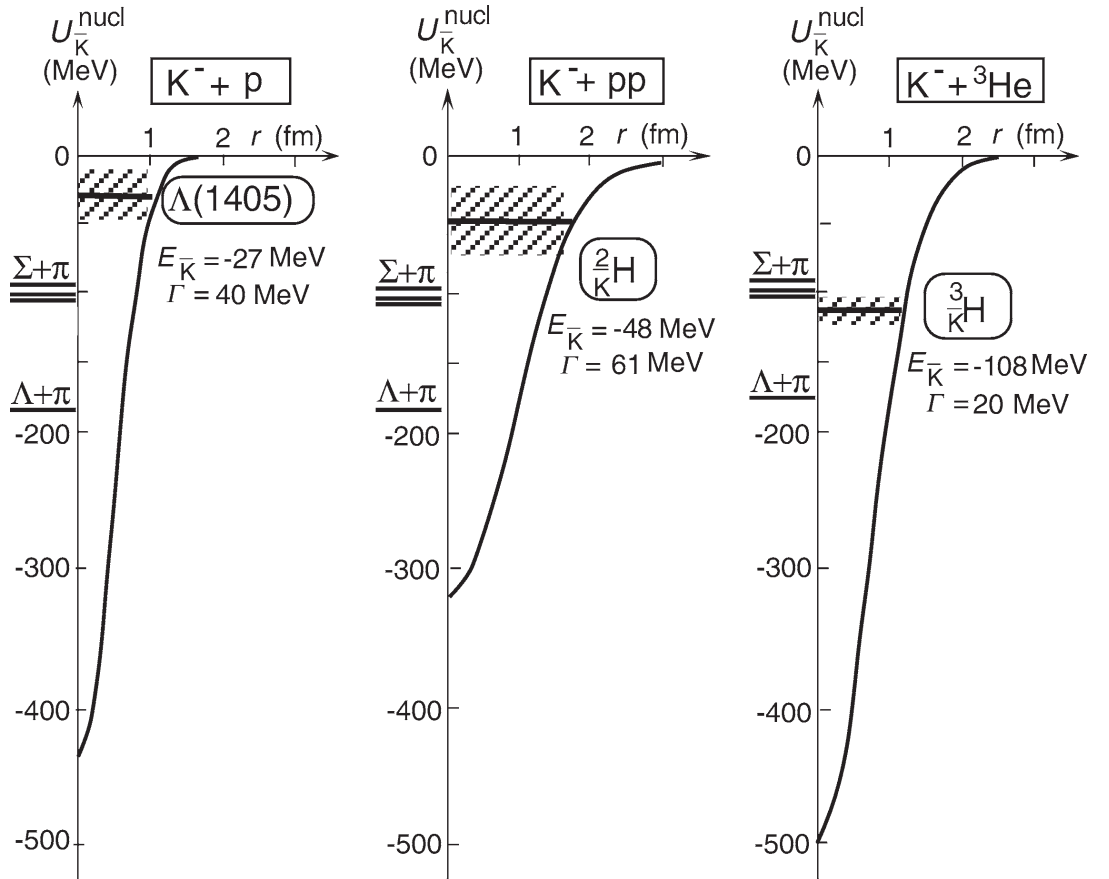


Figure 1.5: Calculated  $\bar{K}N$  and  $\bar{K}$ -nucleus potentials for light nuclei and their B.E.s and  $\Gamma$ s. Taken from [39].

to confirm E471 results[42, 43]. The peak structures in E471 experiment were found to be due to defect of the detector calibration.

In many body systems (larger than mass number four), it would be difficult to separately identify the signal of kaonic nuclei and background, because background processes, i.e. the absorption of  $K^-$  increase. Therefore, the investigation of the simplest kaonic nuclei,  $\bar{K}NN$  state has progressed on both the theoretical and experimental sides. In particular,  $[\bar{K}(NN)_{I=1}]_{I=1/2}$ , so-called  $K^-pp$  state is important, because it has the largest number of  $\bar{K}N$  pairs with  $I = 0$  which is strongly attractive in three charge state. Hereafter, we focus on the topics on the  $\bar{K}NN$  state in the following discussion.

### 1.3 Experiments to search for $\bar{K}NN$ bound state

The efforts to search for the  $\bar{K}NN$  bound state have been performed all over the world. Here, experimental results obtained in those experiments are reviewed.

#### 1.3.1 FINUDA experiment

The FINUDA(Fisica Nucleare a DAFNE) collaboration searched for  $\bar{K}NN$  state via the stopped  $K^-$  reaction on targets ( ${}^6\text{Li}$ ,  ${}^7\text{Li}$  and  ${}^{12}\text{C}$ ) at DAΦNE in Italy[44]. They observed a back-to-back  $\Lambda p$  pair. A bump structure was observed in  $\Lambda p$  invariant mass spectrum as shown Fig. 1.6. They claimed that the observed bump structure is the signal of the  $\bar{K}NN$  bound state which decays to a pair of  $\Lambda$  and proton. Property of the found bump structure, i.e. the binding energy and decay width, is found to be  $115_{-6}^{+6}(\text{stat.})_{-4}^{+3}(\text{syst.})$  MeV and  $67_{-11}^{+14}(\text{stat.})_{-3}^{+2}(\text{syst.})$  MeV, respectively. However, there are some theoretical criticisms that the peak structure can be explained by the re-scattering processes of  $\Lambda p$  inside a nucleus[45]. New analysis with large data sample may help the situation, however no report from the collaboration is made.

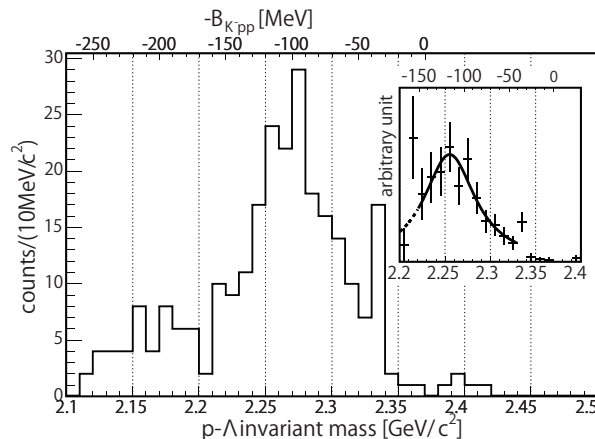


Figure 1.6: The  $\Lambda p$  invariant mass spectrum obtained in the FINUDA experiment. Taken from Ref. [44].

### 1.3.2 DISTO experiment

The DISTO(Dubna-Indiana-Saclay-Torino) collaboration re-analyzed their data on the exclusive  $p + p \rightarrow p + \Lambda + K^+$  events at  $T_p = 2.85$  GeV[46]. Obtained  $K^+$  missing mass spectra tagged with  $\Lambda$  and  $p$  in the final state divided by the spectrum which assumed the final state  $\Lambda p K^+$  are uniformly distributed in phase space is shown in Figure 1.7. The mass and decay width are found to be  $2267 \pm 3$  (stat.)  $\pm 5$  (syst.) MeV/ $c^2$  and  $118 \pm 8$  (stat.)  $\pm 10$  (syst.) MeV, respectively. If we assume that the structure is  $\bar{K}NN$  bound state, the binding energy corresponding to 103 MeV.

A broad bump structure was observed and can be interpreted as  $\bar{K}NN$  state with B.E =  $103 \pm 3$  (stat.)  $\pm 5$  (syst.) MeV and  $\Gamma = 118 \pm 8$  (stat.)  $\pm 10$  (syst.) MeV. The momentum transfer of this reaction is about 1.6 GeV/ $c$ , which corresponds to  $R_{pp} = 1.90$  fm [47]. They also analyzed the data at  $T_p = 2.5$  GeV and found no bump structure observed at  $T_p = 2.85$  GeV[48]. If the  $\bar{K}NN$  observed in the DISTO follows the excitation function in a semi-empirical universal form of Sibirtsev[49], the peak should be observed at  $T_p = 2.5$  GeV. Moreover, significant contribution from  $N^*$  resonance are expected in this reaction channel, therefore there are many open questions to understand the origin of the observed bump structure by DISTO collaboration.

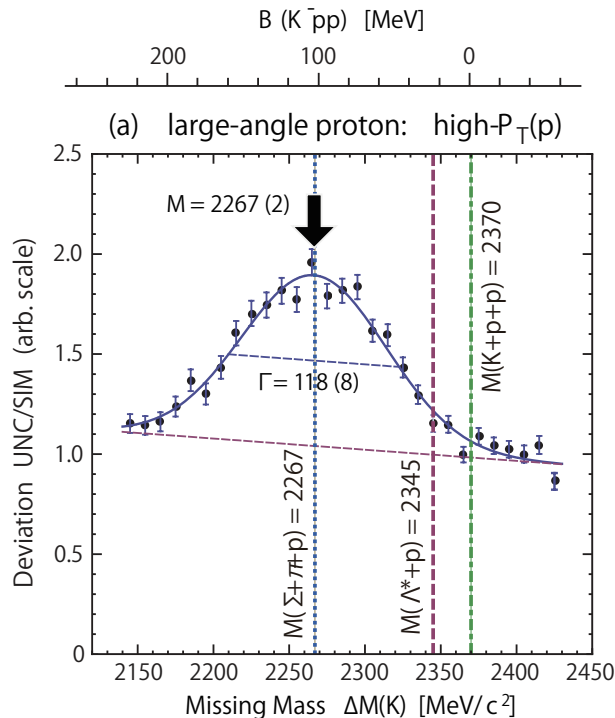


Figure 1.7: The deviation spectrum of the missing-mass spectrum of  $K^+$  in the DISTO experiment. Taken from Ref. [46].

### 1.3.3 OBELIX experiment

The OBELIX experiment was performed at LEAR-CERN using  $\bar{p}$  annihilation reaction at rest on a  ${}^4\text{He}$  target [50]. They analyzed  $\bar{p}+{}^4\text{He}\rightarrow p\pi^-p\pi^+\pi^-nX$  reaction, which corresponds to the  $\bar{p}+{}^4\text{He}\rightarrow(\bar{K}NN)K_s^0nX\rightarrow\Lambda pK_s^0nX$  reaction. They observed a peak in the  $pp\pi^-$  invariant mass spectrum. If it is  $\bar{K}NN$ , binding energy is  $160.9\pm 4.9$  MeV and mass width is  $< 24.4\pm 8.0$  MeV. However, they can not identify clear  $\Lambda$  peak due to poor resolution. They do not insist strongly that the observed peak structure is the  $\bar{K}NN$  bound state.

### 1.3.4 HADES experiment

The HADES (High Acceptance DiElectron Spectrometer) collaboration reported a negative result for  $\bar{K}NN$  bound state via the  $pp\rightarrow K^+X$  reaction at  $T_p=3.5\text{GeV}$ [51]. They observed no significant peak by using same method as one of the DISTO experiment. They found that the phase space simulation cannot reproduce the missing mass, invariant mass and angular distribution of the experimental data simultaneously. Their beam energy is higher than one of DISTO experiment. Thus, background processes opened in their energy is not same as those of DISTO experiment. They pointed out the the DEV spectrum, which is missing mass spectrum as the deviation to uniform phase space distribution of the  $\Lambda pK^+$  final state and used in DISTO experiment, should be treated carefully.

Recently, they performed the Bonn-Gatchina partial wave analysis (PWA) to reproduce the data[52]. They used non-resonant production waves and  $N^*$  resonances. They fitted the data and obtained the four best PWA solutions without assuming the existence of the  $\bar{K}NN$  as shown Fig. 1.8. Error band in Fig. 1.8 shows the systematic differences of the four best PWA solutions. They evaluated the upper limits on the  $\bar{K}NN$  decaying to  $\Lambda p$  in the mass range of 2220–2370 MeV/ $c^2$ . The evaluated upper limits are 1.8–3.9  $\mu\text{b}$  ( $J^p=0^+$ ), 2.1–4.2  $\mu\text{b}$  ( $J^p=1^-$ ) and 0.7–2.1  $\mu\text{b}$  ( $J^p=2^+$ ), respectively. They observed the  $\Lambda(1405)$  production at the same time. The present upper limits are not so tight for the  $\Lambda^*N\rightarrow YN$  conversion probability.

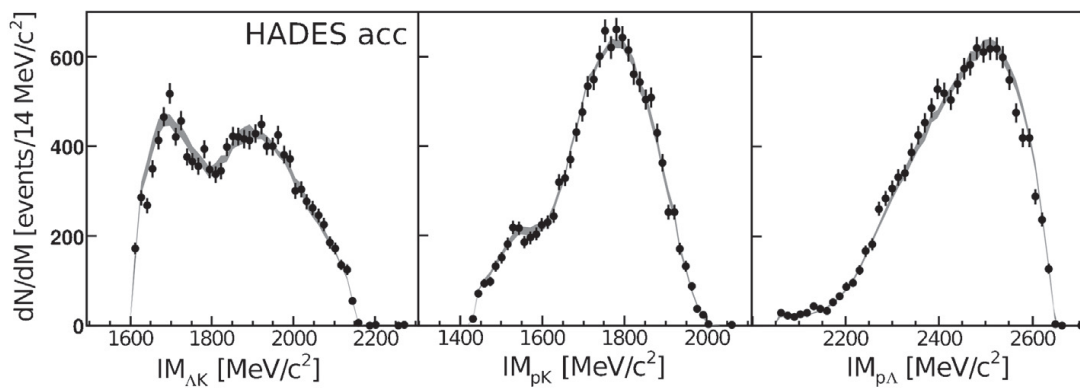


Figure 1.8: The obtained  $\Lambda K^+$ ,  $pK^+$ ,  $p\Lambda$  invariant-mass spectra with the solutions of PWA evaluated in the HADES experiment. Taken from [52].

### 1.3.5 LEPS experiment

$\bar{K}NN$  search via photo-production was performed at the LEPS experiment in the SPring-8. They used  $d(\gamma, K^+\pi^-)$  reaction at  $\gamma$  beam energy of 1.5–2.4 GeV. Missing mass spectrum ( $MM_{K^+\pi^-}$ ) was obtained by detecting forward  $K^+\pi^-$  ( $\cos\theta_{K^+\pi^-}^{\text{lab}}$ ) as shown in Fig. 1.9. The yield of background processes,  $\gamma n \rightarrow \Lambda K^+\pi^-$ ,  $\gamma \rightarrow \Sigma^+ K^+\pi^-$ ,  $\gamma p \rightarrow \Lambda(1520)K^+$ ,  $\gamma n \rightarrow \Lambda\pi^0 K^+\pi^-$ ,  $\gamma n \rightarrow \Sigma^0\pi^0 K^+\pi^-$ , and  $\gamma n \rightarrow \Sigma(1385)^0 K^+\pi^-$  were estimated by using the Log-likelihood ratio method. No peak structure was observed from 2.22–2.36  $\text{GeV}/c^2$ . They estimated the upper limits of the  $\bar{K}NN$  and found to be 0.17–0.55  $\mu\text{b}$  ( $\Gamma = 20$  MeV), 0.55–1.7  $\mu\text{b}$  ( $\Gamma = 50$  MeV) and 1.1–2.9  $\mu\text{b}$  ( $\Gamma = 100$  MeV) at 95% confidence level, respectively.

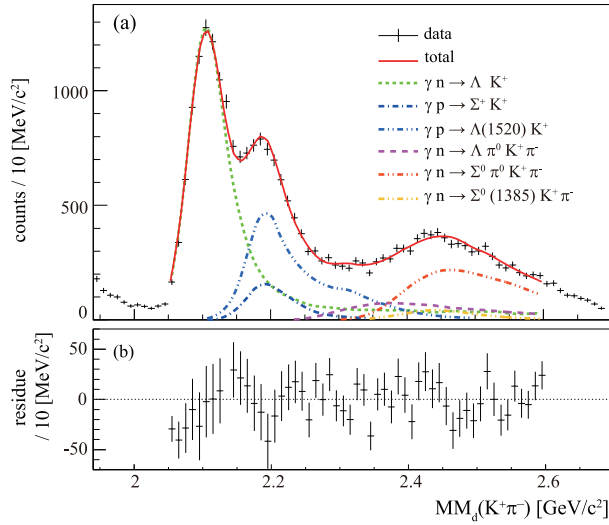


Figure 1.9: The missing mass spectrum for  $MM_d(K^+\pi^-)$  spectrum and fit result with the Monte Carlo generated processes(upper). The residue from the fitting function(lower). Taken from [53].

### 1.3.6 E27 experiment

The E27 experiment was performed to search for  $\bar{K}NN$  state via pion-induced reaction,  $d(\pi^+, K^+)$  reaction in the J-PARC facility[54]. They tagged two protons by range array counters which was located around the target to enhance the signal-background ratio. The acceptance of the range array counters corresponded to proton emission angle range,  $39^\circ < \theta_{lab} < 122^\circ$ . High momentum protons ( $>250$  MeV/c) were tagged. The out-going  $K^+$  momentum was reconstructed with the Superconducting Kaon Spectrometer (SKS) with the momentum resolution of  $\Delta p/p \sim 1 \times 10^{-3}$ .

They estimated ratios of  $\Lambda p$ ,  $\Sigma^0 p$  and  $Y\pi p$  by using missing mass spectra ( $M_X$ ) of  $d(\pi^+, K^+pp)X$  in each mass windows of missing mass ( $MM_d$ ) of  $d(\pi^+, K^+)X$ . Using these ratios, they estimated missing mass spectrum of  $d(\pi^+, K^+)X$  for  $\Sigma^0 p$  mode with acceptance correction, as shown in Fig. 1.10. A wide peak structure was observed and fitted with a relativistic Breit-Wigner function. They found the mass is  $2275_{-18}^{+17}(\text{stat.})_{-30}^{+21}(\text{syst.})$   $\text{MeV}/c^2$  and width is  $162_{-78}^{+66}$  MeV, which corresponds to B.E=  $95_{-18}^{+17}(\text{stat.})_{-30}^{+21}(\text{syst.})$  MeV of  $\bar{K}NN$

state. The obtained values are not inconsistent with the FINUDA and DISTO values within the large error bars.

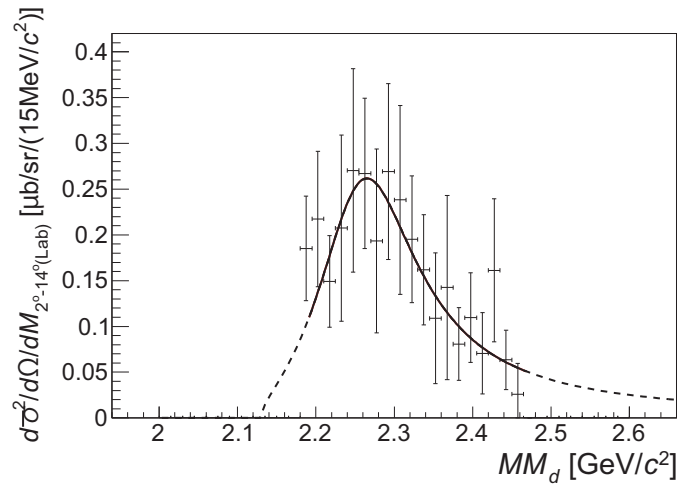


Figure 1.10: Missing-mass spectrum of the  $d(\pi^+, K^+)$  reaction for two-protons coincidence and the  $\Sigma^0 p$  decay branch events. Taken from [54].

## 1.4 Theoretical situation of $\bar{K}NN$ bound state

Many theoretical studies were also progressed in the last decade. The binding energy and width from various theoretical predictions are summarized in Table. 1.1. All calculations support the existence of the  $\bar{K}NN$  bound state. However, values of B.E.s and widths are widely distributed. The calculated B.E.s are 9–95MeV, and widths are 34–110 MeV.

In particular, difference of the  $\bar{K}N$  interaction models has a large effect to the  $\bar{K}NN$  property. There are two types of the  $\bar{K}N$  interaction models: phenomenological(energy independent) models[39, 56, 58, 57, 59, 63] and a chiral SU(3) (energy dependent) models [60, 61, 62, 63]. The phenomenological model treats that the  $\Lambda(1405)$  is the pure  $\bar{K}N$  bound state with B.E. = 27 MeV. While,  $\Lambda(1405)$  is treated as the superposition of two states which couple to two pole channels,  $\Sigma\pi$  and  $\bar{K}N$  in the chiral SU(3) (energy dependent) models. The resonance position coupling to the  $\bar{K}N$  is estimated to be 1420 MeV, which is heavier than the known mass value of the  $\Lambda(1405)$ . Therefore, the  $\bar{K}N$  interaction and also the binding energies in the chiral SU(3) models are weaker than those of phenomenological models.

The calculation methods are also categorized into two types, the variational method and the Faddeev method. In the variational method, the wave function of the system is derived, and the complex  $\bar{K}N$  interaction accounts for the  $\bar{K}N$ - $\pi\Sigma$  two-body coupled channels. On the other hand, direct three-body calculation, i.e.  $\bar{K}NN - \pi YN$  system, are performed in the Faddeev method. The effect of the difference of calculation methods are not large once interaction models are chosen.

Table 1.1: Theoretical results of the  $\bar{K}NN$  bound state.

B.E. [MeV]	$\Gamma_{\bar{K}NN}$	Model	Ref.
Phenomenological (energy independent) $\bar{K}N$ interaction			
48	61	variational model	[39]
50–70	90–110	variational model	[56]
60–95	45–80	Faddeev model	[57]
40–80	40–85	variational model	[58]
45	64	Faddeev model	[59]
46–54	50–66	Faddeev model	[63]
Chiral SU(3) (energy dependent) $\bar{K}N$ interaction			
17–23	40-70	variational model	[60]
9–16	34–46	Faddeev model	[61]
16	41	variational model	[62]
30–32	46–48	Faddeev model	[63]

## 1.5 Summary of $\bar{K}NN$ situation

We summarized the B.E.s and widths,  $\Gamma_{\bar{K}NN}$  of experimental and theoretical results in Fig. 1.11. It is noted that most of the theoretical models assume only mesonic decay mode  $\pi YN$  and experiments observed in non-mesonic decay mode. Thus, we cannot compare the widths observed in experiments to those of theoretical calculations directly.

B.E.s of experimental results are  $\sim 100$  MeV, which are higher than almost all theoretical predictions. Theoretical predictions are also inconsistent with the calculations with the phenomenological  $\bar{K}N$  potential and those with the chiral SU(3)  $\bar{K}N$  potential. The calculations with the chiral SU(3)  $\bar{K}N$  potential indicate lower B.E.s less than  $\sim 30$  MeV.

The nature of  $\bar{K}NN$  bound state has been established. The current situation is still controversial. In order to resolve the situation, more experimental information of  $\bar{K}NN$  bound state are necessary.

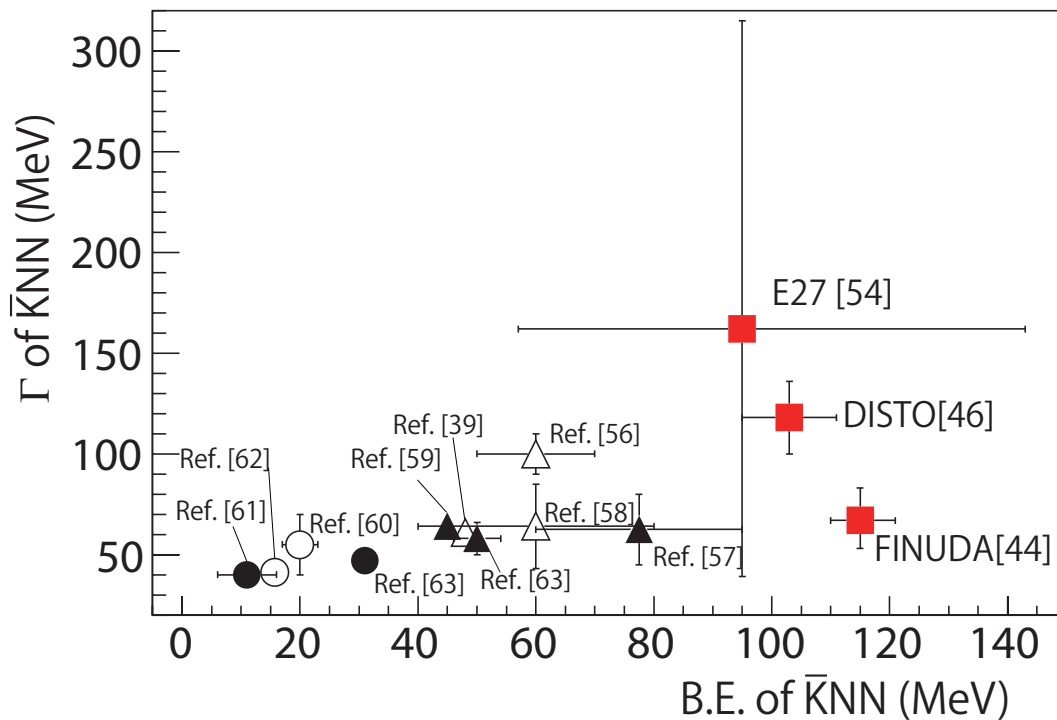


Figure 1.11: 2D plot of B.E.s and  $\Gamma$  of  $\bar{K}NN$  state calculated and observed in the past experiments. Theoretical calculations with the phenomenological potential are plotted by circle, and them with the chiral SU(3) potential are plotted by triangles. Variational model calculations are colored white and Faddeev model calculations are colored black. Red squares show experimental results. Error bars are sum of statistic and systematic ones.

## 1.6 J-PARC E15 experiment

In an attempt to clarify this situation, the E15 experiment on the  $K^- + {}^3\text{He}$  reaction at  $p_{K^-} = 1 \text{ GeV}/c$  was performed at J-PARC (Japan Proton Accelerator Research Complex). The first physics data were accumulated in May 2013.

The beam momentum was selected to be a maximum of the cross section of the elementary  $K^-N$  total reaction as shown in Fig. 1.12. The momentum corresponds to the  $\sqrt{s} \sim 1800 \text{ MeV}$ . By using in-flight reaction, we can suppress or separate kinematically the

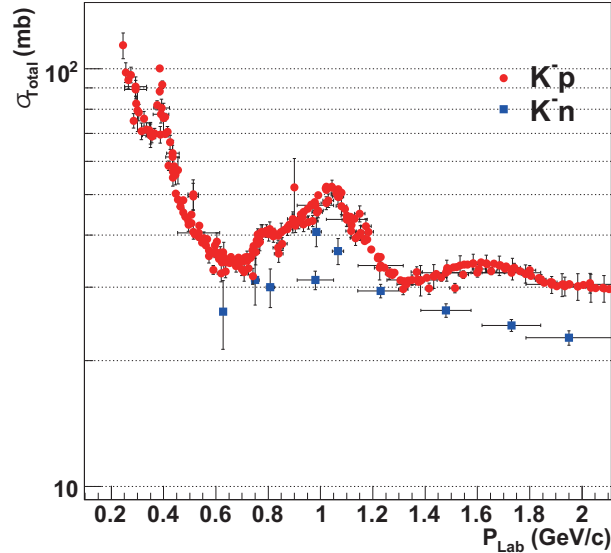


Figure 1.12: The total cross section of  $K^-N$  reactions. The data was taken from Particle Data Group.

background processes such as multi-nucleon absorptions than stopped  $K^-$  reaction. In addition, an exclusive measurement can be performed by using a few body system in  ${}^3\text{He}$  target, which is quite important to reduce ambiguity of observed structure. The  $\bar{K}NN$  bound state is measured via invariant mass spectroscopy,  $\bar{K}NN \rightarrow \Lambda p \rightarrow \pi^- pp$ , and emitted neutron is kinematically identified by missing mass of  ${}^3\text{He}(K^-, \Lambda p)X$  or detected by forward neutron counter. We are able to measure both production and decay of the  $\bar{K}NN$  bound state by using missing mass of neutron and  $\Lambda p$  invariant mass spectra, respectively. If there is a deeply bound state of the  $\bar{K}NN$  observed in FINUDA, DISTO, and E27 experiments, dump structure could be observed in the region lower  $K^- + p + p$  threshold.

### 1.6.1 Semi-inclusive analysis of ${}^3\text{He}(K^-, n)$ reaction

Recently, the semi-inclusive forward neutron spectrum in the E15 experiment has been published[64]. In semi-inclusive analysis, forward neutron was detected and one or more than one charged particles were detected to reconstruct a reaction vertex. Missing mass spectrum of  ${}^3\text{He}(K^-, n)$  is shown in Fig. 1.13. No significant structure was seen in the deeply-bound region which corresponds to B.E. =  $\sim 100 \text{ MeV}$  of  $\bar{K}NN$ . Upper limits of

the production cross section were estimated to be 30–180, 70–250, and 100–270  $\mu\text{b}/\text{sr}$  at  $\theta_n^{\text{lab}}=0^\circ$ , for  $\bar{K}NN$  widths of 20, 60, and 100 MeV, respectively. In the case of a large width of 100 MeV the upper limit was not so stringent. On the other hand, a long sub-threshold tail reaching  $\sim 100$  MeV below the  $\bar{K}NN$  threshold was observed. This sub-threshold tail may come from a shallow bound  $\bar{K}NN$  state, which B.E. is 10–50 MeV or  $Y^*$  production with two nucleon absorption.

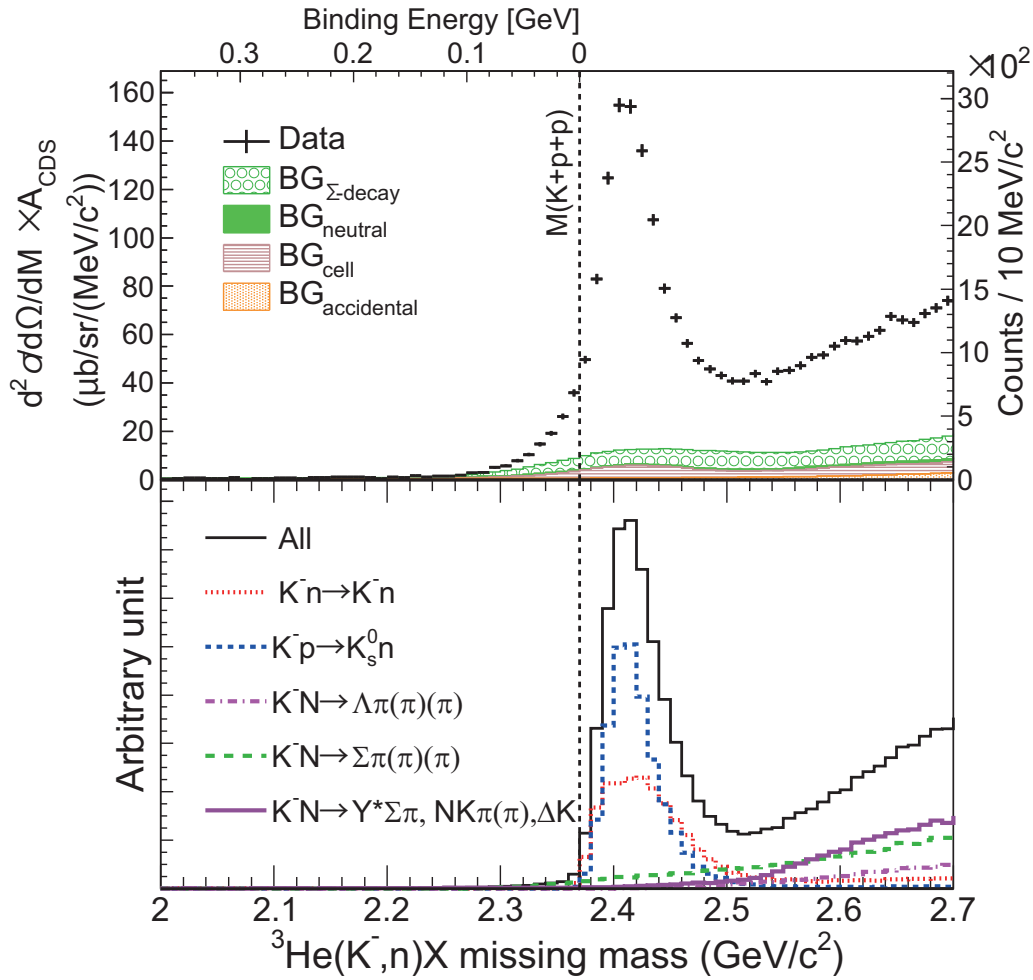


Figure 1.13: Comparison of the  ${}^3\text{He}(K^-, n)X$  semi-inclusive missing-mass spectrum between experimental data (top) and the simulation (bottom). Taken from [64].



cently, 2NA of  $K^-_{stopped}$  reaction on  $^4\text{He}$  target was observed in KEK-PS E549 experiment[42, 43]. On the other hand, there is no experimental data about multi nucleon absorption in in-flight  $K^-$ . Thus, the present analysis is the first measurement of multi-nucleon absorption in in-flight  $K^-$ . We can identify 2NA process, because events of 2NA reaction should be distributed in a narrow region of the edge of the phase space. Also events from 3NA reaction are expected to widely distribute in the phase space, we are able to identify 3NA reaction and the  $\bar{K}NN$  bound state by checking the phase space distribution of the  $\Lambda pn$  events.

The another advantage of exclusive analysis is a large acceptance of neutron. By using missing neutron, we are able to cover a wide range of  $\cos\theta_n^{lab.}$  as shown in Fig. 1.15. The details of the acceptance will be discussed in Section. 3.10. On the other hand, the acceptance of forward neutron counter is very limited as  $\sim 20$  msr, corresponding to  $\cos\theta_n^{lab.} > 0.995$ . Thus, we are able to measure an angular distribution in the  $^3\text{He}(K^-, \Lambda p)n$  reaction. The  $\Lambda$  and proton were detected with a cylindrical detector system which covered 49 to 131 degrees in the Lab., about 66% of  $4\pi$ . The detection thresholds of momentum are  $\sim 120$  MeV/ $c$  for low energy proton and  $\sim 30$  MeV/ $c$  for pions, which limited by geometry of the detectors and materials.

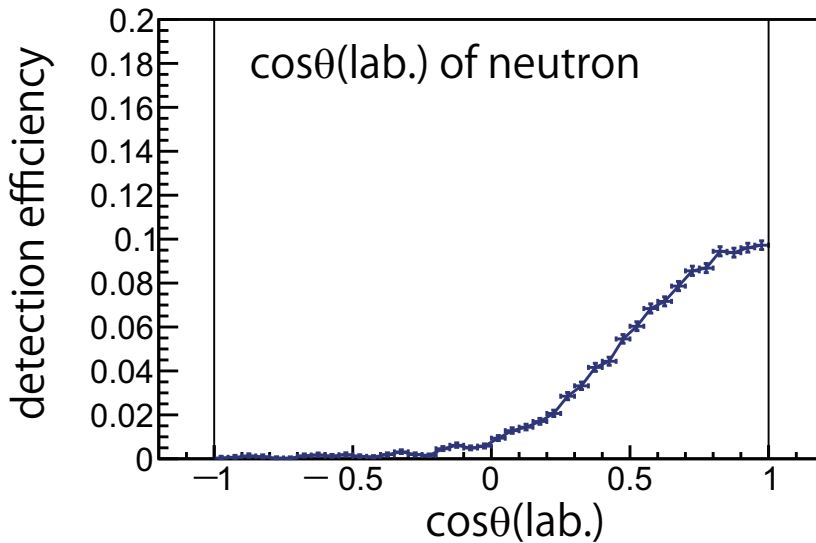


Figure 1.15: Acceptance of  $\cos\theta_n$  in  $\Lambda pn$  events.  $\theta = 0$  is the beam direction in the Lab. frame.

In this analysis, we can search for the  $\bar{K}NN$  bound state including a region near the  $K^-pp$  threshold corresponding to weakly bound state with  $\Lambda p$  invariant mass. In addition, the present analysis is the first measurement of multi-nucleon absorption in in-flight  $K^-$ . Measurement of multi-nucleon absorption in in-flight  $K^-$  is also important to understand background processes in in-flight  $K^-$  reaction.

## 1.8 Thesis overview

In this thesis, the analysis of  ${}^3\text{He}(K^-, \Lambda p)n$  reaction was performed. This thesis is arranged by the following order. The experimental setup are described in Chapter 2. The detail of the analysis, analysis methods and performances of detectors and identification of  ${}^3\text{He}(K^-, \Lambda p)n$  reaction are described in Chapter 3. The results of the analysis and the discussion are described in Chapter 4, where a Daliz plot of the  $\Lambda pn$  final state and an invariant mass spectrum of  $\Lambda p$  are shown. Finally, the conclusion is given in Chapter 5.



# Chapter 2

## Experimental setup

### 2.1 Overview of Apparatus

The experiment was performed at Japan Proton Accelerator Research Complex (J-PRAC) K1.8BR beamline which is located at the Hadron experimental facility. The high intensity primary proton beam is accelerated up to 30 GeV by J-PARC main ring (MR) and delivered to a gold target to produce secondary beam such as  $\pi^\pm$ ,  $K^\pm$ ,  $p$  and  $\bar{p}$ . After separation of  $\pi$ , 1 GeV/c  $K^-$  beam was delivered to the experimental target by the K1.8 beam line spectrometer. Figure 2.1 is a picture of the J-PARC K1.8BR experimental area and Fig. 2.2 shows a schematic view of J-PARC E15 spectrometers. Experimental setup consisted of three major components. First is a beam spectrometer for particle identification and beam momentum reconstruction. A purification for the  $K^-$  beam was performed with an Aerogel Cherenkov counter at online trigger level. The purity of the  $K^-$  was evaluated by time of flight (TOF) analysis in offline analysis between beam hodoscope detector (BHD) and a time-zero counter (T0), which is evaluated to be 99 %. The momentum of  $K^-$  was analyzed by beam line spectrometer which consists by two beam trackers (BLC1 and BLC2) installed before and after the dipole magnet and small drift chamber (BPC) which was located just before final focus.

Second is a liquid  $^3\text{He}$  target system and a cylindrical detector system (CDS) which detects produced particles emitted in the  $K^-$  reaction on  $^3\text{He}$ . A cylindrical target cell, 137 mm long and 68 mm in diameter, was filled with liquid helium-3, placed at the final focus point of the beam line. The density of the target was  $0.081 \text{ g/cm}^3$  at a temperature of 1.4 K. The CDS was placed surrounding the target cell in a solenoid magnet. The momentum of particle tracks was reconstructed with a Cylindrical Drift Chamber (CDC). The field strength in the solenoid magnet was about 0.7 T. The signals from Cylindrical Detector Hodoscope (CDH) which placed outside the CDC were used for particle identification with TOF in offline analysis.

Last component is Forward TOF walls. A Neutron Counter (NC) was 7 layered plastic scintillators of which thick was 5 cm. Charged and neutral forward going particles were separated with a Di-pole magnet (USHIWAKA) which was installed in down stream of the CDS. Positive charged particles were detected in a Proton Counter which was installed in next to the NC. Flight length from the final focus to the Forward TOF walls was about 14–15 m.

In this thesis, data which accumulated in May 2016 have been analyzed. During the run period, events corresponding to  $3.4 \times 10^9$  effective kaons on  ${}^3\text{He}$  target had been collected and used for this analysis.

The Details of each detector are described in the following sections.

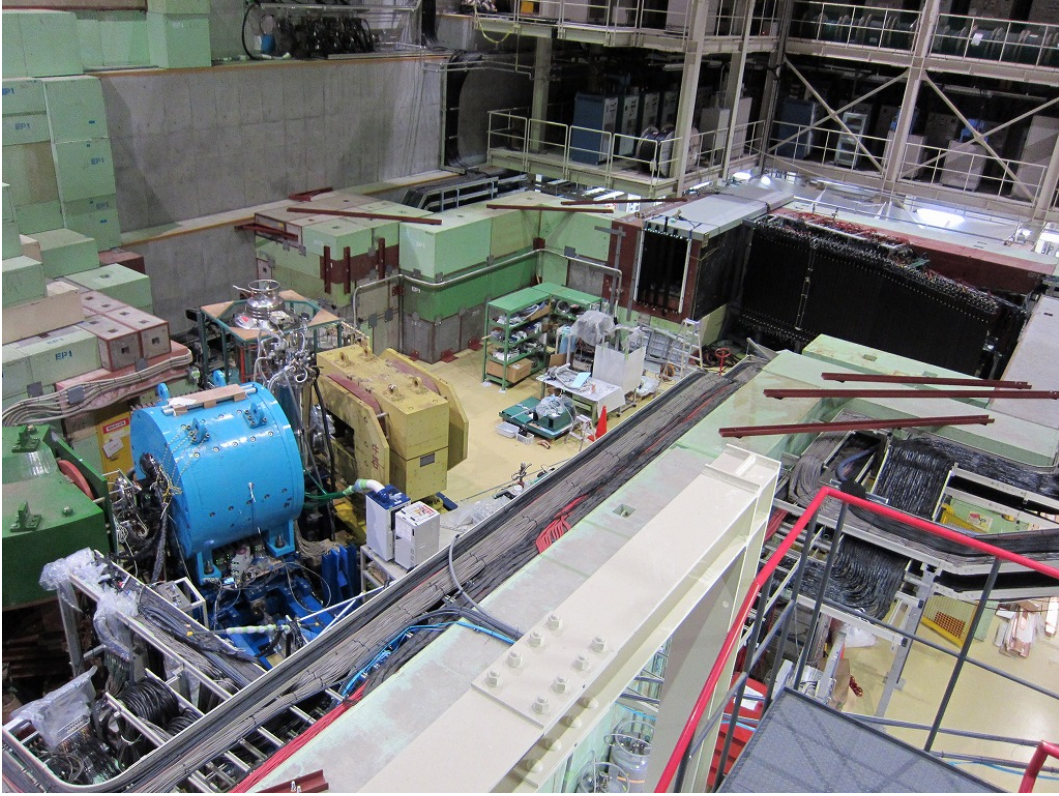


Figure 2.1: Picture of J-PARC K1.8BR experimental area

## 2.2 Accelerator facility and primary beam line

The Japan Proton Accelerator Research Complex (J-PRAC) was constructed in Tokai, Japan. The facility consists of three parts of accelerators, a linear accelerator, a rapid-cycle synchrotron, and a main ring (MR). A primary proton beam is accelerated to 30 GeV in the MR. The proton beam is extracted with slow extraction from the MR and transported to the Hadron Experimental Hall (HD-hall) through a beam-switching yard(SY). The first beam was delivered to HD-hall in January 2009. In May 2013, typical beam intensity of the primary proton beam in MR was  $30 \times 10^{12}$  per spill, where spill length was 2 seconds with a 6 second repetition cycle. Secondary beam was produced at a T1 target(Au, 50 % loss) and delivered to each experimental beam line in the HD-hall. The experiment was performed at K1.8BR beam-line using  $1 \text{ GeV}/c \text{ } K^-$ . Layout of hadron experimental facility is shown in Fig. 2.3.

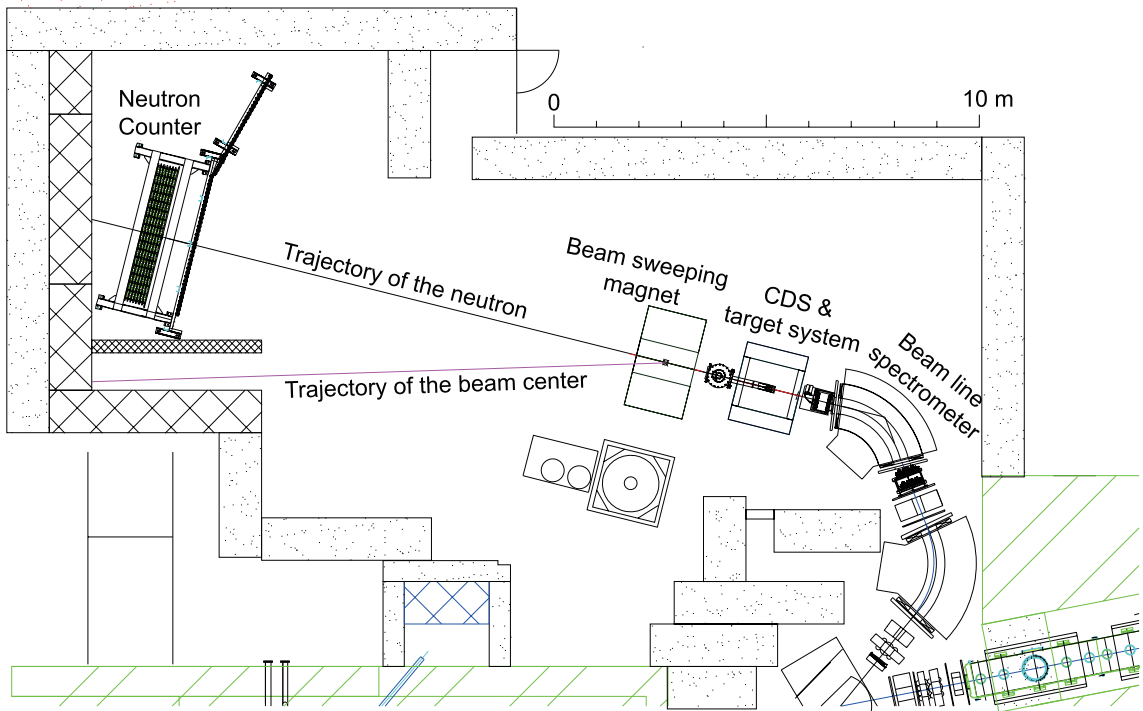


Figure 2.2: Schematic view of J-PARC E15 spectrometers

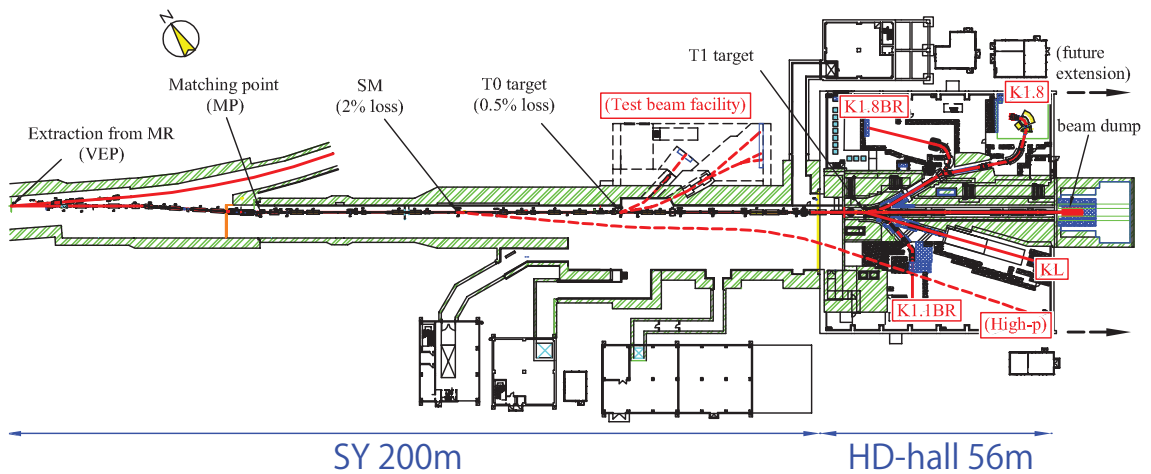


Figure 2.3: Layout of hadron experimental facility (the SY and the HD-hall). [68]

## 2.3 K1.8BR beam line

The configuration of K1.8BR is shown in Fig. 2.4. Secondary beams were produced at the Au target (50 % loss). Central bending angle of K1.8BR beamline respect to primary beam direction was designed to be 6 degree in laboratory system and the beamline acceptance is evaluated to be  $2.0 \text{ msr} \times \%$  ( $\Delta\Omega \times \Delta p/p$ ). In May 2013, typical beam intensity of the primary proton beam from the MR to the HD-hall was  $30 \times 10^{12}$  per spill, where spill length was 2 seconds with a 6 second repetition cycle.

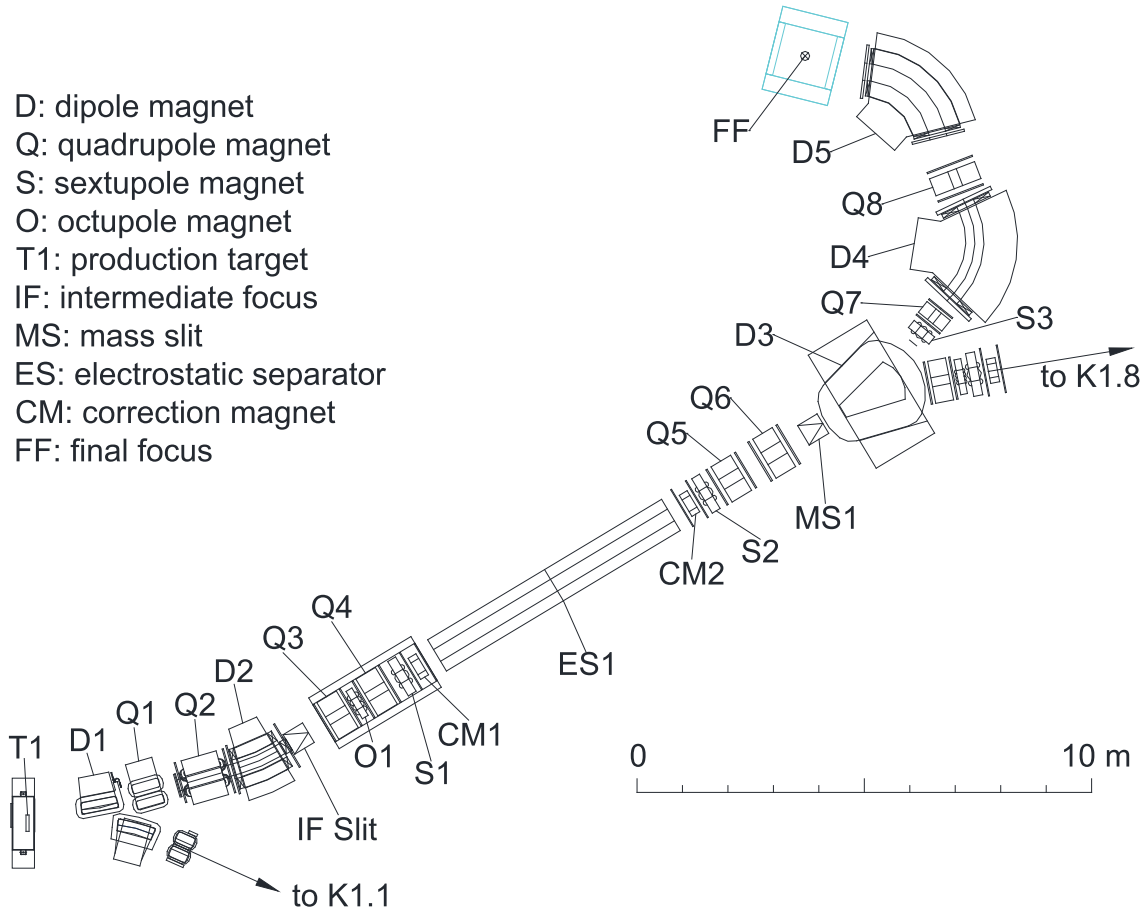


Figure 2.4: Schematic view of K1.8BR beamline. [70]

$\pi^-$  and  $\bar{p}$  in the secondary beam were removed with an electrostatic separator (ES1), and a pair of correction magnet (CM1, CM2). The 6 m-long ES1 vertically separates the particle trajectory by their mass with an applied electric field of 50 kV/cm. Finally, particles with a certain mass are selected by a vertical mass slit (MS1) with a help of two vertical steering magnets, CM1 and CM2. The typical  $K^-/\pi^-$  ratio was 0.45. The first-order beam envelope calculated by the TRANSPORT code is shown in Fig. 2.5. The parameters of magnets and slits are summarized in Table. 2.1. Details of the beam line elements and optical design are described in Ref. [69]. The last component of the beam line magnets were composed of an SQDQD system, which located just downstream of a D3 magnet, were used to analyze the

momentum of the beam particle and identify the particle species. Detail will be discussed in the next sub section.

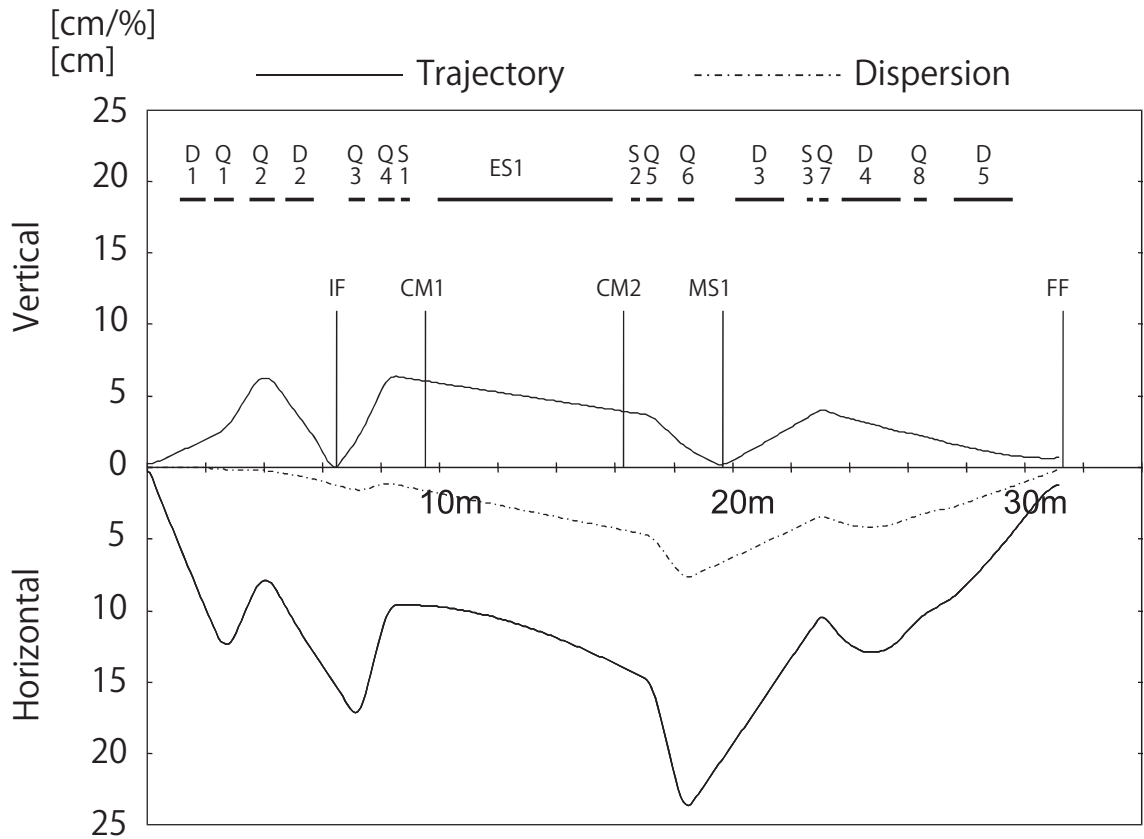


Figure 2.5: First-order beam envelope of the K1.8BR. Taken from [69]

Table 2.1: Parameters of the beam-line magnets and slits.

Element	J-PARC designation	Gap or bore/2 [cm]	Effective length [cm]	Bend [deg]	Current [A]	Field at pole [kG]
D1	5C216SMIC	8	90.05	10	-365 – -374	-6.581 – -6.744
Q1	NQ312MIC	8	67.84		-357	-3.075
Q2	Q416MIC	10	87.04		-668	3.872
D2	8D218SMIC	15	99.65	15	-698	-8.7673
Element	explanation			slit setting [mm]		
IF-H	Movable horizontal slit for acceptance control			110	-110	
IF-V	Movable vertical slit			2.5	-1.1	
Q3	Q410	10	54.72		-679	-4.108
O1	O503	12.5	15		-15	-0.29
Q4	Q410	10	54.72		-776	4.692
S1	SX504	12.5	27.6		-42	-0.29
CM1	4D604V	10	20	(0.856)	419	1.943
ES1	Separator	10	600		E= -500 kV/ 10 cm	
CM2	4D604V	10	20	(0.856)	419	1.940
S2	SX504	12.5	27.6		-136	1.02
Q5	NQ510	12.5	56		-498	4.218
Q6	NQ610	15	57.2		-535	-4.316
MOM	Movable horizontal slit for momentum acceptance control				L 160.0	R -110.0
MS1	Movable vertical slit for $K/\pi$ separation				1.75	-2.45
D3	6D330S	15	165.1	20	210	-7.064
S3	SX404	10	20		-34	-1.062
Q7	Q306	7.5	30.34		-464	4.026
D4	8D440S	20	198.9	60	-1936	-17.8907
Q8	NQ408	10	46.5		-110	0.671
D5	8D240S	20	195.9	55	-1663	-16.413

## 2.4 Beam line detectors

A schematic view of the beam line spectrometer is shown in Fig. 2.6. It was composed of beam line magnets, trigger counters, beam trackers, a kaon identification counter, and a beam defining counter. Two trigger counters, a beam hodoscope detector (BHD) and a time zero counter (T0) detected the timing of the beam particle. Coincidence signals of those two detectors were used for the trigger signal for data acquisition system. Moreover, the particle identification was done by using Time of Flight (TOF) measurement between the BHD and the T0. The flight length between the BHD and the T0 was 7.7 m. The beam momentum was analyzed by a last part of the beam spectrometer which consisted of D5 dipole magnet and two track chambers, BLC1 and BLC2, located upstream or downstream of the D5. The beam tracks were finally reconstructed by a vertex chamber (BPC), which was installed in front of the FF. An aerogel Cherenkov counter (AC) was used to identify 1 GeV/c  $K^-$  at trigger level. The refractive index of the AC was 1.05. The beam defining counter (DEF) was located just upstream of a target cell. The size was almost same as the target cell diameter. Signals of the DEF was also included in the trigger to ensure that the beam particle reached to the target.

### 2.4.1 Beam hodoscope counter (BHD)

The beam hodoscope counter (BHD) was used to generate the beam trigger signal and for reference timing signal for TOF measurement. It was located downstream of the D3 dipole magnet. The effective area was 400 mm (horizontal)  $\times$  160 mm (vertical) segmented into 20 units horizontally. The unit size was 160(height)  $\times$  20(width)  $\times$  5(thickness) mm. The pair of photomultipliers was attached both on top and bottom side of the scintillator. Signal rate of the photomultipliers was expected to 1 M counts. So a high voltage boosters for photomultipliers were added to the last tree dynodes and kept voltages by supplying current.

### 2.4.2 Time zero counter (T0)

Start timing for ToF measurement was generated by the time zero counter (T0), which was located downstream of the D5 dipole magnet. It had 5 segments of scintillators horizontally. Each segment was consist of Saint-Gobain BC420 scintillator (160  $\times$  32  $\times$  10 mm) and two 3/4 inch photomultiplier (Hamamatsu H6612B) attached on top and end of a scintillator. The T0 was rotated by 45 degree in XY plane, to avoid over-concentration of the beam in the center of segment and effect to the PMT by the magnetic field from D5 dipole magnet. The high voltage boosters for photomultipliers were set as same way as the BHD.

### 2.4.3 Beam definition counter (DEF)

The beam definition counter (DEF) was installed upstream of the target system (a vacuum vessel of the target). Under the current setup of beam line spectrometer in the K1.8BR, the size of beam spot was about twice larger than the diameter of  $^3\text{He}$  target cell. Therefore, for the efficient data taking, a counter which ensure the beam particle hit on the target cell were mandatory. Thus the DEF was designed to have almost same size with target cell.

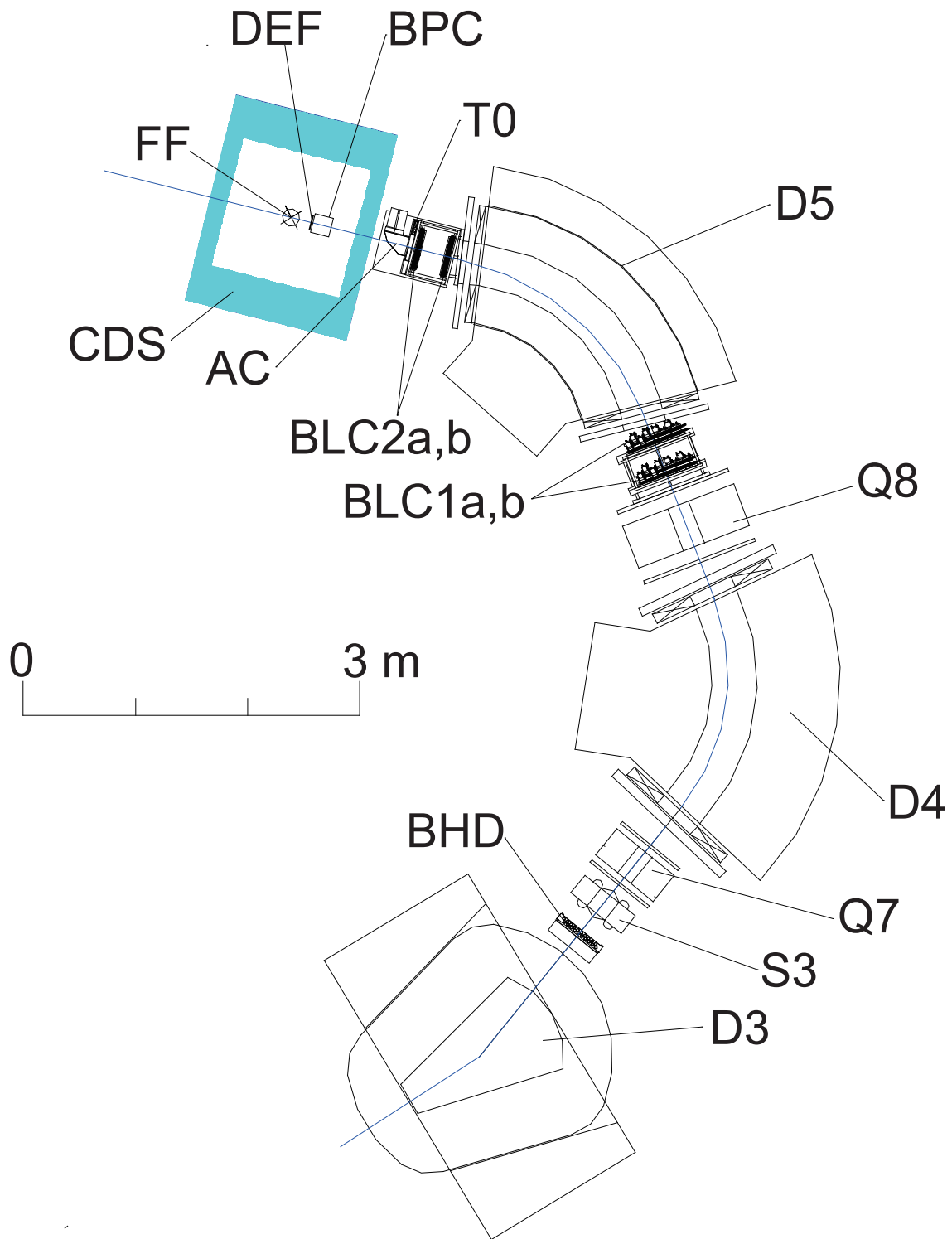


Figure 2.6: Schematic view of spectrometer of K1.8BR beamline. Taken from [70].

By using this counter, the data quality and a data acquisition efficiency were improved. In addition, to minimize energy loss and multiple scattering of the beam particle by the DEF itself, the DEF was made of thin scintillator(ELJEN EJ-202) with the thickness of 3 mm. The schematic view of DEF is shown in Fig. 2.7. The scintillation light was changed its wave-length and translated by a wavelength-shifting fiber (WLS), Kuraray Y-11(200)M, which had 1 mm diameter. This WLS fibers were embedded in the scintillator. The light was detected by multi-pixel photon counters (MPPCs) made by Hamamatsu (S10362-11-100C). MPPCs and WLS fibers were connected by GOMI connectors developed for the T2K experiment [71].

The total trigger rate was suppressed to  $\sim 30\%$  by introducing the coincidence of the DEF signal with the signal from the BHD and T0.

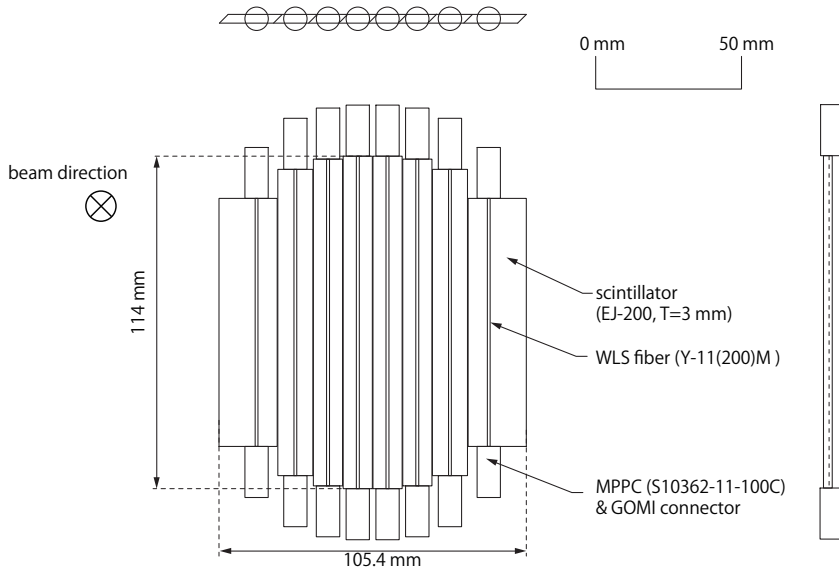


Figure 2.7: Schematic view of beam definition counter (DEF).

#### 2.4.4 Aerogel Cherenkov counter

As described in the previous section, the  $K/\pi$  ratio of the separated beam with the ESS separator was  $\sim 0.45$ . Therefore, further reduction of the pion beam on trigger level is essential to enhance data quality. Thus the Aerogel Cherenkov counter (AC) was installed just downstream of the T0. The AC was the threshold-type Cherenkov counter to reject about 1.0 GeV/ $c$  pions in the beam. Thus, aerogel which had reflection index 1.05 had been chosen as a cherenkov radiator. Figure 2.8 shows schematic view of the AC. The effective area of the AC was 180 mm(width)  $\times$  100 mm(height)  $\times$  100 mm(thickness) which covered fully with the secondary beam. The flinging magnetic field from the D5 and the CDS magnet were rather strong, so a fine-mesh type PMT was selected for photon detector. Four three-inch fine-mesh type photomultipliers (Hamamatsu R5543) were used and those were located at the top and bottom of the aerogel radiator. The radiator was covered with thin mirror

foils which reflected Cherenkov light. The signal with more than seven photoelectrons were identified as pion at online level. A pion rejection efficiency is achieved over 99 % and purity of kaons was about 99 %.

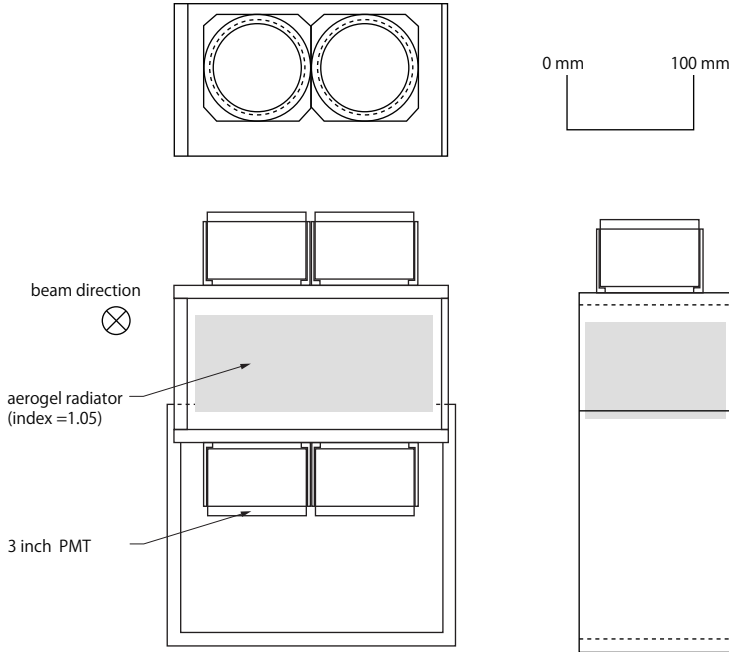


Figure 2.8: Schematic view of aerogel Cherenkov counter (AC).

### 2.4.5 Beam momentum analyzer

The beam momentum was analyzed by the deflection angle of the beam particle in the D5 dipole magnet, which was reconstructed by two planer drift chambers, the BLC1 and BLC2, which located upstream and downstream of the D5 magnet. Their tracks were connected by a second-order transport matrix. A helium bag was installed in the D5 magnet to suppress the effect of multiple scattering. The momentum resolution of the analyzer is estimated to be 0.1 %. The magnetic field inside the D5 magnet was monitored during the period of the experiment with a high-precision Hall probe (Lakeshore 475). The fluctuation of the magnet field was about  $2 \times 10^{-4}$  which corresponds to 0.2 MeV/c for 1.0 GeV/c beam.

#### BLC1 and BLC2

The beam line chamber, BLC1 which was located upstream of D5, consisted of two sets of drift chambers, a BLC1a and a BLC1b. The BLC1a and BLC1b have 8 layers ( $UU'VV'UU'VV'$ ). Angle of wire in the  $U$  and  $V$  was tilted  $\pm 45$  degree from vertical axis. Thirty two sense

wires were in each layer. A drift length was 4 mm. An effective area was  $256 \text{ mm} \times 256 \text{ mm}$ . Total number of readout channels was 512 for sum of the BLC1a and the BLC1b. The BLC1 was installed at 300mm apart from the D5 upstream entrance.

The BLC2 had same structure as the BLC1. The BLC2 also had two sets of drift chambers, a BLC2a and a BLC2b. Each chamber's configuration was 8 layers ( $UU'VV'UU'VV'$ ) with 32 sense wires in each layer. In the  $U$  and  $V$  layers, wires were tilted by  $\pm 45$  degrees. The drift length was 2.5 mm. An effective area was  $160 \text{ mm} \times 160 \text{ mm}$ . The BLC2 was installed at 275 mm apart from the D5 downstream entrance.

Sense wires for both BLC1 and BLC2 had  $12.5 \mu\text{m}$  diameter and were made of gold plated tungsten with 3 % rhenium. Potential wires for these chambers had  $75 \mu\text{m}$  diameter and were made of copper - beryllium. The cathode plane were made of  $12.5 \mu\text{m}$  aluminized Kapton. Same readout electronics were used for both chambers. The read out electronics were consists of a preamplifier-shaper discriminator board (ASD, SONY-CXA3653Q,  $\tau = 80 \text{ ns}$ ), LVDS-ECL converter and a Time-to digital converter (TDC). The signal from the ASD board mounted on the chambers was transferred to LVDS-ECL converter via 7 m twisted pair cables. The converted signal was sent to the TDC in the counting house with 50 m long twisted-pair cables. The gas for chambers was an argon-isobutane mixture with methylal (dimethoxy-methane), which ratio is Ar:  $\text{C}^4\text{H}^{10}$  :methylal = 76:20:4. The methylal was added to the gas by passing through bubbler filled by methylal at  $4 \text{ }^\circ\text{C}$ . The operating high voltages of the BLC1 and the BLC2 were -1.35 kV on both the potential wires and the cathode planes.

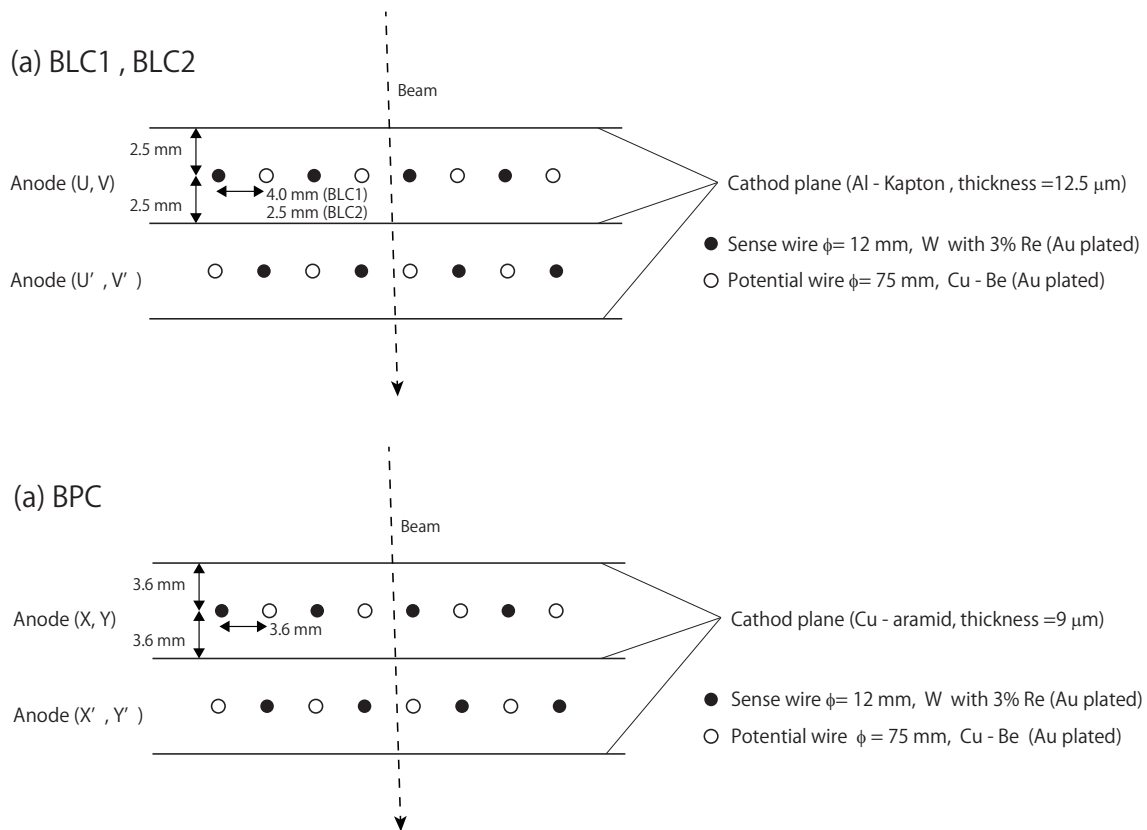


Figure 2.9: Cell and wire geometries of BLC1, BLC2(a) and BPC(b).

Table 2.2: Summary of parameters of the beam-line chambers.

	BLC1a	BLC1b	BLC2a	BLC2b	BPC
number of planes	8	8	8	8	8
plane configuration	$UU'VV'UU'VV'$	$UU'VV'UU'VV'$	$UU'VV'UU'VV'$	$UU'VV'UU'VV'$	$XX'YY'XX'YY'$
number of sense wires	32	32	32	32	15
wire spacing [mm]	4	4	2.5	2.5	3.6
effective area [mm]	$256 \times 256$	$256 \times 256$	$160 \times 160$	$160 \times 160$	$111.6 \text{ mm } \phi$
Sense wire material	Au-plated W (3 % Re)				
diameter [ $\mu\text{m}$ ]	12				
Potential wire material	Au-plated Cu-Be				
diameter [ $\mu\text{m}$ ]	75				
Cathode plane wire material	Alminized-Kapton				
thickness [ $\mu\text{m}$ ]	12.5				
Gas	Ar : isoC <sub>4</sub> H <sub>10</sub> : Metylal = 76 : :20 : 4				
flow [cc/min]	100				
Operation voltage					
potential [kV]	-1.35	-1.35	-1.35	-1.35	-1.5
cathode [kV]	-1.35	-1.35	-1.35	-1.35	-1.5

### 2.4.6 Vertex chamber (BPC)

The BPC (backward proton chamber) was originally developed for the spectroscopic study of  $\Lambda(1405)$  (J-PARC E31 experiment) to detect a backward-scattered proton. In this thesis, the BPC was used as one of beam tracker in front of the target, to determine the reaction vertex point precisely.

The BPC was a circular planer chamber whose size was 168 mm in diameter and 89.7 mm in depth. The effective area was 111.6 mm in diameter. It was installed upstream of the target system. Figure 2.10 shows a schematic view of the BPC. It had 8 layers with a  $XX'YY'XX'YY'$  configuration. The wire of the Y layer were tilted by 90 degree respect to X layers. Each layer had 15 sense wires with a drift length of 3.6 mm. The cathode planes were made of  $9\ \mu\text{m}$  carbon aramid foil. The sense and potential wires, readout electronics, and gas for the BPC were same as ones of the BLC1 and the BLC2. The operating high voltage of the BPC was set at -1.45 kV on both the potential wires and cathode planes.

The summary of the parameters of the beam line chambers and wire geometries are shown in Table 2.2 and Fig. 2.9

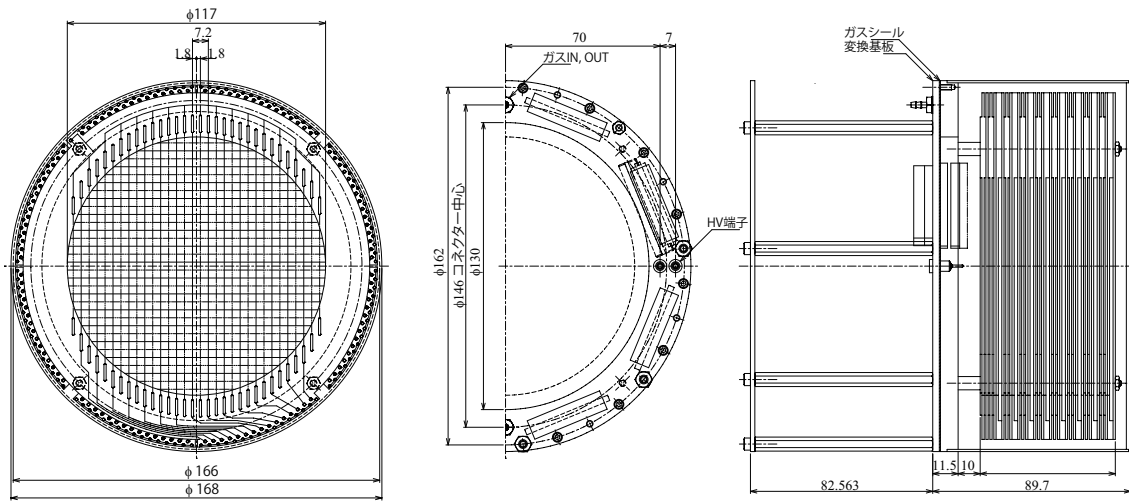


Figure 2.10: Schematic view of the BPC.

## 2.5 Target system

A cryogenic target system for liquid  $^3\text{He}$  was developed for the this experiment. It was based on the the liquid  $^4\text{He}$  target system which was used in a past experiment [72]. Details of this system can be found in elsewhere [73].

The requirements to the target system are summarized as follows.

1. stable operation to reduce uncertainty of the target material,
2. low-material in the region where beam passing through, to suppress the energy loss and reduce the interaction of the  $K^-$  other than  $^3\text{He}$  nucleus, and
3. separate the target cell and cooling system due to the space limitation in detector system and experimental area.

The stable operation was achieved at a test of the target system [73]. To reduce the materials in the region though the beam, the target cell was made by beryllium and a skin of a vacuum chamber was made by carbon fiber reinforced plastic (CFRP). The details of target system and its performance are described in Appendix A.

### 2.5.1 Target cell

The schematic view of the target cell is shown in Fig. 2.11. The side shell of the cell was made of 0.3 mm thick beryllium (more than 99.4 % purity). The caps of the both ends were made of AlBeMet, which was an alloy of aluminum and beryllium. The volume of the target cell was 0.48  $\ell$ . 0.48  $\ell$  liquid  $^3\text{He}$  at 1.3 K was consist of 269  $\ell$  gaseous  $^3\text{He}$  at room temperature.

### 2.5.2 The density of $^3\text{He}$ liquid target

The density of  $^3\text{He}$  liquid target in the experimental period is evaluated to be  $0.0810 \pm 0.0002$  g/cm<sup>3</sup>, which corresponds to 1.11 g/cm<sup>2</sup> thickness for the 138 mm beam direction length. The error was estimated with fluctuation of temperature of  $^3\text{He}$  target in the data taking period and result of a past test of  $^3\text{He}$  target system. The temperature difference between the evaporator, the heat exchanger, and the target cell were less than 0.01 K. It means that the cooling system was worked well. The heat load of the low-temperature region was found to be 0.21 W from the reduction rate of the liquid  $^4\text{He}$  in the evaporator.

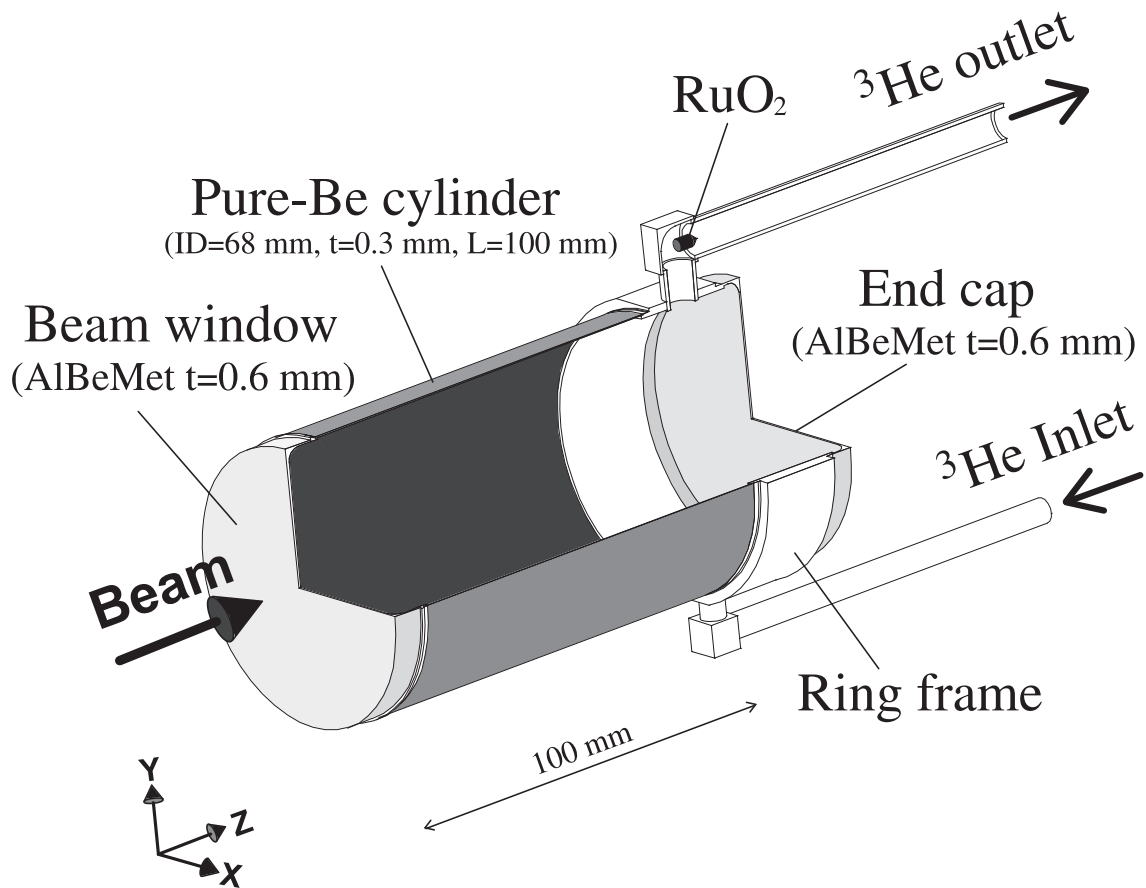


Figure 2.11: Schematic view of the target cell.

## 2.6 Cylindrical detector system

To detect particles generated by  $K^-$  and  ${}^3\text{He}$  reaction, the Cylindrical detector system (CDS) was installed to surround the target cell. A schematic view of the CDS is shown in Fig. 2.12. The CDS consisted of a solenoid magnet with 0.7 T, a cylindrical drift chamber (CDC), a cylindrical detector hodoscope (CDH), a inner hodoscope (IH), and a backward proton detector (BPD). Particle tracks were reconstructed by the CDC. The CDH measures Time-of-flight of the particle. The IH was installed to enlarge the acceptance for the tracks out of the CDH acceptance. The BPD was a dedicated detector to detect backward scattered particles from the reaction, which was developed for other experiment [J-PARC E31:  $\Lambda(1405)$  study via the  $d(K^-, n)$  reaction] [76].

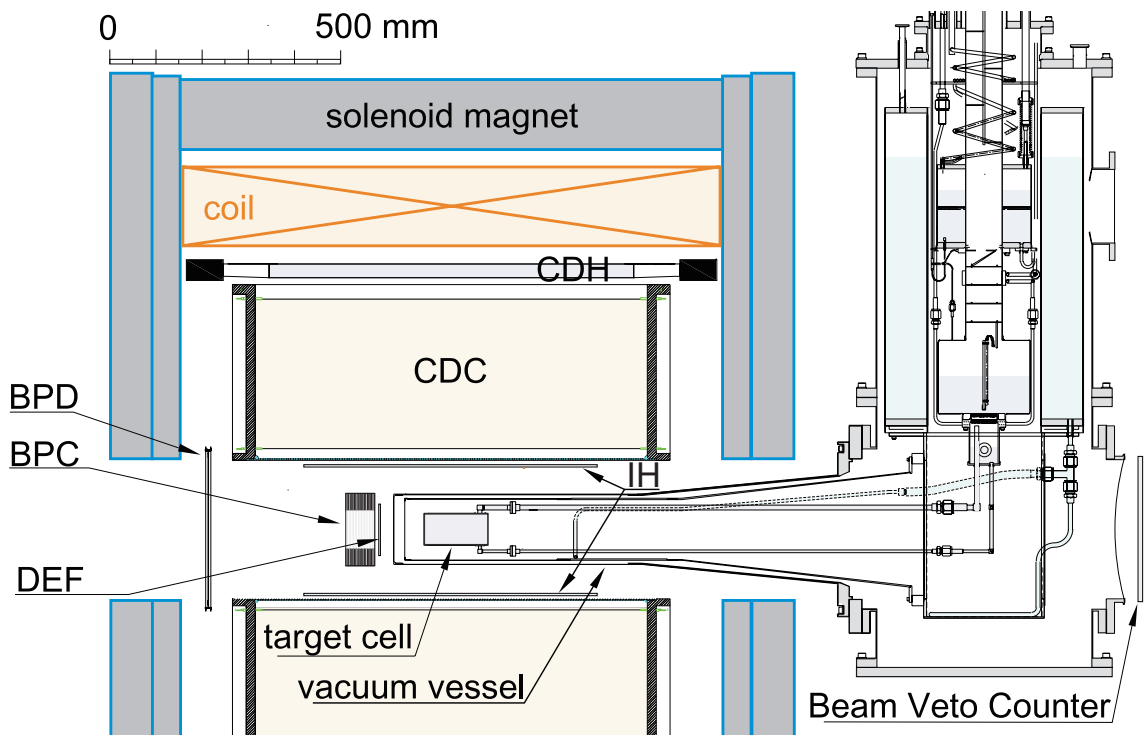


Figure 2.12: Schematic view of the CDS.

### 2.6.1 Solenoid magnet

A solenoid magnet was used for the CDS. Its bore diameter was 1.18 m and its length was 1.17 m and an overall weight was 23 tons. The design of the solenoid magnet is shown in Fig. 2.13. It was installed in the final focus point along the beam line. It was operated at 0.7 T in the present experiment. Figure 2.14 shows a distribution of the strength of the magnet field was calculated by TOSCA[75]. A strength of magnetic field was uniform in sensitive region of the drift chamber. Difference from a center value of magnetic field was less than 0.2 % in sensitive region of the drift chamber.

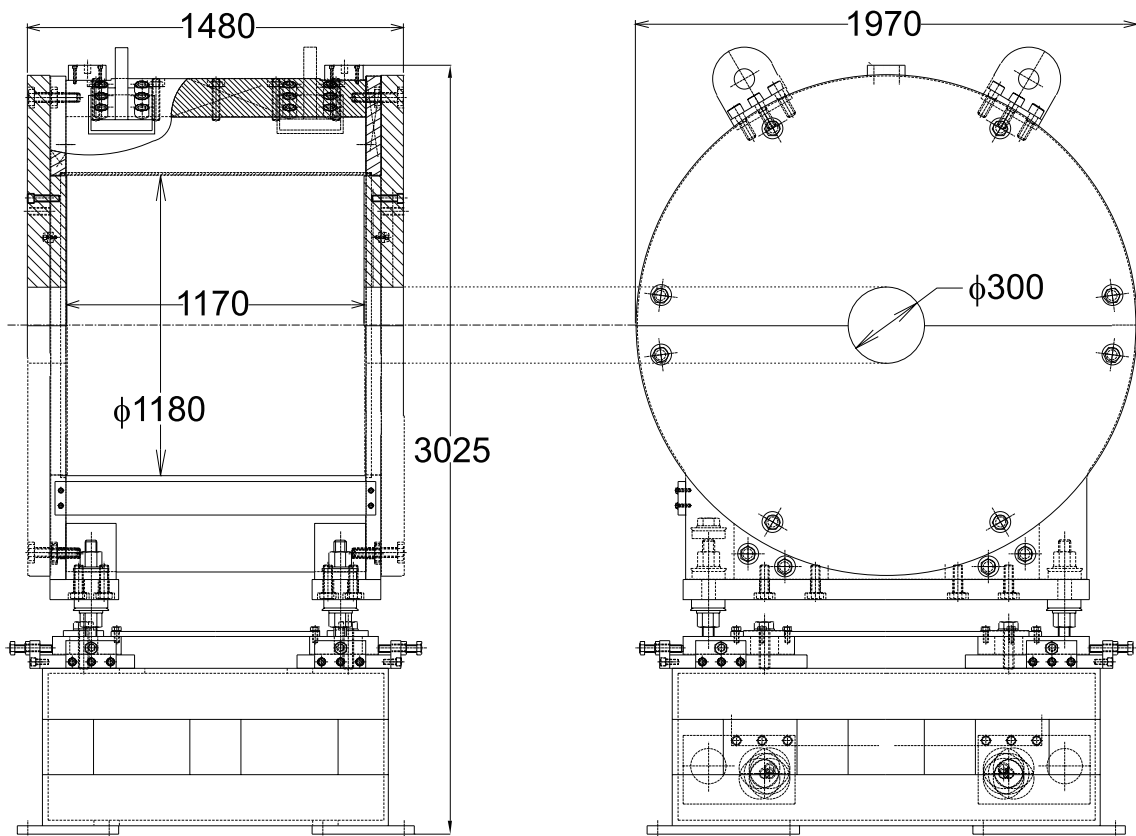


Figure 2.13: Design of the solenoid magnet for the CDS. All dimensions are in mm.

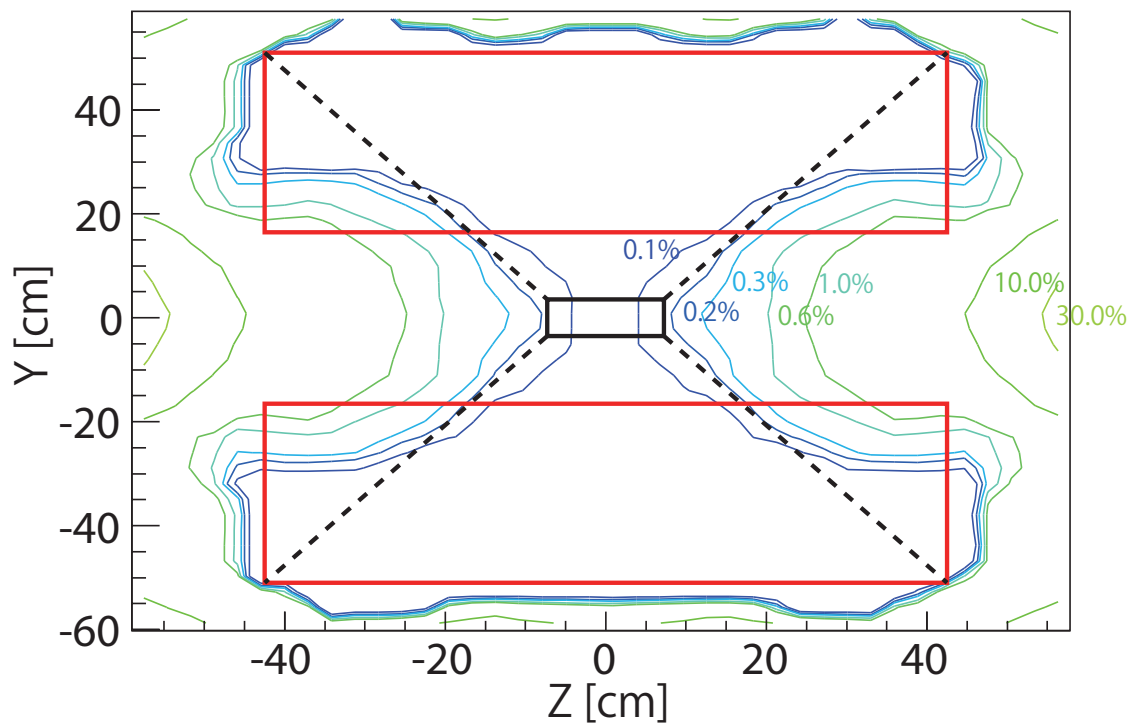


Figure 2.14: Distribution of the strength of magnetic field calculated by TOSCA. Each value was scaled by the value at the center of the solenoid magnet. A red boxes, and black box show sensitive region of the drift chamber and target region, respectively.

## 2.6.2 Cylindrical drift chamber (CDC)

The design of the CDC is shown in Fig. 2.15. The CDC had 15 layer of anode wires. An inner and outer radii were 150 mm, 530 mm respectively. A total length of the CDC was 950 mm. The wire length of axial layer was 833.8 mm. The angle coverage in the polar angle was  $49^\circ < \theta < 131^\circ$ , which corresponds to a solid angle coverage of 66 % of  $4\pi$ . An inner radius wall of the CDC was made of a 1 mm thick CFRP cylinder to reduce inner material. An end-plate of the CDC was 20 mm thick aluminum and six aluminum posts were placed outside of the tracking volume. The sense wires were  $30 \mu\text{m}$   $\phi$  gold-plated tungsten and field and guard wires were gold-plated aluminum of  $100 \mu\text{m}$   $\phi$ . These wires were supported by feed-through with a bushing inserted at the end-plate. Holes of the bushes were 80 and  $200 \mu\text{m}$   $\phi$  for the sense and field(guard) wires, respectively.

The CDC had 15 layers with hexagonal cells, which were grouped into 7 super-layers as shown in Fig. 2.16. A typical drift length was  $\sim 9$  mm. The first layer (Layer #1) was on 190.5 mm in radius and the outer layer (Layer #15) was on 484.5 mm in radius. Wires in 8 stereo layers which give longitudinal information was tilted  $3.5^\circ$ . The total number of wires was 8064 and the number of readout channels was 1816.

The gas of the CDC was mixed argon-ethane (50% : 50 %) with 1 atm. Each values of high voltages applied to field wires in the super-layers were A1 : -2.8kV, U1 : -2.8kV, V1 : -2.7kV, A2 : -2.7kV, U2 : -2.7kV, V2 : -2.7kV, A3 : -2.7kV. And -1.5kV, -1.8kV, and 0.6kV for the innermost, outermost and other guard wires, respectively. The CDC readout electronics were made of a preamp card (ASDs : SONY-CXA3183Q,  $\tau = 16$  ns), an LVDS-ECL converter, and a TDC, which were same as those for the beam line chambers. The details of the CDC's parameters are summarized in Table 2.3.

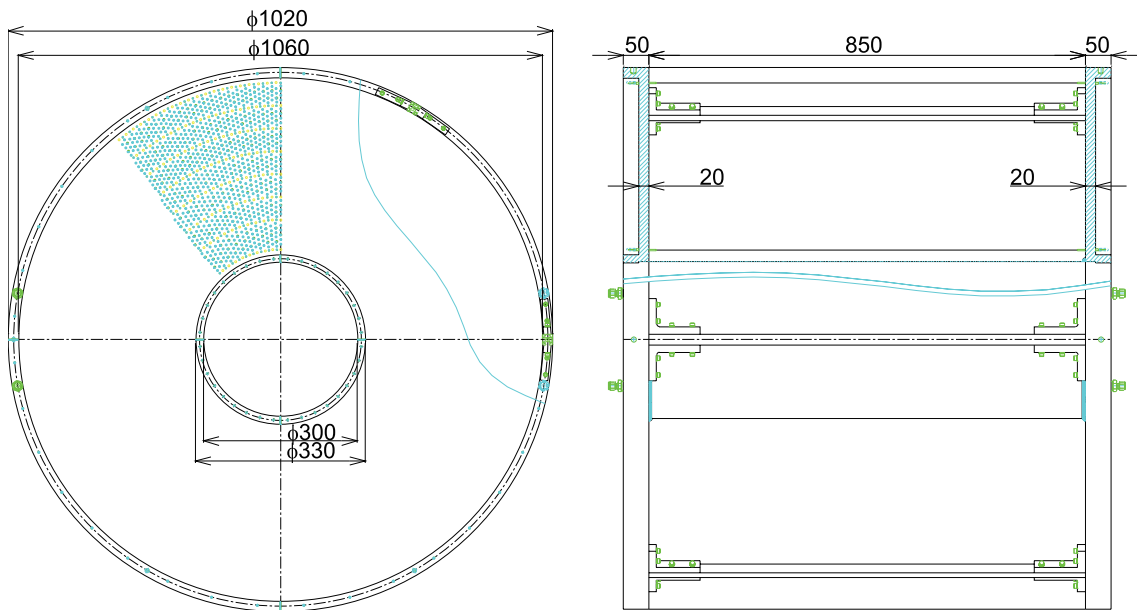


Figure 2.15: Design of the CDC structure. All dimensions are in mm.

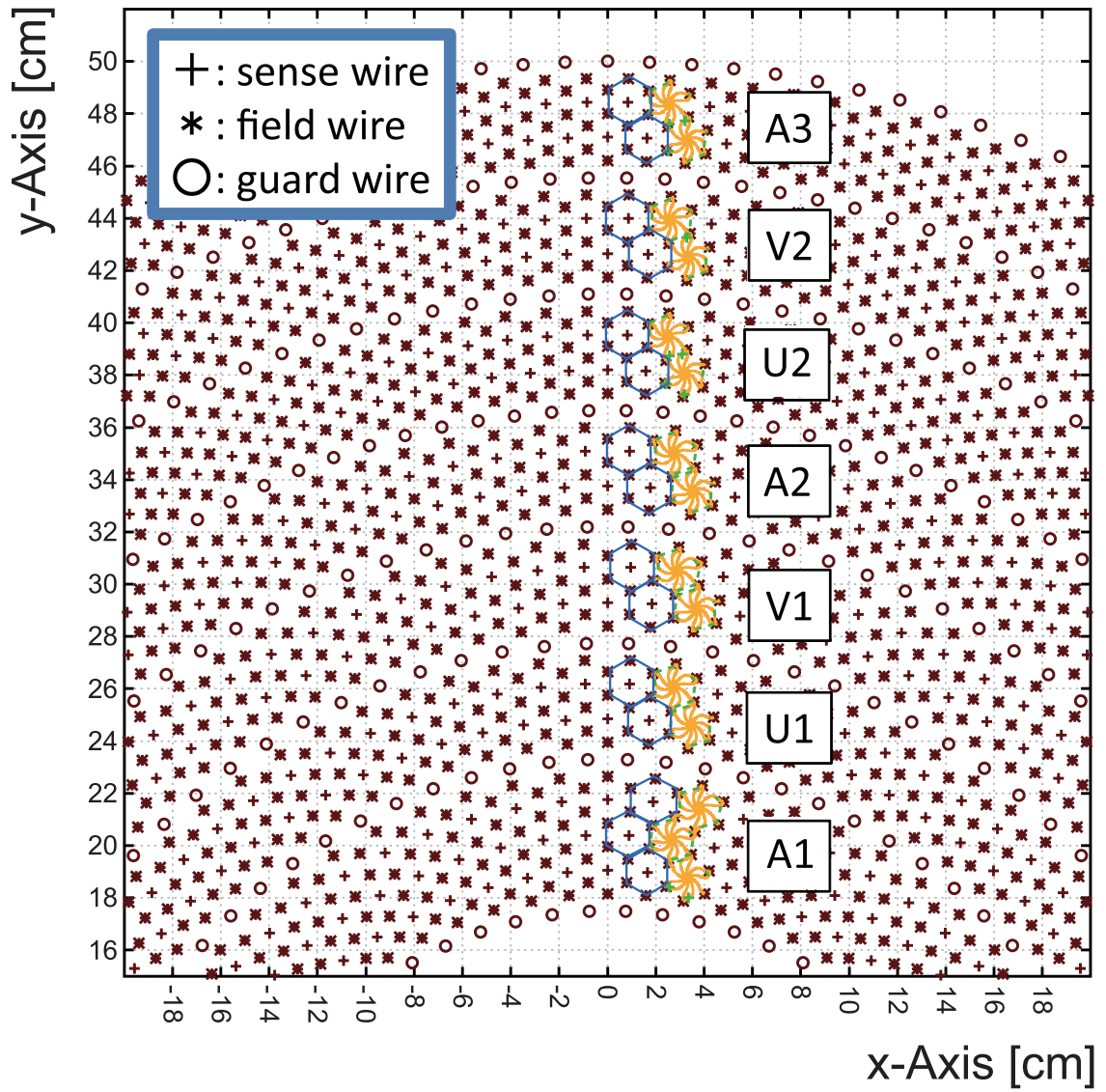


Figure 2.16: Cell geometry of the CDC.

Table 2.3: Wire configuration of the CDC.

Super-layer	layer	Wire direction	Radius [mm]	Cell width [degree]	Cell width [mm]	Stereo angle [degree]	readouts per layer
A1	1	$X$	190.5	5.00	16.7	0	72
	2	$X'$	204	5.00	17.8	0	72
	3	$X$	217.5	5.00	19	0	72
U1	4	$U$	248.5	4.00	17.3	-3.55	90
	5	$U'$	262	4.00	18.3	-3.74	90
V1	6	$V$	293	3.60	18.4	3.77	100
	7	$V'$	306.5	3.60	19.3	3.94	100
A2	8	$X$	337.5	3.00	17.7	0	120
	9	$X'$	351	3.00	18.4	0	120
U2	10	$U$	382	2.40	16	-3.28	150
	11	$U'$	395.5	2.40	16.4	-3.39	150
V2	12	$V$	426.5	2.25	16.7	3.43	160
	13	$V'$	440	2.25	17.3	3.54	160
A3	14	$V$	471	2.00	16.4	0	180
	15	$V'$	484.5	2.00	16.9	0	180

### 2.6.3 Cylindrical detector hodoscope (CDH)

The Cylindrical detector hodoscope (CDH) was a segmented plastic scintillation counter for the trigger and Time-of-flight measurement of charged particle(s) in the reaction on  ${}^3\text{He}$  target. The CDH was installed in a radius of 544 mm from the beam axis. It covered a polar angle range 54 – 126 degree, corresponding to a solid angle coverage of 59 % of  $4\pi$ .

The CDH was made of 36 modules which mounted on the inner wall of the solenoid magnet. The scintillators were Eljen EJ-200, with dimensions of 790 mm in length, 99 mm in width, and 30 mm in thickness. On both ends of scintillator, light guides and PMTs (Hamamatsu R7761 fine-mesh 19-dynode, with 1.5 inches  $\phi$ ) were mounted.

A typical gain of PMT is  $\sim 10^6$  in the 0.7 T magnetic field. From the cosmic ray data, the average time resolution of the CDH without a magnetic field is  $71 \pm 3$  ps ( $\sigma$ ). The error mainly arises the variation among the segments.

### 2.6.4 Inner hodoscope counter (IH)

The inner hodoscope counter (IH) was a segmented plastic scintillation counter installed on the inner wall of the CDC at a radius of 140 mm from the beam axis. The IH covered a polar angle range 27 – 153 degrees, which corresponds to a solid angle coverage of 89 % of  $4\pi$ .

The IH was made of 24 scintillators (ELJEN EJ-200) with dimensions of 600 mm (length)  $\times$  37 mm (width)  $\times$  3 mm (thickness). Each scintillator had overlapped region of 1 mm. Due to the strong magnetic field and a limited space, multi-pixel phton counters(MPPCs : Hamamatsu S10362-33-100C) with a 3 mm  $\times$  3 mm sensitive area were used and mounted a side of each segment. Four wavelength-shifting fibers were embedded in the scintillator

and collects the scintillation light. The wavelength-shifting fibers and the MPPC were connected by specially designed connector. The signal from MPPC was fed to the preamplifier (HOSHIN N018 NIM module) and send it to counting house for ADC measurement. In this analysis, the IH was used to estimate tracking efficiency of the CDC.

### 2.6.5 Backward proton counter (BPD)

The backward proton counter (BPD) was a plastic scintillator hodoscope array which is in 0.5 m upstream from the final focus. This counter were aimed to detect backward going particle for other experiment [J-PARC E31 experiment:  $\Lambda(1405)$  study via the  $d(K^-, n)$  reaction] [76]. The size of the BPD was 350 mm (horizontal)  $\times$  340 mm (vertical)  $\times$  5 mm (width) segmented into 70 units. Scintillator consisted of Eljen EJ-230 (340 mm  $\times$  5 mm  $\times$  5 mm). Due to the strong magnetic field and a limited space, multi-pixel phton counters(MPPCs : Hamamatsu S10362-33-0550C) with a 3 mm  $\times$  3 mm sensitive area were used and mounted both side of each segments. Fast timing amplifier (ORTEC FTA 820) were used for the readout of the MPPCs signal. A typical time resolution of 160 ps was achieved in the engineering run. The BPD was not used in this analysis expect for a calculation of an energy loss for the kaon beam.

## 2.7 Forward TOF detector system

To detect forward going neutron and proton in the  ${}^3\text{He}(K^-, N)$  reaction, a Forward TOF detector system was installed at about 0 degrees with respect to the beam direction. Flight length was 14 – 15 m for both protons and neutrons to achieve good momentum resolution. The Forward detector system consisted of a neutron time-of-flight counter (NC) which is array of plastic scintillators, a proton time-of-flight counter (PC), a charge veto counter (CVC), and a beam sweeping magnet. The schematic view of the forward TOF detector system is shown in Fig. 2.17. The neutron TOF counter, placed at 15 m downstream from the final focus point and detected a forward neutron generated by the in-flight  $(K^-, n)$  reaction. The neutron TOF counter was an array of scintillator counters previously used by KEK-PS E549[78]. The sweeping magnet placed just after the CDS kicked out the kaon beam from the acceptance of the neutron counter. The CVC was located just before the NC to veto charged particles going in the acceptance of the NC. To measure both the  ${}^3\text{He}(K^-, p)$  and the  $(K^-, n)$  reaction, a proton TOF counter was installed on the side of the NC. A comparison of the two kinds of missing-mass spectra will provide unique information about iso-spin dependence of the  $\bar{K}N$  interaction. Trajectories of protons were reconstructed by a forward drift chamber (FDC1) located just upstream of the beam sweeping magnet. At the opposite side of the PC where kaon beam is swept out, a caved beam dump was constructed to reduce background events to the the NC. A beam veto counter (BVC) was located at just downstream of the target system and was used to reduce fake triggers for the forward neutron detection. Table 2.4 summarizes the total size and information of segment of each counter.

Table 2.4: Summary of counters of Forward TOF walls.

name	total size [m] hori.×vert.(×dep.)	scinti. size[mm] L×W×T	scinti. type	segmentation column(×layer)
NC	3.2× 1.5× 0.35	200× 1500× 50	Saint-Gobain BC 408(1,2,3 layers) BC 412(4,5,6 layers)	16× 7
CVC	3.4× 1.5	100× 1500× 30	Ejen EJ-200	34
PC	2.7× 1.5	100× 1500× 50	Saint-Gobain BC 408	27
BVC	0.315× 0.315× 0.01		Saint-Gobain BC 408	1

### 2.7.1 Beam sweeping magnet

A dipole magnet called Ushiwaka was used as the beam sweeping magnet. It was located just downstream of the CDS. The magnet had an aperture of 820 mm (horizontal) × 400 mm (vertical) and a pole length of 700 mm, and was capable of providing a maximum field of 1.6 T. This magnet was operated at  $\sim 1.0$  T in the production run to sweep the kaon beam away from the neutron counter acceptance window and guide the forward proton to the PC.

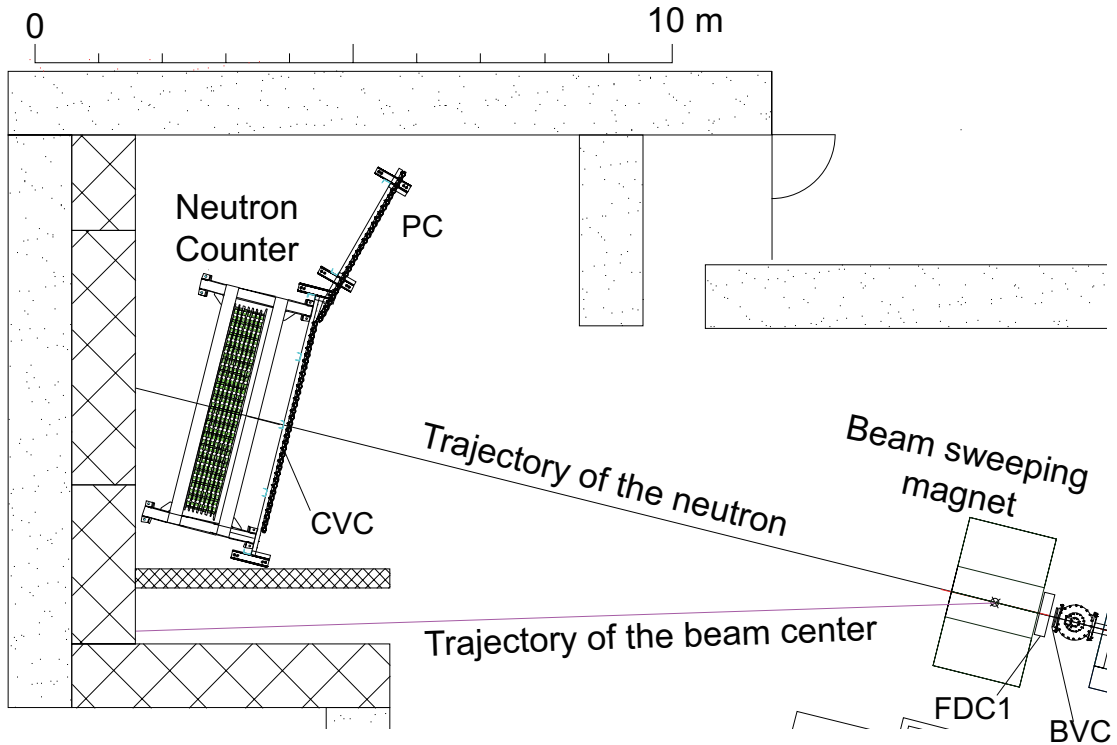


Figure 2.17: Schematic view of Forward TOF walls

### 2.7.2 Neutron time-of-flight counter (NC)

A neutron time-of-flight counter (NC) was an array of plastic scintillators, which has 16-column  $\times$  7-layer segments, and was located 14.7 m away from the final focus point. An effective volume of the NC is 3.2 m (horizontal)  $\times$  1.5 m (vertical)  $\times$  0.35 m (depth), corresponding to the acceptance  $\sim 20$  msr ( $\pm 6.2^\circ$  in the horizontal direction and  $\pm 2.9^\circ$  in the vertical direction). In both ends of segments, 2-inch photomultiplier (Hamamatsu H6410) was attached with a Lucite light guide. The scintillators for the first three layers were made of Saint-Gobain BC408, and these for the other four layers were made of Saint-Gobain BC412. The average time resolution of the segments are found to be  $92 \pm 10$  ps ( $\sigma$ ) in a cosmic ray test. The error represents the variation among the segments.

### 2.7.3 Charge veto counter (CVC)

The charge veto counter (CVC) was located just in front of the neutron counter, 14.0 m away from the final focus point. It had an effective area of 3.4 m (horizontal)  $\times$  1.5 m (vertical) segmented into 34 units. Each scintillation counter was equipped with two 2 inch Hamamatsu H6410 photomultipliers attached to both long sides of the scintillator through a Lucite light guide. The scintillators were of Eljen EJ-200 type. The average time resolution measured with cosmic rays is  $78 \pm 7$  ps ( $\sigma$ ). The error represents the variation among the segments.

### 2.7.4 Proton time-of-flight counter (PC)

The proton TOF counter was installed as the extended wall of the charge veto counter. It had an effective area of 2.7 m (horizontal)  $\times$  1.5 m (vertical) segmented into 27 units. Each scintillation counter consisted of a Saint-Gobain BC408 scintillator and two Hamamatsu H6410 photomultipliers attached to both long sides of the scintillator through a Lucite light guide. The average time resolution of the proton counter, obtained from cosmic ray data, is  $75 \pm 6$  ps ( ). The error represents the variation among the segments.

### 2.7.5 Forward drift chamber (FDC)

The forward drift chamber (FDC) was a feedthrough type chamber having 6 planes with a  $VV'XX'UU'$  configuration. The tilt angles of  $U$  and  $V$  layers were  $\pm 15$  degree. Each layer had 64 sense wires with a drift length of 3 mm. An effective area was 384 (horizontal)  $\times$  264 (vertical). Cell geometry was made of hexagonal cells as shown Fig. 2.18. The sense wires were made of Au-placed W (3% Re) with a diameter of  $20 \mu\text{m}$ . The both field and shield wires were made of Au-placed with a diameter  $80 \mu\text{m}$ . Operation voltages of the FDC were -1.8 V (field) and -1.8 V (shield), respectively. The readout method was the same as those of the beam line chambers.

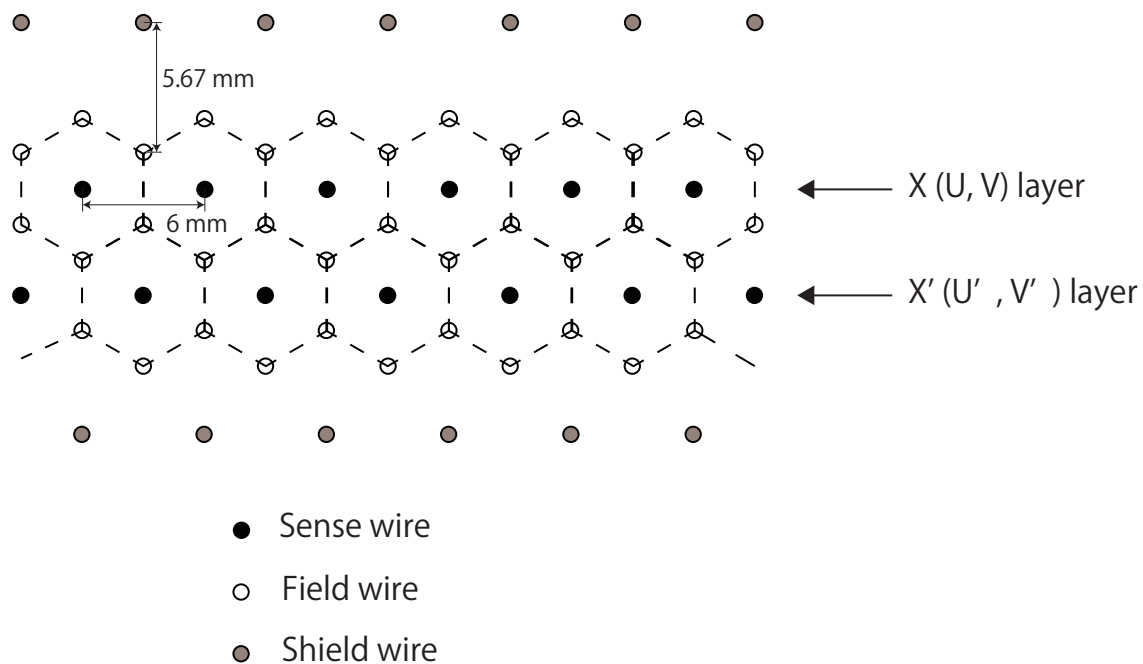


Figure 2.18: Cell geometry of the FDC.

### 2.7.6 Beam veto counter (BVC)

The beam veto counter was installed between the CDS and the beam sweeping magnet. The scintillation light transferred through a light guide was read by a 2 inch fine-mesh

Hamamatsu H6154 photomultiplier. The high voltage bleeder of the photomultiplier was modified to supply additional current to the last three dynodes.

## 2.8 Trigger and Data Acquisition system (DAQ)

For the on-line data acquisition system (DAQ), the TKO [77, 79], VME and Linux PC were used. The detector's signals were inputted to ADC and TDC modules which slotted into 10 TKO crates. These modules were read in parallel with 10 VME-SMPs (super memory partner [80]) via a TKO SCH (super controller head). The data stored in a buffer memory of the SMPs was transferred to the PC through SBS Bit3 VME-to-PCI bridges. Also, other two DAQ systems, a scaler DAQ system and a DAQ system for multi-hit TDC (multi-hit TDC DAQ) of beam-line detector, were used. The scaler DAQ system was set up to monitor spill by spill fractionation for scaler information, such as number of beam particles, trigger rate etc. Data taken by multi-hit TDC DAQ were used to check beam pile up condition at off-line analysis. To ensure event matching for these three DAQ systems, an event and a spill number were distributed by a master trigger module and receiver modules. Event matching was done offline. The status recording and control of the detector system, such as temperature and pressure of the target system and high voltages of detectors, were done by LabVIEW based programs.

The first clear scheme was adopted to efficiently accumulate the forward particle detection events, since current DAQ system had no buffer memory in the TDC and ADC modules. The 1<sup>st</sup> level trigger was constructed by the signals of beam line detectors and the CDH and common start/stop signals for TDC and ADC timing gates were generated from 1<sup>st</sup> level trigger and distributed to each module. Due to the  $\sim 15$  m flight length, signals of the forward counters reached to the counting house 100 ns or more after 1<sup>st</sup> level trigger generation. A 2<sup>nd</sup> level trigger was generated by these signals of forward counters. If 2<sup>nd</sup> level trigger is not accepted, analog-to-digital conversion of each module is suspended and all modules are initialized (*FastClear*).

The dead time of analog-to-digital conversion in the ADC/TDC and data-transfer from the TKO-SCH to the VME-SMP was about 120  $\mu$ s and 230  $\mu$ s, respectively. The dead time of data transfer between VME-SMP and Linux PC was negligible because VME-SMP has two buffers and uses them by turns. When the *FastClear* was used, it took  $\sim 3$   $\mu$ s to be ready to take next event. A typical DAQ rate was  $\sim 800$  events per spill with live rate of  $\sim 80$  % during the production run for this analysis.

### 2.8.1 Trigger scheme

A trigger scheme was constructed to satisfy physical requirement. Table 2.5 shows a list of trigger modes used in this production run. A logical diagram of the trigger is shown in Fig. 2.19.

#### Kaon beam Trigger

The elementary beam trigger was constructed by a coincidence of signals from the BHD, T0, and DEF counters. The kaon beam trigger ( $K_{beam}$ ) and the pion beam trigger were selected by using signal from the AC (*i.e.* to select kaon beam, a veto signal of the AC ( $\overline{AC}$ ) was used). It should be noted that contamination of antiprotons was negligible because they were eliminated by the separator (ES1) and beam line slit (CM1 and CM2). A logical

expressions of the kaon beam and the pion beam triggers are given as

$$(K_{beam}) \equiv (\text{BHD}) \otimes (\text{T0}) \otimes (\text{DEF}) \otimes \overline{\text{AC}}, \quad (2.1)$$

$$(\pi_{beam}) = (\text{BHD}) \otimes (\text{T0}) \otimes (\text{DEF}) \otimes \text{AC}, \quad (2.2)$$

respectively.

### Trigger for forward particle detection

A two level trigger was used for in-flight  ${}^3\text{He}(K^-, N)$  reaction in which  $N$  was outgoing forward direction. To reconstruct reaction vertex, one or more charged particle was required in the CDH ( $\text{CDH}^{1hit}$ ) in the first level. In the second level, (Neutral) and (Charged) triggers were required. The neutral trigger was made of one or more hits of the neutron counter (NC) and a veto signal of the CVC ( $\overline{\text{CVC}}$ ). The charged trigger (Charged) was composed of one or more hits of the proton counter (PC) and/or one or more hits of the CVC. The trigger for forward particle detection (Forward) is given as

$$(\text{Forward}) \equiv (K_{beam}) \otimes (\text{CDH}^{1hit}) \otimes ((\text{Neutral}) \cup (\text{Charged})), \quad (2.3)$$

where

$$((\text{Neutral}) \equiv (\text{NC}) \otimes (\overline{\text{CVC}}),$$

$$(\text{Charged}) \equiv (\text{PC}) \cup (\text{CVC}).$$

### Neutron counter calibration Trigger

A time offset calibration is important for the forward neutron or proton TOF measurement. Gamma rays from the target were used for the NC calibration run by run. Gamma ray events were contaminated in trigger for forward particle detection, but it was not enough for the calibration. Thus, two additional triggers were used which given as

$$(\pi_{beam}) \otimes (\overline{\text{BVC}}) \otimes (\text{Neutral}) \quad (2.4)$$

$$(K_{beam}) \otimes (\overline{\text{BVC}}) \otimes (\text{Neutral}), \quad (2.5)$$

where the (Neutral) is second level.

Table 2.5: Summary of trigger conditions.

	request / spill	pre-scale factor	accept / spill	main usage
$\text{BHD} \otimes \text{T0}$	610 k	50 k	10	monitor for beam-line counters
$K_{beam}$	145 k	7 k	17	normalization
$K_{beam} \otimes \text{CDH}^{1hit}$	48 k	70	70	CDH calibration
$K_{beam} \otimes \text{CDH}^{2hit}$	21 k	7	280	$\Lambda$ p event analysis
$K_{beam} \otimes \text{CDH}^{1hit} \otimes \text{Neutral}$	230	1	170	$(K^-, n)$ event
$K_{beam} \otimes \text{CDH}^{1hit} \otimes \text{Charged}$	130	1	100	$(K^-, p)$ event
$\pi_{beam} \otimes \overline{\text{BVC}} \otimes \text{Neutral}$	480	10	40	NC calibration
$K_{beam} \otimes \overline{\text{BVC}} \otimes \text{Neutral}$	850	10	70	
Total	850 k		680	(1 <sup>st</sup> accept $\sim$ 6.9 k)

### $K_{beam} \otimes$ CDH Trigger

To measure  $\Lambda p \rightarrow \pi^- pp$  events in the CDS,  $K_{beam} \otimes$  CDH<sup>2hit</sup> Trigger was introduced.  $K_{beam} \otimes$  CDH<sup>2hit</sup> trigger was generated when there are two or more than two hits of the CDH in one event. In this trigger, the rather large acceptance was available because there was no limit of the forward counter. Although the first motivation of the E15 experiment was to measure  ${}^3\text{He}(K^-, n_{forward})$  reaction,  $K_{beam} \otimes$  CDH<sup>2hit</sup> trigger was pre-scaled with factor of 7 not to suppress trigger for forward particle detection. In this analysis, data of this trigger was used mainly.  $K_{beam} \otimes$  CDH<sup>1hit</sup> trigger was introduced for the CDH calibration.

### Trigger for normalization

For the evaluation of reaction cross sections, the total kaon flux on the target is very important. Thus, elementary kaon beam data ( $K_{beam}$ ) was also recorded. (BHD  $\otimes$  T0) trigger data, minimum biased data, was also recorded for the check of the beam-line detectors performance.

### Cosmic ray trigger

A cosmic data was recorded by using two or more CDH hits during the offspill period. These data was used for checking the CDC and CDH performance.

## 2.8.2 DAQ efficiency

The DAQ efficiency was obtained as a ratio of the number of accepted 1st-level triggers to that of requested 1st-level triggers. The DAQ efficiency was found to be  $81.5 \pm 0.7$  %, where the error is estimated as fluctuation in the experimental period. Typical numbers of accepted and requested 1st-level triggers were about 6900 and 8500 per spill, respectively.

## 2.8.3 Trigger efficiency

The trigger efficiency of the main trigger,  $K_{beam} \otimes$  CDH<sup>2hit</sup> was evaluated by using the  $K_{beam}$  trigger which is the minimum-biased trigger. In the data of the  $K_{beam}$  triggers, Events including CDH two or more than two hits were reconstructed and checked the  $K_{beam} \otimes$  CDH<sup>2hit</sup> trigger flag to estimate the trigger efficiency. The trigger efficiency was found to be  $99.6 \pm 0.1$  %, where error is statistical one.

## 2.8.4 Data summary

The production of this experiment was done from May 18th to May 23th 2013, after beam turning and calibration run. The calibration runs contained target empty runs for the fiducial volume study, proton beam trough runs to calibrate the beam absolute momentum and pion beam runs for chamber position and ADC calibrations. In addition, special calibration runs, which scanned the field of the beam sweeping magnet, were taken to irradiate pions on the all segments of the NC and the PC.

The total primary beam power in MR during the physics run was  $\sim 12 \text{ kW} \times \text{week}$ . The integrated number of kaons evaluated by scaler of the kaon trigger was  $7.62 \times 10^9$ .

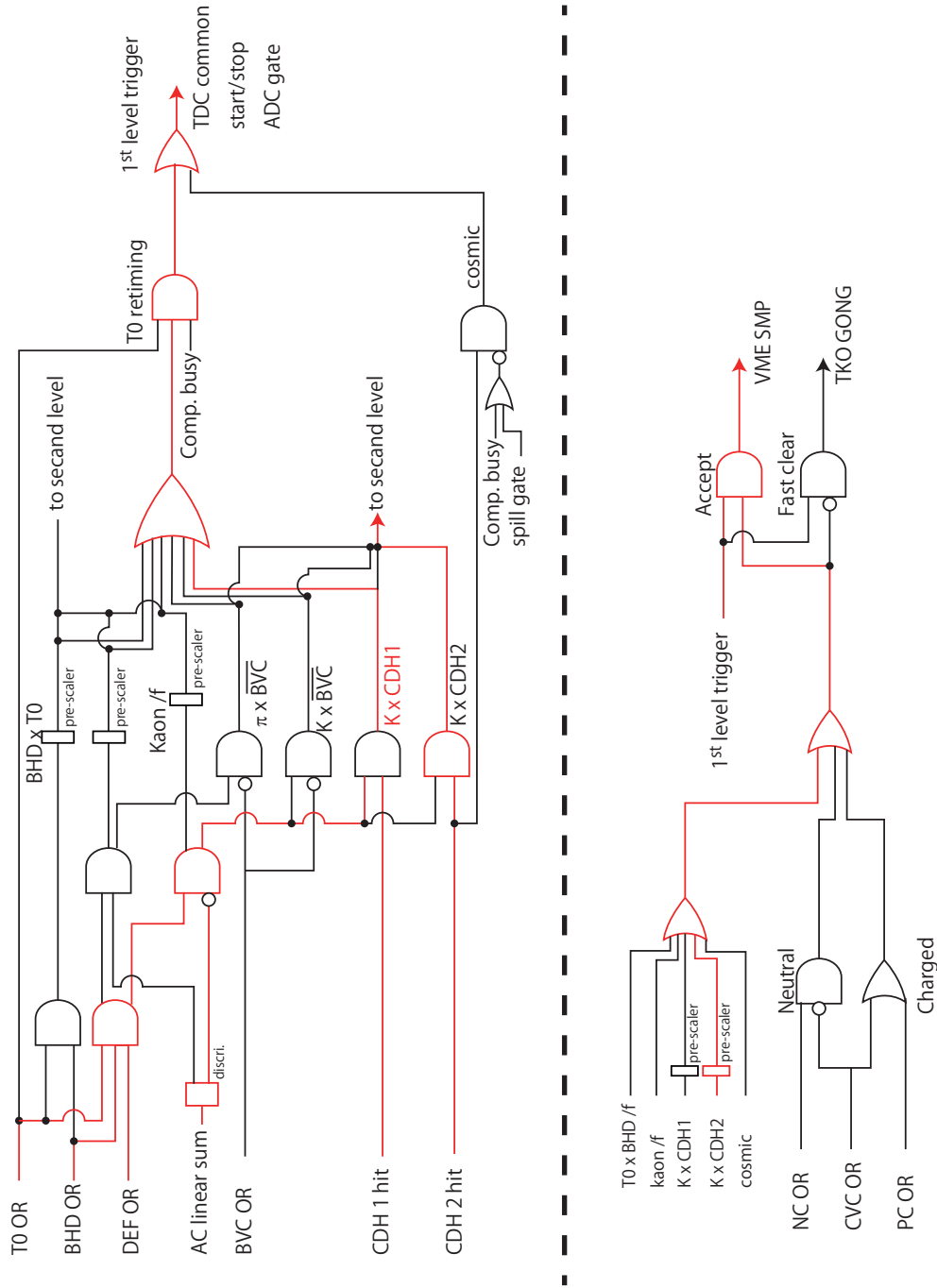


Figure 2.19: Trigger diagram.

# Chapter 3

## Data Analysis

### 3.1 Outline of the Data Analysis

The data used in this analysis was accumulated for about 90 hours from 18th May 2013 to 23th May 2013 corresponding the  $12 \text{ kW} \times \text{week}$  beam power. The  $7.62 \times 10^9$  kaons were in this data set. Details of the data are summarized in Table 3.1. By using this data set, analysis for the  ${}^3\text{He}(K^-, \Lambda p n_{\text{missing}})$  reaction has been performed.

Table 3.1: Data taking period and the number of kaons in this analysis.

date	period [hour]	Beam power [kW $\times$ week]	Number of kaons
18th May - 23th May 2013	87.5	12.5	$7.62 \times 10^9$

A common procedure for all detectors is described in Sec.3.2. In Sec.3.3, calibrations for beam-line hodoscopes and chambers are described. An analysis of the CDS is described in Sec.3.5. The performances of the CDC and CDH, and tracking method are written. Offset for center value of magnetic field strength of the solenoid magnet is evaluated by using reconstructed  $K_s^0$  and  $\Lambda$  particles. Finally, an analysis for  $\Lambda p n$  events is described in Sec. 3.9. First of all,  $\Lambda p \rightarrow p \pi p$  events are selected. Then  $\pi^-$ -proton pairs from  $\Lambda$  decay are identified by Log-Likelihood method. An acceptance of  $\Lambda p n$  events is evaluated by the Monte Carlo simulation using the GEANT4.

#### 3.1.1 Definition of the axis coordinate

In this analysis the right-handed system was employed. A z-axis is defined as designed beam axis and x-axis and y-axis correspond to horizontal and vertical axis, respectively as shown in Fig. 3.1. A positive x position corresponds to right-hand side from the beam axis (z-axis) when one looks from downstream of the beam line. A point at  $(X,Y,Z)=(0,0,0)$  is defined as a the center of the CDS.  $\theta$  and  $\varphi$  angle are defined as shown in Fig. 3.1.

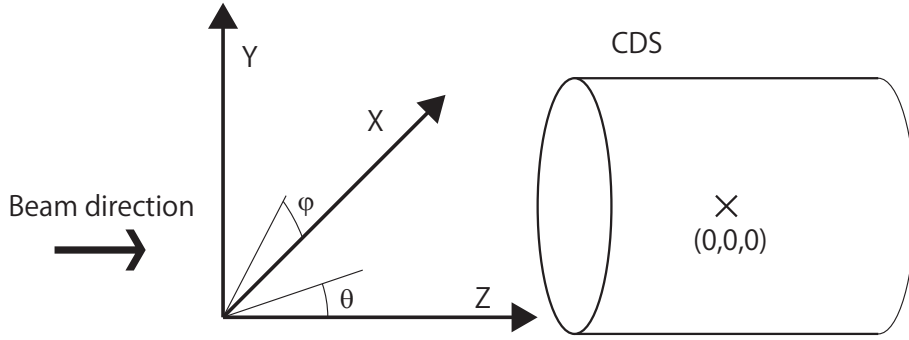


Figure 3.1: Definition of the axis coordinate.

## 3.2 Common procedure of all detectors

### 3.2.1 Conversion to the time of TDC data

TDC calibration was performed channel by channel to convert TDC channel to the time. For the calibration, A time calibrator (ORTEC 662) was used. The calibration runs were performed before the experiment. A linear function was used for conversion function to the time.

### 3.2.2 Conversion to the gain of ADC data

For the beam line detectors, energy deposits by  $1 \text{ GeV}/c \pi^-s$  ( $\sim 2 \text{ MeV} / 1 \text{ g}/\text{cm}^2$ ) were used to convert ADC channels to energy scale. For calibrations for forward counters, i.e. the PC and NC,  $\pi^-$  beam were irradiated to all segments by changing magnetic field of the beam sweeping magnet. This calibration runs for forward counters were performed before the experimental runs and once during the experiment. For the CDH and IH, pions reconstructed in the CDS were used for energy calibration. For the CDH calibration, path length in the counters was took into account for energy deposit calculation.

### 3.2.3 Time-walk correction for scintillation counters

In the experiment, timing of counter hit is digitized by a threshold-type discriminator. Thus, timing dependence of pulse height, the time-walk effect, should be corrected. By assuming the liner correlation between pulse height and integrated charge generated by counters, the relation between pulse height and time walk can be characterized by the following empirically function with three parameters ( $p_1, p_2, p_3$ ),

$$p_0 + \frac{p_1}{\sqrt{dE}} + p_2 \cdot dE \quad (3.1)$$

where  $dE$  is energy deposit in the counter. Parameters of this function were evaluated by iterative corrections of the  $dE$  and timing dependence with fast  $\pi$ s for charged particle detectors or  $\gamma$ -rays for the NC. The timing offsets were adjusted run by run (for Forward

counters) or every 4 – 6 hours for the CDH. Mean value of two timing which attached on to each side of hodoscope were used for timing information of each detector segment.

### 3.3 Beam analysis

For kaon beam analysis, single track events which is identified as kaon by beam line detectors were selected. It is very crucial for the analysis. Because, two particles are coming together which will be reconstructed as a two-track event, however the spectrometer can not distinguish which track make the start timing with the T0, because the T0 counter can accept single hit in each segment. To eliminate such multi-track events, following cut conditions (requirements of single T0 hit and single track in the beam-line chambers) were applied;

1. Selecting single T0 hit event,
2. Selecting kaon by Time-of-flight of the BHD and T0,
3. Requiring single track in the beam-line chambers (BLC1, BLC2, and BPC),
4. Checking connection between the BLC2 and BPC,
5. Reconstructing beam momentum, and
6. Requiring that beam track is in the fiducial volume of the target.

Details of each condition are described in the following subsections.

#### 3.3.1 Single T0 hit event Selection

Timing information of the T0 hit make the start timing of all other counters. Thus, a event with only one T0 hit was selected to identify the start timing safety and to suppress multi-track events. Distribution of multiplicity of the T0 hits are shown in Fig. 3.2. T0 single hit events are about 95 % of total events.

#### 3.3.2 TOF measurement between T0 and BHD for kaon identification

An event with kaon is selected in the trigger level with the AC. However there are still contamination of pions about 1 %. Thus, kaon identification was performed using TOF between the T0 and BHD. The time offsets and time-walk effects of BHD segments were calibrated with the T0 #3 segment, which is in the center of the T0, by assuming of 7.7 m fixed flight length for 1.0 GeV/c pions. A TOF distribution between the BHD and T0 is shown in Fig. 3.3. A kaon peak was fitted with a Gaussian and kaons were selected with a gate (dotted lines in Fig. 3.3) of  $\pm 3$  standard deviation ( $\sigma$ ) of a peak. A typical TOF time resolution was found to be  $\sim 160$  ps for 1 GeV/c pions.

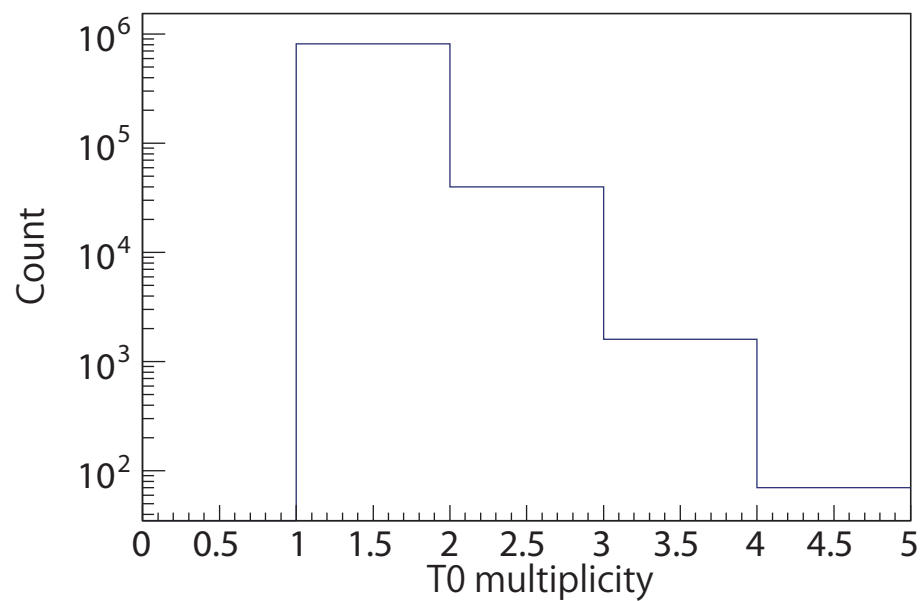


Figure 3.2: Distribution of multiplicity of the T0 hits.

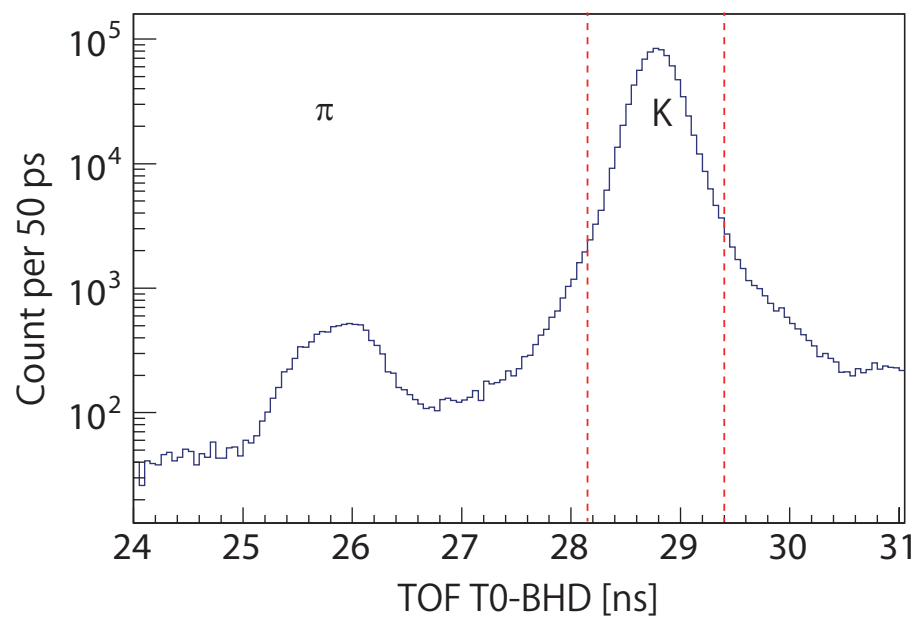


Figure 3.3: A typical TOF distribution between the BHD and T0. A peak in the right is Kaons. Dotted lines indicate  $\pm 3\sigma$  selection points for kaon identification.

### 3.3.3 Analysis for beam-line chambers

#### Time to drift length conversion of beam-line chambers

To convert the timing information to drift length, conversion functions of their relation (X-T curve function) are needed. This conversion functions were obtained by the integrals of the time distribution. The maximum of the integrated time was set to the maximum length of the cell. The X-T curves were obtained wire by wire of each chamber with kaon beam, and adjusted for every a few runs ( $\sim 3$  hours). The relative time offset was adjusted by edge of timing distribution. Figure 3.4 shows a typical distribution of the drift time of beam line chamber and X-T curve function.

#### Linear Tracking method for beam-line chambers

Beam track was reconstructed by minimum  $\chi^2$  method using hit position from each beam line chamber. Local hit positions of the track are evaluated by wire positions with hits and drift length. Although drift direction (left or right from wire plane) can not be determined by only hit data. All combinations of drift direction(L or R) in hit wire are examined and the track with smallest  $\chi^2$  was selected. The three dimensional linear fitting ( $\chi^2/NDF$ ) is defined as,

$$\chi^2/NDF = \frac{1}{N-4} \sum \left( \frac{x_i - f(z_i)}{\sigma_i} \right)^2 \quad (3.2)$$

$$f(z_i) = \cos \theta(a + bz) + \sin \theta(c + dz) \quad (3.3)$$

where N is number of hits,  $x_i$  is local position of hit perpendicular to the wire and beam directions,  $\sigma_i$  is the position resolution,  $f(z_i)$  is calculated hit position from track,  $z_i$  is z position of hit wire,  $\theta$  is rotated angle of the chamber, and  $a, b, c, d$  is free parameters for fitting. As position resolution of each chamber, values in Table. 3.2 are used.

Tracking was performed in each beam-line chamber, indecently. For the BLC1 and BLC2, to have hits in more than 5 planes is requested to reconstruct a track. For the BPC, hits on all 8 planes are requested because there is no dead plane. The procedure of tracking is, at first finding a track candidate by only wire positions, then fitting and finding a track. This procedure is iterated until there are no enough hits to reconstruct a track candidate.

Typical reduced  $\chi^2$  distributions of beam-line chambers are shown in Fig. 3.5. For good-track selection, reconstructed track with  $\chi^2/NDF$  more than 10 are rejected. In addition, to avoid beam pile-up event, single track event within the timing window of -30 – 100 ns was selected as shown Fig. 3.6. The track time is an average of all hit wire timing and is calibrated to be 0 when track comes in true beam timing. Tracks were also requested to be in timing window of trigger timing. The timing windows were defined to be -5 – 5 ns and -10 – 10 ns for the BLCs and BPC, respectively. The multiplicity of each chamber is also shown in Fig. 3.6.

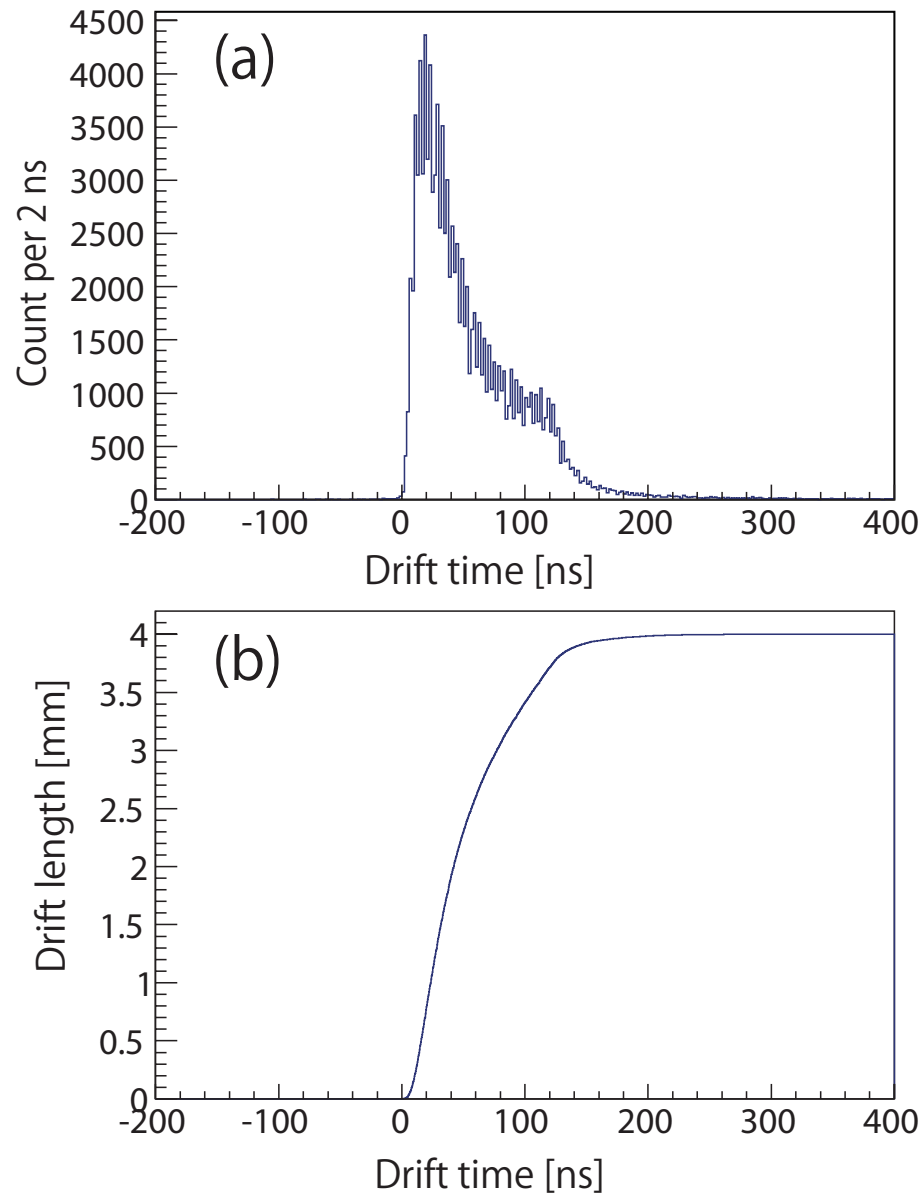


Figure 3.4: (a) Typical distribution of the drift time of beam line chamber. (b) Typical beam-line chamber's correlation function of drift time and drift length. Both figures show those of the BLC1a.

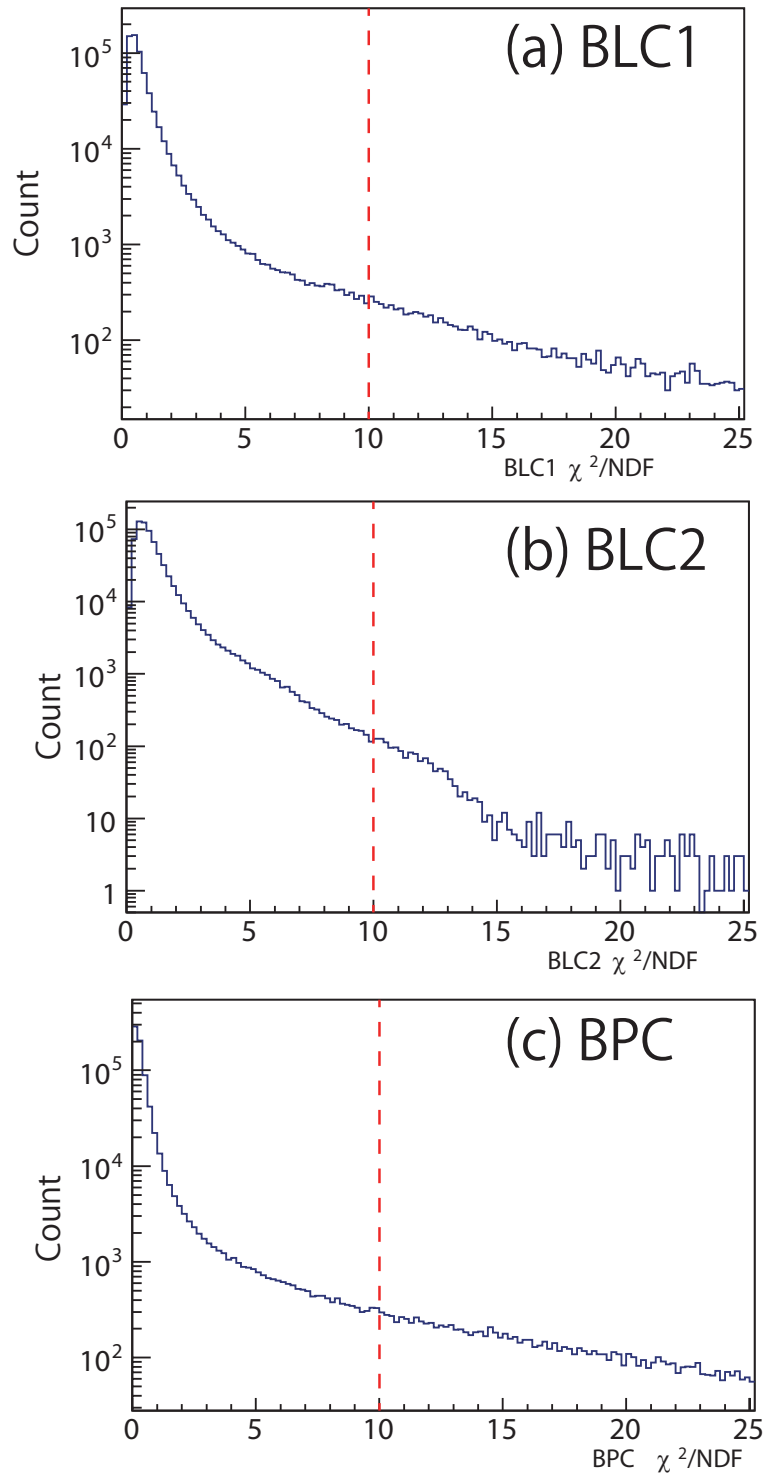


Figure 3.5:  $\chi^2/NDF$  distributions of beam line chambers

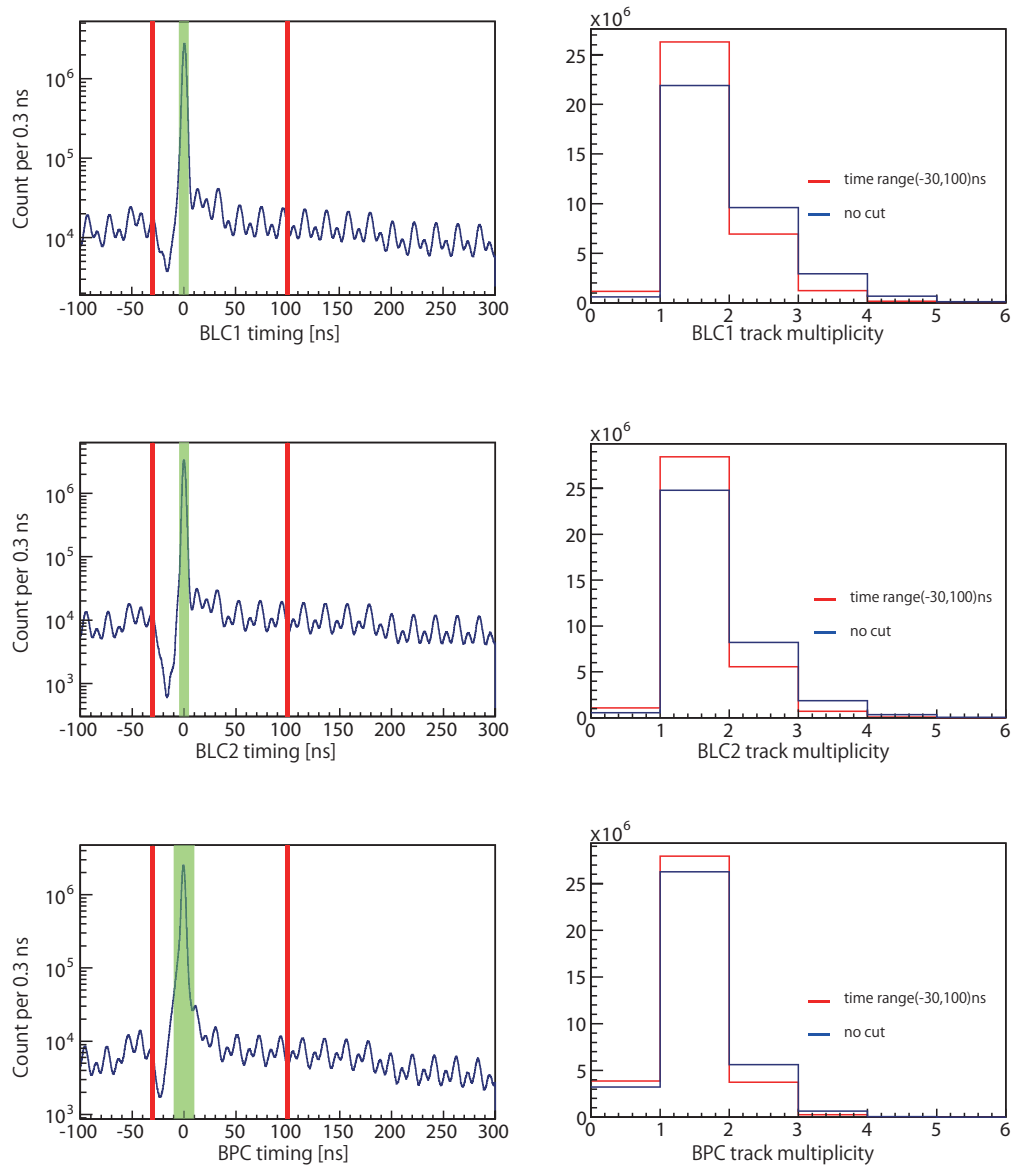


Figure 3.6: Track times and multiplicity of each beam-line chambers.

### 3.3.4 Performance of the beam line chambers

#### Position resolution

An intrinsic position resolution of each chamber was estimated by the residual distribution. From the residual distribution, we obtained the  $\sigma$  from a Gaussian fit. The intrinsic position resolution for each chamber was obtained by considering the geometrical factors assuming they were all the same. Typical intrinsic position resolutions of the beam line chambers are listed in Table. 3.2.

#### Tracking efficiency

A tracking efficiency of the beam line chambers was evaluated by requesting a single track in each of other two beam line chambers. For the BPC, a track extrapolated from the BLC2 was requested to be at in the BPC acceptance. Typical values of the tracking efficiencies are listed in Table. 3.2.

	BLC1a	BLC1b	BLC2a	BLC2b	BPC
Position resolution [ $\mu\text{m}$ ]	130	180	170	180	110
Tracking efficiency [%]	98.5		97.2		98.2

Table 3.2: Typical values of performance of the beam line drift chambers.

### 3.3.5 Distributions of the beam at final focus

Distributions ( $X$ ,  $Y$ ,  $dX/dZ$ , and  $dY/dZ$ ) of the beam at final focus were reconstructed by the BPC as shown in Fig. 3.7. Both  $X$  and  $Y$  distribution of the beam was within  $\pm 6$  cm, which was almost same size of the target cell. The  $dX/dZ$  distribution was wide due to the D5 di-pole magnet.

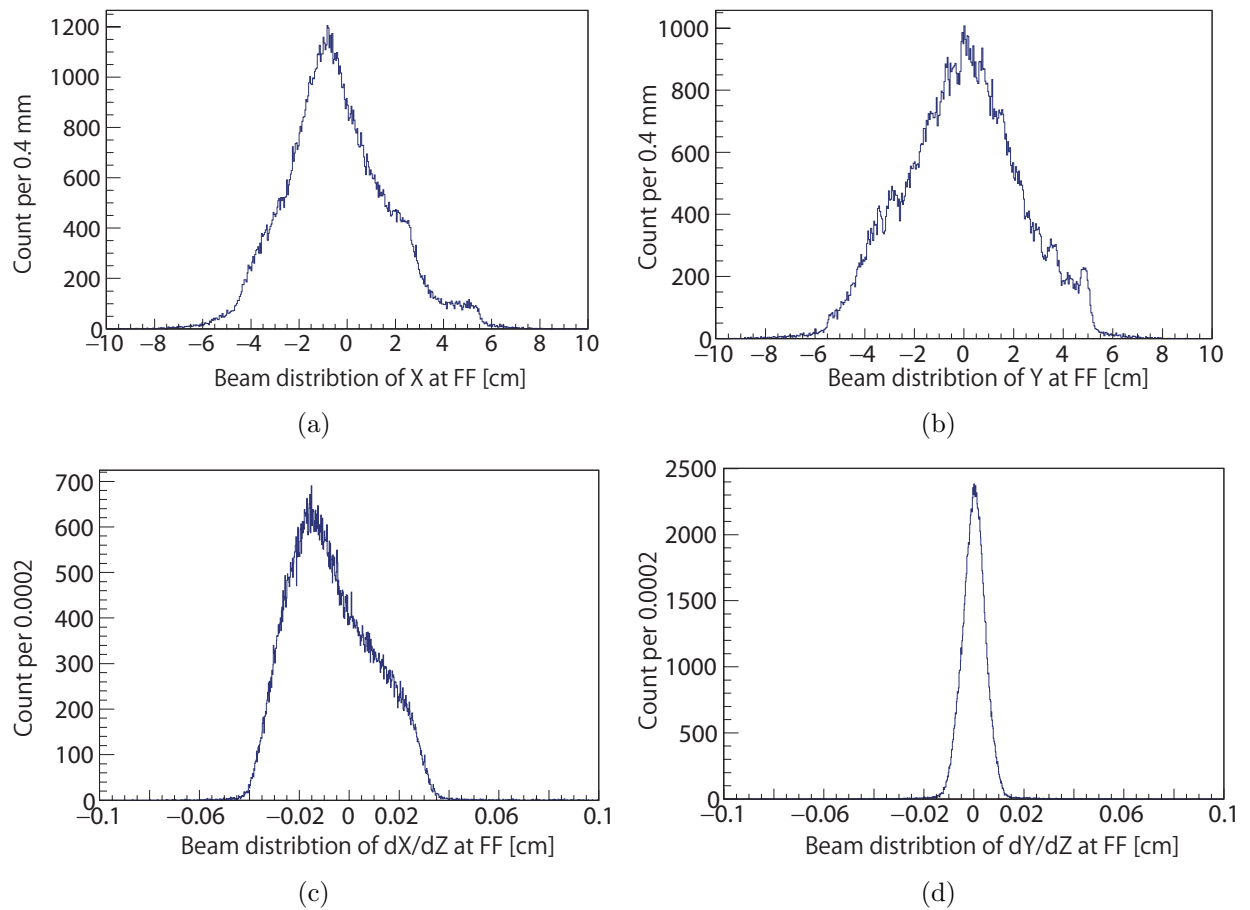


Figure 3.7: Distributions (X, Y ,dX/dZ, and dY/dZ) of the beam at final focus.

### 3.3.6 Beam momentum reconstruction

The BLC1 and BLC2 tracks were connected using transfer matrix (second order) calculated by TRANSPORT[81] code with additional parameters for the beam momentum. The definition of  $\chi^2/NDF$  is essentially same as Eq. 3.3, expect additional degrees of freedom for beam momentum. TMinuit code was used for the calculation for minimization of the  $\chi^2$ . The reduced  $\chi^2$  distribution of connection of the BLC1 and BLC2 tracks is shown in Fig. 3.8. The events with reduced  $\chi^2$  were used to select correct track for this analysis. The reduced  $\chi^2$  distribution is shown in Fig. 3.8. The events with  $\chi^2/NDF < 20$  were accepted.

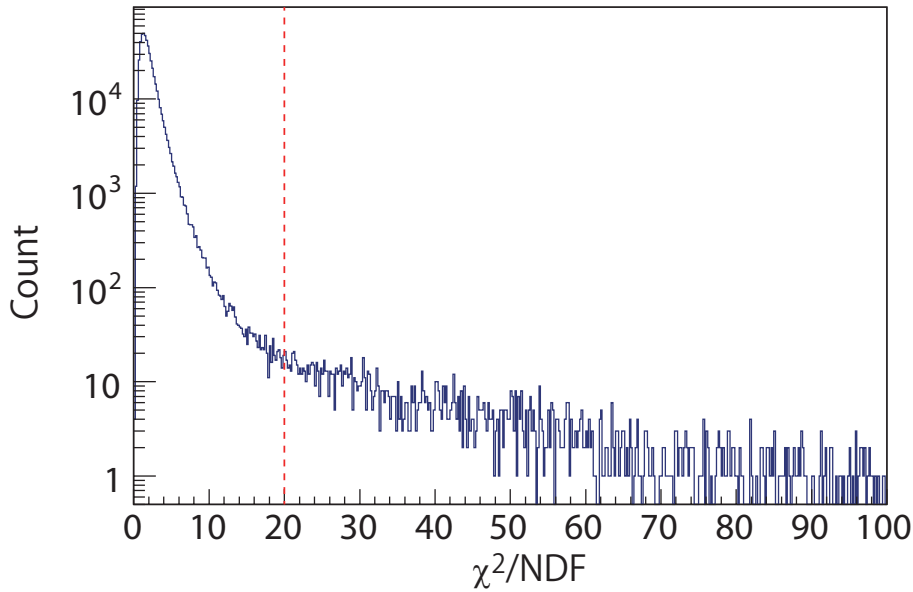


Figure 3.8:  $\chi^2/NDF$  Distribution of the connection fitting of the BLC1 and BLC2. Dotted line on  $\chi^2/NDF = 20$  shows the threshold for event selection.

### 3.3.7 Resolution of beam momentum

The resolution of beam momentum was estimated with the  $\pi^-$  through data in which the beam sweeping magnet was off. A distribution of the difference of the reconstructed beam momentum and the momentum calculated with TOF between the CVC and T0 are shown in Fig. 3.9. Time resolution of the TOF between the CVC and T0 was evaluated to be 130 ps with  $\gamma$ -ray events. Thus, resolution of reconstructed momentum was  $2.2 \pm 0.2$  MeV/c. It should be noted that absolute value of the momentum of TOF(CVC-T0) was not fixed due to energy loss correction in forward counters. Although fine tune of Forward TOF walls for charged particles is not necessary in this analysis. Thus, absolute value of beam momentum was tuned with missing mass scales described in a following subsection.

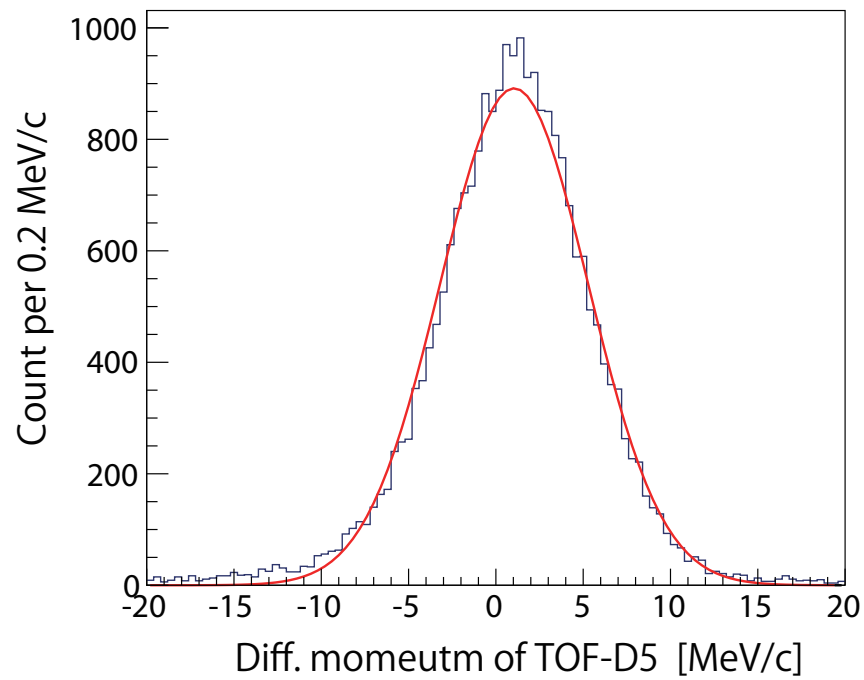


Figure 3.9: A distribution of the difference of the reconstructed beam momentum and the momentum calculated with TOF between the CVC and T0. It should be noted that absolute value of the momentum of TOF(CVC-T0) was not fixed due to energy loss correction in forward counters.

### 3.3.8 Fine tuning of the absolute values of the beam momentum

Fine tuning of the absolute values of the beam momentum was performed with values of missing proton, neutron and deuteron in  ${}^3\text{He}(K^-, K^-pn)X$ ,  ${}^3\text{He}(K^-, K_s^0pn)X$ , and  ${}^3\text{He}(K^-, K_s^0p)X$  reactions, respectively. Fig 3.10 shows difference of each mass and PDG value. The center value of the kaon beam was adjusted with weighted center value of these three points. The NC was used to measure these reactions. The calibration of the Forward TOF walls and the details of analysis of these reactions are described in Appendix B.

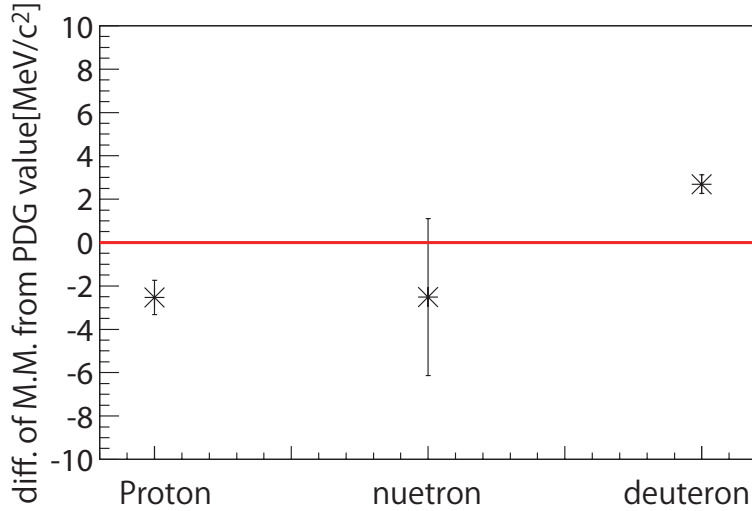


Figure 3.10: Mass deviations between the reconstructed values and the PDG ones for each particle.

### 3.3.9 Event selection

#### BLC2-BPC track connection

Connection between the BLC2 and BPC tracks was checked to ensure that kaon beam comes to the BPC without decay or reacting or scattering in materials, In Fig 3.11, a distribution of position(X, Y) and  $dX/dZ$ ,  $dY/dZ$  difference between BLC2 track and BPC track at the plain which located at the center of two chambers are shown. Three  $\sigma$  cut was applied to select matching of the BLC2 and BPC tracks.

#### Fiducial volume cut at the final focus point

The fiducial volume cut was applied to select events in which kaon beam hits  ${}^3\text{He}$  target. The fiducial volume region is defined as a cylinder which has 3 cm diameter and  $\pm 10$  cm from the center of the target cell. Fig 3.12 shows that distribution of vertex position reconstructed by BPC track at the  $z = 0$ . Note that the fiducial volume was defined in three-dimensionally as described in Sec. 3.6.5.

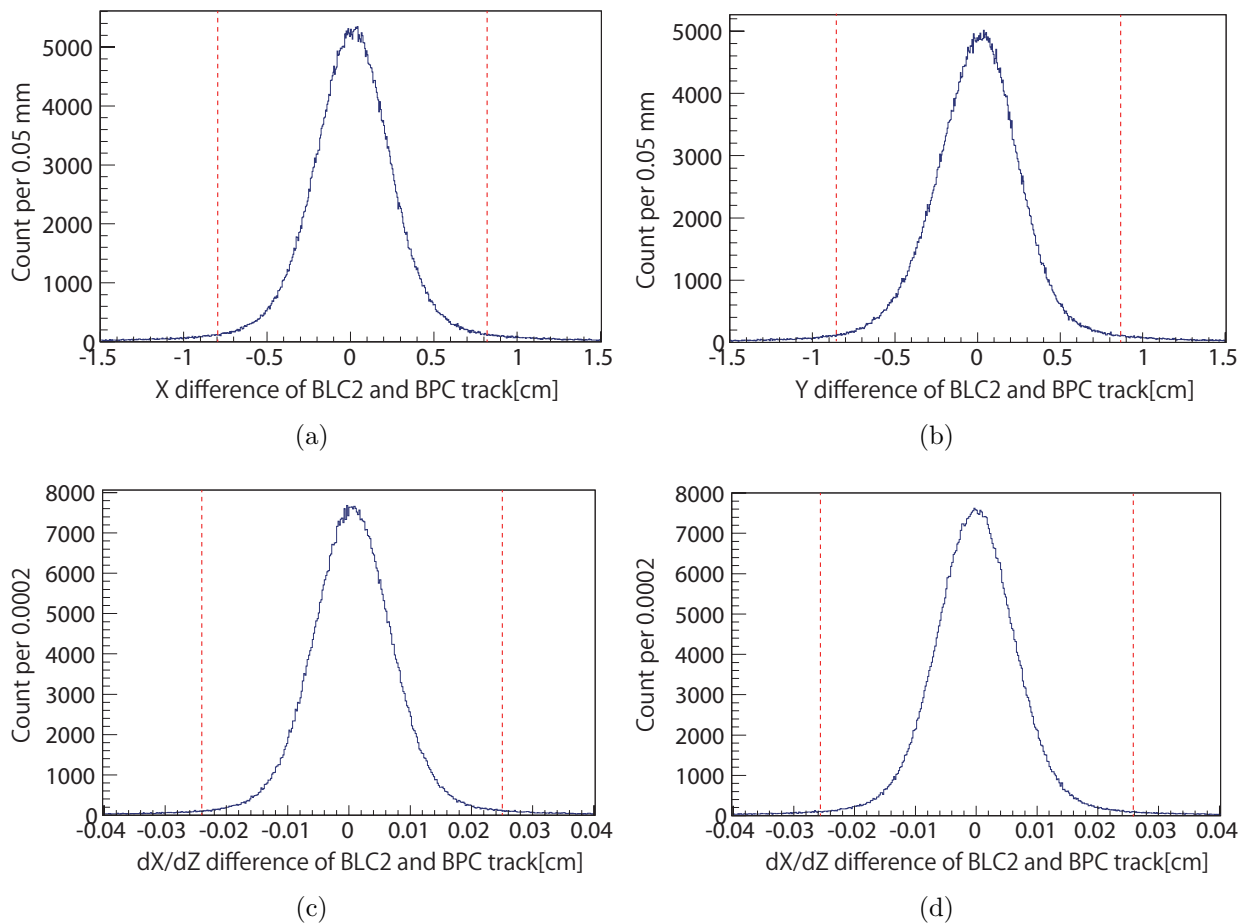


Figure 3.11: Track matching between the BLC2 and BPC tracks at  $z=-75$  cm where is the center of two chambers. The regions between dotted lines in each histogram show accepted regions as three  $\sigma$ .

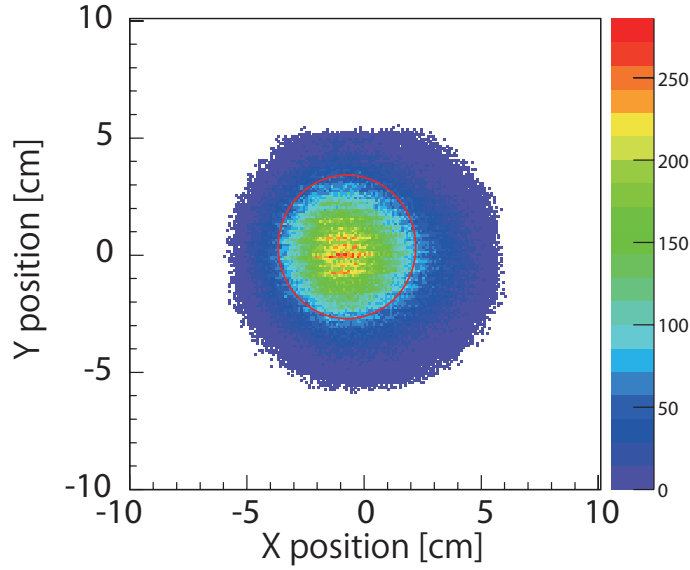


Figure 3.12: Kaon beam profile at the FF. The red colored circle shows the fiducial region at the FF.

## 3.4 Effective luminosity

### 3.4.1 Decay and reaction loss

The requirement of the beam track connecting with BPC is ensured that kaon beam is alive at the final plane of the BPC.

Thus, loss probability of the decay and reaction between the final plane of the BPC ( $z = -18$  cm) and the FF ( $z = 0$ ) was estimated. For a fixed beam momentum of  $1 \text{ GeV}/c$ , kaon decay loss was calculated to be  $2.4 \%$  with  $c\tau = 33.712$  m. The relative position uncertainty of  $\sim 1$  cm between the BPC and the FF gives  $0.2 \%$  systematic error. The effect of the beam momentum bite with approximately  $2 \%$  is smaller than  $0.1 \%$ . For the estimation of the reaction loss, the elementally  $KN$  reaction cross section was simply scaled by the size of nucleus  $A^{2/3}$ . The materials considered in the evaluation were the DEF, the cap of the target vessel ( $\sim 0.67 \text{ g}/\text{cm}^2$ ). The reaction loss rate was obtained to be  $0.7 \%$  and the uncertainty of the estimation for the  $KN$  reaction cross section was considered to give  $20 \%$  systematic error due to the thickness of the DEF.

### 3.4.2 Summary of effective luminosity

We summarize effective luminosity in this analysis condition in table 3.3. Estimated factor for effective luminosity is  $45.92\% \pm 0.09\%(\text{stat}) \pm 1.97\%(\text{sys})$ . Systematic error is estimated from fluctuation of each value in run by run. Total kaon number from scaler value in data is  $7.556 \times 10^9$  and effective luminosity in this analysis is  $3.470 \times 10^9 \pm 0.003 \times 10^9(\text{stat}) \pm 0.068 \times 10^9(\text{sys})$ .

Kaon number counted by Scaler		$7.556 \times 10^9$	
effective luminosity	survival ratio	error(stat.)	error(sys.)
T0 single	95.17	0.02	0.32
TOF T0-BHD	94.77	0.02	1.32
BPC	91.92	0.03	0.38
BLC	88.32	0.04	0.79
BLC2-BPC	90.96	0.04	0.04
Momentum spectrometer	99.45	0.01	0.09
Fiducial volume	69.33	0.06	1.09
decay loss	97.62		0.2
reaction loss	99.33		0.3
effective kaon	$3.363 \times 10^9$	$0.003 \times 10^9$	$0.067 \times 10^9$
target number	1.625 [g/cm <sup>2</sup> ]		0.004 [g/cm <sup>2</sup> ]
effective luminosity	546.5 [ $\mu b^{-1}$ ]	0.5 [ $\mu b^{-1}$ ]	10.9 [ $\mu b^{-1}$ ]

Table 3.3: Typical values of the survival rate at each step of event selection. Systematic error is estimated from fluctuation of each value in run by run.

## 3.5 CDS analysis

The cylindrical detector system(CDS) is used to reconstruct particle trajectory and momentum, and to identify particle species (PID). To reconstruct  $\Lambda p$  invariant mass from pppi events, the CDS is the most important detector.

An analysis procedure of the CDS is as follows,

1. CDC hit calibration,
2. Track finding & fitting in the CDC.
3. Search for associated hits on the CDH for each CDC track.
4. Reconstruct a vertex point with a beam track and calculate mass-squared of the tracks.
5. Re-fit the tracks after applying fine time corrections on the CDC hits, and re-calculate the mass-squared.
6. identify particle species of each track.
7. Re-calculate the vertex point, and obtain the momentum at the vertex point with correction of energy loss in the target and inner materials.

### 3.5.1 CDC hit calibration

To convert TDC data to drift length of the CDC, relative time offset and drift length to time function (XT curve) were adjusted. Relative time offset was obtained by fitting the rise time of the drift time distribution with the error function (Fig 3.13). CDC XT curve is fixed each layers by fitting to drift time and drift length correlation with 5th polynomials (Fig 3.14). It is noted that the time offset of drift time is related to the timing when a track reaches the CDC cell and timing dependence of pulse height. To correct these effects, track reconstruction and particle identification are necessary. Thus fine tuning is done after tracking and particle identification as described in Sec 3.5.6.

### 3.5.2 Track finding and reconstruction

Track finding and reconstruction were performed as follow,

1. Clustering hits in the super layer,
2. Finding track candidates by using hit clusters in axial super layers,
3. Circle fitting,
4. Finding hits in stereo layers,
5. Helix fitting.

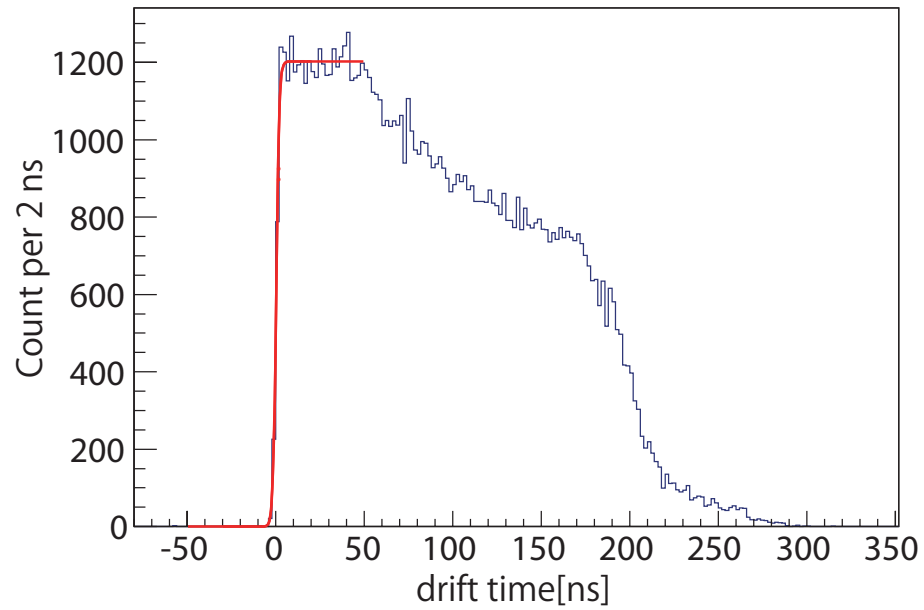


Figure 3.13: Typical timing distribution of the CDC hit.

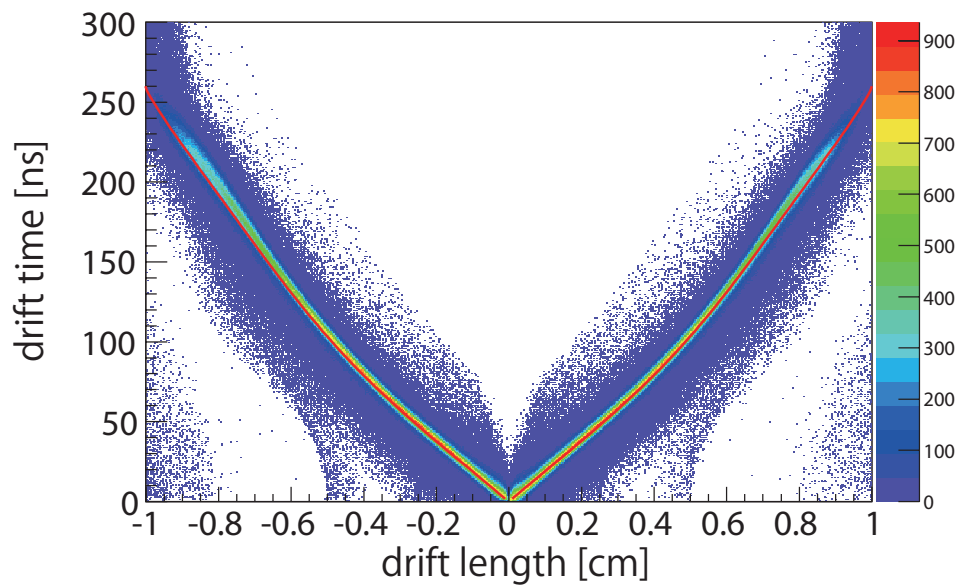


Figure 3.14: Typical correlation between the drift time and drift length (XT curve). Sign of drift length is plus (minus) when the center of the cell is left (right) side of the track from the view on the track direction.

**Clustering hits in the super layer**

The CDC had 7 super layers (A1, U1, V1, A2, U2, V2, A3). Hits next to each other in same super layer were clustering. Only one hit which is next to no other hit also became hit cluster expect to A1 super layer. Minimum hit number in the A1 super layer was two, because A1 super layer had three layers. If there are more than one hits next to other hit, every combination of hits became each cluster. Thus, hit clusters have only one hit in each layer. A position of hit cluster was defined as mean of positions of hit wire in the cluster. Figure 3.15 shows examples of hit clusters.

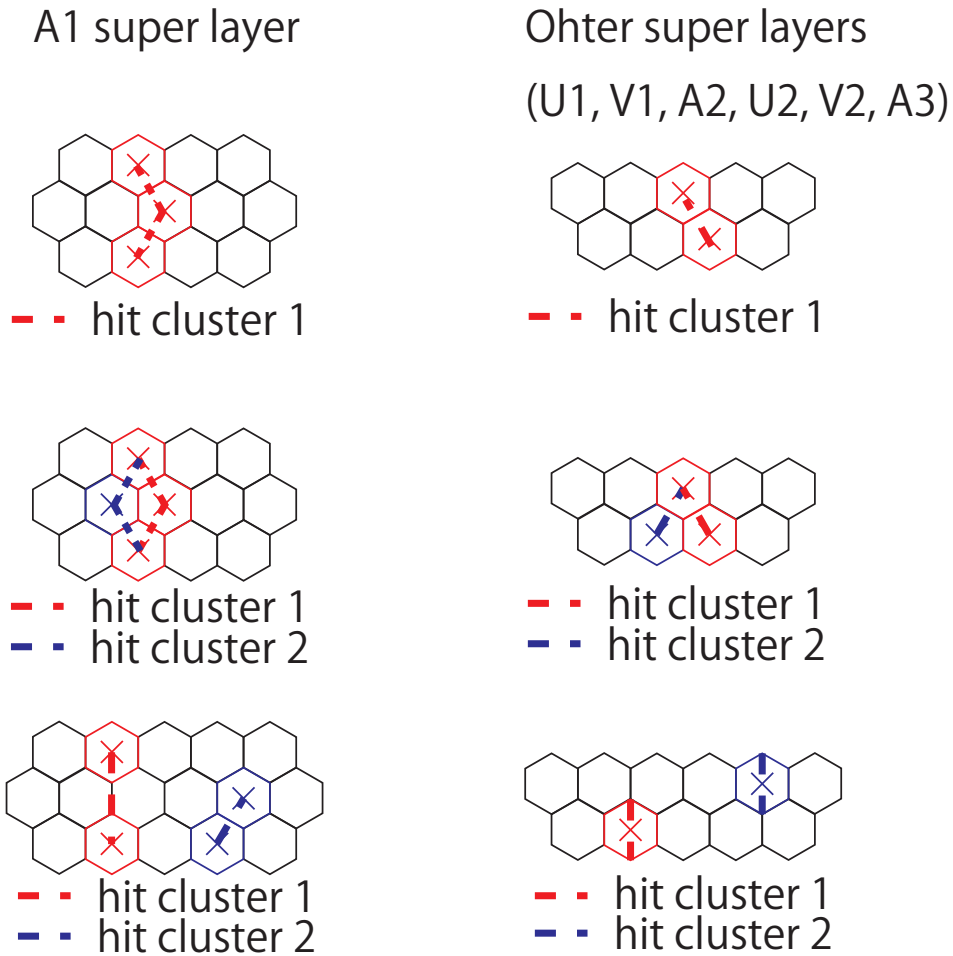


Figure 3.15: Examples of hit clusters in the super layer of the CDC.

**Finding track candidates by using hit clusters in axial super layers**

Finding track candidates was performed with hit clusters in axial super layers (A1, A2, A3). Every combination of hit clusters in A1, A2 and A3, was scanned. we treated the combination of A1, A2, and A3 as track candidates, when a distance between position of mid axial super layer A2 and a line connecting positions of cluster A1 and A2 is less than a

limit length(25 cm). The limit length was defined to be enough longer than a geometrical limit of the CDC $\sim 17$  cm, to detect hits of track with all layer of the CDC, corresponding  $Pt \sim 30$  MeV/c. Track candidates were requested to have 4 or more hits in axial layers.

### Circle fitting

Track candidates were fitted with circle (the center position (X,Y) and radius) by using the hits in axial layers. Fitting was performed to minimize the reduced  $\chi^2$  defined as,

$$\chi^2/ndf = \frac{1}{n-3} \sum_i^n \left( \frac{\delta_i - dl_i}{\sigma_i} \right)^2, \quad (3.4)$$

where  $n$  is number of hits in axial layers,  $\delta_i$  is distance between wire position and nearest point on circle,  $dl_i$  is drift length,  $\sigma_i$  is the spatial resolution of the CDC, and  $ndf$  is the degree of freedom which is  $n-3$  in this definition. Track candidates with large reduced  $\chi^2$  ( $\chi^2/ndf > 90$ ) were rejected.

### Finding hits in stereo layers

Hit clusters in stereo super layers (U1, V1, U2, V2) were connected to track candidates by using positions of hit clusters and circle track. Positions of hit clusters in stereo layers should be close to the circle track with considering the tilt angle of stereo layers. All possible combinations of circle tracks and hit clusters in stereo layers were included to track candidates. Track candidates were required to have 4 or more hits in axial layers, and at least 5 hits in stereo layers. Thus in total 10 or more hits were required to reconstruct track.

### Helix fitting

To reconstruct a trajectory of a charged particle, we used a helix parametrization as follows,

$$x(\phi) = d_\rho \cos \phi_0 + \frac{1}{\rho} (\cos \phi_0 - \cos (\phi_0 + \phi)) \quad (3.5)$$

$$y(\phi) = d_\rho \sin \phi_0 + \frac{1}{\rho} (\sin \phi_0 - \sin (\phi_0 + \phi)) \quad (3.6)$$

$$z(\phi) = d_z - \frac{1}{\rho} \tan \lambda \phi, \quad (3.7)$$

where  $d_\rho$  is the distance of the helix from pivotal point in the xy plane,  $\phi_0$  is the azimuthal angle to specify the pivotal point with respect to the helix center,  $\rho$  is the inverse of the signed radius of the helix,  $d_z$  is the distance of the helix from the pivotal point in the direction,  $\tan \lambda$  is the dip angle, and  $\phi$  is the deflection angle for parameter in helix measured from pivotal point. Notice that a negatively charged particle travels in the increasing  $\phi$  direction, while a positively charged particle travels in the decreasing  $\phi$  direction as shown Fig. 3.16.

The momentum of the charged particle is expressed with the helix parameters as,

$$\mathbf{p} = \frac{cB}{\rho} \begin{pmatrix} -\sin (\phi_0 + \phi) \\ \cos (\phi_0 + \phi) \\ \tan \lambda \end{pmatrix}, \quad (3.8)$$

where  $c$  is the light velocity and  $B$  is the strength of the magnetic field in the  $z$  direction.

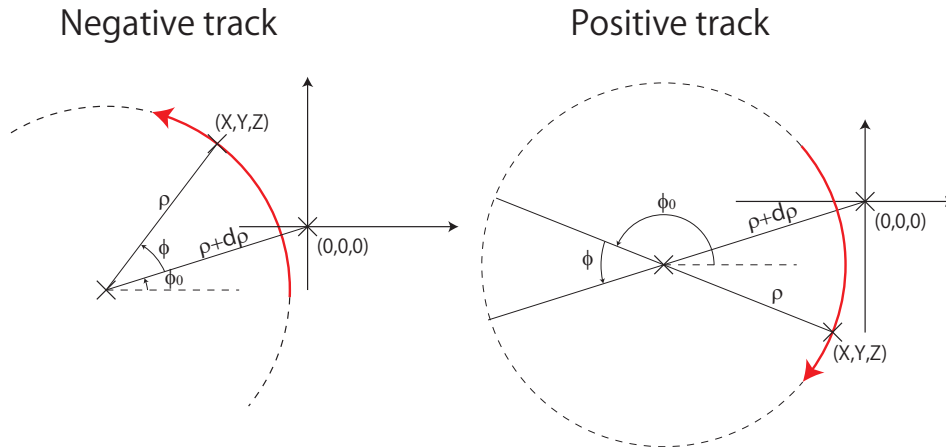


Figure 3.16: Parametrization of helix trajectory. Left is for negative track and right is for positive track.

Finally, full helix fitting was performed to reconstruct the momentum by minimizing the reduced  $\chi^2$  defined as,

$$\chi^2/ndf = \frac{1}{n-5} \sum_i^n \left( \frac{\delta_i - dl_i}{\sigma_i} \right)^2, \quad (3.9)$$

where  $n$  is number of CDC hits,  $\delta_i$  is distance between wire position and nearest point on helix,  $dl_i$  is drift length,  $\sigma_i$  is the spatial resolution of the CDC, and  $ndf$  is the degree of freedom which is  $n - 3$  in this definition. Tracks with  $\chi^2/ndf < 30$  were defined as “good tracks”. Figure 3.17 shows  $\chi^2/ndf$  distribution.

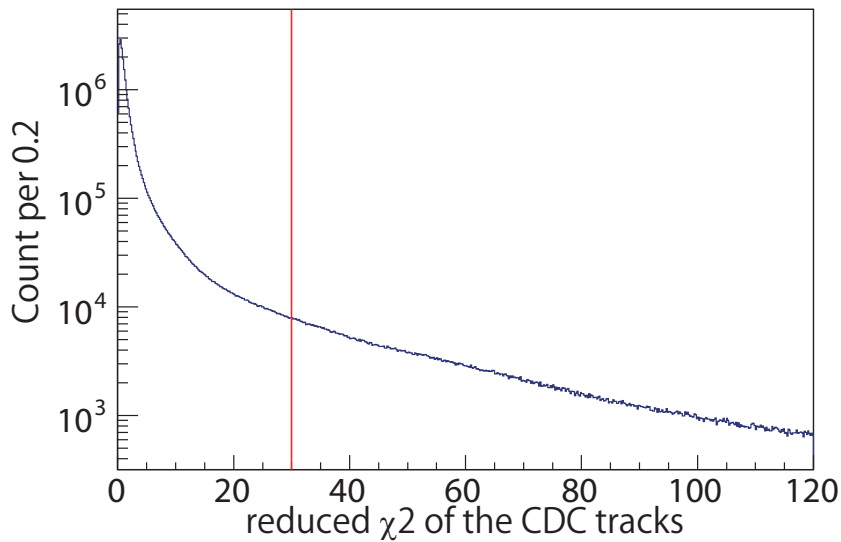


Figure 3.17:  $\chi^2/ndf$  distribution of the CDC tracks.

### 3.5.3 Associated CDH hits search and CDH calibration

Associated CDH hits for CDC track were determined by using track position at the CDH surface. Geometrical matching was checked at each CDH segment. If multiple CDH hits were associated with one CDC track, the nearest CDH hit to the track was selected.

### 3.5.4 Vertex reconstruction

For the CDS calibration, a beam-CDC track vertex was used. The beam-CDC track vertex was reconstructed for each CDC track and beam track as shown in Fig. 3.18. PID and the CDC and CDH calibration described following sections were performed by using this beam-CDC vertex.

beam - CDC track vertex

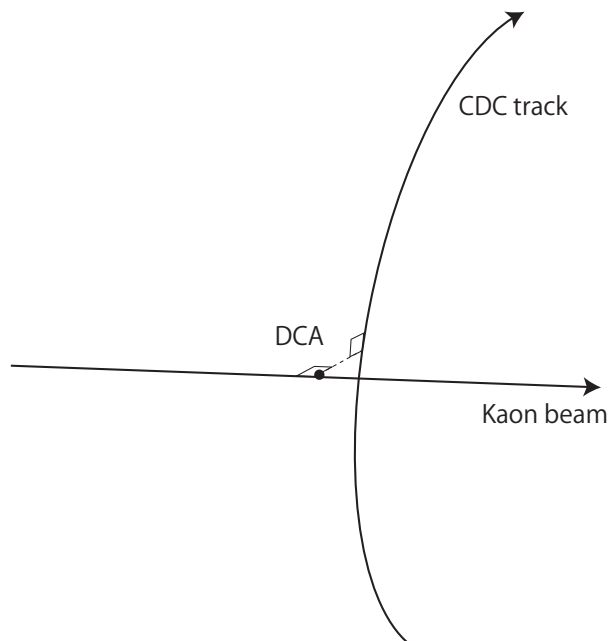


Figure 3.18: Definitions of the beam - CDC track vertex.

### 3.5.5 Particle identification

Particle identification (PID) was performed by reconstructed momentum with CDC and  $\beta$  from TOF of CDH-T0. To define the cut conditions of the PID, we parametrized the width of mass squared distributions which were calculated from obtained momentum and  $\beta$  of particle using a function as described below in Eq. 3.11.

$$\sigma_{m^2}^2 = 4m^2 \left( \frac{\sigma_p}{p} \right)^2 + \frac{4p^4}{\beta^2} \left( \frac{\sigma_{TOF}}{L} \right)^2, \quad (3.10)$$

$$\sigma_{m^2}^2 = 4m^2 p^2 C_{angle} + 4m^4 \left( 1 + \frac{m^2}{p^2} \right) C_{multi} + 4p^2 (m^2 + p^2) C_{TOF}, \quad (3.11)$$

where  $m$  is mass of the particle,  $p$  is momentum, and free parameters are  $C_{angle}$ ,  $C_{multi}$ , and  $C_{TOF}$ , which are related to angle resolution, multiple scattering and time resolution of TOF. Cut conditions of PID are set at  $\pm 2.5 \sigma$  from Fig. 3.20. To avoid misidentification, regions of overlap were excluded, resulting in an estimated purity of 99.5 % for protons and pions.

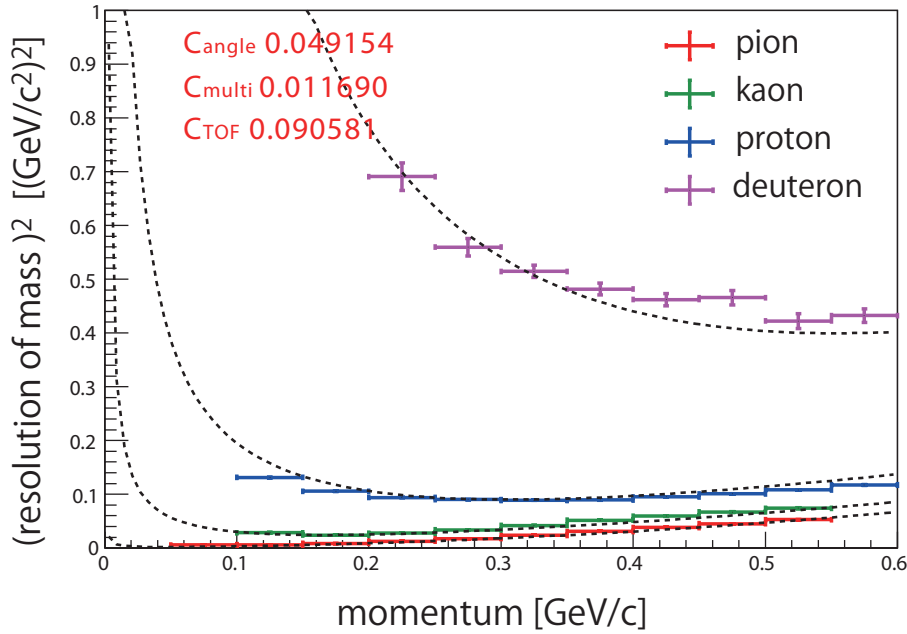


Figure 3.19: Correlation of Mass squared and squared of resolution of mass of each particle. Dotted lines show fitting result with PID function (Eq. 3.11).

### 3.5.6 Fine correction of CDS track

#### Retiming of the CDC drift time

The TDC data of the CDC contained the drift time and the flight time between the T0 and the CDC cell. To extract pure time information of drift time, flight time should be calculated as shown in Eq. 3.12.

$$T_{CDC} - T_{CDH} = t_{drift} + t_{CDC_{cell}-CDH}^{calc}, \quad (3.12)$$

where  $T_{CDC}$  is time information of the CDC,  $T_{CDH}$  is time information of the CDH,  $t_{drift}$  is drift time of the CDC cell,  $t_{CDC_{cell}-CDH}^{calc}$  is calculated flight time between CDC cell position and CDH position.

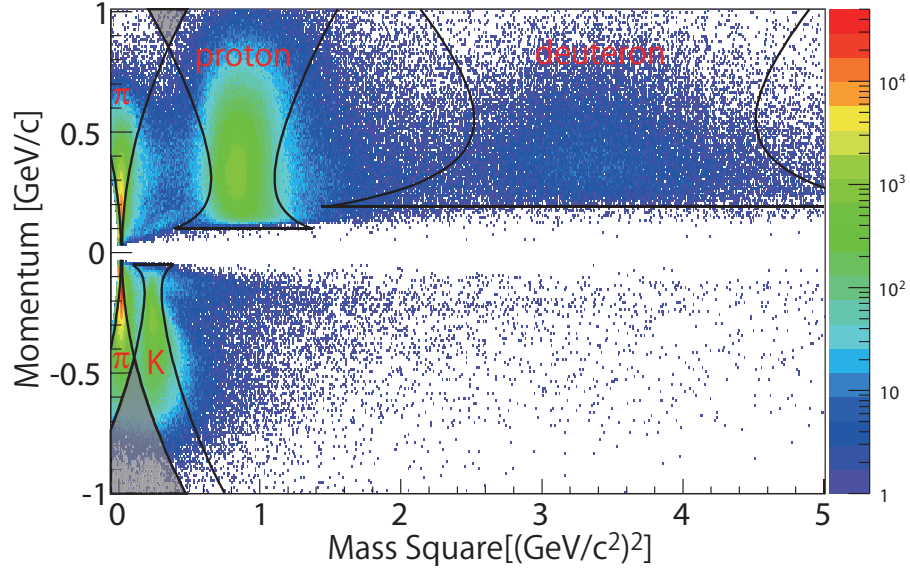


Figure 3.20: Scatter plot between momentum and mass squared of the CDS. The cut region for each particle is indicated as black curves corresponding to  $2.5 \sigma$ . Overlapped regions are excluded as shown gray colored regions.

### $1/\beta^2$ correction of CDC timing

CDC hit timing data had a correlation of energy deposit due to threshold of TDC signal. We corrected this correlation by using  $1/\beta^2$  of particle in CDS. Figure 3.21 shows the correction between  $1/\beta^2$  and the residual of the CDC timing .

### 3.5.7 CDH calibration

CDH calibration was performed by using calculated time between the T0 and CDH( $t_{CDH-T0}^{cal}$ ) as,

$$t_{CDH-T0}^{cal} = \frac{L_{T0-vtx}}{c\beta_{beam}} + \frac{L_{vtx-CDH}}{c\beta_{CDC}} \quad (3.13)$$

where  $L_{T0-vtx}$  is distance between the T0 and the vertex,  $L_{vtx-CDH}$  is flight length between the vertex and the CDH,  $\beta_{beam}$  is calculated  $\beta$  of kaon beam, and  $\beta_{CDC}$  is calculated  $\beta$  of CDC track. Then by comparing this calculated flight time and measured TOF between T0 and CDH, timing offset and time-walk effect were adjusted. For this calibration, only single pion events were used.

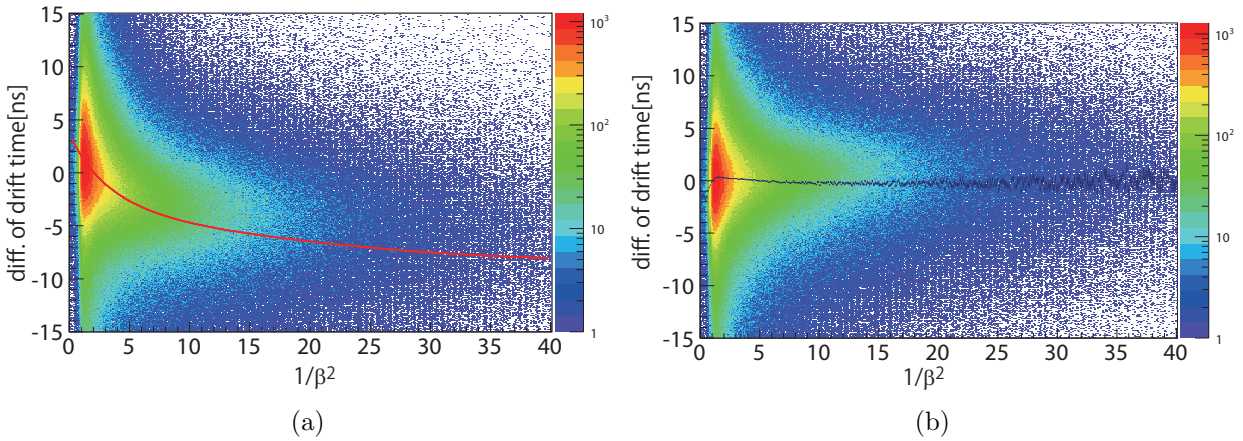


Figure 3.21: Correlation of CDC timing residual and  $1/\beta^2$  of particle. left figure is before the correction, right figure is after the correction.

### 3.6 CDS performance

#### 3.6.1 CDC position resolution

CDC intrinsic position resolution was estimated by comparing the CDC drift length residual with Monte Carlo simulation. Figure 3.22 shows a correlation of drift time and residual. In this figure, the residual distribution of the 1st layers is shown together with a Gaussian fit. Obtained width of each layer is shown in Fig. 3.23. Each colored line is a result of simulation in which CDC intrinsic resolution is set to be 160, 180, and 200  $\mu\text{m}$ . From this plot, we estimate that CDC position resolution is about 150  $\mu\text{m}$ .

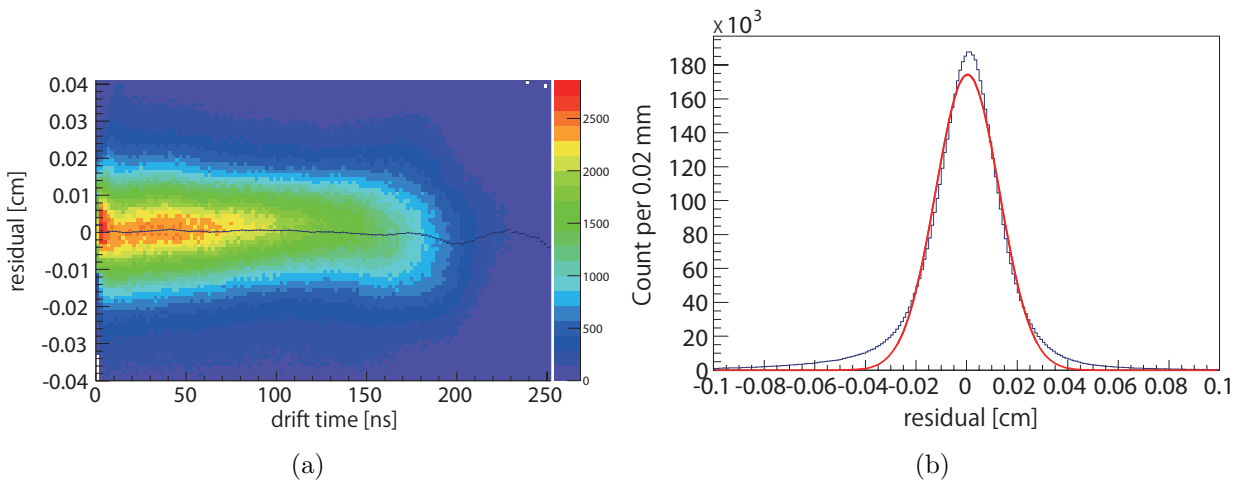


Figure 3.22: CDC drift time and residual correlation and projected residual distribution in CDC layer 1.

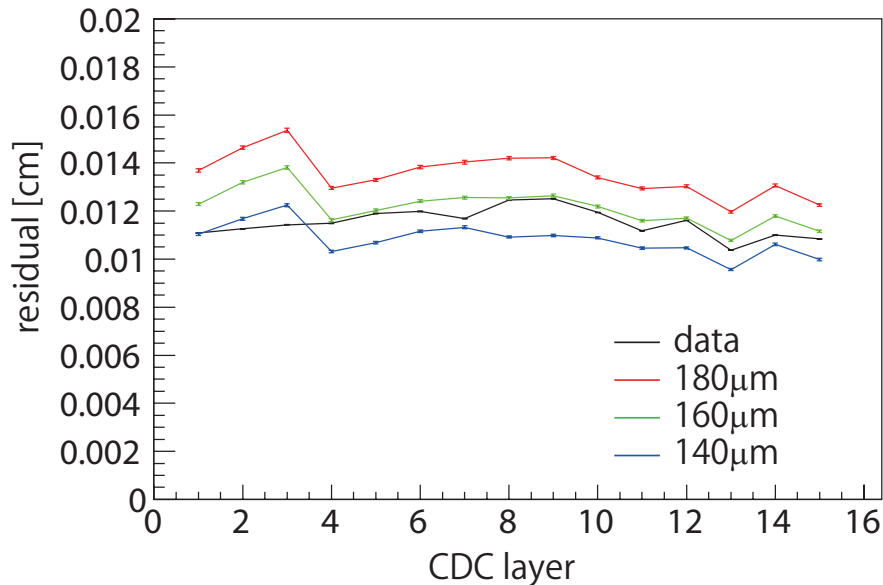


Figure 3.23: CDC width distribution in each layer.

### 3.6.2 CDC momentum resolution

The momentum resolution of the CDC, shown in Fig. 3.24, was estimated with a Monte Carlo simulation considering the CDC intrinsic position resolution. Each particles were generated with uniformly distribution of  $\varphi$  and  $\theta$  angle. The calculated transversed momentum  $p_t$  resolution was  $5.3\% p_t \oplus 0.5\% /\beta$ , which is about 2.5 % on 500 GeV/c particles.

### 3.6.3 Vertex resolution

The vertex resolution was evaluated with the kaon beam and CDC track. By using events in target cell around  $Z = 0$  and  $Y = 0$ , two clear peaks from the target cell are seen of which thickness 0.3 mm as shown Fig. 3.25(left). Those peaks are fitted with a Gaussian and radial (xy) vertex resolution was evaluated to be  $1.5 \pm 0.1$  mm. To estimate vertex resolution in z direction, events in the DEF selected  $\sqrt{(x^2 + y^2)} < 2$  cm were used. A peak around -16 cm corresponds to the DEF in Fig. 3.25(right). By fitting and considering the DEF thickness of 3 mm, z vertex resolution was evaluated to be  $6.5 \pm 0.2$  mm.

### 3.6.4 CDH performance

#### CDH efficiency

The CDH efficiency was defined as

$$\varepsilon_{CDH} \equiv N_{CDHhit} / N_{\text{track in CDH}}, \quad (3.14)$$

where  $N_{\text{track in CDH}}$  is number of reconstructed tracks in which the particle is in a CDH segment region, and  $N_{CDHhit}$  is the number of hits in the CDH segment. The CDH segment region was defined that width is in  $\pm 47.6$ mm (CDH fullsize:49.5mm), length is within

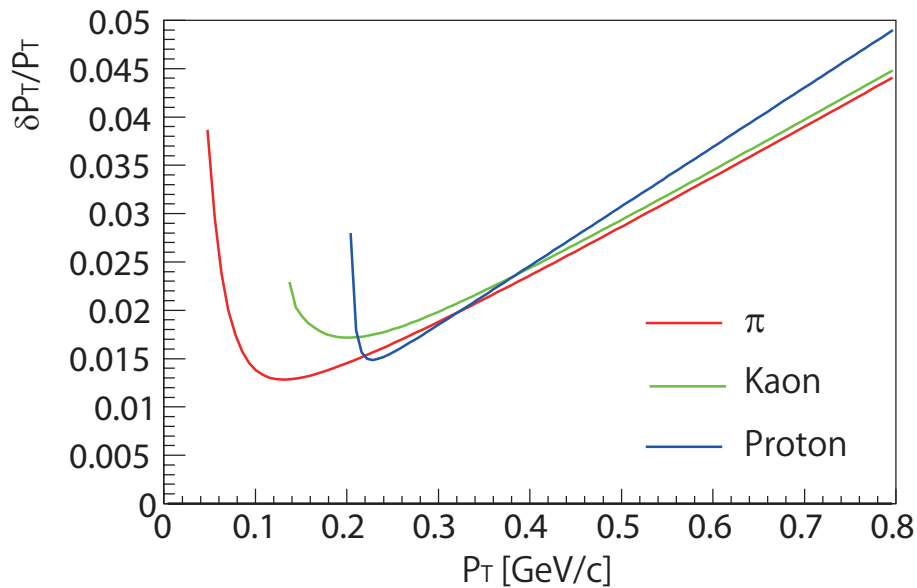


Figure 3.24: The simulated  $p_t$  resolution  $\delta p_t/p_t$  of the CDC for each particle as a function of  $p_t$ .

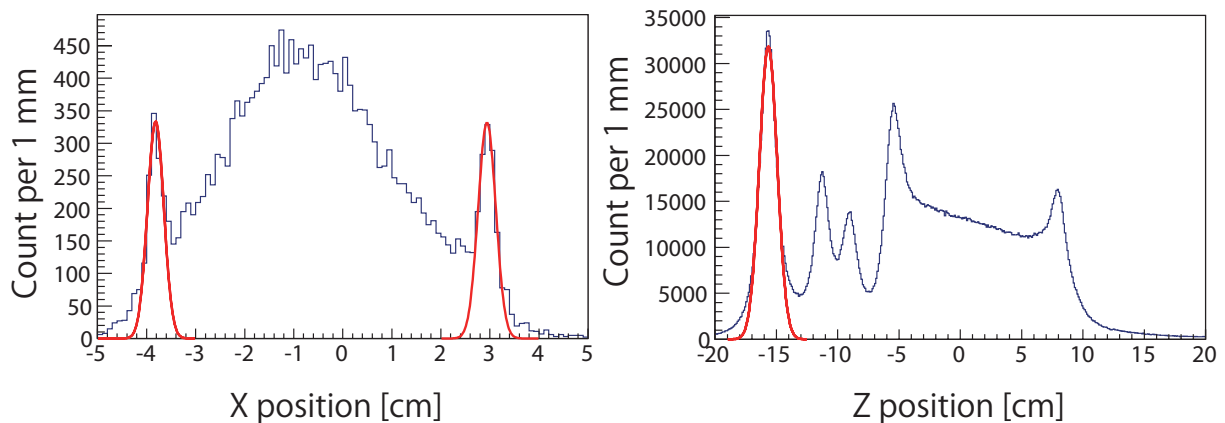


Figure 3.25: (left) Reconstructed x position vertex distribution around  $y=0$  and  $z=0$  cm. The two peaks correspond to the target cell. (right) Reconstructed z position vertex distribution with  $\sqrt{(x^2 + y^2)} < 2$  cm. The peak around  $z = -16$  cm corresponds to the DEF.

389.5mm (CDH fullsize:395mm) ). Energy deposit of the CDH was requested over 0.3 MeV. Efficiencies of CDH all segments were over 99.5% as shown in Fig. 3.26.

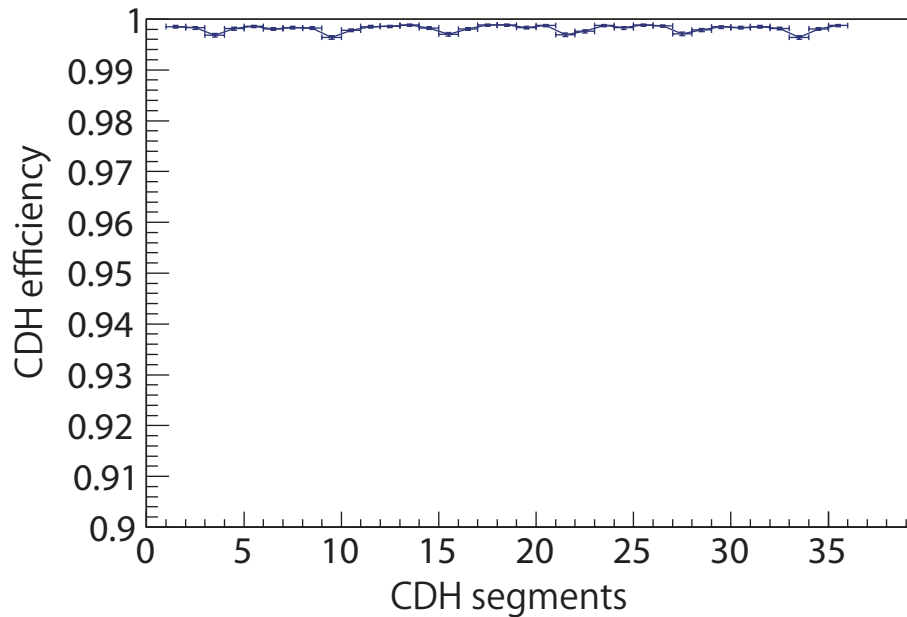


Figure 3.26: Efficiencies for each segment of the CDH.

### CDH-T0 timing resolution

Time resolution of TOF was estimated by comparing the TOF of T0-CDH with a calculated time by track trajectory and reconstructed momentum between the T0 and CDC. Typical distribution of difference of the measured TOF and calculated TOF is shown in Fig. 3.27, and time resolution of each CDH segment is shown in Fig. 3.28. The overall time resolution was evaluated to be about 150 ps.

### 3.6.5 Fiducial volume selection

Figure 3.29 shows the vertex distribution of xz and yz planes. The target components, the cell, the vacuum vessel, the thermal radiation shield,  $^3\text{He}$  transfer pipes, and the DEF are clearly identified. The fiducial volume of the target was defined as the black boxes in Fig. 3.29. The size of fiducial volume was 30 mm in radius  $\times$  100 mm in length. The fiducial volume was apart from the target cell by more than 3 times the vertex resolution to avoid contaminations from beryllium.

## 3.7 Adjustment of the CDS magnetic field strength

CDS Magnetic field was roughly set at 0.7 T by monitoring with a gauss meter. However, the measured value could have a few % error due to the accuracy of the meter. Therefore for

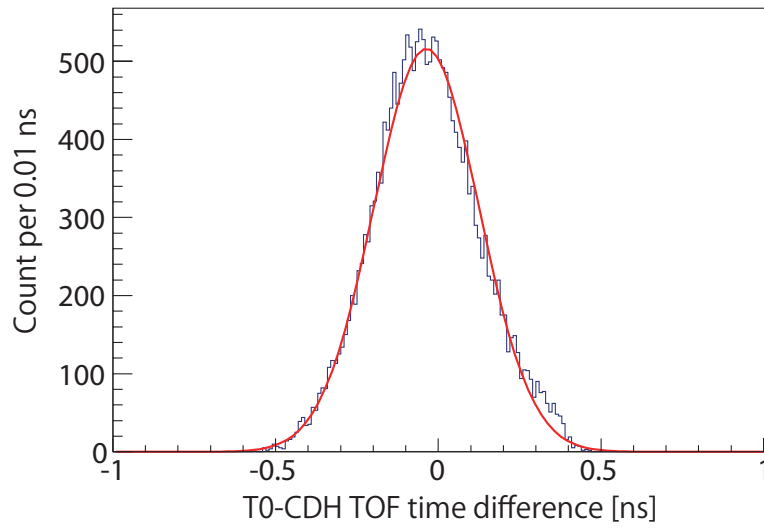


Figure 3.27: Typical distribution of difference of the TOF of T0-CDH. Time resolution of T0-CDH was estimated as  $\sigma$  of Gaussian fitting.

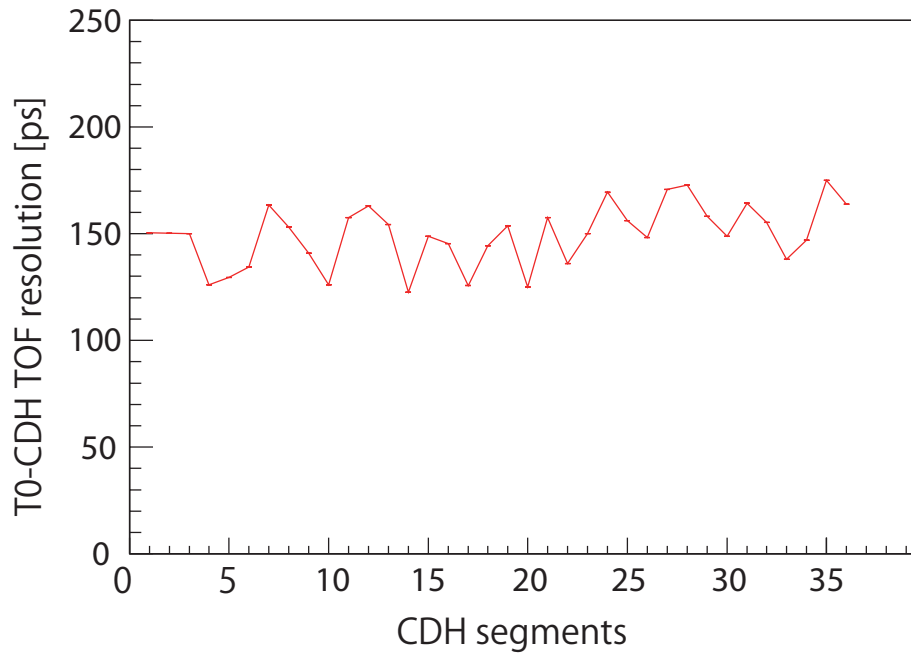


Figure 3.28: Segments dependence of CDH-T0 TOF time resolution.

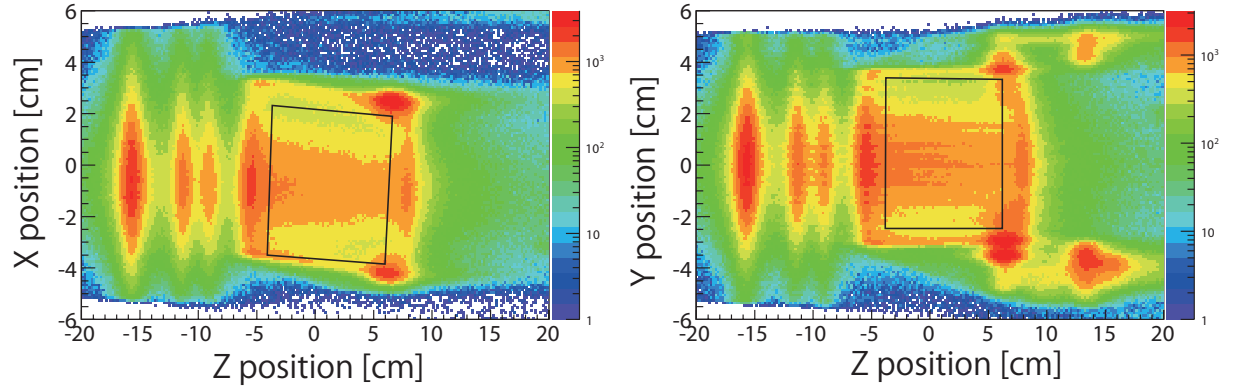


Figure 3.29: Reconstructed vertex distributions in zx (left) and zy (right) planes. The fiducial volume is defined as the black boxes.

fine adjustment intrinsic magnetic field of the CDS, field strength was calibrated by using reconstructed masses of  $K_s^0$  and  $\Lambda$ . Events were selected so as to DCA of  $p\pi^-(\pi^+\pi^-) < 2$  cm. Figure 3.30 shows CDS magnetic field dependence of masses of  $K_s^0$  and  $\Lambda$ . From this figure, CDS Magnetic field was determined as 0.715 T. As the result,  $\Lambda$  mass is  $1.115570 \pm 5.4 \times 10^{-6}$  GeV/ $c^2$  and  $\sigma$  is  $2.02633 \times 10^{-3} \pm 6.5 \times 10^{-8}$  GeV/ $c^2$  when field strength is 0.715 T as shown in Fig. 3.31.  $K_s^0$  mass is  $0.49742 \pm 4.2 \times 10^{-5}$  GeV/ $c^2$  and  $\sigma$  is  $6.0400 \pm 1.5 \times 10^{-3}$  MeV from fitting result with a Gaussian and third-order polynomials as shown in Fig. 3.32.

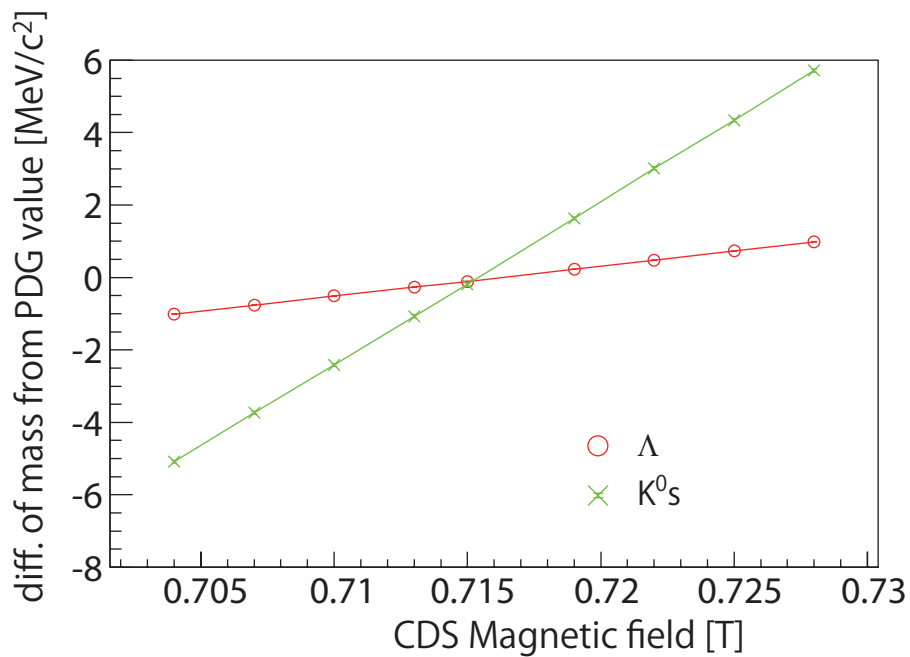


Figure 3.30: The correlation between deviations of  $K_s^0$  and  $\Lambda$  mass from the PDG values and the CDS Magnetic field.

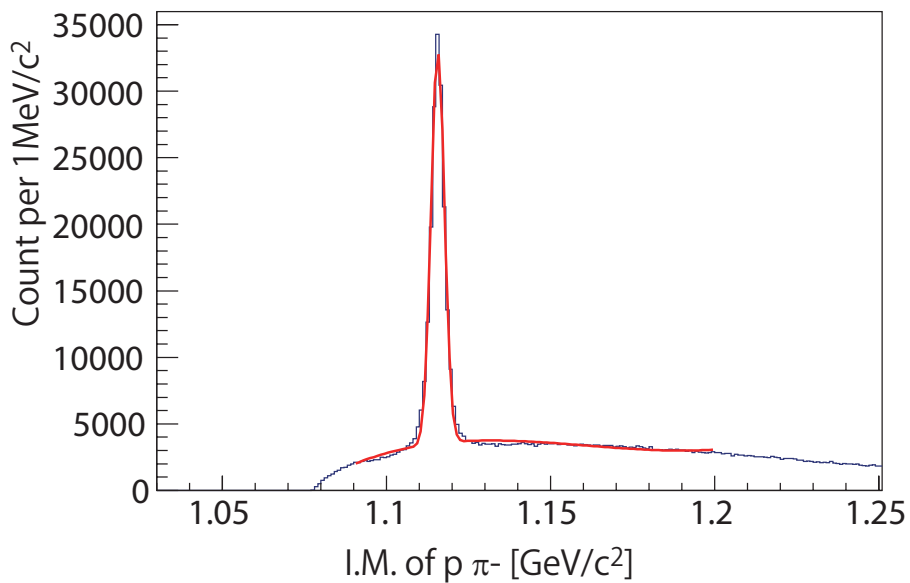


Figure 3.31: Invariant mass distribution of  $p\pi^-$  pairs. Events were selected to DCA of  $p\pi^- < 2$  cm. The reconstructed  $\Lambda$  peak was fitted with Gaussian and third-order polynomial. A red curve shows the fitting result.

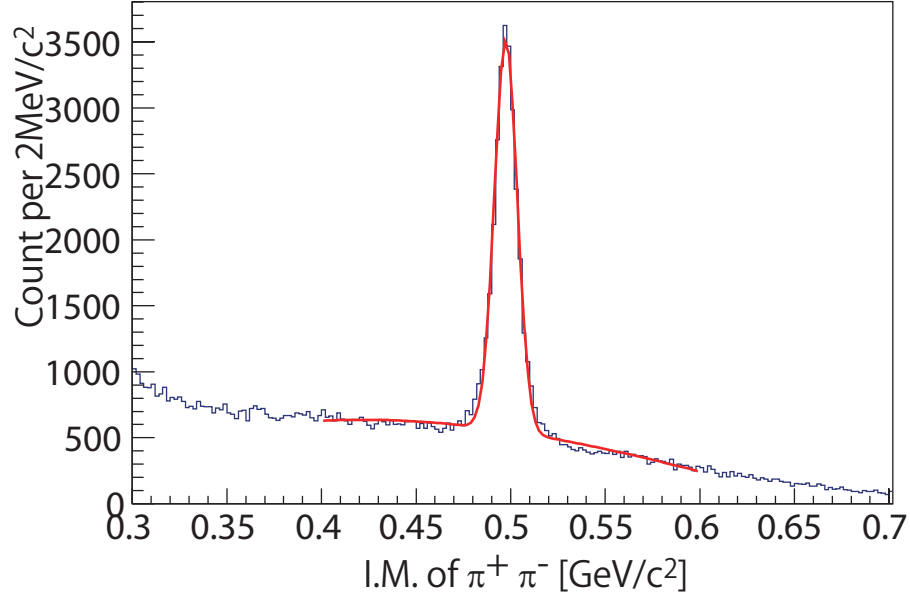


Figure 3.32: Invariant mass distribution of  $\pi^+$  and  $\pi^-$  pairs. Events were selected to DCA of  $\pi^+\pi^- < 2$  cm. The  $K_s^0$  peak was fitted with Gaussian and third-order polynomial. The red curve shows the fitting result.

## 3.8 CDC tracking efficiency

### 3.8.1 tracking efficiency for a single track

Tracking efficiency of the CDC was estimated by using the IH and CDH hits to select good hits. CDC tracking efficiency was defined as

$$\varepsilon_{tracking} \equiv N_{\text{CDCtrack}}/N_{\text{IHhit\&CDHhit}}, \quad (3.15)$$

where  $N_{\text{IHhit\&CDHhit}}$  is the number of events which has a single hit both in CDH and IH, and  $N_{\text{CDCtrack}}$  is the number of CDC tracks which correspond to the segments of the IH and CDH hits. To select M.I.P events, CDH energy deposit was selected over 5.5 MeV and under 9 MeV, TOF of CDH-T0 is in 5.0 to 9.5 ns, and IH energy deposit was in 0.3 to 0.9 MeV. The  $\varphi$  angle difference between the IH and CDH segments was requested under 90 degree to ensure that hits correspond to the same track. Figures 3.33 and 3.34 show  $\varphi$  and  $\theta$  angle dependence of the CDC tracking efficiency. There is no geometrical asymmetry of the CDS. Overall tracking efficiency of the CDS was evaluated to be  $96.23 \pm 0.03$  %.

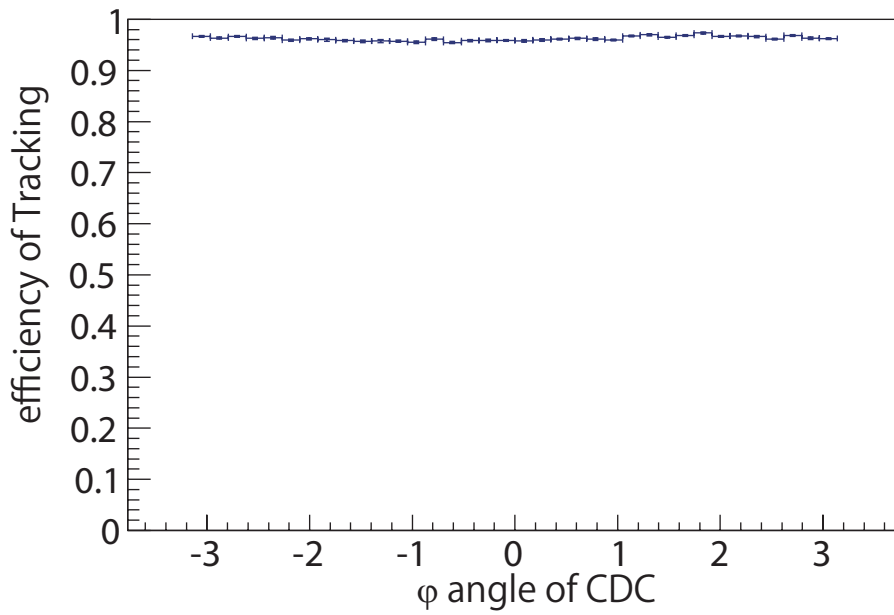


Figure 3.33: The  $\phi$  angle dependence of the CDC tracking efficiency.

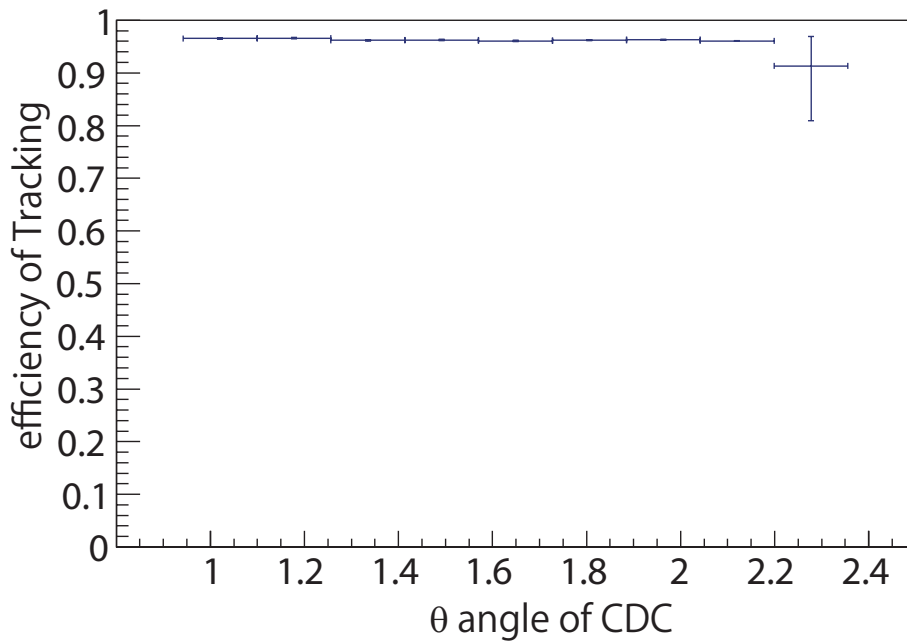


Figure 3.34: The  $\theta$  angle dependence of the CDC tracking efficiency.

## 3.9 Event reconstruction for ${}^3\text{He}(K^-, \Lambda p)n$ reaction

### 3.9.1 ${}^3\text{He}(K^-, pp\pi^-)$ event selection

${}^3\text{He}(K^-, pp\pi^-)$  event selection was performed as follows.

1. Selecting just three tracks in the CDS in single event,
2. Requesting a veto of the BVC,
3. Performing PID for each track and selecting “ $\pi^-pp$ ” events,
4. Selecting reaction vertex in the fiducial volume,

At first, events with “ $\pi^-pp$ ” in the CDS were selected. Only three tracks were requested in the CDS and particles should be identified as  $pp\pi^-$ . Also veto of the BVC which located just downstream of the CDS was requested to reject forward going charged particles. The  $\theta_{lab}$  angles of  $\pi^-pp$  tracks should be in 49 to 131 degrees from the geometry of the CDS. Minimum momenta of  $\pi^-$  and proton tracks in the CDS which were limited by the geometrical condition of the CDS and energy loss in materials were  $\sim 30$  and  $120$  MeV/ $c$ , respectively. For PID, each track should have each associated CDH hit. Thus, we just requested CDH hit number  $\geq 3$ . There were some accidental hits in the CDH, which we considered due to neutral particles from the environment. Therefore, we allowed that CDH hit number over than three.

The reaction vertex was defined as the mid-point of  $\Lambda$ -track and proton track along the beam trajectory as shown in Fig.3.35. A  $\Lambda$  vertex was defined as the center of the distance of closest approach (DCA) between a  $\pi^-$  and  $p$  pair. We requested that the reaction vertex was in the fiducial volume.

There are two combinations of  $\pi^-p$  pair in the  ${}^3\text{He}(K^-, pp\pi^-)$  events. Figure 3.36 shows a scatter plot between the  $\pi^-p$  invariant mass of two combinations. Clear lines from  $\Lambda$  decays are seen both horizontal and vertical axis. However, there were events in the region in which two lines crossed and we can not identify the true  $\pi^-p$  pair from  $\Lambda$  with only invariant mass distribution. Thus, a Log-likelihood method was applied to identify  $\pi^-p$  pair from  $\Lambda$  as described the following subsection.

### 3.9.2 Log-likelihood method for $\pi^-p$ pair selection

To identify the  $\pi^-p$  pair associated with a specific  $\Lambda$  decay in a  $\pi^-pp$  event, a Log-likelihood method was used on the product of five probability density functions:

1. distance of closest approach (DCA) between a  $\pi^-p$  pair candidate for  $\Lambda$  decay ( $f_{DCA(\pi p)}$ ),
2. DCA between the kaon beam and an un-paired proton ( $f_{DCA(K-p)}$ ),
3. DCA between the kaon beam and a reconstructed  $\Lambda$  track ( $f_{DCA(K-\Lambda)}$ ),
4. A distance between nearest points on  $K^-$  beam to proton and  $\Lambda$  track ( $L(\Lambda p)$ ), and
5. Invariant mass distribution of the  $\pi^-p$  pair candidate ( $f_{M_{inv.\pi-p}}$ ).

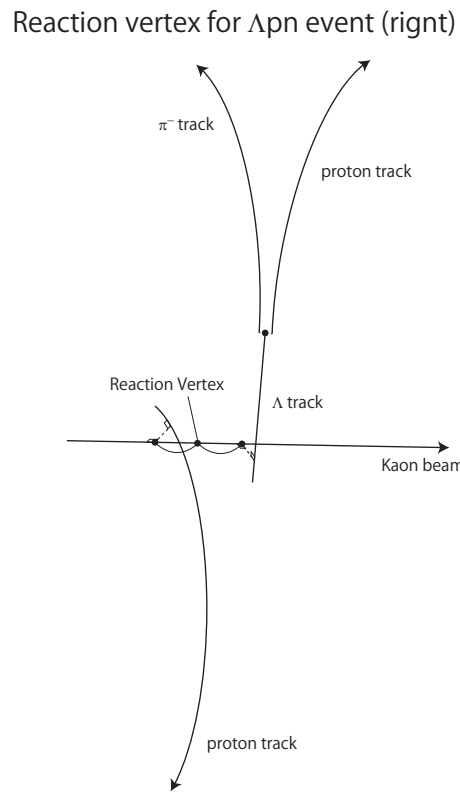


Figure 3.35: Definitions of the reaction vertex.

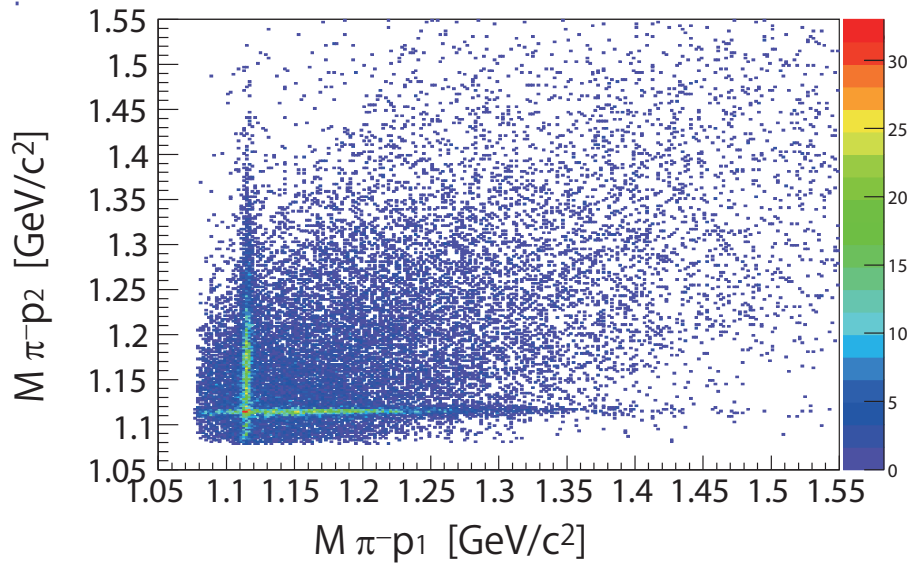


Figure 3.36: 2D plot of  $\pi^- p$  invariant mass distribution of each pair in  $\pi^- pp$  events.

One can calculate the relative probability to obtain an event according to the relative yield of distributions on these five quantities based on a simulation.

### Monte Carlo simulation for $\Lambda pn$ final state

A Monte Carlo simulation was performed to evaluate distributions on these five quantities for the Log-likelihood method. In the simulation, we assume that final state is  $\Lambda pn$  and a uniform distribution (S-wave) over the three-body phase space based on the phase volume, namely:

$$\frac{d^2\sigma_{3\text{NA}(\Lambda\text{pn})}}{dT_n^{CM} d\cos\theta_n^{CM}} \propto \rho_3(\Lambda pn), \quad (3.16)$$

where  $\sigma_{3\text{NA}(\Lambda\text{pn})}$  is the simulated event distribution for the  $\Lambda pn$  final state,  $T_n^{CM}$  is the kinetic energy of the neutron in the CM frame, and  $\cos\theta_n^{CM}$  is the neutron emission angle in the CM frame. Plain wave approximation was employed to generate the final state particles  $\Lambda pn$ , distribution for the final state particles  $\Lambda pn$  are scattered equally in phase space. GEANT4 [82] was utilized to take into account geometrical information for all detectors and their resolution. In addition, we analyzed simulated data by using the same method in the data analysis. Thus, this simulation should reproduce energy loss, each resolution and acceptance of the detectors.

### DCA distributions generated by simulation

Figure 3.37 shows each DCA distributions generated by the Monte Carlo simulation.

Each distribution is normalized so that the maximum value to be 1. The probability density functions were obtained by fitting the distributions with a function as:

$$f_{DCA_s}(x) = p_0 \exp(p_1 x) + p_2 \exp(p_3(x - p_4)^{p_5}), \quad (3.17)$$

where  $x$  is each DCA value,  $p_i$ s are free parameters. For probability density function of invariant mass distribution of the  $\pi^- p$  pair candidate ( $f_{M_{inv.\pi^-p}}$ ), a Gaussian function was used, of which mean value is  $\Lambda$  mass and  $\sigma$  is 1.9 MeV/ $c^2$  that is evaluated by Monte Carlo simulation.

### 3.9.3 Definition of the log likelihood function

By using these probability density functions, the log likelihood function ( $\ln L$ ) is defined as:

$$\ln L = -\ln(f_{DCA(\pi p)} \times f_{DCA(K^- p)} \times f_{DCA(K^- \Lambda)} \times f_{L(\Lambda p)} \times f_{M_{inv.\pi^-p}}). \quad (3.18)$$

$\ln L$  distributions for MC simulations as well as for the data are shown in Fig. 3.38. We calculated this  $\ln L$  for two combinations of  $\pi^- p$  pairs and the pair having smaller  $\ln L$  were chosen as the correct  $\pi^- p$  pair from  $\Lambda$  decay. In addition, events with smaller  $\ln L > 6$  were rejected. Based on our simulation, the incorrect  $\pi^- p$  pair selection probability is estimated to be less than 0.5 % of the total simulated events. It should be noted that the present criteria to utilize  $\ln L$  function is valid for  $\Lambda pn$  three body final state, and could be less effective for other reaction channel, although the effect would be very small. Using this method, the  $\Lambda pn$  events were selected from the data.

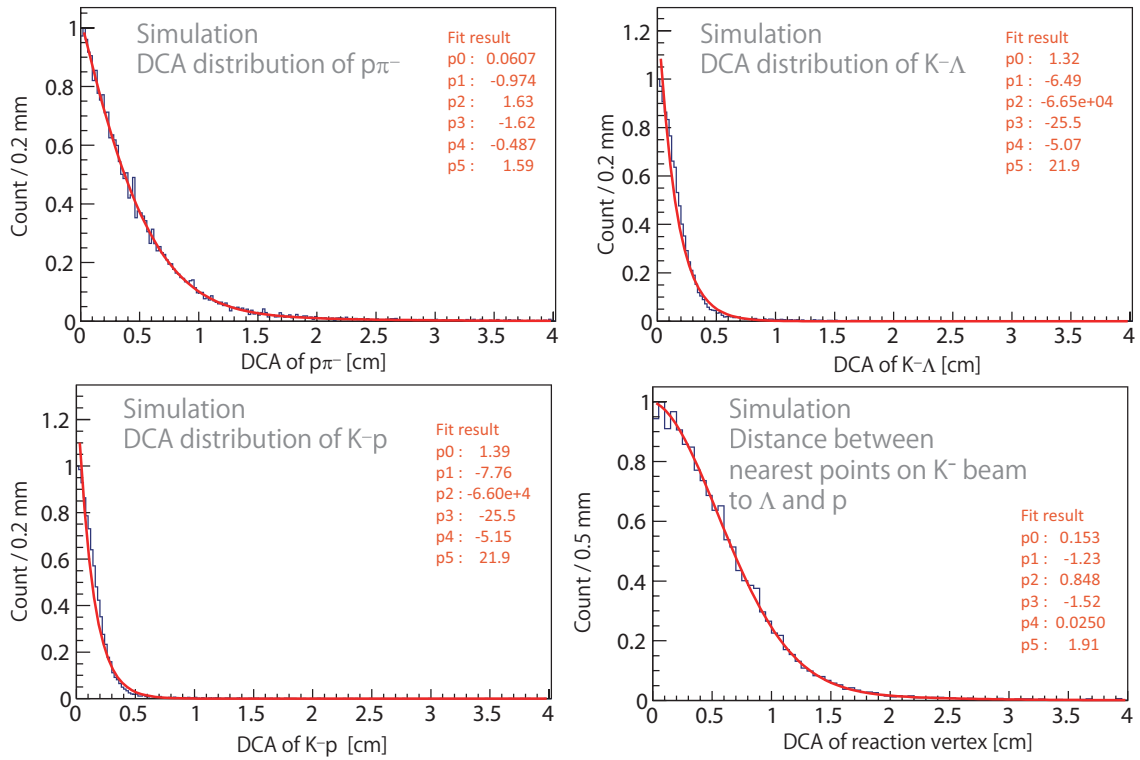


Figure 3.37: DCA distributions generated by Monte Colro simulation.

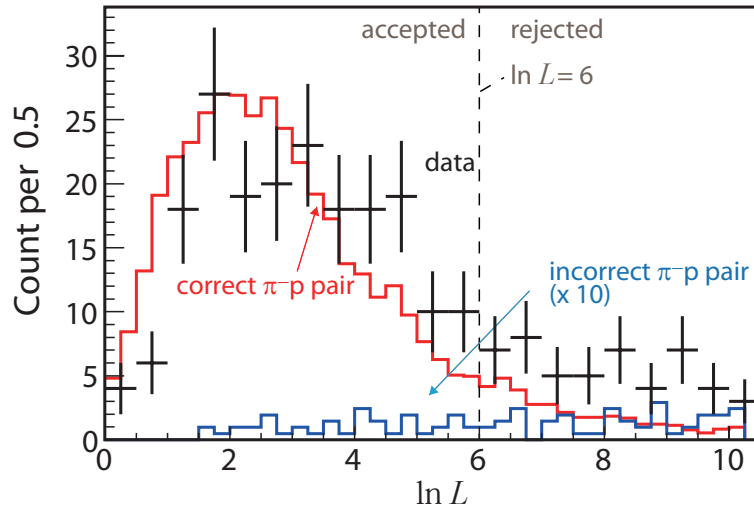


Figure 3.38: Likelihood function ( $\ln L$ ) distribution. Black crosses are  $\ln L$  of data. Since there are two possible pairs, the pair having smaller  $\ln L$  is plotted. The red histogram shows the simulated  $\ln L$  of the correct  $p\pi^-$  pair from  $\Lambda$  decay in a  $pp\pi^-$  event. The blue histogram is  $\ln L$  of the incorrect pair of  $p\pi^-$  in a  $\Lambda$  decay. The blue histogram is vertically scaled 10 times.

### 3.10 Detection efficiency

In the  $\Lambda pn$  events, there are many factors to be considered to estimate the detection efficiency; the geometrical acceptance of the CDS, kinematical limit of momentum which was caused by energy loss in materials, and effect of multi-track which means tracking efficiency of very near two tracks and probability to hit same CDH segment with multi-tracks. These effects could have correlations each other, and it is difficult to evaluate each effect separately. Thus, we estimated overall detection efficiency of the CDS over the  $\Lambda pn$  final state with the simulation.

Figure 3.39 shows overall detection efficiency distributions as functions of  $p_\Lambda^{lab}$ ,  $p_p^{lab}$ ,  $p_n^{lab}$ ,  $\cos\theta_\Lambda^{lab}$ ,  $\cos\theta_p^{lab}$ , and  $\cos\theta_n^{lab}$ . It should be noted that momenta of each particle were the values at the reaction vertex. The minimum momentum of proton is about 220 MeV/c. Edge of the minimum momentum of  $\Lambda$  is not sharp because  $\Lambda$  momentum is a composition of momenta of  $\pi^- p$ . Efficiency distributions of  $\cos\theta_\Lambda^{lab}$  and  $\cos\theta_p^{lab}$  are in the CDS geometry as shown by red dashed lines in Fig. 3.39. The efficiency distribution of  $\cos\theta_n^{lab}$  covers mainly in the forward region because  $\Lambda$  or proton is out of the CDS acceptance when neutron is emitted in the backward direction. This effect is also shown in Fig 3.39(c) as a bump in high neutron momentum which prefers the forward direction.

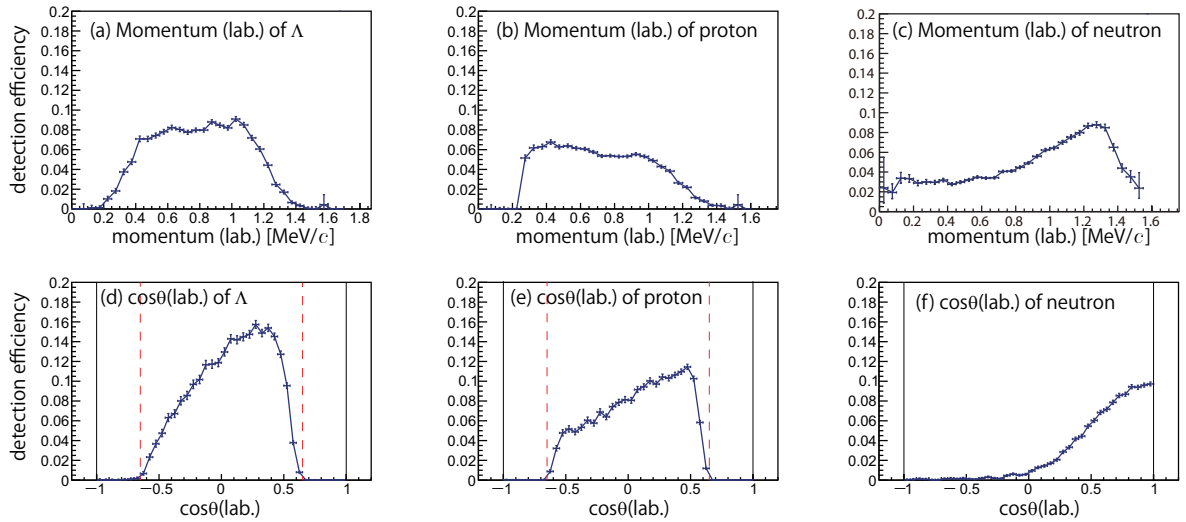


Figure 3.39: Overall detection efficiency distributions as functions of  $p_\Lambda^{lab}$  (a),  $p_p^{lab}$  (b),  $p_n^{lab}$  (c),  $\cos\theta_\Lambda^{lab}$  (d),  $\cos\theta_p^{lab}$  (e), and  $\cos\theta_n^{lab}$  (f). Red lines in (d) and (e) show the CDS geometry.

The efficiency on a Dalitz plot with kinetic energy of  $\Lambda$ , proton and neutron in CM frame, normalized to the  $Q$ -value of the reaction are also shown in Fig. 3.40. Usually, Dalitz plot[83] means a 2D plot plotted with two pairs of invariant mass squared  $m_{12}^2$  and  $m_{23}^2$  with three particles in the final state. We used a 2D plot of  $T_n^{CM}/Q^{CM}$  and  $(T_p^{CM} - T_\Lambda^{CM})/\sqrt{(3)}Q^{CM}$ , where  $T_n^{CM}$ ,  $T_p^{CM}$  and  $T_\Lambda^{CM}$  are kinetic energy of neutron, proton and  $\Lambda$  and  $Q^{CM}$  is the  $Q$ -value of the reaction. Energy limit makes a triangle and perpendicular directions to each side of the triangle mean kinetic energies of particles normalized by the  $Q$  value in the plot.

This Dalitz plot also shows almost flat distribution if  $\Lambda pn$  events are distributed uniformly in phase space. Figure 3.40 indicates that our detector system has a fairly flat acceptance over the  $\Lambda pn$  phase space, expect for upper-left and upper-right corners. Acceptance reduction of these corners come from lower kinetic energy of  $p$  and  $\Lambda$ , so that we cannot detect them. On the other hand, we have enough acceptance at the bottom, where two-nucleon kaon absorption with a spectator neutron  $n_s$ ,  $K^- + {}^3\text{He} \rightarrow \Lambda p + n_s$ , is expected, if the proton and  $\Lambda$  are emitted in our acceptance of Fig. 3.39.

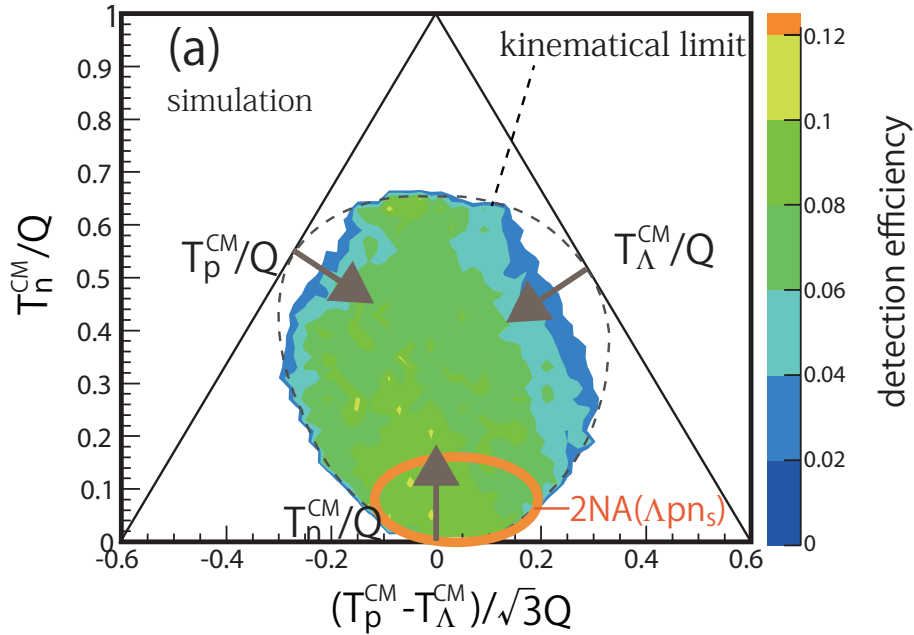


Figure 3.40:  $\Lambda pn$  overall detection efficiency on the Dalitz plot. The 2NA process,  $K^- + {}^3\text{He} \rightarrow \Lambda pn_s$  events are expected in the region marked by the orange circle.

### 3.11 Resolution of $\Lambda p$ invariant mass and missing mass of ${}^3\text{He}(K^-, \Lambda p)$

Resolution of  $\Lambda p$  invariant mass was estimated by the Monte Colro simulation. Mass resolution of  $\Lambda p$  invariant mass was evaluated by fitting the  $\Lambda p$  invariant mass distribution difference between the simulation and evaluated invariant mass with a Gaussian. Figure 3.41 shows the  $\Lambda p$  invariant mass resolution as a function of the mass. Mass resolution in the region of interest around  $K^- pp$  threshold ( $2.37 \text{ MeV}/c^2$ ) is about  $10 \text{ MeV}/c^2$ .

Resolution of missing mass of  ${}^3\text{He}(K^-, \Lambda p)$  was also estimated from the missing neutron peak by the Monte Colro simulation. By fitting the missing mass of  ${}^3\text{He}(K^-, \Lambda p)$  distribution with a Gaussian, we evaluated missing mass resolution at neutron mass to be  $45 \text{ MeV}/c^2$ .

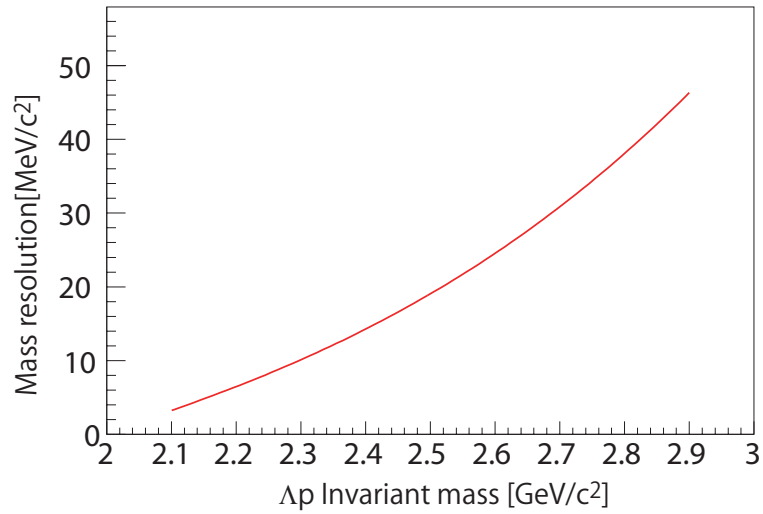


Figure 3.41: Relation of  $\Lambda p$  invariant mass resolution and mass. This values were estimated by the Monte Colro simulation. Mass resolution in the region of interest, which is around  $K^-pp$  mass threshold ( $2.37 \text{ MeV}/c^2$ ), is about  $10 \text{ MeV}/c^2$ .

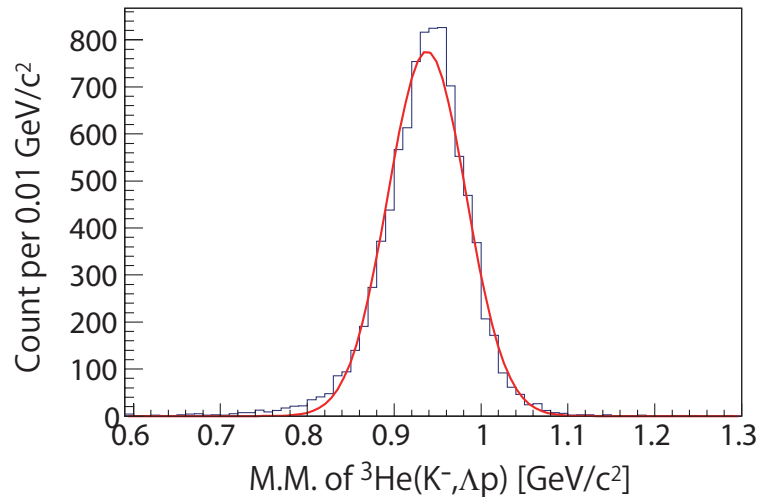


Figure 3.42: Relation of missing mass of  ${}^3\text{He}(K^-, \Lambda p)$ . With a Gaussian fitting, we evaluated the missing mass resolution at neutron mass to be  $45 \text{ MeV}/c^2$ .



# Chapter 4

## Results and discussion

### 4.1 ${}^3\text{He}(K^-, \Lambda p)X$ events

Figure 4.1 shows  $\Lambda p$  invariant-mass(a) and missing-mass spectra(b) for the  ${}^3\text{He}(K^-, \Lambda p)X$  reaction. No clear structure is seen in the invariant mass distribution(Fig. 4.1(a)). In this reaction, there are many channels contributing to the  $\Lambda p$  in the final state, for example  $\Lambda p\pi^0$  and  $\Sigma^0 p \rightarrow \Lambda p\gamma$ . Thus, it is difficult to discuss  $\bar{K}NN$  state with  ${}^3\text{He}(K^-, \Lambda p)X$  events. We focused to more simple state, the  $\Lambda pn$  final state which is the non-mesonic mode of kaon absorption. The missing mass of the  ${}^3\text{He}(K^-, \Lambda p)X_{miss.}$  reaction was obtained kinematically, and a neutron peak was clearly seen, as shown in Fig. 4.1(b). The  $\Lambda pn$  final state events can be selected by setting the neutron window to be  $0.85 < M_X < 1.03 \text{ GeV}/c^2$ . For simplicity, we denote those events in the neutron window as “ $\Lambda pn$  events”.

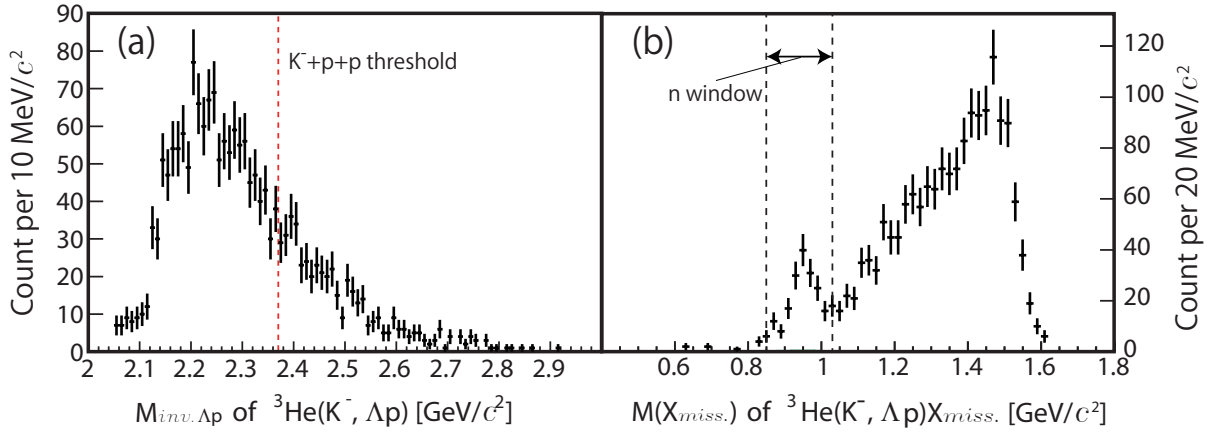


Figure 4.1: (a)  $\Lambda p$  invariant mass distribution and (b) missing mass  $M_X$  spectrum of  ${}^3\text{He}(K^-, \Lambda p)X_{miss.}$ .

### 4.2 ${}^3\text{He}(K^-, \Lambda p)n$ events

For the  $\Lambda pn$  events, the  $\Lambda p$  invariant mass and the phase space distribution(b) are shown in Fig. 4.2. Figure 4.2(b) is a Dalitz plot of  $T_n^{CM}/Q^{CM}$  and  $(T_p^{CM} - T_\Lambda^{CM})/\sqrt{3}Q^{CM}$ ,

where  $T_n^{CM}$ ,  $T_p^{CM}$  and  $T_\Lambda^{CM}$  are kinetic energy of neutron, proton and  $\Lambda$  in the center of mass system and  $Q^{CM}$  is the  $Q$ -value of the reaction. This Dalitz plot shows almost flat distribution if  $\Lambda pn$  events are distributed uniformly in the phase space. The details of this plot were already described in Section 3.10.

The events in the Dalitz plot indicate two components; one component widely distributed in the three-body phase space uniformly, and the other concentrates at a specific neutron energy corresponding a peak structure near  $K^-pp$  threshold in invariant mass spectrum. We will discuss each component in the following sections.

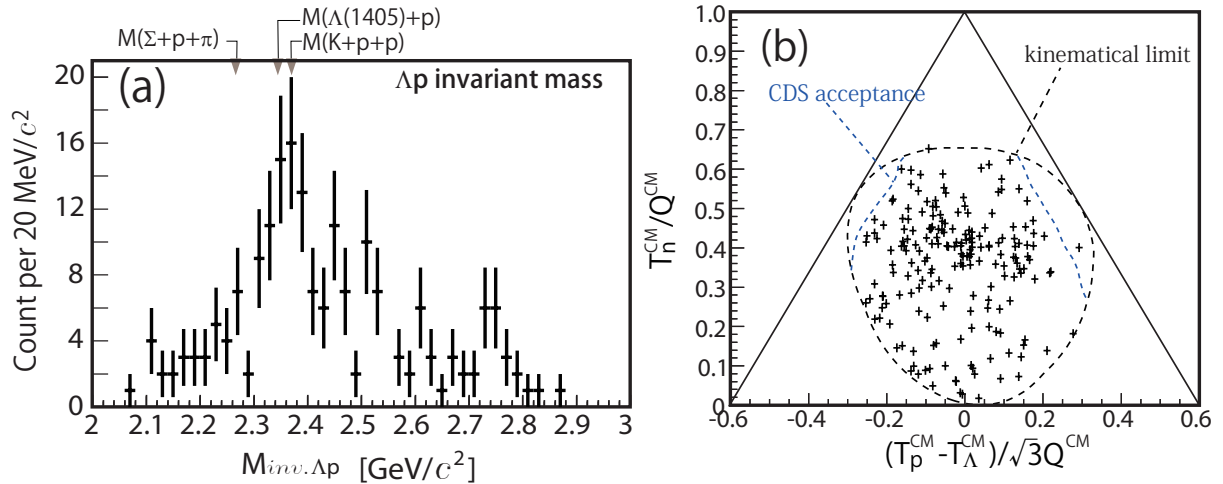


Figure 4.2:  $\Lambda p$  invariant mass(a) distribution and Dalitz plot(b) of the selected  $\Lambda pn$  events

### 4.3 Multi-nucleon absorption of $K^-$

Genuine multi-nucleon absorption of  $K^-$  is an expected process in  ${}^3\text{He}(K^-, \Lambda p)n$  reaction.

Two-nucleon absorption (2NA) process ( $K^-NN \rightarrow \Lambda N$ ) was observed in stopped  $K^-$  absorption reactions in high fraction ( $\sim 20\%$ ). Fig. 4.3 shows the simulation for 2NA events. Apparently, such a component is not prominent in the data. In this analysis, events of 2NA process were generated by flat distribution in the  $\Lambda p$  two body phase space. The Fermi momentum distribution of a spectator neutron was considered as that of a past measurement[84] in offshell, which means that binding energy of  ${}^3\text{He}$  is not considered.

Figure 4.4 shows  $\Lambda p$  invariant mass(a) distribution and Dalitz plot(b) of the simulated three-nucleon absorption of  $K^-$  (3NA) reaction events in which  $\Lambda pn$  are distributed uniformly in the phase space. Events of Fig. 4.4(b) is consistent with the component of the data which is widely distributed in the phase space. This is the first evidence of the three-nucleon absorption in in-flight kaon reactions. However, we observed a significant excess over the smooth phase space distribution near the  $K^-pp$  threshold as shown in Fig. 4.2(a).

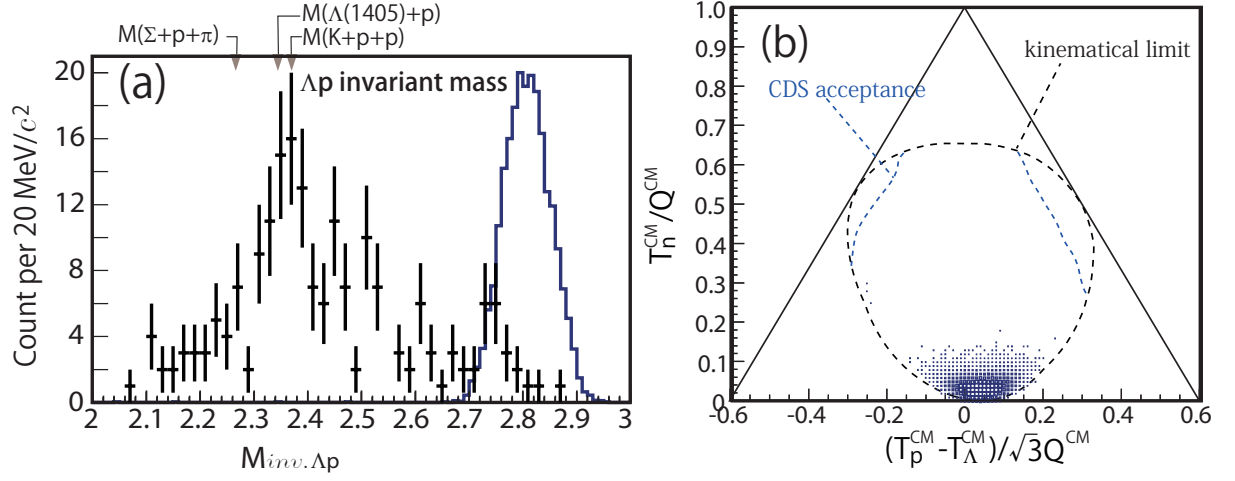
2NA( $\Lambda pn_s$ )Simulation

Figure 4.3:  $\Lambda p$  invariant mass(a) distribution and Dalitz plot(b) of the simulated 2NA events ( $K^- pp \rightarrow \Lambda p$ )

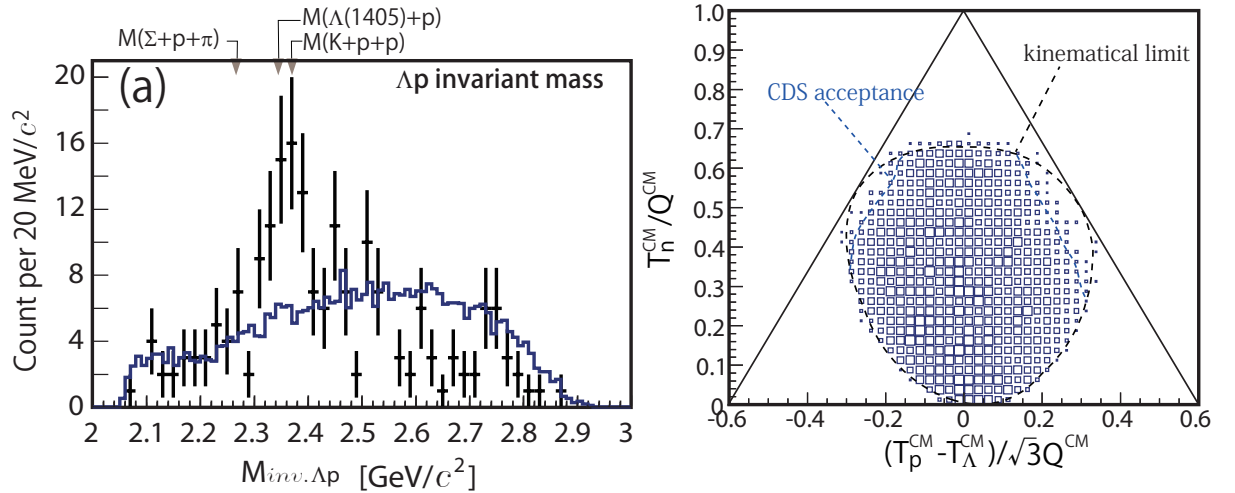
3NA( $\Lambda pn$ )Simulation

Figure 4.4:  $\Lambda p$  invariant mass(a) distribution and Dalitz plot(b) of the simulated 3NA events ( $K^- ppn \rightarrow \Lambda pn$ )

### 4.3.1 Contamination of other processes in “ $\Lambda pn$ ” events

The component widely distributed in the three-body phase space uniformly in the data could be considered as 3NA( $\Lambda pn$ ) process. However, there should be contamination of processes like a  $\Sigma^0 pn$  state in missing neutron region. Because E15 spectrometer is only sensitive to the charged particles, reactions i.e.  ${}^3\text{He}(K^-, \Sigma^0 p)n_{miss.}$ ,  ${}^3\text{He}(K^-, \Lambda^0 p\pi)n_{miss.}$ , will not be distinguished with genuine  ${}^3\text{He}(K^-, \Lambda p)n$  reaction, where  $\Sigma^0 \rightarrow \Lambda\gamma$  will be identified as  $\Lambda$  and  $\pi^0 \rightarrow \gamma\gamma$  cannot be seen in the E15 spectrometer.

Therefore before going into the details of analysis, we study the contaminations in the  $\Lambda pn$  events.

Then, the purity of the  $\Lambda pn$  events in the missing neutron region was estimated by using “multi-channel global fit”. A “multi-channel global fit” was applied simultaneously to the  $\Lambda p$  invariant mass and the missing mass spectra in Fig. 4.1, with simulated physics processes which might contribute to these two spectra, namely multi-nucleon kaon absorption with multi-pion emission. We denoted each process as 2NA( $YNN_s + \#n\pi$ ) and 3NA( $YNN + \#n\pi$ ), where  $Y$  is for  $\Lambda$  or  $\Sigma^0$ ,  $N$  is for nucleon,  $N_s$  is for spectator nucleon, and  $\#n$  is for the number of pions. By fitting invariant mass spectrum simultaneously, information about 2NA contribution can be extracted. Detail of these process is discussed in the following subsection.

### 4.3.2 Simulation study for expected processes in ${}^3\text{He}(K^-, \Lambda p)$ analysis

Study for expected processes in  ${}^3\text{He}(K^-, \Lambda p)$  analysis was performed by simulation to estimate contamination in the  ${}^3\text{He}(K^-, \Lambda p)n_{miss.}$  reaction. Multi-nucleon absorption of Kaon is one of the expected processes. Kaon is absorbed by two or three nucleons (2NA, 3NA) and produced  $\Lambda$  or  $\Sigma^0$ . A list of studied processes are listed in Table 4.1.

Table 4.1: A list of simulated processes expected in  ${}^3\text{He}(K^-, \Lambda p)$  reaction

process name	
2NA ( $\Lambda pn_s$ )	$K^- + NN(N_s) \rightarrow \Lambda pn_s$
2NA ( $\Sigma^0 pn_s$ )	$K^- + NN(N_s) \rightarrow \Sigma^0 pn_s$
2NA ( $\Lambda pn_s + \pi$ )	$K^- + NN(N_s) \rightarrow \Lambda p + \pi n_s$
2NA ( $\Sigma^0 pn_s + \pi$ )	$K^- + NN(N_s) \rightarrow \Sigma^0 p + \pi n_s$
3NA ( $\Lambda pn$ )	$K^- + NNN \rightarrow \Lambda pn$
3NA ( $\Sigma^0 pn$ )	$K^- + NNN \rightarrow \Sigma^0 pn$
3NA ( $\Lambda pn + \pi$ )	$K^- + NNN \rightarrow \Lambda pn + \pi$
3NA ( $\Sigma^0 pn + \pi$ )	$K^- + NNN \rightarrow \Sigma^0 pn + \pi$
3NA ( $\Lambda pn + 2\pi$ )	$K^- + NNN \rightarrow \Lambda pn + 2\pi$
3NA ( $\Sigma^0 pn + 2\pi$ )	$K^- + NNN \rightarrow \Sigma^0 pn + 2\pi$
3NA ( $\Lambda pn + 3\pi$ )	$K^- + NNN \rightarrow \Lambda pn + 3\pi$
3NA ( $\Sigma^0 pn + 3\pi$ )	$K^- + NNN \rightarrow \Sigma^0 pn + 3\pi$

Each process was generated to be flat distribution in the phase space of the final state, as

$$\frac{d^2\sigma_{\text{NA}(Y_{pn+\#\pi})}}{dT_n^{CM}d\cos\theta_n^{CM}} \propto \rho_3(Y_{pn+\#\pi}), \quad (4.1)$$

where  $\sigma_{\text{NA}(Y_{pn+\#\pi})}$  is the simulated event distribution for the particles in final state,  $T_n^{CM}$  is the kinetic energy of the neutron in the CM frame, and  $\cos\theta_n^{CM}$  is the neutron emission angle in the CM frame. If there is a spectator nucleon, the Fermi momentum distribution was considered [84].

Invariant mass and missing mass spectra of each process are shown in Appendix C.

### 4.3.3 Result of Multi-channel global fit

A minimum  $\chi^2$  fit for multi-channel global fit was performed by changing the intensity of each process as free parameters. A list of physics processes, taken into account for the global fit, is shown in Table 4.2, together with the obtained relative yields of each process. The fit result is shown in Fig. 4.5. Two spectra are well described by the processes listed in Table 4.2.  $\chi^2$  and DOF of the fit are 122 and 147, respectively.

Figure 4.5(c) shows a close up view in the missing neutron region. This close up view indicates that the fit result of  $\Lambda pn$  yield is less than the data (about 83 % compared to data). It can be attributed to the contribution of the peak structure, which is not included in the global fit.

From the global fit, it was found that three channels,  $3NA(\Lambda pn)$ ,  $3NA(\Sigma^0 pn)$ , and  $2NA(\Lambda pn_s)$ , contribute in the neutron window ( $n$ -window) at the ratio of 0.62 : 0.20 : 0.01.

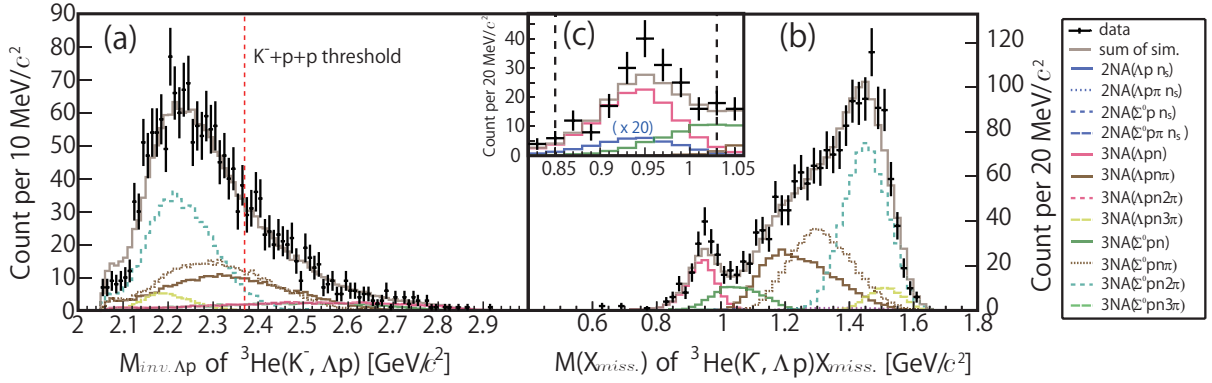


Figure 4.5: Inclusive spectra of the  ${}^3\text{He}(K^-, \Lambda p)$  reaction and the global fit result of simulation with multi-nucleon absorption processes. (a)  $\Lambda p$  invariant mass distribution. (b) missing mass  $M(X_{miss.})$  spectra of  ${}^3\text{He}(K^-, \Lambda p)X_{miss.}$  and (c) the close up view of (b) around the missing neutron region. In Figure (c),  $2NA(\Lambda pn_s)$  is vertically scaled 20 times. The dashed vertical lines in (c) shows the neutron selection gate.

Table 4.2: Relative yield of each component in the global fit, normalized to data (same for each component in the  $n$ -window normalized by the data in the  $n$ -window). Note that the spectral shapes of some reaction channels are quite similar, especially for the channels given in a row.

process	relative yield		process	relative yield	
	all	$n$ -window		all	$n$ -window
$2NA(\Lambda pn_s)$	0.001	0.01	$2NA(\Sigma^0 pn_s)$	$< 10^{-4}$	$< 10^{-2}$
$2NA(\Lambda pn_s + \pi)$	$< 10^{-4}$	$< 10^{-2}$	$2NA(\Sigma^0 pn_s + \pi)$	0.010	$< 10^{-2}$
$3NA(\Lambda pn)$	0.072	0.62	$3NA(\Sigma^0 pn)$	0.058	0.20
$3NA(\Lambda pn + \pi)$	0.199	$< 10^{-2}$	$3NA(\Sigma^0 pn + \pi)$	0.239	$< 10^{-2}$
$3NA(\Lambda pn + 2\pi)$	$< 10^{-4}$	$< 10^{-2}$	$3NA(\Sigma^0 pn + 2\pi)$	0.354	$< 10^{-2}$
$3NA(\Lambda pn + 3\pi)$	0.039	$< 10^{-2}$	$3NA(\Sigma^0 pn + 3\pi)$	$< 10^{-4}$	$< 10^{-2}$

#### 4.3.4 Distribution of the $M_{\Lambda p}$ and $\cos \theta_n^{CM}$

Distribution of the  $\Lambda p$  invariant mass and the calculated neutron emission-angle are shown in Fig. 4.6(b) and (c), together with the scatter plot of the two(a). We also plotted the spectra for multi-nucleon processes with a ratio obtained in “Multichannel global fit” ( $3\text{NA}(\Lambda pn) : 3\text{NA}(\Sigma^0 pn) : 2\text{NA}(\Lambda pn_s) = 0.62 : 0.20 : 0.01$ ) and scaled with total number of  $\Lambda pn$  events ( $\sim 200$ ). As shown in Fig. 4.6(c), the neutrons in the peak structure clearly concentrated at the forward region, where the momentum transfer to the  $\Lambda p$  system ( $\mathbf{q}_{\Lambda p} \equiv \mathbf{p}_{K^-}^{lab} - \mathbf{p}_n^{lab} = \mathbf{p}_{\Lambda}^{lab} + \mathbf{p}_p^{lab}$ ) is minimum. Figure 4.7 shows a scatter plot of the distribution of the  $\Lambda p$  invariant mass and the momentum transfer to the  $\Lambda p$ . The excess is concentrated in low momentum transfer region ( $< 0.4$  MeV/c). Fitting result indicates the component widely distributed in the three-body phase space can be explained by 3NA processes and there is the excess which has a peak structure in  $\Lambda p$  invariant mass spectrum.

A  $\chi^2$  comparative test was performed in the  $\Lambda p$  invariant mass and neutron emission-angle spectra with a ratio obtained in “Multichannel global fit” ( $3\text{NA}(\Lambda pn) : 3\text{NA}(\Sigma^0 pn) : 2\text{NA}(\Lambda pn_s) = 0.62 : 0.20 : 0.01$ ) to confirm the existence of the peak structure. The values obtained for  $\chi^2 / \text{ndf}$  in Fig. 4.6(b) and (c) are 135 / 43, and 138 / 76, respectively. This large  $\chi^2$  values resulted the existence of the peak structure on multi-nucleons absorption processes.

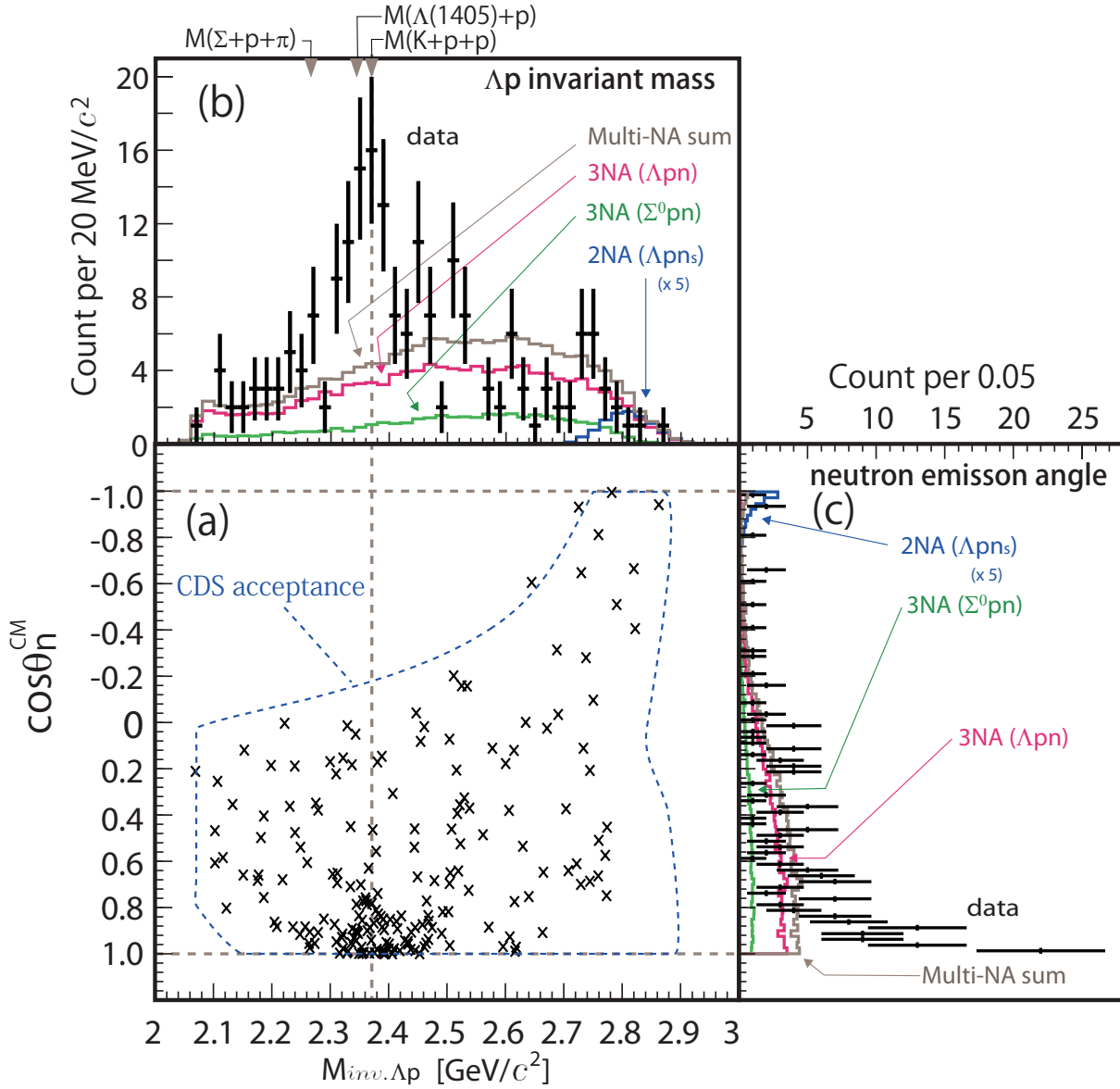


Figure 4.6: (a) 2-D distribution of the  $\Lambda p$  invariant-mass and the emission-angle of the missing neutron. The blue dashed lines shows crude CDS acceptance boundary for the  $\Lambda pn$  events. (b)  $\Lambda p$  invariant mass with simulated spectra obtained in the global fit in the neutron window. (c) Angular distribution of the missing neutron, kinematically reconstructed, as a function of  $\cos \theta_n^{CM}$ . The histograms show the contributions of the three remaining channels in the  $n$ -window, considered in the global fit.

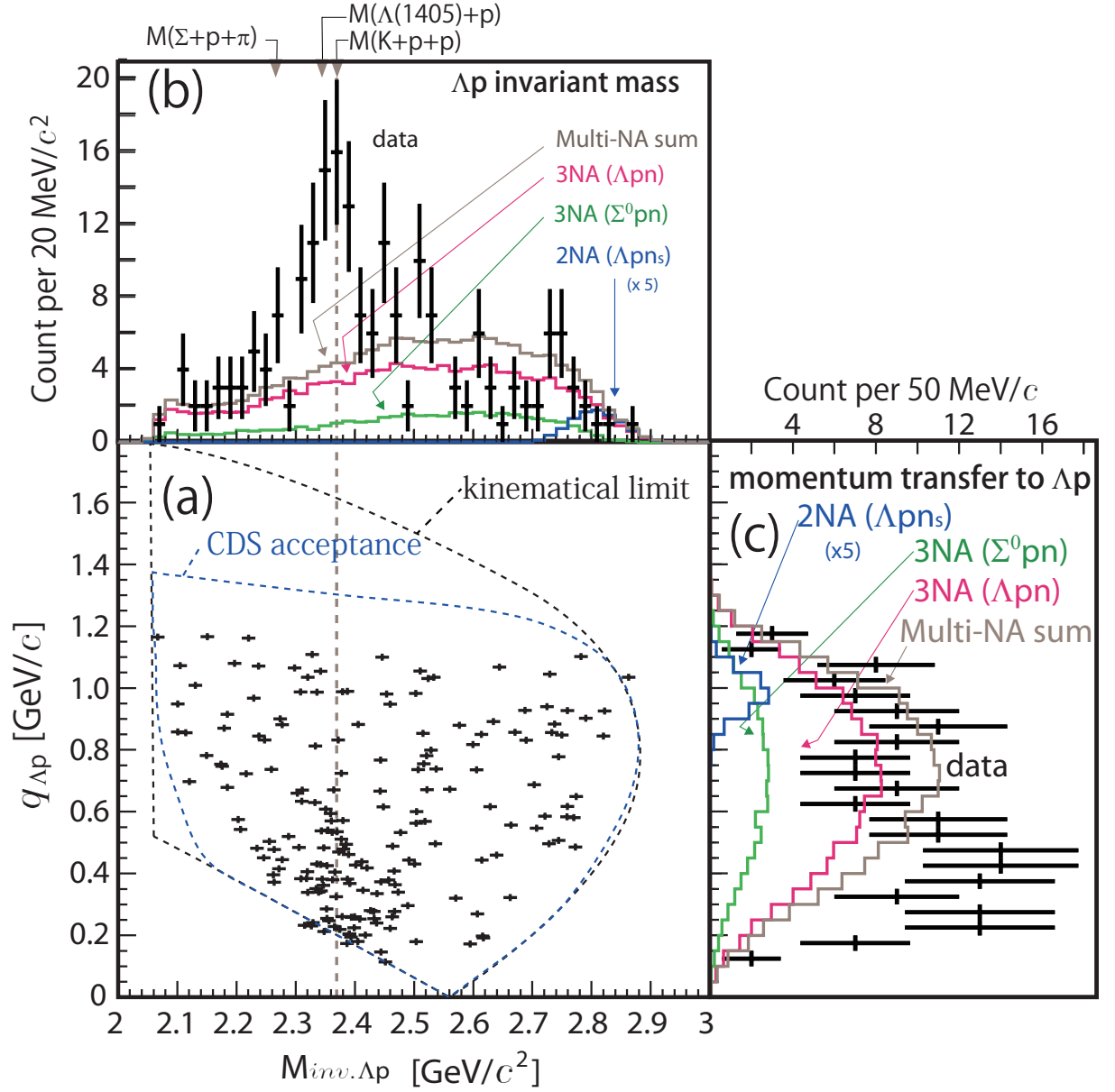


Figure 4.7: (a) 2-D distribution of the  $\Delta p$  invariant mass and the momentum transfer to  $\Delta p$ . (b) the fit result of the  $\Delta p$  invariant mass spectrum. (c) distribution of the momentum transfer to  $\Delta p$  and the fit results of simulation.

## 4.4 Candidates for the peak structure

Here we discuss possible interpretations for this excess in the data.

### 4.4.1 Scattered $\bar{K}$ absorption ( $K^-N \rightarrow \bar{K}N$ following $\bar{K}NN \rightarrow \Lambda p$ )

If scattered  $\bar{K}$ s coming from quasi-free reaction ( $K^-N \rightarrow \bar{K}N$ ) are absorbed by two nucleons, a peak structure is generated as shown in Fig. 4.8. Here we assumed the  $\bar{K}$  at the intermediate stage is on-mass shell. Angular distribution of the  $K^-N$  quasi-free reaction was generated as in the past experimental data [85]. The two body phase space of  $\Lambda p$  generated with absorption of the scattered  $\bar{K}$  was uniform in this simulation. However, the peak position is higher than  $K^-pp$  threshold and not consistent with the data's one.

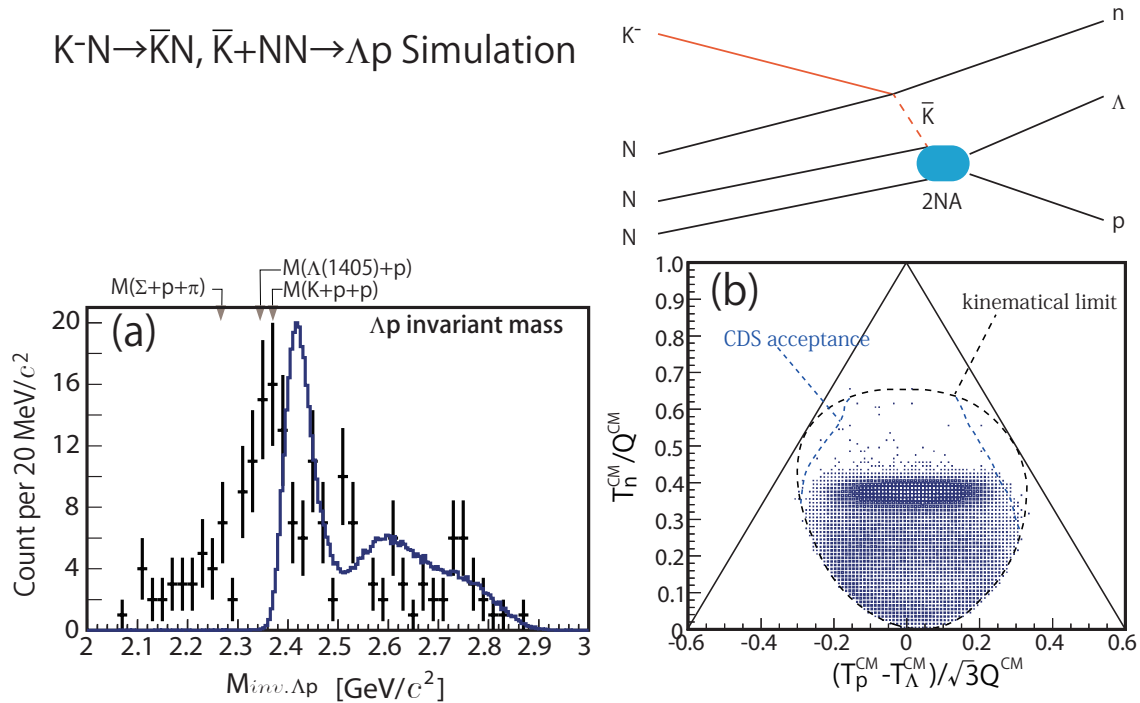


Figure 4.8:  $\Lambda p$  invariant mass(a) distribution and Dalitz plot(b) of the simulated scattered  $\bar{K}$  absorption events

### 4.4.2 $2NA + \Sigma\Lambda$ conversion ( $K^-NN \rightarrow \Sigma N$ following $\Sigma N \rightarrow \Lambda p$ )

$2NA + \Sigma\Lambda$  conversion is a 2-step reaction as  $K^-N \rightarrow \bar{K}N$  following  $\bar{K}N_s N_s \rightarrow \Lambda p$ . Final states of each step were generated as phase space uniformly. When  $\Sigma$  is converted with spectator neutron, a peak structure is seen in  $\Lambda p$  invariant mass distribution. This peak position is too low compared with the observed peak as shown in Fig. 4.9.

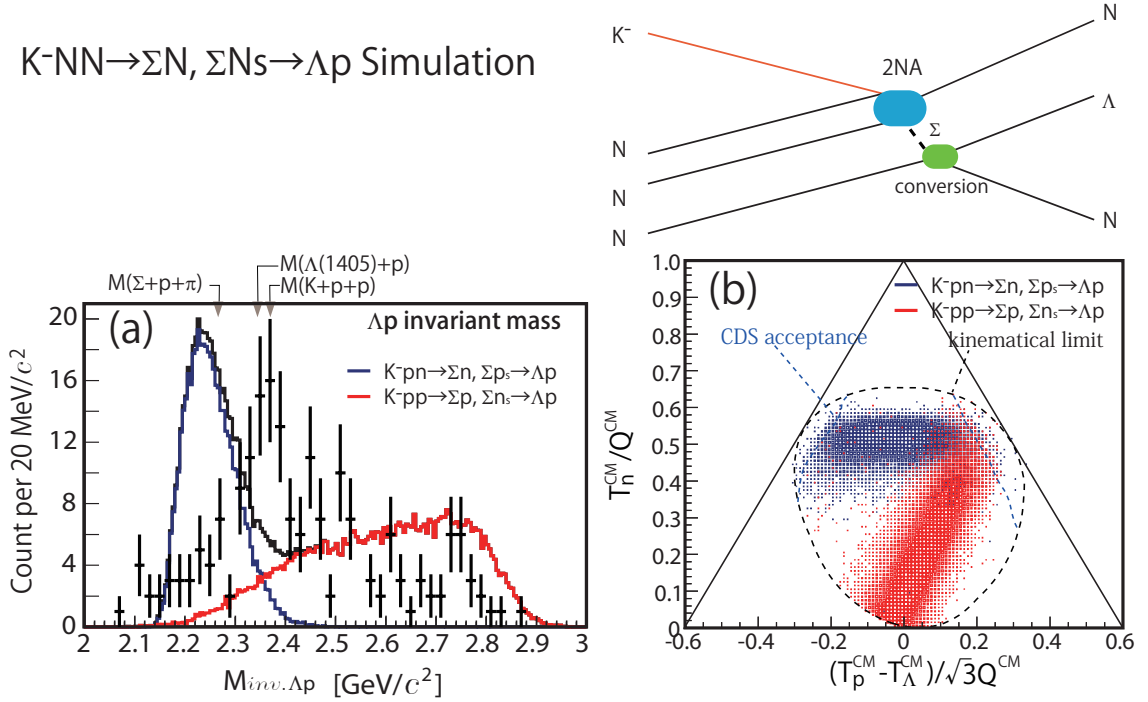


Figure 4.9:  $\Lambda p$  invariant mass(a) distribution and Dalitz plot(b) of the simulated  $\Sigma\Lambda$  conversion events

#### 4.4.3 $\Lambda(1405)\Lambda$ conversion ( $K^-NN \rightarrow Y^*N$ following $Y^*N_s \rightarrow \Lambda p$ )

$\Lambda(1405)\Lambda$  conversion is a 2-step reaction like  $\Sigma\Lambda$  conversion. A treatment of the final states of each step was also same as  $\Sigma\Lambda$  conversion process. We assumed mass and full width of  $\Lambda(1405)$  are 1405 MeV/ $c^2$  and 50.5 MeV, respectively taken from the Particle Data Group. This peak position is very near the observed one, but slightly heavier than it. In addition, there is no component of conversion of  $\Lambda(1405)$  and spectator neutron as shown with the red points in Fig. 4.10 in the data.

#### 4.4.4 Deeply bound $\bar{K}NN$ state

The  $\bar{K}NN$  state with B.E = 100 and  $\Gamma = 100$  MeV, were observed in FINUDA[44], DISTO[46], and E27[54] experiments. Both production and decay to  $\Lambda p$  were assumed as S-wave. The peak position is 2237 MeV/ $c^2$ , which is much lower than the observed peak position in this analysis.

If  $\bar{K}NN$  decay to  $\Sigma^0 p \rightarrow \Lambda p \gamma$ , a peak in  $\Lambda p$  invariant mass is shifted to lower mass region due to the missing  $\gamma$ .

In summary, it is difficult to explain the peak structure in the data with these simple candidates. Then, in the following section, we assumed new assumption to explain the peak structure.

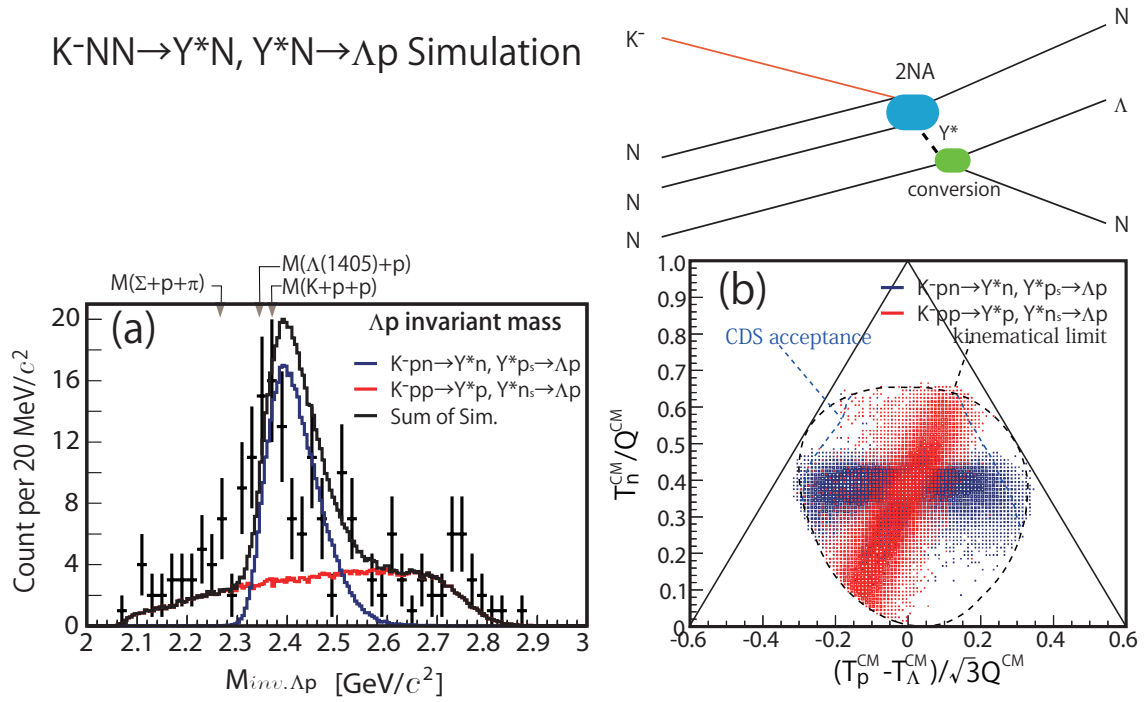


Figure 4.10:  $\Lambda p$  invariant mass(a) distribution and Dalitz plot(b) of the simulated  $\Lambda(1405)\Lambda$  conversion events

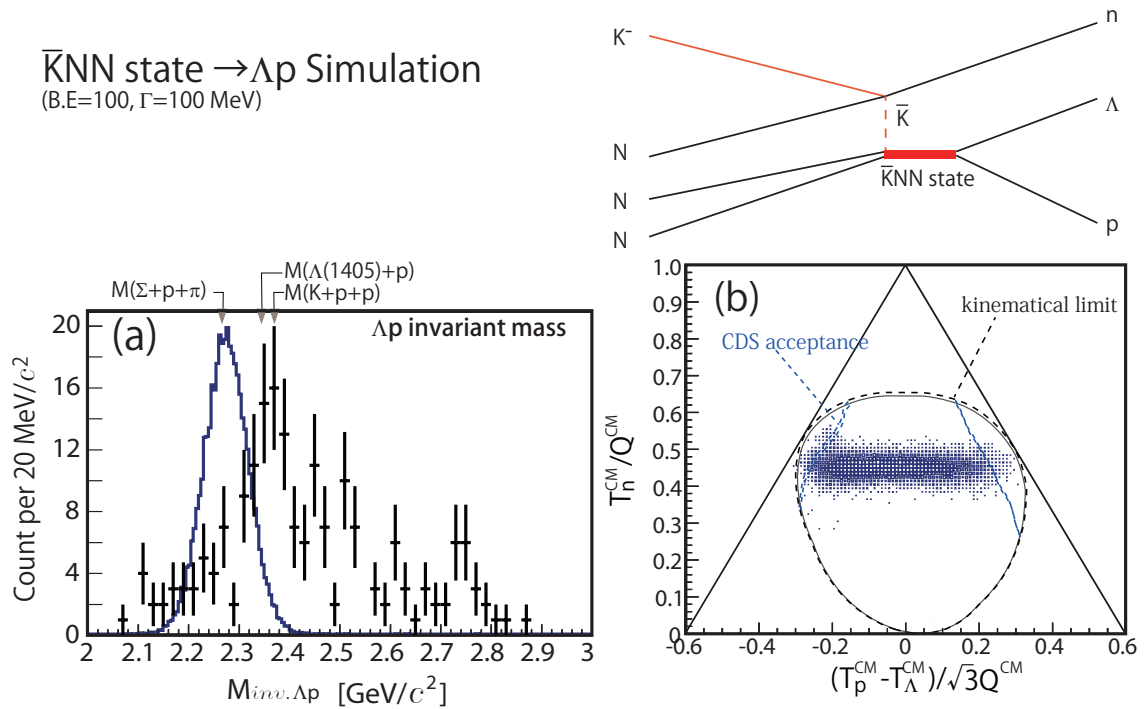


Figure 4.11:  $\Lambda p$  invariant mass(a) distribution and Dalitz plot(b) of the simulated deeply bound  $\bar{K}NN$  state(B.E = 100,  $\Gamma = 100$  MeV) events

## 4.5 S-wave single-pole structure

To explain the peak structures in the  $\Lambda pn$  events which can not be explained with known processes, the existence of a simple finite-size S-wave single-pole structure over the three-body phase space which decays to  $\Lambda p$  in the final state is assumed. Both of the peak structure in  $\Lambda p$  invariant mass spectrum and excess in low momentum transfer ( $q_{\Lambda p}$ ) region should be explained simultaneously. Thus the formation cross-section ( $\sigma_X$ ) of the pole is assumed as:

$$\frac{d^2\sigma_X}{dM_{inv.\Lambda p}dq_{\Lambda p}} \propto \rho_3(\Lambda pn) \times \frac{(\Gamma_X/2)^2}{(M_{\Lambda p} - M_X)^2 + (\Gamma_X/2)^2} \times |\exp(-q_{\Lambda p}^2/2Q_X^2)|^2, \quad (4.2)$$

where  $M_{\Lambda p}$  is the invariant mass of  $\Lambda p$ ,  $q_{\Lambda p}$  is the momentum transfer of the reaction ( $q_{\Lambda p} = |\mathbf{p}_\Lambda + \mathbf{p}_p|$ ),  $M_X$  is the energy,  $\Gamma_X$  is the decay-width, and  $Q_X$  is a free parameter which can be interpreted as the form factor parameter of the pole. The first term in the formula is the three-body Lorentz-invariant phase space of  $\Lambda pn$ , the second the Breit-Wigner formula, and the third the square of the form-factor, which can be also interpreted as the sticking probability of a plain-wave having  $q_{\Lambda p}$  to a harmonic oscillator having finite size  $\approx \hbar/Q_X$ .

We generated events according to Eq.4.2 in the simulation with various values of  $M_{\Lambda p}$ ,  $\Gamma_X$  and  $Q_X$ . A  $\chi^2$  comparative test was made between the experimental data and the simulated pole together with the multi-nucleon absorption processes. We fitted the spectra keeping the yields of  $3NA(\Lambda pn)$  and single-pole as a free parameters, because we introduced a new pole, which decays to the  $\Lambda p$  final state. The other two yields for  $3NA(\Sigma^0 pn)$  and  $2NA(\Lambda pn_s)$  are fixed as 0.20 : 0.01 for total yield of the data which are given by the global fit. We first assumed  $Q_X = \infty$  and made a two-dimensional  $\chi^2$  map on the  $M_X$  and  $\Gamma_X$  plane to define the minimum  $\chi^2$  for the invariant mass spectra. Then,  $Q_X$  is chosen to have minimum  $\chi^2$  for the momentum transfer distribution, at a given  $M_X$  and  $\Gamma_X$ . This process was iterated until the parameters converged. The two-dimensional  $\chi^2$  map as a function of the  $M_X$  and  $\Gamma_X$  is shown in Fig. 4.12(a). Figure 4.12(b) plots  $\chi^2$  as a function of momentum transfer. The minimum  $\chi^2$  point is at  $M_X = 2355_{-8}^{+6}$  (stat.)  $\pm 12$  (syst.) MeV/c<sup>2</sup>, intrinsic  $\Gamma_X = 110_{-17}^{+19}$  (stat.)  $\pm 27$  (syst.) MeV/c<sup>2</sup>, and  $Q_X = 400_{-40}^{+60}$  (stat.) MeV/c. The statistical error is defined as  $\chi_{min}^2 + 1$  contour. The systematic uncertainties are evaluated by considering the magnetic field strength in the CDS, the likelihood threshold to select the  $\Lambda p$  pair, and binning of the invariant mass spectra listed in Table. 4.3. The fit results are shown in Fig. 4.13. The values obtained for  $\chi^2 / \text{DOF}$  in Fig. 4.13(b) and (c) are 68 / 45, and 23 / 27, respectively. By assuming new pole, we can explain both spectra of  $\Lambda p$  invariant mass and momentum transfer to  $\Lambda p$ , simultaneously.

Table 4.3: The list of systematic uncertainty of mono-pole structure.

Source	Uncertainty	
	mass[MeV/c <sup>2</sup> ]	full width[MeV/c <sup>2</sup> ]
magnetic field	3.5	-
likelihood threshold	6.1	15
fitting (binding)	9.7	21.7
total	12	27

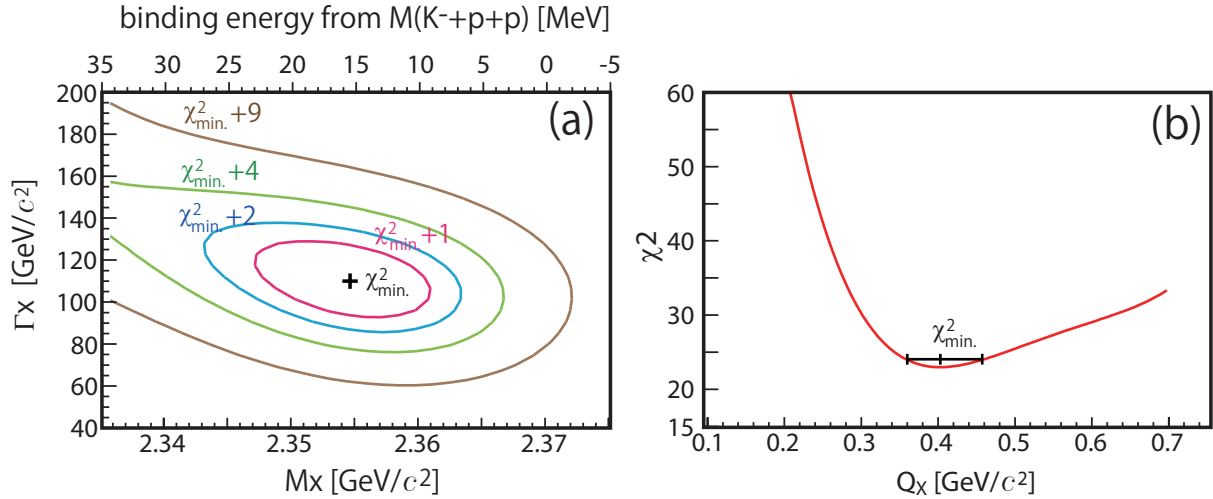


Figure 4.12: (a) two dimensional  $\chi^2$  map of mass and width of pole structure. (b)  $\chi^2$  change as a function of  $Q_X$ .

#### 4.5.1 Total cross section of each process

To obtain the cross section, one needs to know the detailed event distribution and the acceptance. If we assume that all the angular distributions can be given by the fit result, so the acceptance correction can be applied under this assumption. The cross sections can be evaluated as a following equation;

$$\sigma_{process}^{total} = \frac{1}{L} \frac{N_{process}}{\Omega_{process} \epsilon}, \quad (4.3)$$

$$\epsilon = (\epsilon_{tracking})^3 \times \epsilon_{DAQ} \times \epsilon_{trig.} \times 1/C_{prescale}, \quad (4.4)$$

where  $L$  is effective luminosity  $546 \mu b^{-1}$ ,  $N_{process}$  is the number of each process,  $\Omega_{process}$  is the overall detection efficiency of each process including the acceptance,  $\epsilon_{tracking}$  is the efficiency of the CDS tracking,  $\epsilon_{DAQ}$  is DAQ efficiency,  $\epsilon_{trig.}$  is trigger efficiency, and  $C_{prescale}$  is pre-scale factor of the trigger. Total cross sections were obtained to be, resonance pole :  $7 \pm 1 \mu b$ ,  $3NA(\Lambda pn)$  :  $17 \pm 2 \mu b$ , and  $2NA(\Lambda pn_s)$  :  $0.8_{-0.8}^{+2.7} \mu b$ . If we rely on the global fit and event distribution outside of the neutron window, then we can also determine the  $3NA(\Sigma^0 pn)$  cross section to be  $28 \pm 5 \mu b$  in total. Errors were mainly statistical ones due to limited statistics of each process. The existence of 3NA channel is already quite interesting, because it seems to follow simple phase space as in Eq. 3.16. In contrast, absorption by two nucleons is rather weak compared to three nucleons. The ratio of  $2NA(\Lambda pn_s)/3NA(\Lambda pn)$  is found to be 0.05 or less.

There could be many interpretations for the pole found in the  $\Lambda p$  invariant mass distribution in the  ${}^3\text{He}(K^-, \Lambda p)n_{miss.}$  reaction channel at  $p_K = 1 \text{ GeV}/c$ , even if the simplest present assumption of Eq. 4.2 is valid. A naïve interpretation of the pole would be a  $\bar{K}NN$  bound state, since the pole position is located below the  $M(K^- + p + p)$  threshold of 2370  $\text{MeV}/c^2$ . It could also be a shallow bound or unbound resonance of the  $Y^*p$  system, because the  $Y^*p$  threshold is located at 2343  $\text{MeV}/c^2$  (assuming  $Y^* = \Lambda(1405)$  at 1405  $\text{MeV}/c^2$ ).

However, there is no clear discrimination between the two interpretations given above, if we assume  $\Lambda(1405)$  to be a  $K^-p$  bound state.

The  $Q_X$  of  $\sim 400$  MeV/ $c$  is rather large compared to the Fermi-motion in light nuclei by about 100 MeV/ $c$ , and it implies a short interaction range of about 0.5 fm[86].

It should be noted that the pole position is close to the two threshold energies,  $M(K^- + p + p)$  and  $M(\Lambda(1405) + p)$  and  $M(\Sigma(1385) + p)$ , thus the symmetric Breit-Wigner formula could be too simple. For example, the  $\bar{K}NN$ -decay channel opens at the  $K^-pp$  threshold, so the spectral function observed in the  $\Lambda p$ -decay channel could be suppressed above the corresponding thresholds.

A recent calculation by T. Sekihara, E. Oset, and A. Ramos [87] claims that there is a two peak structure in our peak. Two peak structure in the  $\Lambda p$  invariant mass was generated by a quasi-elastic in the first collision of kaon with a nucleon, and the production of the  $\bar{K}NN$  bound state. Detail was described in Appendix D.

There might be totally different approach to account for the peak structure. About  $2NA + Y^*N \rightarrow \Lambda N$  conversion (described in Sec. 4.4.3), we assumed  $2NA$  in first step occurs in both  $K^-pn \rightarrow Y^*n$ ,  $K^-pp \rightarrow Y^*p$  channel and produced in the two-body phase space uniform. However, if  $2NA$  occurs in only  $K^-pn \rightarrow Y^*n$  channel and a neutron in  $2NA$  is emitted only very forward angle, a peak-like structure like the observed one is produced. In this case, the peak position naturally depends on the momentum transfer as  $M_X(q_{\Lambda p})$  (or  $\cos\theta_n^{CM}$ ). Although the statistics is limited, there is no clear hint of momentum dependence of the peak structure as shown both in Fig. 4.6 and Fig. 4.13.

On the other hand, there is no clear structure in deeply bound region of  $\bar{K}NN$  of which binding energy about 100 MeV, although the statistics is limited to conclude.

We found the peak structure near the  $K^- + p + p$  threshold. Although other interpretations are still remained, this observed peak can be considered as a weakly bound state of the  $\bar{K}NN$ . Figure 4.14 shows this result and theoretical calculations and past experimental results. Observed binding energy is consistent with theoretical calculations with SU(3) potential, but mass width is rather larger than theoretical ones. It can be considered due to too simple assumption as single pole. Observed peak structure may have a component from a quasi-elastic in the first collision of kaon with a nucleon which T. Sekihara, E. Oset, and A. Ramos claims [87]. However, a relation between this peak structure and the deeply bound  $\bar{K}NN$  observed in past experiments is not clear. To clear these issues, we consider that the following measurement is important.

- Mesonic channel( $\pi\Sigma N$ ) of the  $\bar{K}NN$  state,
- Spin-parity measurement.

Mesonic channel of the  $\bar{K}NN$  state should be open if the  $\bar{K}NN$  state is weakly bound ( $< \sim 100$  MeV). Many theoretical calculations assumed this channel decay, but there is no experimental measurement. To measure mesonic channel(i.e.  $\pi^\pm\Sigma^\mp p \rightarrow \pi^\pm\pi^\mp np$  or  $\pi^0\Sigma^0 p \rightarrow \gamma\gamma\Lambda\gamma p$ ), detectors for neutral particles is necessary. Identification of spin-parity of the peak is also important. For example, angular distribution of decay plane of the  $\bar{K}NN$  might give us information for spin-parity.

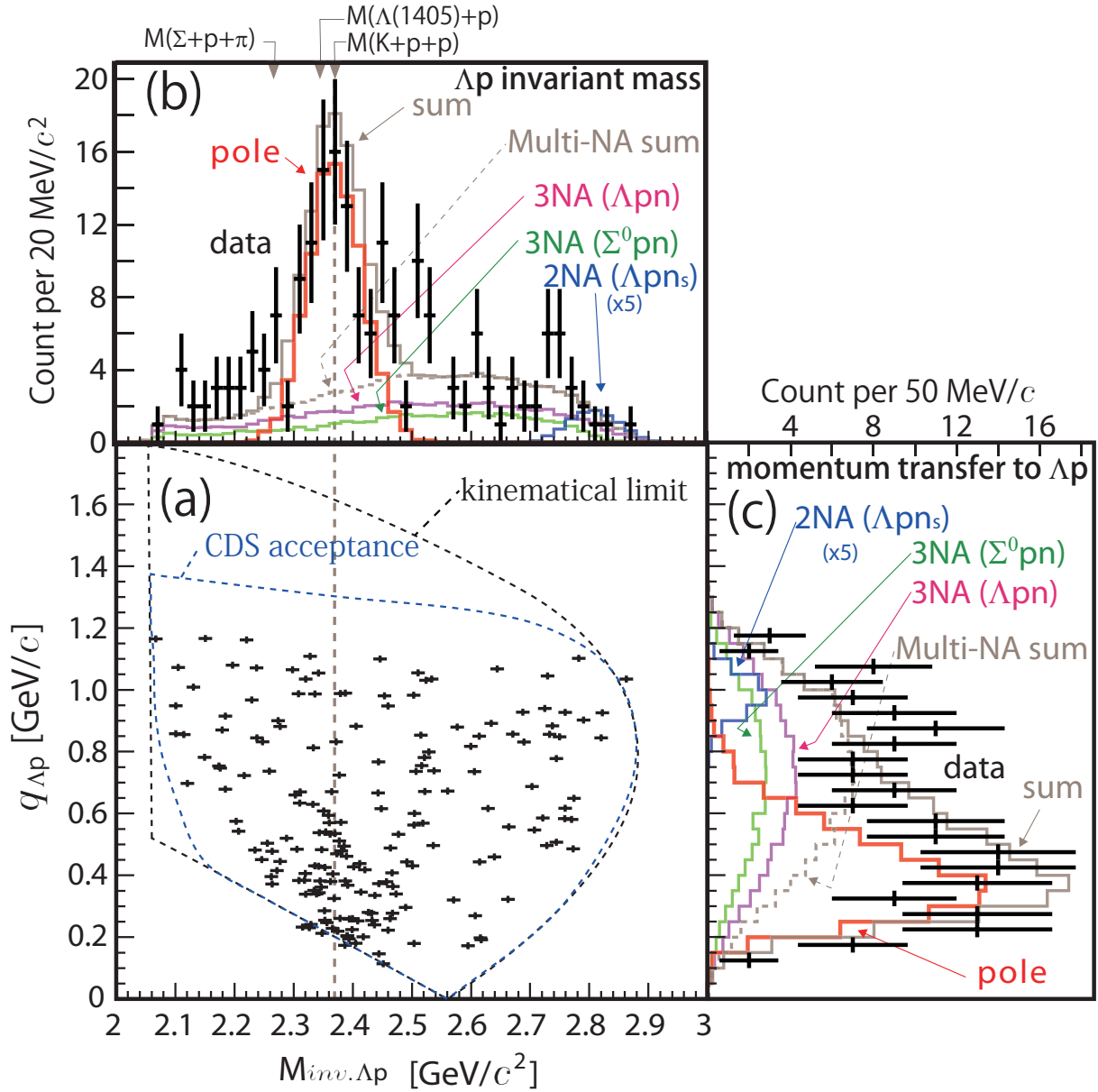


Figure 4.13: (a) 2-D distribution of the  $\Lambda p$  invariant mass and the momentum transfer to  $\Lambda p$ . (b) the fit result of the  $\Lambda p$  invariant mass spectrum. (c) distribution of the momentum transfer to  $\Lambda p$  and the fit results of simulation.

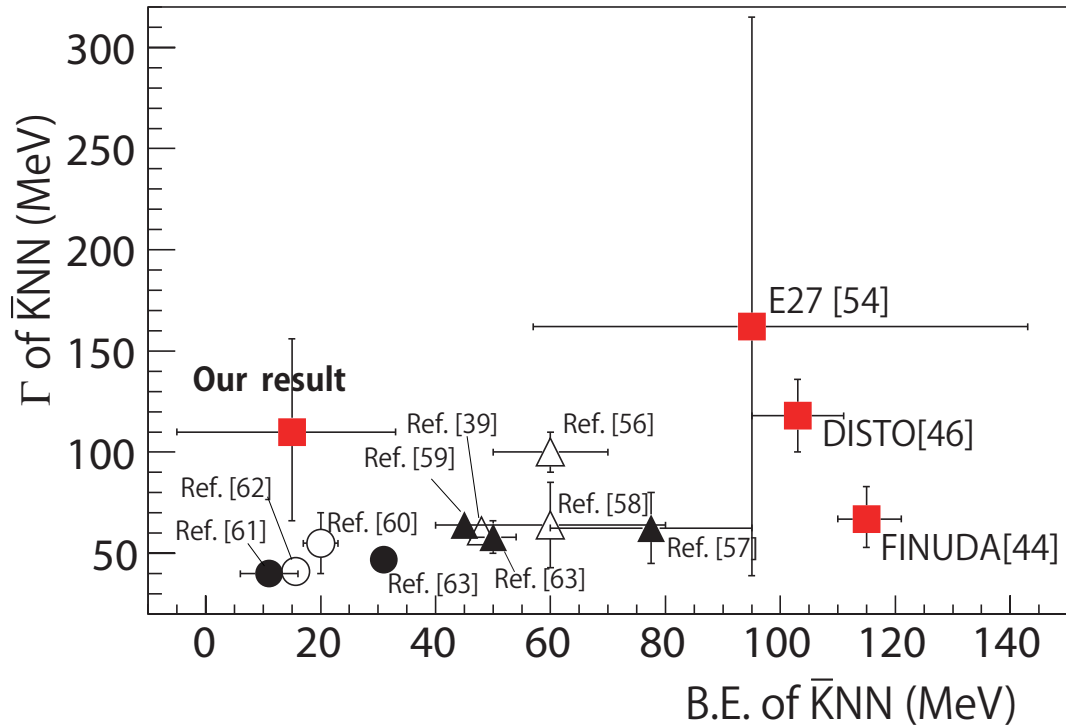


Figure 4.14: 2D plot of B.E.s and  $\Gamma$  of  $\bar{K}NN$  state calculated and observed in the past experiments and our result. Theoretical calculations with the phenomenological potential are plotted by circle, and them with the chiral SU(3) potential are plotted by triangles. Variational model calculations are colored white and Faddeev model calculations are colored black. Red squares show experimental results. Error bars are sum of statistic and systematic ones.



# Chapter 5

## Conclusion

The  ${}^3\text{He}(K^-, \Lambda p)n_{\text{miss}}$  reaction has been studied with an incident  $K^-$  momentum of 1.0 GeV/ $c$  for the first time in J-PARC E15 experiment. The primary purpose of the experiment is to search for the  $\bar{K}NN$  bound state, the simplest bound state of anti-kaon with two nucleons by the strong interaction. The existence of such state is theoretically predicted based on the strongly attractive interaction of  $\bar{K}N$  in  $I = 0$  channel. The data was obtained in the year 2013 for about 90 hours, corresponding to  $3.4 \times 10^9$  effective kaons on the target. The  $\Lambda$  and proton were detected with a cylindrical detector system(CDS) which covered from 49 to 131 degrees in the Lab., about 66% of  $4\pi$ . The detection threshold of pions and proton were  $\sim 30$  MeV/ $c$  and  $\sim 120$  MeV/ $c$  in the CDS region.

The missing neutron was clearly identified in the missing-mass spectrum of X in the  ${}^3\text{He}(K^-, \Lambda p)X$  with a mass resolution of 45 MeV and  $K^-ppn \rightarrow \Lambda + p + n$  events were identified. From the Dalitz plot of  $\Lambda + p + n$  events, we can identify two components; one component widely distributed in the three-body phase space uniformly, another concentrates at a specific neutron energy in the forward direction in a low momentum transfer to the  $\Lambda p$  system.

The former one is the first evidence of genuine three-nucleon absorption following the three-body phase space. The existence of this channel is already quite interesting, because it seems to follow simple phase space. We found that the total cross section of genuine three-nucleon absorption to be  $17 \pm 2 \mu\text{b}$ .

For the latter component, the  $\Lambda p$  invariant mass distribution showed a peak structure near the  $K^-pp$  threshold in the low momentum-transfer to the  $\Lambda p$  system. This structure can not be explained with known simple processes. Then, we have fitted with single-pole assumption, a Breit-Wigner type s-wave resonance introducing a gaussian form factor. Fit results show that the pole has a mass of  $2355^{+6}_{-8}$  (stat.)  $\pm 12$  (syst.) MeV/ $c^2$  and a width of  $110^{+19}_{-17}$  (stat.)  $\pm 27$  (syst.) MeV/ $c^2$ , respectively, and a form factor parameter  $Q_x$  of 400 MeV/ $c$ . This single-pole structure could be interpreted as a weakly bound  $\bar{K}NN$  state.



# Acknowledgment

I would like to express my sincere gratitude to Prof. T. Nagae. He is my supervisor since I was master course student in Kyoto University and the co-spokesperson of the present experiment. He always gave me the fruitful suggestions even after I left Kyoto University. I would have not been able to complete this work without his shrewd advice and suggestions.

I gratefully acknowledge Prof. M. Iwasaki, who is a leader of “Advanced Meson Science Laboratory” in RIKEN and the co-spokesperson of the present experiment. I belonged to his group during doctor course and has been encouraged, advised, and supported by him. Especially, his great support when I published a paper encouraged me.

I wish to acknowledge Prof. Y. Yosoi for his support during the period I belong to the “Research Center for Nuclear Physics” (RCNP).

I would like to express my great thanks to Dr. H. Fujioka. He always gave me comments and advices since I was master course student. In particular, it helped me greatly that he gave me comments about almost all my presentation files.

I wish to acknowledged all the J-PARC E15 collaborators. I express my thanks to Dr. Ohishi, Dr. Sakuma, Dr. M. Sato, Dr. M. Iio, Dr. Tsukada Dr. H. Outa and Dr. Y. Ma for their helpful advices at every stage of the experiment. I learned so many experimental techniques and analysis methods from them. I also would like to express my thanks to Prof. G. Beer and Prof. C. Curceanu for their advices and the intensive correction of the English expressions in the published article. I would like to thank to Prof. H. Noumi and Dr. K. Shirotori for their supports and advices in RCNP. I would like to thank Mr. S. Enomoto, Mr. M. Tokuda, Dr. T. Hashimoto, Mr. K. Inoue, Dr. S. Kawasaki and Mr. T. Yamaga, who worked with in J-PARC. I could enjoy a life in Tokai, J-PARC with them.

I have spent my graduate school days as a member of the “Experimental Nuclear and Hadron Physics Laboratory (NH)” in Kyoto University. I would like to express my thanks to Prof. T. Kawabata, Dr. T. Murakami, and Dr. M. Niiyama for the advices and encouragements. Prof. T. Kawabata gave me comments and advices about both the experiment and private. Dr. T. Murakami always care about progress of my work and myself. Dr. M. Niiyama support my work in the RCNP and advised and encouraged me. I thank to Dr. M. Moritsu and Dr. A. Tokiyasu, who are senior colleague. They lectured me experimental techniques at first time and gave many advices form a view of students. Mr. S. Adachi, Dr. H. Asano, Mr. M. Sako, and Dr. H. Sugimura. are my colleague who entered Kyoto University in the same year. I enjoyed discussion with them and shared the same hardship.

I would like to thank the Hadron beam channel group, accelerator group, and cryogenics section in J-PARC for their great and continuous efforts on stable machine operation and beam quality improvement. We have performed the present experiment successfully to overcome the earth quark in 2011, owing to the staffs of J-PARC and KEK. Especially, I

would like to acknowledge Prof. T. Takahashi and Prof. M. Ieiri for supports of planing the schedule of beam time.

Finally, I express my appreciation to my wife Saki, my dear daughter Azusa, my parents Izumi and Etsuko, and my sister Ayumi for their lasting assistance and encouragements.

# Appendix A

## Target system

### A.1 Mechanism of cooling

The components of cooling system was made of three parts: a  $^4\text{He}$  separator, a  $^4\text{He}$  evaporator, and a heat exchanger between  $^3\text{He}$  and  $^4\text{He}$ . A 1 m long pipes were located between the heat exchanger and the target cell. A liquid nitrogen tank ( $\text{LN}^2$  tank) covered all low-temperature component to reduce the radiation of infrared light from the room temperature parts.

The  $^4\text{He}$  evaporator generated a cooling power with a rotary pump. A pumping speed of the rotary pump was  $120 \text{ m}^3/\text{h}$  and a heat-removal capability was  $2.5 \text{ W}$  at  $2 \text{ K}$ . The heat of  $^3\text{He}$  gas was translated with the heat exchanger and  $^3\text{He}$  gas was liquefied. The flow of  $^3\text{He}$  gas was controlled by a gas-tight handling system. The leak rate of  $^3\text{He}$  gas was less than  $10^{-10} \text{ Pa}\cdot\text{m}/\text{sec}$ . The “siphon method”, which used a convection of the liquid, was used for the heat transport to the target cell 1 m apart from the heat exchanger. The cooled  $^3\text{He}$  liquid by the heat exchanger went and fed the target cell though a lower pipe and the warmed  $^3\text{He}$  liquid (by the heater inside the cell) returned to the heat exchanger though an upper pipe. Details of this method is described in [73].

### A.2 Performance of the operation

It took about 6 hours to liquify the  $^3\text{He}$  gas in the heat exchanger and achieved thermal equilibrium about  $1.4 \text{ K}$  from the liquid nitrogen temperature. Figure A.2(left) shows the stability of the temperature at the target cell during the experiment. The spike structures in the figure are due to the work to refilling the  $^4\text{He}$  liquid to the evaporator.  $^4\text{He}$  liquid should be refilled once per 24 hours. The work refilling the  $^4\text{He}$  liquid and recovery time to thermal equilibrium took  $\sim 1$  hour.  $^4\text{He}$  liquid at  $4.2 \text{ K}$  was transported to the evaporator through the separator, which was closed off during the normal operation. In the data taking period, the temperature was in the range  $1.37$  to  $1.44 \text{ K}$ , which corresponds to the density fluctuation of liquid  $^3\text{He}$  is estimated to be about  $0.2 \%$  as the density and temperature correlation curve for  $^3\text{He}$ , which is shown in Fig. A.2(right) [74]. The equilibrium temperature was  $\sim 1.4 \text{ K}$ , which is about  $0.1 \text{ K}$  higher than that of the test operation [73]. Therefore, it was also taken into account for the uncertainty of the density of  $^3\text{He}$ . The density of  $^3\text{He}$  liquid target in

the experimental period is evaluated to be  $0.0810 \pm 0.0002 \text{ g/cm}^3$ , which corresponds to  $1.11 \text{ g/cm}^2$  thickness for the 138 mm beam direction length. The temperature difference between the evaporator, the heat exchanger, and the target cell were less than 0.01 K. It means that the “siphon method” was worked well. The heat load of the low-temperature region was found to be 0.21 W from the reduction rate of the liquid  $^4\text{He}$  in the evaporator. The details of the operational values of the target system are summarized in Table A.1.

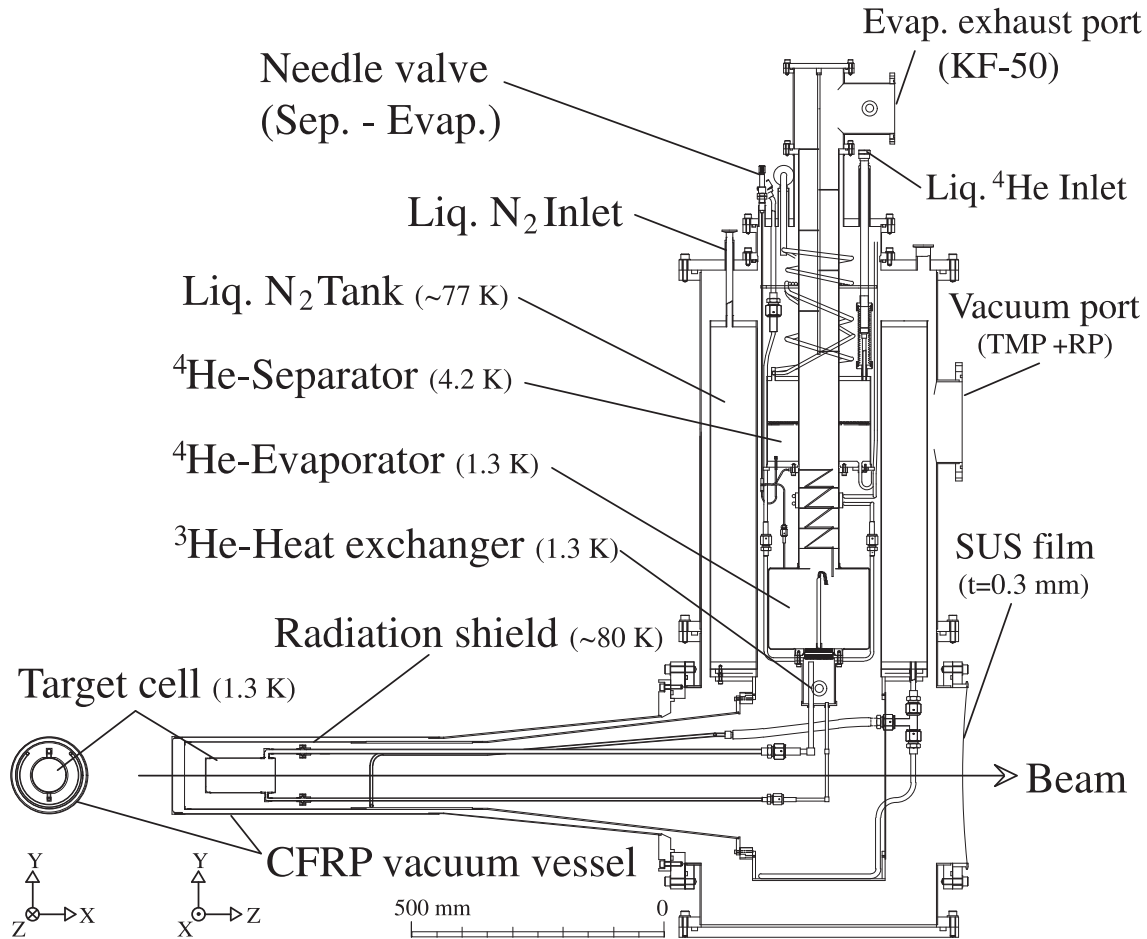


Figure A.1: Schematic view of the target system.

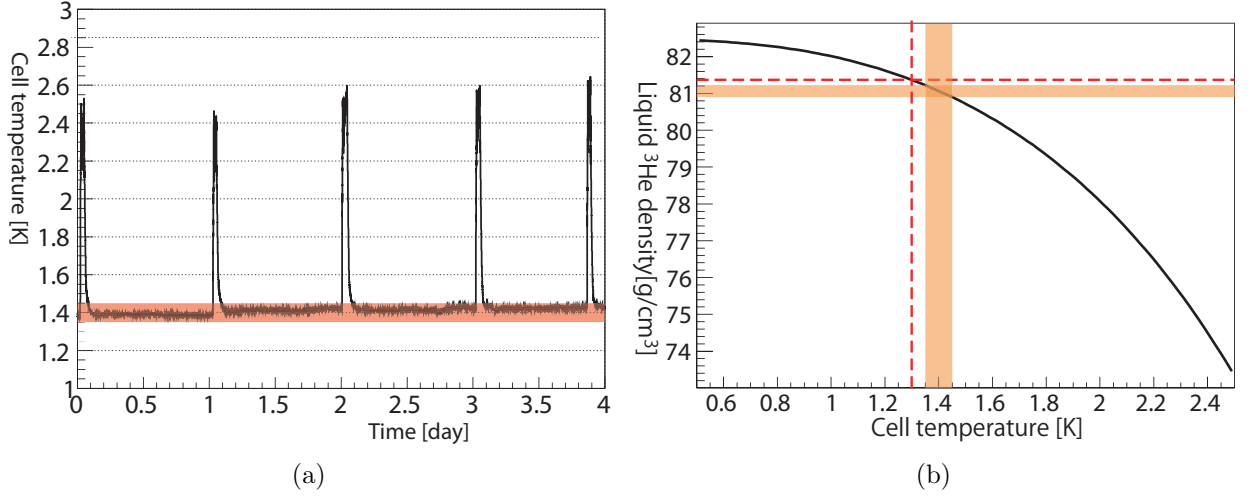


Figure A.2: Left : Stability of the temperature at the target cell during the production run. Right : Density equation of  $^3\text{He}$  [74]. The hatched regions represent the uncertainty of the temperature measurement and the density of the liquid  $^3\text{He}$ . The red dotted line represents the result of the test operation of the target system [73].

Table A.1: Summary of the operation conditions of the  $^3\text{He}$  target system.

Vacuum level	$< 10^{-6}$	[mbar]
Leak rate of the $^3\text{He}$ system	$< 10^{-10}$	[Pa·m <sup>3</sup> /sec]
Temperature in the target cell	1.4	[K]
Vapor pressure in the target	33	[mbar]
Heat load to low-temperature part	0.21	[W]
Liquid $^4\text{He}$ consumption	50	[ℓ/day]
Liquid N <sub>2</sub> consumption	50	[ℓ/day]



# Appendix B

## Forward Counter analysis

The velocity of forward particles are expressed as,

$$\beta_{NC} = \frac{L_{vertex-NC}}{T_{T0-NC}^{measured} - T_{T0-vertex}^{calc.} \times c}, \quad (\text{B.1})$$

where  $L_{vertex-NC}$  is the flight length between the hit position on the NC and reaction vertex,  $T_{T0-NC}^{measured}$  is the measured flight time between T0 and NC, and  $T_{T0-vertex}^{calc.}$  is the calculated time between T0 and vertex by beam momentum. The energy losses in the materials between vertex and the T0 were considered.

### B.1 NC hit selection

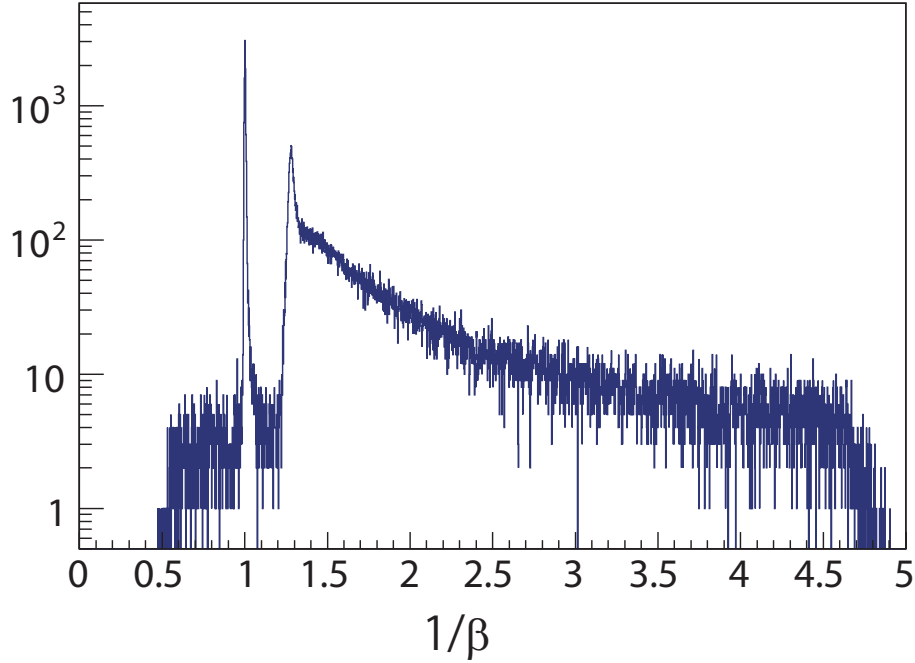
To obtain the flight time of the neutral particle and its hit position on the NC, the most upstream segment of the NC whose energy deposit was above the offline analysis threshold. The offline analysis threshold was set to 5 MeVee which is enough higher than online threshold value, 0.5 MeVee. the hit position of x-z direction was defined as center of the hit segment, and y position was evaluated from the time difference of the two PMT signals on both ends of the segment. The effective light propagation velocity to convert time difference to the y position was measured with  $^{90}\text{Sr}$  checking source and evaluated to be 14cm/ns.

#### B.1.1 Charged particles removal

To veto charged particle signal in the NC, the BVC and the CVC were used. No signal in the BVC and the CVC was requested to define neutral particle hit in the NC.

#### B.1.2 $\gamma$ - neutron separation with $1/\beta$ distribution

Figure B.1 shows  $1/\beta$  distribution of the neutral particles. The  $\gamma$  peak is shown at  $1/\beta = 1$  in Fig. B.1. With the  $\gamma$  peak, the relative time offset of the NC was calibrated. Neutrons were measured as continuous distribution in the larger  $1/\beta$  region. The TDC range was adjusted to detect the particles with -25 – 175 ns offset from the  $\gamma$ -ray. It corresponds to down to 200 MeV/c neutrons. A peak structure around  $1/\beta = 1.3$  is the quasi-free peak as the reaction of  ${}^{35}\text{S}(\text{K}^-, \text{N})\text{K}$ . Neutrons were identified with threshold of  $1/\beta > 1.15$ .

Figure B.1:  $1/\beta$  distribution of the NC.

## B.2 Momentum resolution of the neutrons

The  $1/\beta$  resolution of the neutrons can be defined as,

$$\sigma_{\frac{1}{\beta}} = \frac{1}{L_{vertex-NC}} \sqrt{c^2 \sigma_t^2 + \left( \frac{1}{\beta} - \frac{1}{\beta_{beam}} \right) \sigma_z^{vertex} + \left( \frac{\sigma_z^{NC}}{\beta} \right)}, \quad (\text{B.2})$$

where  $L_{vertex-NC}$  is the length between reaction vertex and the NC,  $\sigma_t^2$  is the time resolution of the TOF between the T0 and the NC,  $\sigma_z^{vertex}$  is z resolution of the reaction vertex which was evaluated to be 0.65 cm in Sec. 3.6.3, and  $\sigma_z^{NC}$  is z-resolution of the NC hit which value was estimated to be  $5\text{cm} / \sqrt{12} = 1.44\text{cm}$  with thickness of the NC segments.

Figure B.2 shows distributions of  $1/\beta$  resolution and momentum resolution of neutrons.  $\sigma_t$  was evaluated to be 140 ps from width of the  $\gamma$  peak in Fig. B.1. The momentum resolution of neutrons was evaluated to be 5 MeV/c at neutron momentum is 1.0 MeV/c.

## B.3 Precision of the Missing mass scale

To check missing mass resolution and center value of beam momentum, three reaction  ${}^3\text{He}(K^-, K^-pn)X$ ,  ${}^3\text{He}(K^-, K_s^0pn)X$ ,  ${}^3\text{He}(K^-, K_s^0n)X$  were checked. From these three reaction, values of missing masses of proton, neutron and deuteron were obtained.

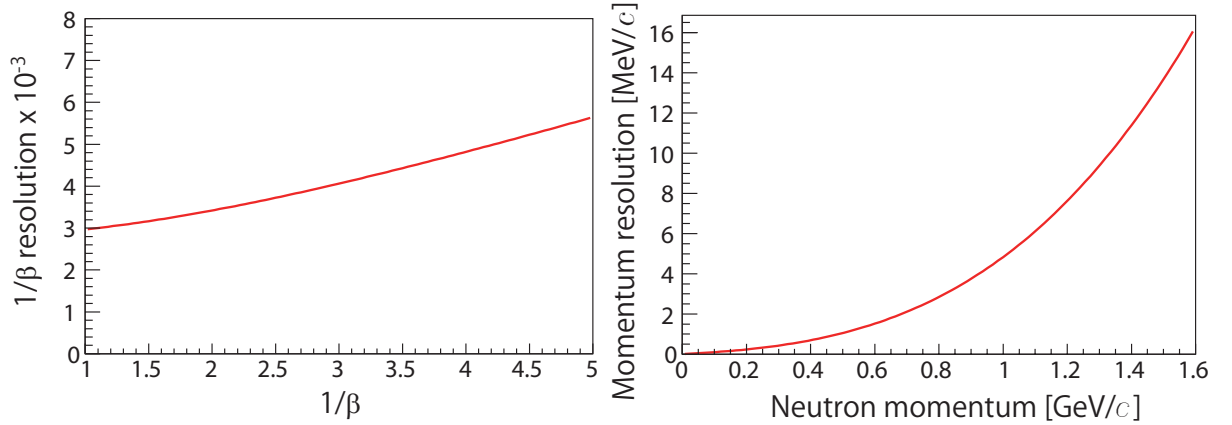


Figure B.2:  $1/\beta$  resolution distribution of the NC(left) and neutron momentum resolution (right).

### B.3.1 ${}^3\text{He}(K^-, K^-pn)X$ reaction

To detect missing proton mass,  ${}^3\text{He}(K^-, K^-pn)X$  reaction was used.  $K^-$  and proton are detected by the CDS, and neutron is detected by the NC. Figure B.3 shows distribution of the missing mass spectra in the  ${}^3\text{He}(K^-, K^-pn)X$  reaction. In Fig B.3, a peak of missing proton are clearly seen. By fitting with Gaussian, missing proton center of mass is  $937.0 \pm 0.9 \text{ MeV}/c^2$ ,  $\sigma$  of mass is  $18.2 \pm 0.9 \text{ MeV}/c^2$

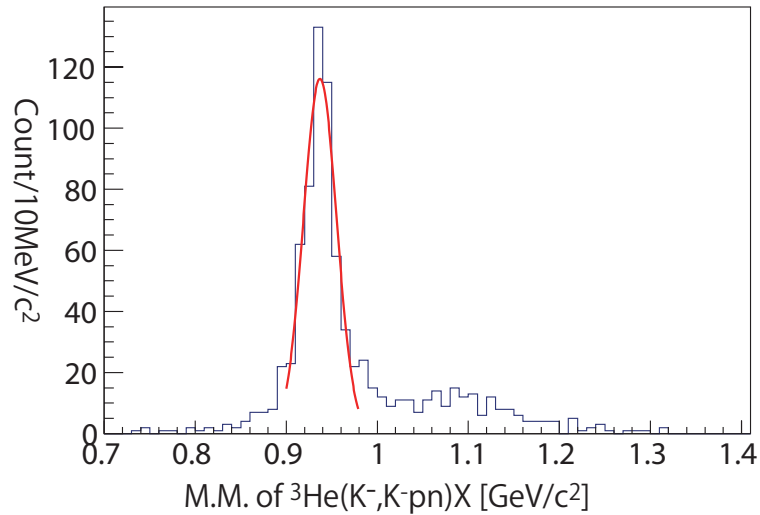


Figure B.3: Missing mass distribution of  ${}^3\text{He}(K^-, K^-pn)X$

### B.3.2 ${}^3\text{He}(K^-, K_s^0 pn)X$ reaction

To detect missing neutron mass,  ${}^3\text{He}(K^-, K_s^0 pn)X$  reaction was used.  $K_s^0$  is reconstructed by  $\pi^+\pi^-$  detected by the CDS. A peak of missing neutron is seen in Fig B.4. Missing proton center of mass is  $935.7 \pm 4.5 \text{ MeV}/c^2$ ,  $\sigma$  of mass is  $23.6 \pm 5.6 \text{ MeV}/c^2$

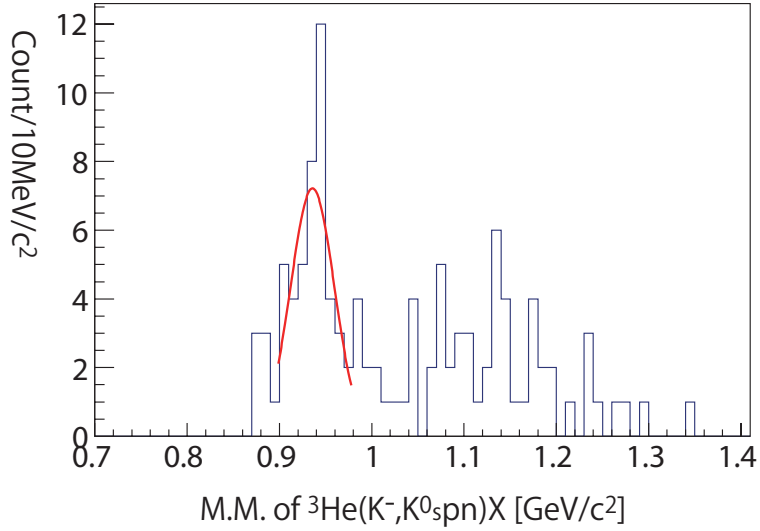
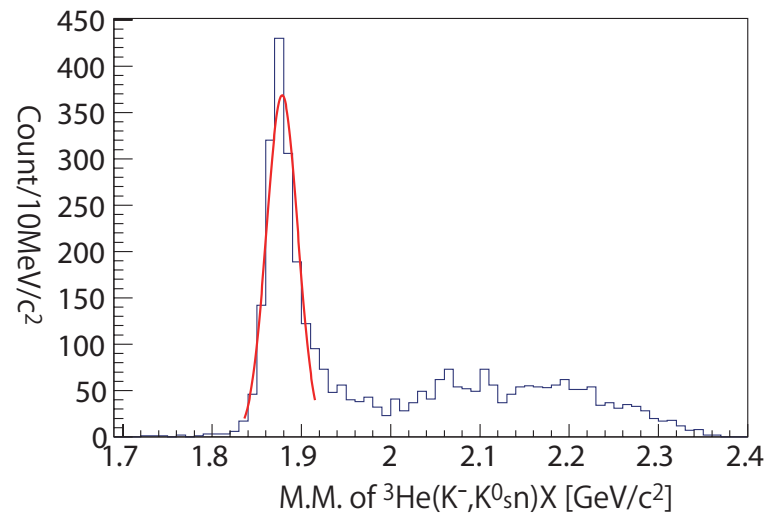


Figure B.4: Missing mass distribution of  ${}^3\text{He}(K^-, K_s^0 pn)X$

### B.3.3 ${}^3\text{He}(K^-, K_s^0 n)X$ reaction

To check a value of missing mass of deuteron,  ${}^3\text{He}(K^-, K_s^0 n)X$  reaction was analyzed. A peak of missing deuteron is seen in Fig B.5. Missing deuteron center of mass is  $1878.3 \pm 0.5 \text{ MeV}/c^2$ ,  $\sigma$  of mass is  $17.5 \pm 0.5 \text{ MeV}/c^2$

Figure B.5: Missing mass distribution of  ${}^3\text{He}(K^-, K_s^0)nX$



# Appendix C

## Simulation study for expected processes

Study for expected processes in  ${}^3\text{He}(K^-, \Lambda p)$  analysis was performed by simulation to estimate contamination in the  ${}^3\text{He}(K^-, \Lambda p)n_{\text{miss}}$  reaction. Multi-nucleon absorption of Kaon is a one of the expected processes. Kaon is absorbed by two or three nucleons (2NA, 3NA) and produced  $\Lambda$  or  $\Sigma^0$ .

Each process was generated to be flat distribution in the phase space of the final state, as

$$\frac{d^2\sigma_{\text{NA}(Ypn+\#\pi)}}{dT_n^{CM}d\cos\theta_n^{CM}} \propto \rho_3(Ypn + \#\pi), \quad (\text{C.1})$$

where  $\sigma_{\text{NA}(Ypn+\#\pi)}$  is the simulated event distribution for the particles in final state,  $T_n^{CM}$  is the kinetic energy of the neutron in the CM frame, and  $\cos\theta_n^{CM}$  is the neutron emission angle in the CM frame. If there is a spectator nucleon, the Fermi momentum distribution was considered [84].

Invariant mass and missing mass spectra of each process are shown in the following sections

### C.1 Spectra of 2NA( $\Lambda pn_s$ ) reaction

Invariant mass of 2NA process is distributed in high energy region ( $2.8 - 3 \text{ GeV}/c^2$ ) due to  $\Lambda(\Sigma^0)p$  pair have all energy of the reaction.

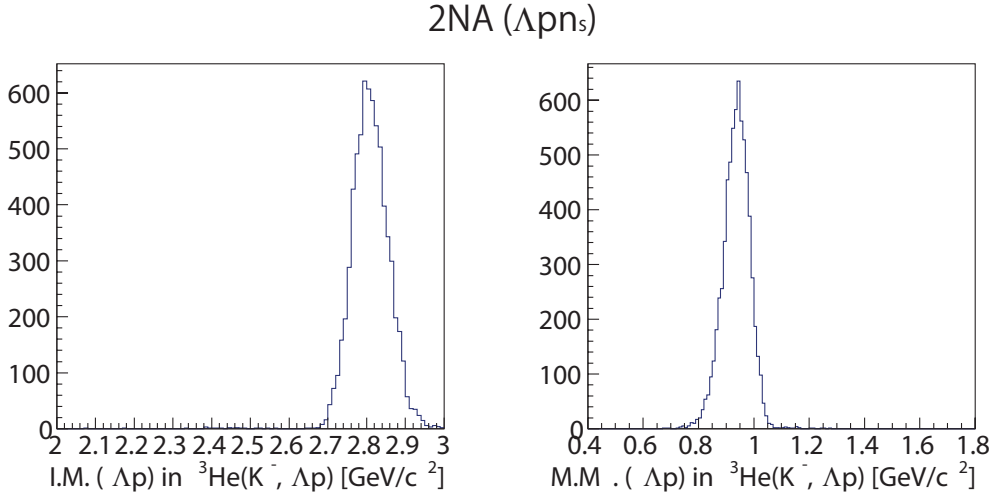


Figure C.1: Invariant mass (left) and missing mass spectra of simulated  $2\text{NA}(\Lambda p n_s)$  reaction.

## C.2 Spectra of $2\text{NA}(\Lambda p n_s + \pi)$ reaction

Due to additional pion, invariant mass distribution is broader than one of  $2\text{NA}(\Lambda p n_s)$  reaction.

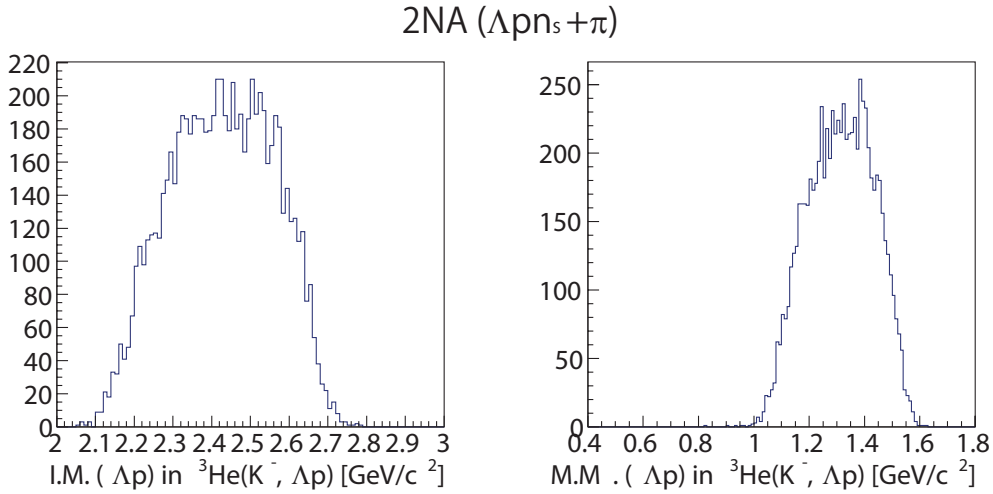


Figure C.2: Invariant mass (left) and missing mass spectra of simulated  $2\text{NA}(\Lambda p n_s + \pi)$  reaction.

## C.3 Spectra of $2\text{NA}(\Sigma^0 p n_s)$ reaction

Invariant mass peak is shifted lower and missing mass peak is shifted higher than them of  $2\text{NA}(\Lambda p n_s)$  reaction because of missing  $\gamma$  from  $\Sigma^0 \rightarrow \Lambda \gamma$  decay. However, missing mass distribution sit almost around "missing neutron" position, because missing energy by decayed  $\gamma$  from  $\Sigma^0$  is as small as only 80 MeV.

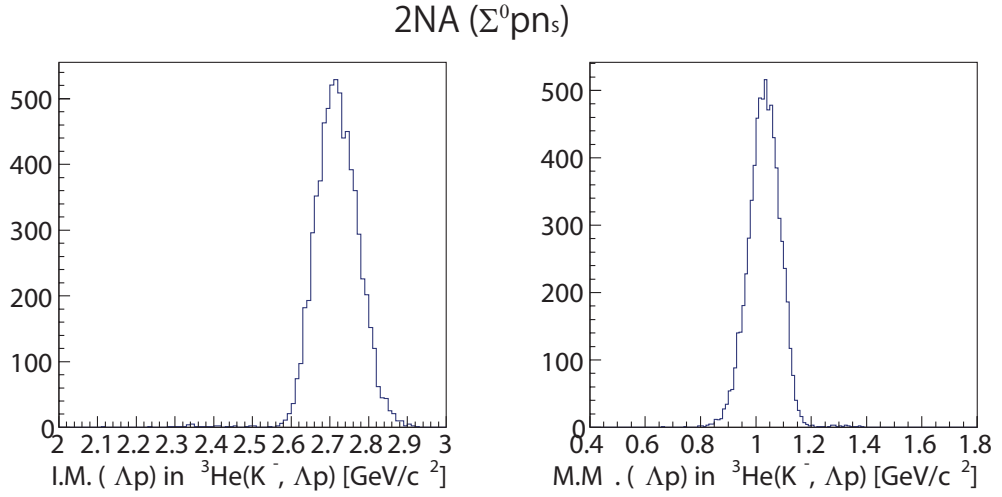


Figure C.3: Invariant mass (left) and missing mass spectra of simulated  $2\text{NA}(\Sigma^0 p n_s)$  reaction.

## C.4 Spectra of $2\text{NA}(\Sigma^0 p n_s + \pi)$ reaction

Additional pion with  $\Sigma^0 p n$  production is also simulated. Due to the additional pion production together with missing  $\gamma$  from  $\Sigma^0$  decay push missing mass distribution higher than genuine  ${}^3\text{He}(K^-, \Lambda p)n$  reaction.

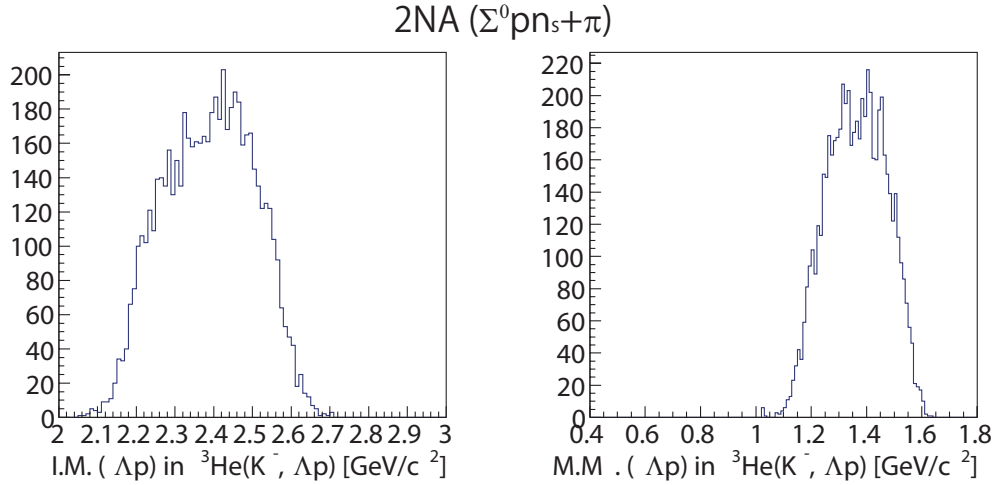


Figure C.4: Invariant mass (left) and missing mass spectra of simulated  $2\text{NA}(\Sigma^0 p n_s + \pi)$  reaction.

## C.5 Spectra of $3\text{NA}(\Lambda p n)$ reaction

Invariant mass shows almost flat distribution. Reduction of a detection efficiency in low mass region (mass  $< 2.4 \text{ GeV}/c^2$ ) is caused the reductions of acceptance of low energy  $\Lambda$

and proton.

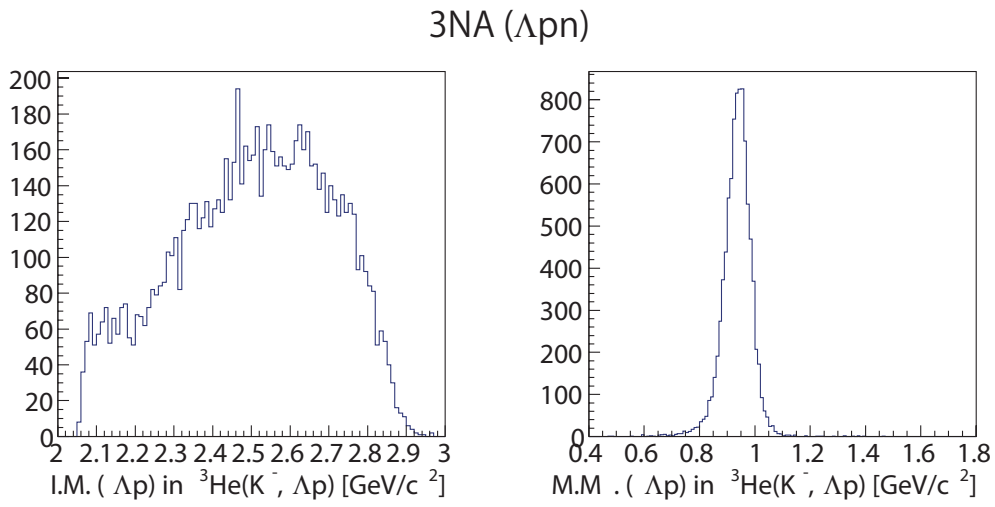


Figure C.5: Invariant mass (left) and missing mass spectra of simulated 3NA( $\Lambda p n$ ) reaction.

## C.6 Spectra of $3\text{NA}(\Lambda pn + \pi)$ reaction

When emitted pions are increase, distribution of invariant mass shifted lower side due to energy conservation.

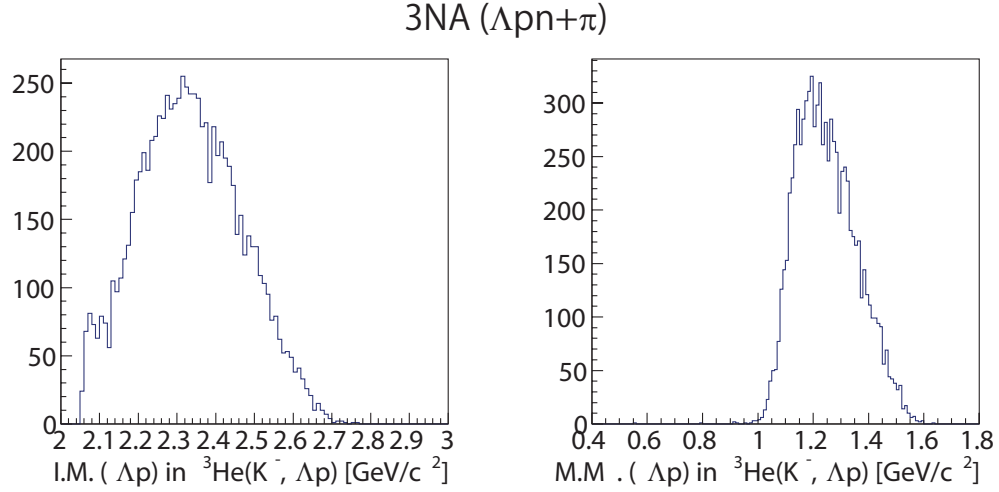


Figure C.6: Invariant mass (left) and missing mass spectra of simulated  $3\text{NA}(\Lambda pn + \pi)$  reaction.

## C.7 Spectra of $3\text{NA}(\Lambda pn + 2\pi)$ reaction

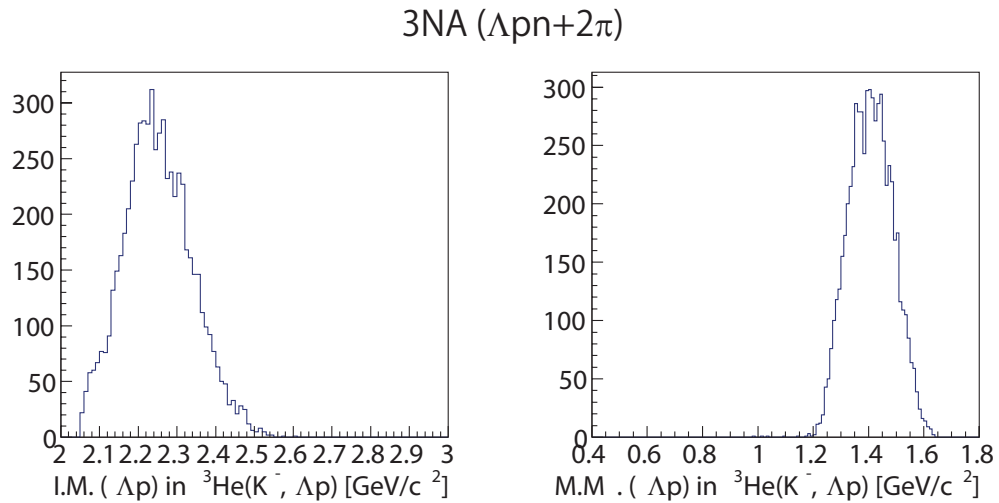


Figure C.7: Invariant mass (left) and missing mass spectra of simulated  $3\text{NA}(\Lambda pn + 2\pi)$  reaction.

## C.8 Spectra of $3\text{NA}(\Lambda pn + 3\pi)$ reaction

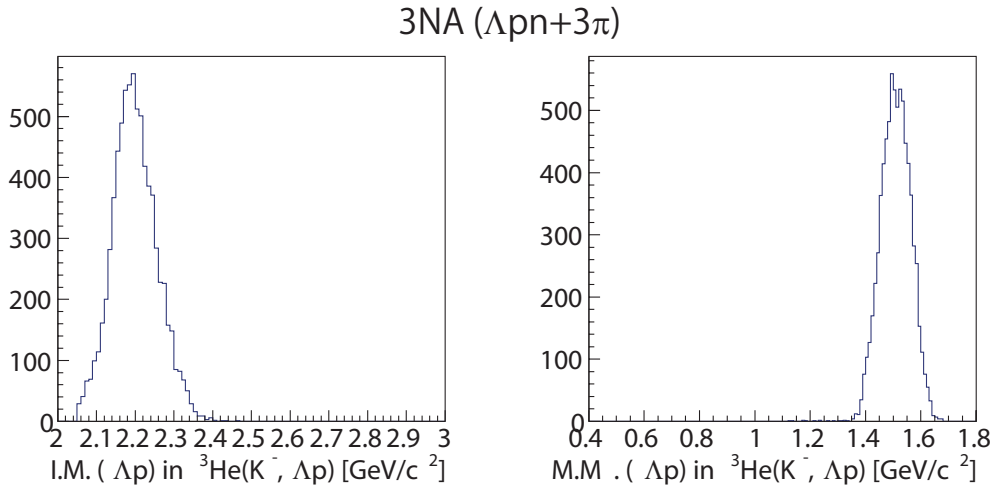


Figure C.8: Invariant mass (left) and missing mass spectra of simulated  $3\text{NA}(\Lambda pn + 3\pi)$  reaction.

## C.9 Spectra of $3\text{NA}(\Sigma^0 pn)$ reaction

property of invariant mass spectrum is same as that of  $3\text{NA}(\Lambda pn)$  reaction. Missing mass peak shifted higher due to missing  $\gamma$  of  $\Sigma^0$  decay.

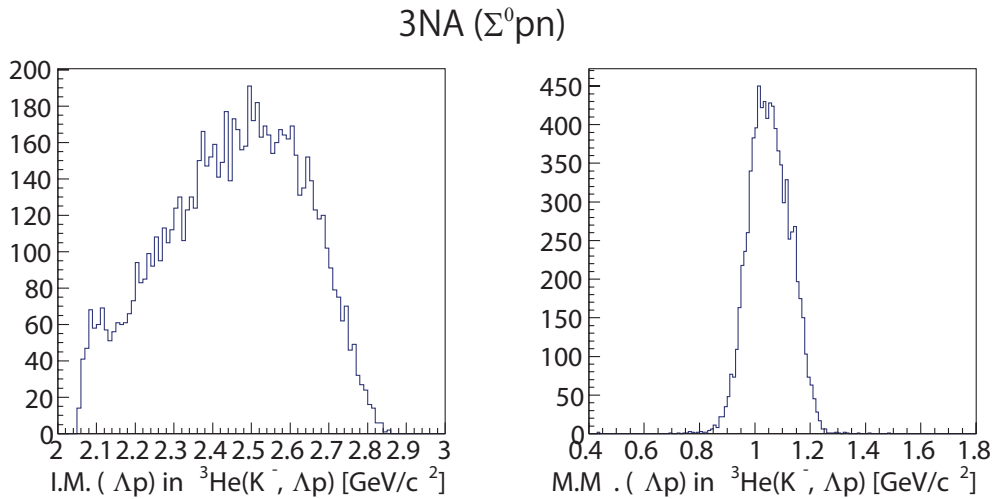


Figure C.9: Invariant mass (left) and missing mass spectra of simulated  $3\text{NA}(\Sigma^0 pn)$  reaction.

## C.10 Spectra of $3\text{NA}(\Sigma^0 pn + \pi)$ reaction

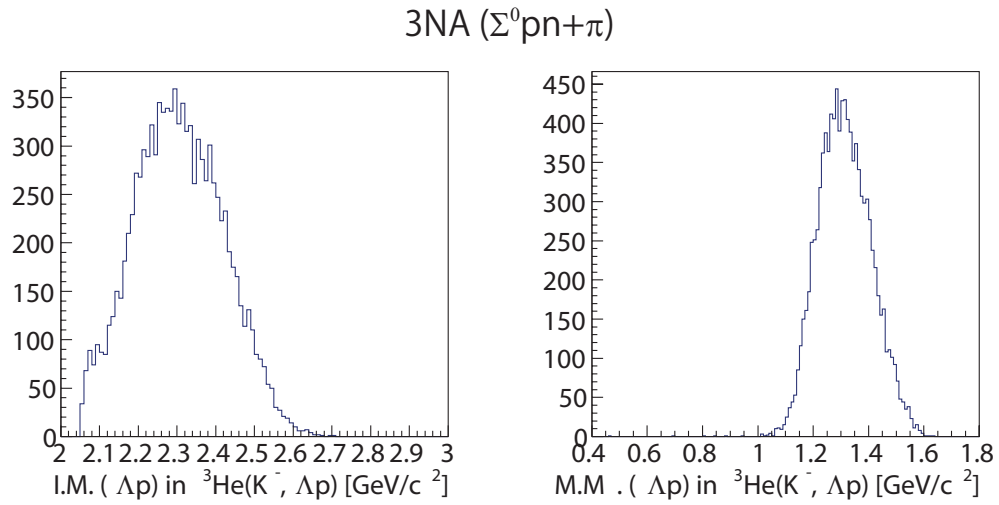


Figure C.10: Invariant mass (left) and missing mass spectra of simulated  $3\text{NA}(\Sigma^0 pn + \pi)$  reaction.

## C.11 Spectra of $3\text{NA}(\Sigma^0 pn + 2\pi)$ reaction

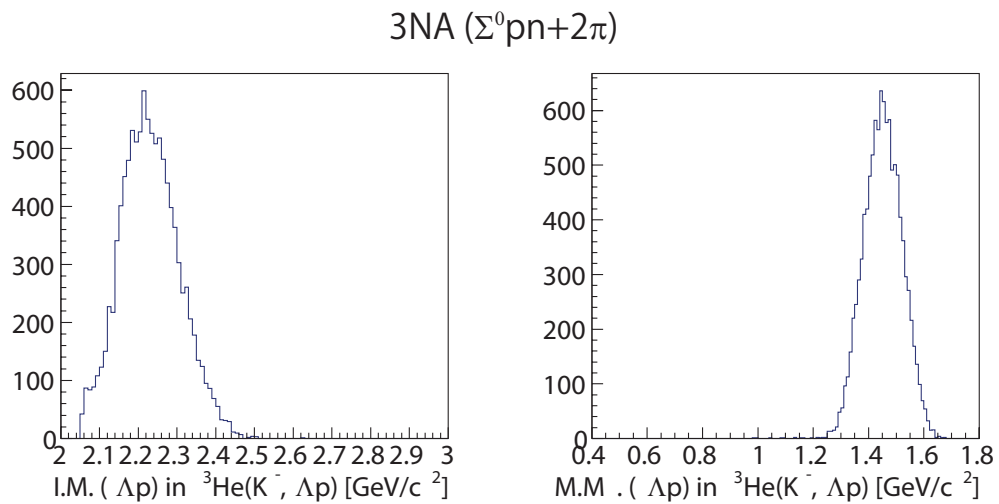


Figure C.11: Invariant mass (left) and missing mass spectra of simulated  $3\text{NA}(\Sigma^0 pn + 2\pi)$  reaction.

## C.12 Spectra of $3\text{NA}(\Sigma^0 pn + 3\pi)$ reaction

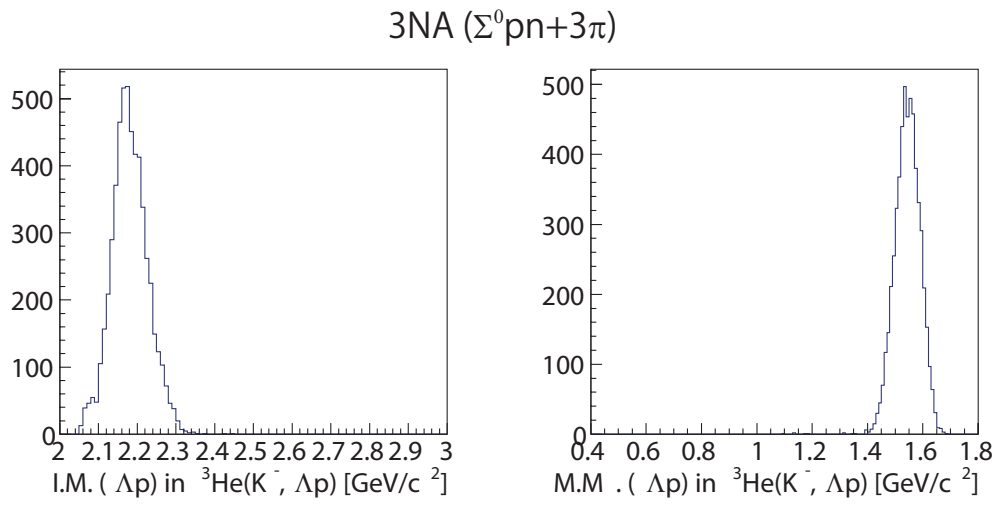


Figure C.12: Invariant mass (left) and missing mass spectra of simulated  $3\text{NA}(\Sigma^0 pn + 3\pi)$  reaction.

# Appendix D

## Theoretical investigation of the data of ${}^3\text{He}(K^-, \Lambda p)n$ events

T. Sekihara, E. Oset, and A. Ramos done a theoretical investigation of the peak structure in our data[87]. They estimated  $\Lambda p$  invariant mass spectrum assuming two scenarios to interpret the peak structure. One is  $\Lambda(1405)$  p resonance, not forming a bound state which converted to  $\Lambda$  p. The other is  $KNN$  bound state which decays to  $\Lambda p$ . In both scenarios, the induced kaon is scattered with a nucleon in  ${}^3\text{He}$ , and scattered slow kaon is absorbed by the remaining  $NN$  pair. They employed a fully antisymmetrized  ${}^3\text{He}$  wave function, which leads to many different combinations of the first and second scattering processes. They also used Jacobi coordinates to describe  ${}^3\text{He}$  system. The  $\bar{K}N$  interaction around threshold is obtained within a chiral unitary approach, and the interaction of the kaon with the two nucleons was treated in terms of the fixed center approximation to the Faddeev equation.

Figure D.1 shows differential cross section of the in-flight  ${}^3\text{He}(K^-, \Lambda p)n$  reaction for the  $\Lambda(1405)$  p resonance. A blue colored line shows fitting result of Eq. 4.2. A plotted data points was scaled to fitting result of Eq. 4.2, and are shown in arbitrary units. It is difficult to explain the data, especially the behavior of the lower tail about  $2.3 \text{ GeV}/c^2$  in  $\Lambda p$  invariant mass by only  $\Lambda(1405)$  p resonance scenario.

Then, Figure D.2 shows differential cross section of the in-flight  ${}^3\text{He}(K^-, \Lambda p)n$  reaction for the  $KNN$  bound state. Fitting result was scaled to be total cross section becomes  $7\mu\text{b}$ . Two peak structure in the  $\Lambda p$  invariant mass was generated by a quasi-elastic in the first collision of kaon and a nucleon, and the production of the  $\bar{K}NN$  bound state. A binding energy and a mass width of calculated  $\bar{K}NN$  is about  $15 \text{ MeV}$ , and  $70\text{MeV}/c^2$ . The total cross sections and the binding energies of calculation and data fitting result are good agreement. The mass width of calculation is smaller than it of data fitting ( $\sim 110 \text{ MeV}/c^2$ ). It may indicate the peak structure in the data have two-peak like as theoretical calculation.

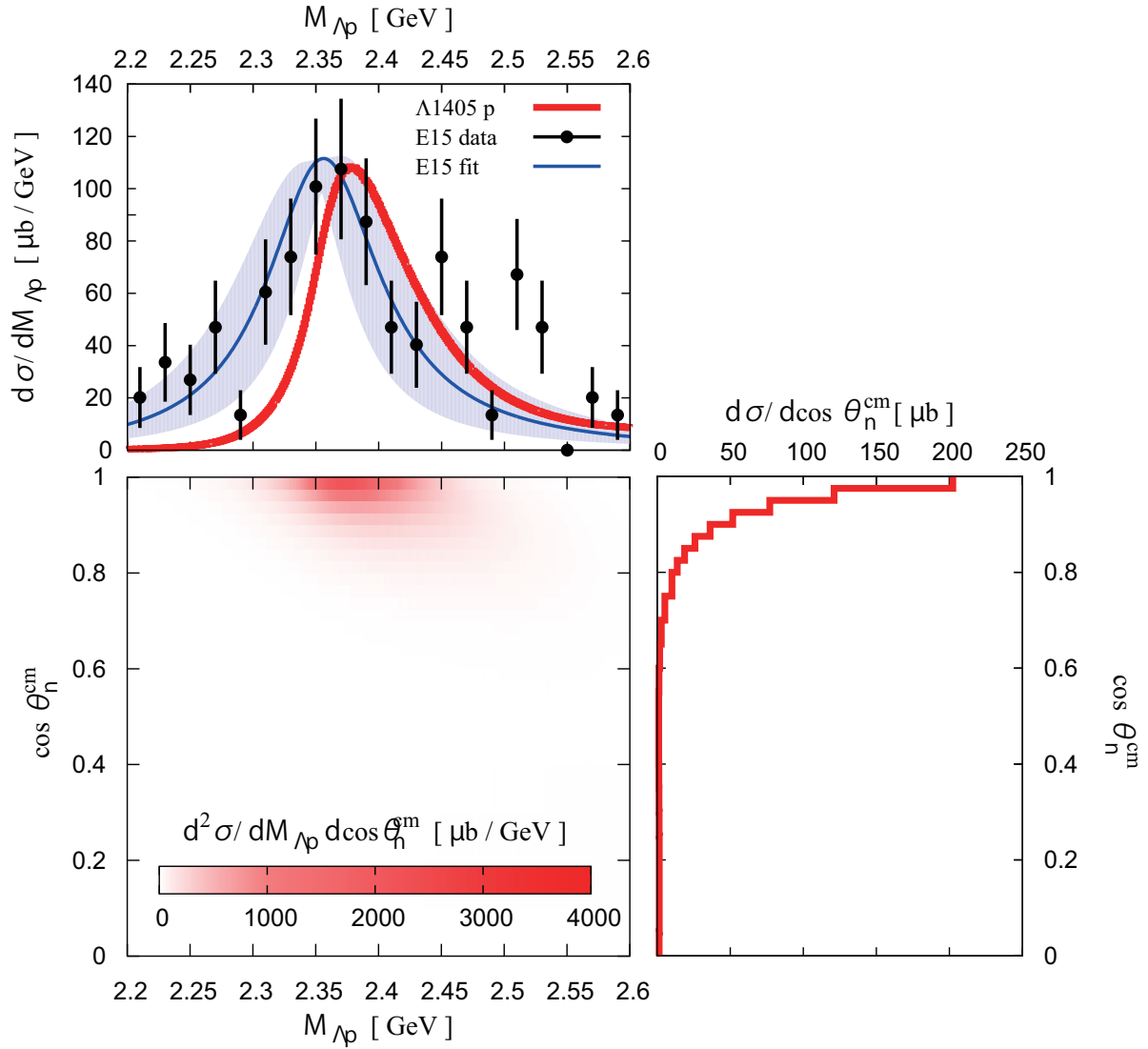


Figure D.1: differential cross section of the in-flight  ${}^3\text{He}(K^-, \Lambda p)n$  reaction for the  $\Lambda(1405)$  p resonance. Taken from [87]. A blue colored line shows fitting result of Eq. 4.2. A plotted data points was scaled to fitting result of Eq. 4.2, and are shown in arbitrary units.

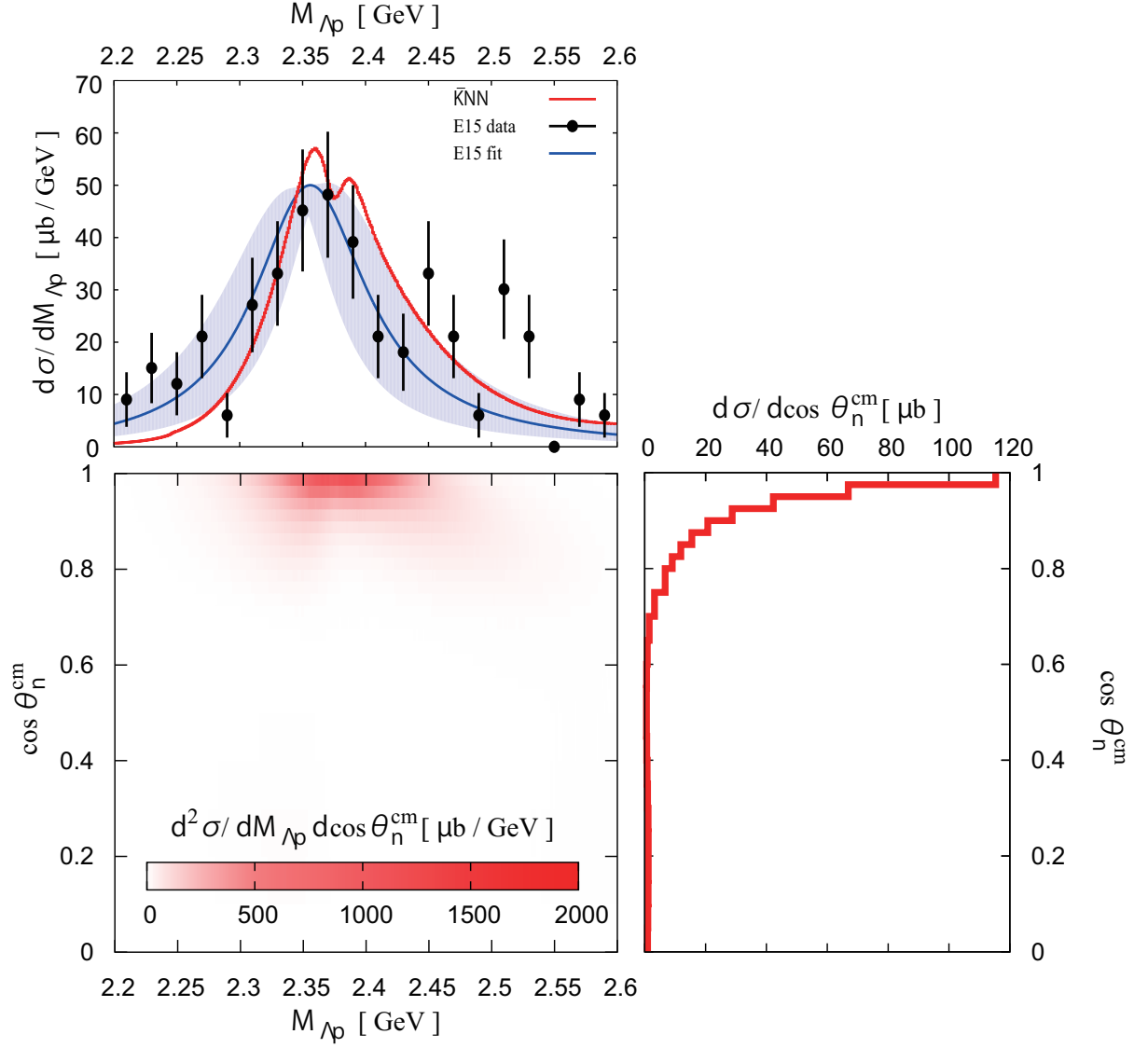


Figure D.2: Differential cross section of the in-flight  ${}^3\text{He}K^-, \Lambda p)n$  reaction for the  $KNN$  bound state. Taken from [87]. A blue colored line shows fitting result of Eq. 4.2[87]. Fitting result was scaled to be total cross section becomes  $7\mu\text{b}$ . A plotted data points was scaled to fitting result of Eq. 4.2, and are shown in arbitrary units.



# Appendix E

## Fermi momentum distribution of ${}^3\text{He}$

In the Monte Colro simulation, the Fermi momentum distribution of a spectator nucleon was produced by the data of a past measurement[84] in which proton momentum distribution of  ${}^3\text{He}$  was measured by using the reaction  ${}^3\text{He}(e, e'p)$  at  $p_e = 310$  MeV/c. We fitted the data with the following empirical equation as,

$$\exp(p_0 + p_1x + p_2 \exp(p_3x)), \quad (\text{E.1})$$

where  $p_x$ s are free parameters. Figure E.1 shows proton momentum distribution of  ${}^3\text{He}$  and fitting result. Obtained function was used to generate Fermi momentum of a spectator in the simulation.

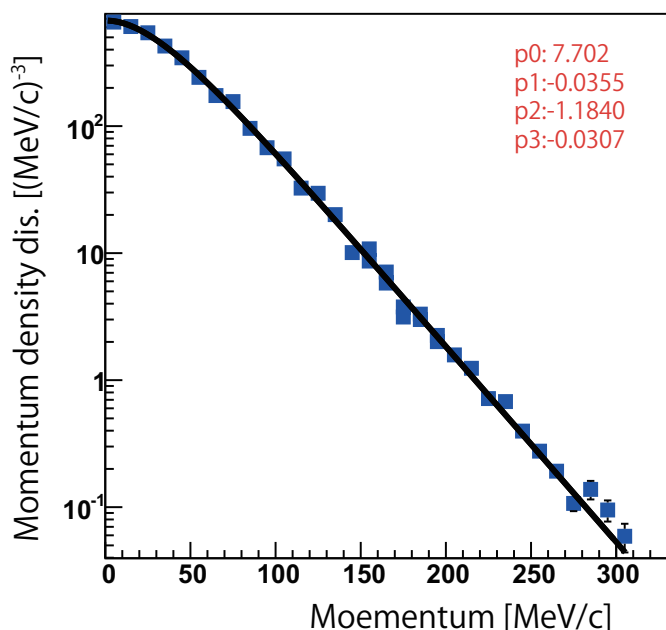


Figure E.1: Proton momentum distribution of  ${}^3\text{He}$  and fitting result. The blue boxes show the data taken from [84].



# reference

- [1] A. D. Martin, Nucl. Phys. B **179**, 33 (1981).
- [2] W. E. Humphrey and R. R. Ross, Phys.Rev. **127**, 1305 (1962).
- [3] M. Sakitt, T. Day, R. Glasser, N. Seeman, J. Friedman, *et al.*, Phys.Rev. **139**, B719 (1965).
- [4] T. Mast, M. Alston-Garnjost, R. Bangerter, A. Barbaro-Galtieri, F. Solmitz *et al.*, Phys.Rev. D **11**, 3078 (1975).
- [5] T. S. Mast, M. Alston-Garnjost, R. O. Bangerter, A. S. Barbaro-Galtieri, F. T. Solmitz, *et al.*, Phys.Rev. D **14**, 13 (1976).
- [6] J. Kadyk, Y. Oren, G. Goldhaber, G. Goldhaber, and G. Trilling, Phys.Rev.Lett. **17**, 599 (1966).
- [7] G. Sayer, E. Beall, T. Devlin, P. Shepard, and J. Solomon, Phys.Rev. **169**, 1045 (1968).
- [8] R. Nowak, J. Armstrong, D. Davis, D. Miller, D. Tovee *et al.*, Nucl. Phys. B **139**, 61 (1978).
- [9] S. Deser, M. Goldberger, K. Baumann, and W. E. Thirring, Phys. Rev. **96**, 774 (1954).
- [10] T. Trueman, Nucl. Phys. **26**, 57 (1961).
- [11] M. Iwasaki, R. Hayano, T. Ito, S. Nakamura, T. Terada *et al.*, Phys. Rev. Lett. **78**, 3067 (1997).
- [12] T. Ito, R. Hayano, S. Nakamura, T. Terada, M. Iwasaki *et al.*, Phys. Rev. C **58**, 2366 (1998).
- [13] G. Beer *et al.*, Phys. Rev. Lett. **94**, 212302 (2005).
- [14] M. Bazzi, G. Beer, L. Bombelli, A. Bragadireanu, M. Cargnelli *et al.*, Phys. Lett. B **704**, 113 (2011).
- [15] M. Bazzi, G. Beer, L. Bombelli, A. Bragadireanu, M. Cargnelli *et al.*, Nucl. Phys. A **881**, 88 (2012).
- [16] Y. Ikeda, T. Hyodo, and W. Weise, Phys. Lett. B **706**, 63 (2011).

- [17] Y. Ikeda, T. Hyodo, and W.Weise, Nucl. Phys. A **881**, 98 (2012).
- [18] M. Mai and Ulf-G. Meißner, Nucl. Phys. A **900**, 51 (2013).
- [19] A. Cieplé and J. Smejkal, Nucl. Phys. A **881**, 115 (2012).
- [20] Z.-H. Guo and J.A. Oller, Nucl. Phys. Rev. C **87**, 035202 (2013).
- [21] T. Hyodo, Nucl. Phys. A **914**, 260 (2013).
- [22] E. Friedman and A. Gal, Nucl. Phys. A **899**, 60 (2013).
- [23] E. Friedman, A. Gal, and C. Batty, Phys. Lett. B **308**, 6 (1993).
- [24] C. Batty, E. Friedman, and A. Gal, Phys. Rept. **287**, 385 (1997).
- [25] T. Waas, N. Kaiser, and W. Weise, Phys. Lett. B **379**,34 (1996).
- [26] T. Waas, N. Kaiser, and W. Weise, Phys. Lett. B **365**, 12 (1996).
- [27] A. Ramos and E. Oset, Nucl. Phys. A **671**, 481 (2000).
- [28] T. Kishimoto, T. Hayakawa, S. Ajimura, S.Minami, A. Sakaguchi *et al.*, Nucl. Phys. A **754**, 383 (2005).
- [29] T. Kishimoto, T. Hayakawa, S. Ajimura, F. Khanam, T. Itabashi *et al.*, Prog. Theor. Phys. **118**, 181 (2007).
- [30] V.Magas, J. Yamagata-Sekihara, S. Hirenzaki, E. Oset, and A. Ramos, Phys. Rev. C **81**, 024609 (2010).
- [31] D.W. Thomas *et al.*, Nucl. Phys. B **56**, 15 (1973).
- [32] R.J. Hemingway, Nucl. Phys. B **253**, 742 (1985).
- [33] K. Moriya *et al.*, (CLAS Collaboration) Phys. Rev. Lett. **112**, 082004 (2014).
- [34] N. Isgur, G. Karl, Nucl. Phys. Rev. D **18**, 4187 (1978).
- [35] R.H. Dalitz, T.C. Wong and G. Rajasekaran, Phys. Rev. **153**, 1617 (1967).
- [36] Jonathan M. M. Hall *et al.*, Phys. Rev. Lett. **114**, 132002 (2015).
- [37] D. Jido *et al.*, Nucl. Phys. A **725**, 181 (2003).
- [38] Y. Nogami, Phys. Lett. **7**, 288 (1963).
- [39] Y. Akaishi and T. Yamazaki, Phys. Rev. C **65**, 044005 (2002).
- [40] T. Suzuki, H. Bhang, G. Franklin, K. Gomikawa, R. Hayano, *et al.*, Phys. Lett. B **597**, 263 (2004).

- [41] T. Suzuki, H. Bhang, G. Franklin, K. Gomikawa, R. Hayano, *et al.*, Nucl. Phys. A **754**, 375 (2005).
- [42] M. Sato, H. Bhang, J. Chiba, S. Choi, Y. Fukuda, *et al.*, Phys. Lett. B **659**, 107 (2008).
- [43] H. Yim, H. Bhang, J. Chiba, S. Choi, Y. Fukuda, *et al.*, Phys. Lett. B **688**, 43 (2010).
- [44] M. Agnello *et al.*, Phys. Rev. Lett. **94**, 212303 (2005).
- [45] V. Magas, E. Oset, A. Ramos, and H. Toki, Phys. Rev. C **74**, 025206 (2006).
- [46] T. Yamazaki *et al.*, Phys. Rev. Lett. **104**, 132502 (2010).
- [47] T. Yamazaki and Y. Akaishi, Phys. Rev. C **76**, 045201 (2007).
- [48] P. Kienle *et al.*, Eur. Rev. J. A **48**, 183 (2012).
- [49] S. Sibirtsev, Phys. Lett. B **359**, 29 (1995).
- [50] G. Bendiscioli, A. Fontana, L. Lavezzi, A. Panzarasa, A. Rotondi, *et al.*, Nucl. Phys. A **789**, 222 (2007).
- [51] L. Fabbietti *et al.*, Nucl. Phys. A **914**, 60 (2013).
- [52] G. Agakishiev *et al.*, Phys Lett. B **742**, 242 (2015).
- [53] A. O. Tokiyasu *et al.*, Phys.Lett. B **728**, 616 (2014).
- [54] Y. Ichikawa *et al.*, Prog. Theor. Exp. Phys. 021D01 (2015).
- [55] T. Yamazaki and Y. Akaishi, Phys. Lett. B **535**, 70 (2002).
- [56] N. V. Shevchenko, A. Gal, and J. Mares' Phys. Rev. C **76**, 044004 (2007).
- [57] Y. Ikeda, and T. Sato, Phys. Rev. C **79**, 035201 (2009).
- [58] S. Wycech, and A. M. Green , Phys. Rev. C **79**, 014001 (2009).
- [59] S. Maeda, Y. Akaishi, and T.Yamazaki, Proc. Jpn. Acad., Ser. B **89**, 418 (2013).
- [60] A. Doté, T. Hyodo, and W. Weise, Phys. Rev. C **79**, 014003 (2009).
- [61] Y. Ikeda, H. Kamano, and T. Sato, prog. Theor. Physy. **124** 533 (2010).
- [62] N. Barnea, A. Gal, and E. Z. Liverts, Phys. Lett. B **712** 132 (2012).
- [63] J. Revai, and N. V. Shevchenko, Phys. Rev. C **90**, 034004 (2014).
- [64] T. Hashimoto(E15 collaboration)., Prog. Theor. Exp. Phys. 061D01 (2015).
- [65] D. Gotta, *et al.*, Phys. Rev. C **51**, 2 (1995).

- [66] G. Backenstoss *et al.*, Phys. Rev. Lett **55**, 25(1985).
- [67] V. Vander, Velde-Wilquet *et al.*, Nuovo Cimento Soc. Ital. Fis. **39A**, 538 (1977).
- [68] K. Agari *et al.*, Prog. Theor. Exp. Phys. 02B008 (2012).
- [69] K. Agari *et al.*, Prog. Theor. Exp. Phys. 02B009 (2012)
- [70] K. Agari *et al.*, Prog. Theor. Exp. Phys. 02B011 (2012).
- [71] H. Kawamuko, T. Nakaya, K. Nitta, and M. Yokoyama, PoS **PD07** 043 (2006).
- [72] M. Sato *et al.*, Nucl. Inst. and Meth. A **606** 233 (2009).
- [73] M.Iio *et al.*, Nucl. Inst. and Meth. A **687** 1 (2012).
- [74] Y.H. Huang, G. B. Chen, X. Y. Li, and V. Arp, International Journal of Thermodynamics **26** 729 (2005).
- [75] TOSCA
- [76] H. Noumi *et al.*, J-PARC E31 proposal.  
[http://j-parc.jp/researcher/Hadron/en/pac\\_0907/pdf/Noumi.pdf](http://j-parc.jp/researcher/Hadron/en/pac_0907/pdf/Noumi.pdf)
- [77] T. K. Ohsaka *et al.*, Nuclear Science, IEEE Transactions on **33**, 98 (1986).
- [78] M. Sato *et al.*, Phys. Lett. B **659** 107 (2008).
- [79] KEK report **85-10**, (1985).
- [80] M. Shiozawa, O. Sasaki, M. Nomachi, and T. K. Ohsaka, A new TKO system manager board for a dead-time-free data acquisition system, in 1944 *IEEE Nuclear Science Symposium – NSS'94*, pages 632–635, IEEE, 1994.
- [81] TRANSPORT
- [82] S. Agostinelli *et al.*, (GEANT4 Collaboration), Nucl. Instrum. Meth. A **506**, 250 (2003).
- [83] R. H. Dalitz., Phys. Rev. **94** 1046 (1954).
- [84] E. Jans *et al.*, Phys. Rev. Lett. **49**, 974 (1982).
- [85] V. Flaminio, W. G. Moorhead, D. R. O. Morrison, and N. Rivoire., CERN HERA 83-2 (1983).
- [86] T. Harada, Private communication (2016).
- [87] T. Sekihara, E. Oset, and A. Ramos., Prog. Theor. Exp. Phys. 123D03 (2016).